



HAL
open science

Theoretical study of superfluid helium nanodroplet dynamics: cluster formation, ion solvation, Coulomb explosion, and nucleation and quantum vortex detection

Ernesto García-Alfonso

► **To cite this version:**

Ernesto García-Alfonso. Theoretical study of superfluid helium nanodroplet dynamics: cluster formation, ion solvation, Coulomb explosion, and nucleation and quantum vortex detection. Physics [physics]. Université de Toulouse, 2024. English. NNT: 2024TLSES069 . tel-04701599

HAL Id: tel-04701599

<https://theses.hal.science/tel-04701599v1>

Submitted on 18 Sep 2024

HAL is a multi-disciplinary open access archive for the deposit and dissemination of scientific research documents, whether they are published or not. The documents may come from teaching and research institutions in France or abroad, or from public or private research centers.

L'archive ouverte pluridisciplinaire **HAL**, est destinée au dépôt et à la diffusion de documents scientifiques de niveau recherche, publiés ou non, émanant des établissements d'enseignement et de recherche français ou étrangers, des laboratoires publics ou privés.

Doctorat de l'Université de Toulouse

préparé à l'Université Toulouse III - Paul Sabatier

Etude théorique de la dynamique de nanogouttes d'hélium
superfluide : formation d'agrégats, solvatation d'ions,
explosion coulombienne, et nucléation et détection de vortex
quantiques.

Thèse présentée et soutenue, le 29 mai 2024 par

Ernesto GARCÍA ALFONSO

École doctorale

SDM - SCIENCES DE LA MATIERE - Toulouse

Spécialité

Physique de la Matière

Unité de recherche

LCAR - Laboratoire Collisions Agrégats Réactivité

Thèse dirigée par

Nadine HALBERSTADT

Composition du jury

Mme Pina ROMANIELLO, Présidente, CNRS Occitanie Ouest

M. Lionel POISSON, Rapporteur, CNRS Île-de-France Meudon

Mme Alexandra VIEL, Rapporteur, CNRS Bretagne et Pays de la Loire

M. Marcel MUDRICH, Examineur, Aarhus University

Mme Nadine HALBERSTADT, Directrice de thèse, CNRS Occitanie Ouest

Membres invités

M. Marti PI PERICAY, Universitat de Barcelona

**Theoretical study of superfluid
helium nanodroplet dynamics:
cluster formation, ion solvation,
Coulomb explosion, quantum
vortex nucleation and detection.**

by

Ernesto García Alfonso

2024

Toulouse. France

“We must not forget that when radium was discovered no one knew that it would prove useful in hospitals. The work was one of pure science. And this is a proof that scientific work must not be considered from the point of view of the direct usefulness of it. It must be done for itself, for the beauty of science, and then there is always the chance that a scientific discovery may become like the radium a benefit for humanity.”

Marie Curie

Dedicated to :

all my loved ones

Acknowledgements

First of all, I would like to thank my family who have always supported me in all my decisions and encouraged me to study abroad and come out of my home. Special thanks to my parents, my twin brother and my whole family living in Barcelona. Also, I would like to thanks Grace-Marie for her love during this time.

Relevant thanks to my former tutors Jesús Rubayo Soneira and Maykel Marquez Mijares for teaching me and introducing me to the scientific world. I would like also to highlight the role done by Manuel Barranco and Martí Pi, with whom we had many interactions during my thesis: they taught me about the He Density Functional Theory and its programs. This thesis is also dedicated to you.

The dynamics simulations presented in this work have been carried out thanks to the HPC resources of CALMIP supercomputing center (<https://www.calmip.univ-toulouse.fr/>). Thanks also to the Laboratoire Collisions Agrégats Réactivité (LCAR, <https://www.lcar.ups-tlse.fr/>) at Paul Sabatier University (Toulouse III, <https://www.univ-tlse3.fr/>) for allowing me to be part of it and to the persons managing the s09 computing cluster (Didier Lemoine and David Sanchez).

Finally, and do not less important I thanks to Nadine Halberstadt for her superb pieces of advice and for teaching me about almost everything both scientific and personal issues. I will always be thankful for allowing me to spend these three years under her supervision and for leading me to be a better person.

Abstract

Several dynamical processes involving Helium-4 nanodroplets (HNDs) are studied theoretically, in relation with experiments. HNDs are clusters of several hundred to several hundred billions of ^4He atoms which exhibit remarkable properties: very low temperature, $T \sim 0.4\text{K}$, superfluid properties, ability to pickup any dopant, weak interaction with any atom or molecule. The studied processes reflect the two main interests in HNDs: characterizing superfluid properties in a finite-size system (quantum vortex nucleation and detection), and using HNDs as an ideal environment to study dopant spectroscopy and dynamics (clustering, ion solvation, and Coulomb explosion).

Extensive simulations are conducted using ^4He -Density Functional Theory (^4He -DFT) and its time-dependent version (^4He -TDDFT). This approach can successfully simulate the equilibrium and dynamics of droplets of several thousand of atoms and provide detailed insight into the structural dynamics of the entire system which is not accessible experimentally: visualization of solvation shells, nature of helium droplet excitations.

Rare gas (Rg) cluster formation is studied inside He_N under realistic conditions where one Rg atom collides with a solvated n -atom cluster to form the $(n+1)$ -atom cluster. The ^4He -DFT simulation results are compared to those of approximate atomistic approaches. Although quantum and superfluidity effects are better described with ^4He -TDDFT, several common features are demonstrated. The most stable gas phase configuration is usually not produced, but an isomer with fewer bonds instead, and/or more dilute structures because of the rigidity of the helium solvation shell around the Rg atoms.

The sinking of alkali (Ak) cations in HNDs is simulated in parallel with experimental investigations in the group of Stapelfeldt (Aarhus), in complement to earlier studies on Na^+ sinking. It aims at shedding some light on the primary steps of solvation, by suddenly ionizing the alkali atom sitting in a dimple at the droplet surface. The build up of the first solvation shell around the ions is shown to be progressive, pointing to a Poissonian mechanism in which each He atom binds independently to the ion. For the lighter alkalis, the solvation shell is incomplete at the end of the dynamics, suggesting a kinetic rather than thermodynamical control of its formation.

Coulomb explosion simulations of Ak_2 molecules initially sitting at the droplet surface and suddenly ionized are conducted in order to understand the effect of the HNDs on Ak_2^{++} fragmentation dynamics. The corresponding experiment in Stapelfeldt's group in Aarhus aimed at measuring the proportion of triplet to singlet state in the formation of Ak_2 , and at imaging the vibrational wave function. Several parameters are examined in the simulations: droplet size, zero point motion of Ak_2 vibration, and orientational distribution of Ak_2 on the droplet surface. The results validate the experimental approach, and evidence an unexpected curvature of the ion trajectories which could be used to measure droplet sizes individually, something that has only been possible up to now for very large sizes (by X-ray diffraction).

The nucleation of quantum vortices, a characteristic of helium superfluidity, has been revealed in very large droplets (VLD) and attributed to angular momentum created by friction of the liquid in the nozzle prior to expansion and cooling. Here droplet-droplet collisions are explored as an alternative mechanism. The results show the nucleation of quantum vortices at indentations of the merged droplet, a mechanism general for all droplet sizes. However, no signature has been found to detect vortices in smaller droplets so far. In this work, fluorescence absorption or excitation spectroscopy of alkali atoms is proposed: a vortex is shown to shift and broaden the alkali spectrum. The effect could be measurable above the first excited states.

Résumé

On étudie des processus dynamiques de nanogouttes d'hélium-4 (HND), en relation avec des expériences. Les HND sont des agrégats de centaines à des centaines de milliards d'atomes d' ^4He aux propriétés remarquables : très basse température ($T \sim 0.4\text{K}$), superfluidité, capacité à capturer n'importe quel dopant, interaction faible avec tout atome ou molécule. Les processus étudiés se rangent selon deux axes: caractérisation de propriétés superfluides dans un système de taille finie (nucléation et détection de vortex quantiques), et utilisation de HND comme environnement idéal pour étudier la spectroscopie et la dynamique de dopants (formation d'agrégats, solvation d'ions et explosion coulombienne).

L'outil principal des simulations est l'approche de la fonctionnelle de la densité d'hélium indépendante (^4He -DFT) ou dépendante du temps (^4He -TDDFT). Elle permet de simuler la structure et la dynamique de gouttelettes de plusieurs milliers d'atomes et donne un aperçu détaillé de la dynamique du système qui n'est pas accessible expérimentalement : visualisation des couches de solvation, nature des excitations de l'hélium.

On étudie la formation d'agrégats de gaz rares (Rg) en nanogouttes en modélisant la collision d'un atome de Rg avec un agrégat solvatoé de n atomes pour former l'agrégat $(n+1)$. La ^4He -TDDFT, qui décrit mieux les effets quantiques et de superfluidité, est comparée à des méthodes atomistiques approchées. Plusieurs résultats sont communs: on n'obtient généralement pas la configuration la plus stable en phase gazeuse, mais un isomère avec moins de liaisons, et/ou des structures diluées par la couche rigide de solvation d'hélium autour des atomes Rg.

La solvation de cations d'alcalins (Ak) dans les HND est simulée parallèlement à des expériences du groupe de Stapelfeldt (Aarhus) d'ionisation soudaine de l'atome Ak initialement en surface, en complément d'études antérieures sur Na^+ . L'objectif est d'éclairer les étapes élémentaires de la solvation. La formation de la première couche de solvation des ions s'avère progressive, et compatible avec un mécanisme de Poisson où chaque hélium se lie à l'ion de façon indépendante. Pour les alcalins plus légers, cette couche est incomplète à la fin de la dynamique, ce qui indique un contrôle cinétique plutôt que thermodynamique de sa formation.

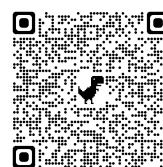
Des simulations d'explosion coulombienne par ionisation instantanée de molécules Ak_2 initialement en surface de nanogouttes sont effectuées afin de comprendre

l'effet des HND sur la dynamique de fragmentation d' Ak_2^{++} . L'expérience correspondante menée dans le groupe de Stapelfeldt visait à mesurer la proportion d'état triplet/singulet dans la formation d' Ak_2 , et à imager la fonction d'onde vibrationnelle. On examine dans les simulations l'influence de la taille des nanogouttes, du mouvement de point zéro de la vibration d' Ak_2 et de la distribution d'orientations d' Ak_2 en surface. Les résultats valident l'approche expérimentale et montrent une importance inattendue de la courbure des trajectoires des ions qui pourrait être utilisée pour mesurer la taille des gouttelettes, ce qui n'a été possible jusqu'à présent que pour de très grandes tailles (par diffraction des rayons X)

La nucléation de vortex quantiques, caractéristique de la superfluidité, a été démontrée dans de très grosses gouttelettes (VLD) et attribuée au moment angulaire créé par friction du liquide dans la buse avant expansion et refroidissement. On étudie ici les collisions entre gouttelettes comme mécanisme alternatif. Les résultats montrent la nucléation de vortex quantiques au niveau d'indentations de la gouttelette fusionnée, un mécanisme général pour toutes les tailles. Cependant, aucune signature n'a été trouvée jusqu'à présent pour détecter des vortex dans les plus petites gouttelettes. Ce travail propose la spectroscopie de fluorescence d'atomes Ak en montrant qu'un vortex déplace et élargit leur spectre de façon mesurable au-dessus des premiers états excités.

List of publications related to this thesis

Ernesto García-Alfonso, Manuel Barranco, Nadine Halberstadt and Martí Pi. “*Time-resolved solvation of alkali ions in superfluid helium nanodroplets*”. **The Journal of Chemical Physics**. **160**, 164308 2024 <https://doi.org/10.1063/5.0205951>



Ernesto García-Alfonso, Francesco Ancilotto, Manuel Barranco, Martí Pi, Nadine Halberstadt . “*Quantized vortex nucleation in collisions of superfluid nanoscopic helium droplets at zero temperature*”. **The Journal of Chemical Physics**. **159**, 074305, 2023 <https://doi.org/10.1063/5.0165820>



Ernesto García-Alfonso, Manuel Barranco, David A. Bonhommeau, Nadine Halberstadt, Martí Pi and Florent Calvo. “*Clustering, collision , and relaxation dynamics in pure and doped helium nanoclusters: Density -vs- particle based approaches*”. **The Journal of Chemical Physics**. **157**, 014106, 2022 <https://doi.org/10.1063/5.0091942>



Ernesto García-Alfonso, Francois Coppens, Manuel Barranco, Martí Pi, Frank Stienkemeier and Nadine Halberstadt. “*Alkali atoms attached to vortex-hosting helium nanodroplets*”. **The Journal of Chemical Physics**. **152**, 194109, 2020 <https://doi.org/10.1063/5.0008923>



TABLE OF CONTENTS

Acknowledgements	III
Abstract	IV
Résumé	VI
List of publications	VIII
I. Introduction to Superfluid Helium	1
I-1. Bulk Superfluid Helium	2
I-1.1. Superfluid properties	2
I-1.2. Superfluidity at the atomic scale	4
I-1.3. The two-fluid model	4
I-1.4. Landau's criterion for superfluidity	6
I-2. Superfluid He droplets	9
I-3. Vorticity in superfluid ^4He droplets	12
I-4. Energetic balance	13
I-5. How droplets are obtained in experiments	14
II. Density functional theory of liquid ^4He at zero temperature	21
II-1. Density functional theory for helium	22
II-2. The Orsay-Trento density functional	23
II-3. Time-Independent ^4He -DFT for doped droplets	25
II-4. Time Dependent DFT (^4He -TDDFT)	27
II-5. Technical details	29
II-5.1. Imaginary time propagation	29
II-5.2. Predictor-corrector propagator	31
II-5.3. Absorption box	31
II-6. Vortices within the ^4He -DFT framework	32
II-6.1. Irrotationality within ^4He -TDDFT	32
II-6.2. Quantization of the circulation around a vortex line	33
II-6.3. Vortex core	34
II-6.4. Velocity field in cylindrical symmetry	34
II-6.5. Energy of a linear vortex in cylindrical symmetry	35
II-6.6. Total angular momentum of a linear vortex	35

II-6.7. How to imprint a vortex line in ^4He -DFT	36
III. Clustering in Helium Nanodroplets	37
III-1. Introduction	37
III-2. Method	38
III-3. Results	40
III-3.1. Formation of Ar dimer	41
III-3.2. Formation of Ar trimer	41
III-3.3. Formation of Ar pentamer	42
III-4. Conclusion	44
IV. Alkali ion solvation into a $^4\text{He}_{2000}$ droplet	67
IV-1. Introduction	67
IV-2. Method	68
IV-3. Results	69
IV-4. Conclusions	74
V. Ak_2 Coulomb Explosion on a ^4He nanodroplet	87
V-1. Introduction	87
V-1.1. Coulomb explosion as a tool to differentiate singlet from triplet Ak_2	88
V-1.2. Dynamics simulation upon double ionization of $\text{Ak}_2@^4\text{He}_N$	89
V-1.3. An Experimental setup	90
V-2. Method	92
V-2.1. ^4He -TDDFT applied to Coulomb explosion	92
V-2.2. Width due to the diatomic vibrational amplitude	94
V-2.3. Width due to the diatomic angular distribution on the droplet surface	94
V-3. Results of the Coulomb explosion dynamics	97
V-3.1. Kinetic energy distribution of the ions	100
V-3.2. Influence of the droplet size	101
V-3.3. Widths of the ions kinetic energy distribution due to vibration	105
V-3.4. Effect of the angle of the diatomic molecule with the surface of the droplet	107
V-4. Ions trajectory deviation by the helium droplet	109
V-4.1. Simulation results	110
V-4.2. A model to estimate the ions trajectory deflection for large droplets	112
V-4.2.1. The Rigid Sphere Model	113
V-4.2.2. Equations of Motion and Dynamics	115
V-4.2.3. Results	119
V-4.2.4. Analytical fit	119
V-5. Conclusions	121
VI. Droplets Coalescence and Quantum Vortex Nucleation	123

VI-1. Introduction	123
VI-2. Method	124
VI-3. Results	126
VI-4. Conclusions	131
VII. Alkali Spectroscopy for Vortex Detection in Nanodroplets	145
VII-1. Ak@ ⁴ He ₁₀₀₀	145
VII-2. Method	146
VII-3. Results	147
VII-4. Conclusion	151
VIII. To Conclude	167
VIII-1. Summary of the work	167
VIII-2. Future prospects	169
References	171
Annexes	183
A. ⁴ He and ³ He physical properties	184
B. OT-DFT parameters	185
C. Simulation of absorption and emission spectra using the density fluctuation method	186
D. Details of the Coulomb explosion simulation	189
D.4.1. Ak ₂ (<i>v</i> = 0) wave function	189
D.4.2. Ak ⁺ -Ak ⁺ interaction	190
E. Details about the Coulomb explosion results	191
E.5.1. Ak ₂ @ ⁴ He _N equilibrium configuration	191
E.5.2. Effect of Ak ₂ bond length distribution on the final angle between the ions velocity vectors	192
E.5.3. Check on the effect of the three-body potential for Rb ₂ ³ Σ _u ⁺	193
F. Main characteristics of the interaction potentials	195
G. Technical details for the ⁴ He-TDDFT calculations	196
Résumé étendu en français	197
1. Introduction	197
2. Les méthodes ⁴ He-DFT et ⁴ He-TDDFT	199
2.1. ⁴ He-DFT pour des nanogouttes pures	199
2.2. ⁴ He-(TD)DFT pour des nanogouttes dopées	201
2.3. Vortex linéaire	202
2.4. Bilan énergétique	203
3. Formation d'agrégats en nanogouttelettes d'hélium	205
3.1. Méthode	206
3.2. Formation de dimères d'argon	208
3.3. Formation d'un trimère d'argon	208
3.4. Formation de pentamères d'argon (Ar ₅)	209

3.5.	Conclusions	211
4.	Solvatation d'ions alcalins Ak^+ en nanogoutte d'hélium ${}^4\text{He}_{2000}$. . .	213
4.1.	Introduction	213
4.2.	Méthode	214
4.3.	Résultats	215
4.4.	Conclusions	220
5.	Ak_2 Coulomb Explosion	223
5.1.	Introduction	223
5.2.	Méthode	224
5.3.	Résultats	225
5.3.1.	Influence de la taille des gouttelettes	225
5.3.2.	Largeurs de la distribution d'énergie cinétique des ions due aux vibrations	227
5.3.3.	Effet de l'angle de la molécule diatomique avec la surface de la nanogoutte	229
5.3.4.	Déviaton de la trajectoire des ions par la nanogoutte d'hélium	232
5.4.	Conclusion	233
6.	Coalescence de nanogouttes et nucléation de vortex quantiques . . .	235
6.1.	Introduction	235
6.2.	Méthode	235
6.3.	Résultats	237
6.4.	Conclusions	240
7.	Spectroscopie d'alcalins pour la détection de vortex en nanogouttes	243
7.1.	Détection de vortex quantiques dans les nanogouttes	243
7.2.	Méthode	244
7.3.	Résultats	244
7.4.	Conclusion	249
	List of Figures	250
	List of Tablas	255
	Curriculum Vitae	259

 CHAPTER I

INTRODUCTION TO SUPERFLUID HELIUM

Helium is the only natural element exhibiting superfluidity. Unlike all other substances, it remains liquid even down to absolute zero temperature. The most abundant helium isotope is ^4He which becomes superfluid at temperatures below 2.17K and saturated vapor pressure (λ -point, see Fig I.1). The different statistical character of the two helium isotopes produces dramatic differences in their physical properties (boson and fermion for ^4He and ^3He respectively), see Table A.1 in annex A for further physical comparison. Therefore, in the following sections, we only focus on the superfluidity of the bosonic isotope ^4He .

In figure I.1 a pressure-temperature phase diagram of ^4He in double logarithmic scale is shown. The dashed horizontal line marks atmospheric pressure. The critical point (c.p.) corresponds to a temperature of ($T=5.2$) K and pressure ($P=2.27$ bar). Furthermore, the λ -point ($T=2.17$ K) is characterized by the coexistence of the gas-liquid (He I) and superfluid (He II) states. The λ -line marks the transition between normal liquid He I and superfluid He II.

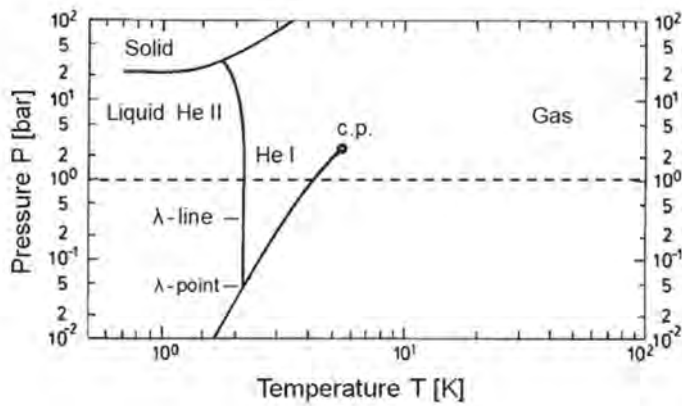


Figure I.1. Pressure-temperature phase diagram of ^4He in double logarithmic scale. Graph extracted from Slenczka and Toennies [1]

I-1. Bulk Superfluid Helium

I-1.1. Superfluid properties

One of the earliest and perhaps still the most spectacular manifestation of superfluidity is the “fountain effect” [2]. A He II fountain can be turned on and off by turning a heater on and off. The fountain effect is one of a number of effects called “thermomechanical effects”. The commonly accepted physical explanation for the fountain effect as an osmotic pressure is due to Tisza [3]. It is based on his two-fluid model [4] (see section I-1.3).

The helium fountain can be built by taking a tube with a wide opening at one end and a tiny opening at the other (see Fig I.2). The tube then is inserted into the helium II on the side where the wider opening is blocked with a porous plug (any material having small pores). A small heater is installed inside. When applying a small amount of heat to the heater, pressure builds up in the tube until a small fountain of liquid helium spouts from the tiny opening at the top.

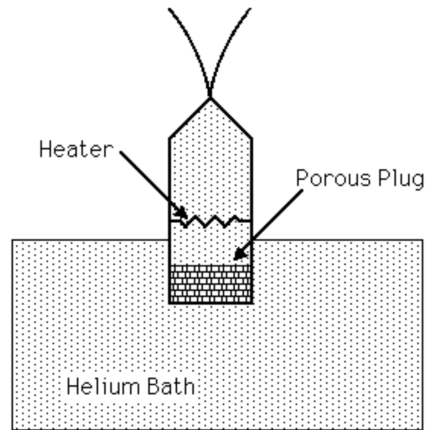


Figure I.2. A helium II fountain. A tube (containing a heater and a porous plug inside) embedded into a superfluid He II by its wider orifice. Figure taken from https://cryo.gsfc.nasa.gov/introduction/liquid_helium_D.html#fount_img

Another example of the flow properties of liquid ${}^4\text{He}$ below the λ point is provided by the “film” which covers the exposed surface of a body partially immersed in He II [5]. An empty beaker lowered into a He II bath begins to fill with bulk liquid, even though the rim is kept well above the bath surface (Figure I.3) because of the presence of the film on its walls. The filling process continues until the inner level reaches the level of the bath, at which point it stops. If the beaker is now raised, it empties itself again, and if it is raised clear of the bath, drops are seen to fall from the base of the beaker.

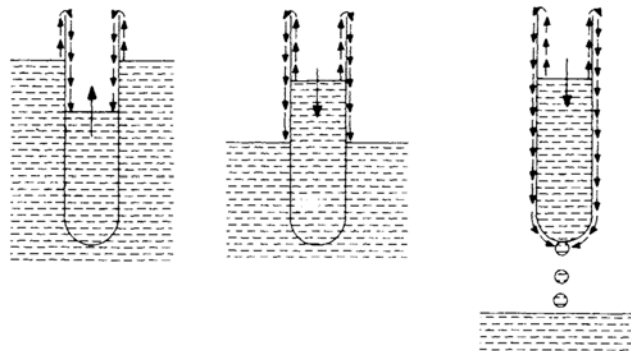


Figure I.3. Film flow of He II over the walls of a beaker. Figure taken from Ref [5]

Superfluidity means that a non-dissipative, irrotational flow can develop when liquid He is flowing in tubes or pipes [4]. At the same time, it means that an

object could move through the liquid without being hindered by the viscous drag that any normal fluid would be exerting on it because of viscosity (see Section I-1.4). It can also host quantum vortices (Section. I-3) whose characteristics are completely different from those of classical vortices.

I-1.2. Superfluidity at the atomic scale

On the atomic scale, helium superfluidity originates from the relatively weak atom-atom interactions combined with the low ^4He mass. The amplitude of the zero-point motion is larger than the average distance between atoms, hence exchange statistics effects are important. At this temperature range, quantum effects begin to be of primary importance in the properties of fluids, which are then called “quantum fluids”. When liquid helium is cooled below its superfluid transition temperature, a significant fraction of the ^4He atoms condense into the same lowest-energy quantum state, producing a macroscopic quantum state in which all participating particles travel together.

As a fermion, the ^3He isotope does not exhibit superfluid properties. However, it does become superfluid at $T \leq 2.7$ mK and a pressure of 33 atm [6]. This is due to the pairing of two fermions to form a boson. Comparing it with ^4He , ^3He is much lighter and less abundant [1].

I-1.3. The two-fluid model

Helium superfluid properties at temperatures between 0 and T_λ are often described in the framework of the two-fluid model [4]. It consists of an inviscid superfluid (density ρ_s), conventionally referred to as He II, and a viscous normal fluid (density ρ_n), or He I, with two independent velocity fields v_s and v_n . The resulting total density is expressed as

$$\rho = \rho_n + \rho_s \tag{I.1}$$

The mixing ratio of the two fluids depends on temperature. The viscosity of the liquid drops to near zero when it is cooled down below the λ -point, corresponding to a raise in the proportion of the superfluid component.

A necessary, though not sufficient, condition for superfluidity to appear is that the substance forms a condensate [7]. It must be found in a single coherent quantum state of the whole system that contains a macroscopic fraction of the substance. The nature of the normal fluid is believed to be composed of the “dilute gas” of the thermal excitations of the superfluid, for example: phonons, rotons, and ^3He atoms.

Tisza [3] provided an explanation of the helium fountain based on this two-fluid model. When the heater in the tube is turned on, the liquid helium in the tube begins to warm up. Since superfluid helium flows from cool areas to warm areas, it flows into the tube through the porous plug. Normal fluid is too viscous to flow out through the porous plug. Therefore, when the tube fills with liquid helium, the only way out for the normal fluid is to squirt out of the hole at the top.

As a summary, bulk superfluid helium is characterized by the following properties: it carries no thermal energy (no entropy); all of the heat energy is in the normal component; it has no viscosity; it can also flow through tiny holes and towards areas where the helium II is heated; a flow of superfluid into the heated area cools that area and restores the uniform mixture of normal and superfluid; heat causes superfluid to convert to normal.

Another property which was concluded from the the phenomenon shown in figure Fig I.3, is that the superfluid fraction flows through the film whenever there is a height difference between the two bulk liquid levels. In other words, the film acts like a siphon, the driving force for the superfluid being provided by the gravitational potential difference between the ends of the film. By observing the rate at which the beaker liquid level changes, the superfluid velocity may be determined; a typical value is 20 cm s^{-1} .

I-1.4. Landau's criterion for superfluidity

A quite simple argument, based on energy and momentum conservation, has been given by Landau in order to explain superfluidity in terms of the shape of the dispersion curve of elementary excitations [4], see Fig I.4. Let us consider a massive object moving through the stationary fluid with a given initial velocity v_i and a mass m much heavier than the ^4He atom mass. Energy dissipation corresponds to the transfer of kinetic energy from the moving object to create excitations in the liquid. It can only occur if suitable excitations can exist in the liquid, while conserving energy and momentum.

In an elementary event of energy exchange between a particle and the liquid, energy and momentum conservation are expressed as:

$$\frac{1}{2}mv_i^2 = \frac{1}{2}mv_f^2 + \epsilon \quad (\text{I.2})$$

and

$$m\mathbf{v}_i = m\mathbf{v}_f + \hbar\mathbf{k} \quad (\text{I.3})$$

where an elementary excitation with energy ϵ and momentum $\hbar k$ is created and the particle velocity is decreased from v_i to v_f .

From Eq.(I.2) and (I.3) we obtain

$$v_i \cos \theta = \frac{\epsilon}{\hbar k} + \frac{\hbar k}{2m} \quad (\text{I.4})$$

where θ is the angle between the momentum of the ion and that of the quasiparticle. Since $|\cos \theta| \leq 1$, the above equation results in the following relationship

$$v_i \geq \frac{\epsilon}{\hbar k} + \frac{\hbar k}{2m} \quad (\text{I.5})$$

Since it was assumed that the moving ion has a very large mass (compared to that of the ^4He atoms composing the fluid), the second term in the right-hand

side of Eq. (I.5) is negligible. The minimum value of $(\epsilon(k)/\hbar k)$ is found by setting $d(\epsilon(k)/\hbar k)/dk = 0$, yielding

$$\frac{d\epsilon(k)}{dk} = \frac{\epsilon(k)}{k}, \quad k \neq 0 \quad (\text{I.6})$$

re-writing the equation above we obtain

$$\epsilon(k) = k \frac{d\epsilon(k)}{dk} \quad (\text{I.7})$$

The minimum energy of an elementary excitation of the fluid which verifies energy and momentum conservation is when $\epsilon(k)$ is equal to the tangent of the $\epsilon(k)$ curve going through the origin.

For an ideal gas Eq.(I.6) can be verified from $\epsilon = 0$ since the excitation/dispersion curve $\epsilon(k)$ starts tangent to the momentum axis, whereas for superfluid helium it starts with a non-zero derivative. The smallest excitation energy is not zero and we can define the so-called Landau critical velocity v_L as

$$v_L = \left(\frac{\epsilon}{\hbar k} \right)_{\min} \quad (\text{I.8})$$

Below this threshold velocity, the moving object has no possibility to dissipate its kinetic energy into the fluid and therefore, it does not experience any friction. In other words, the fluid shows “superfluidity” ($v_L > 0$)

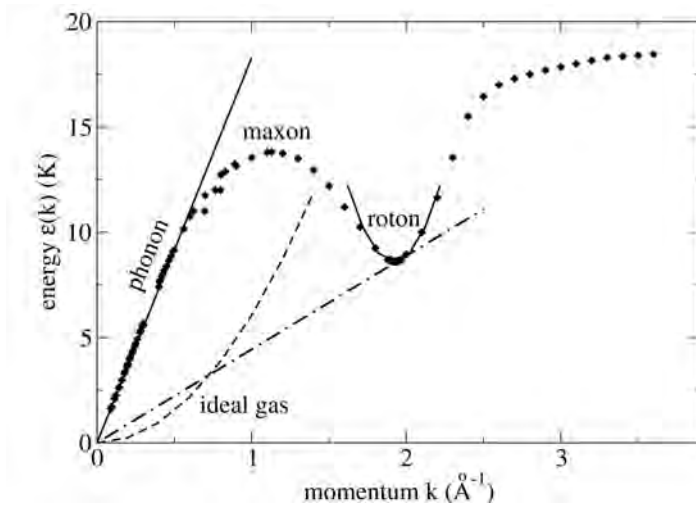


Figure I.4. Qualitative sketch of the energy spectrum of excitations in liquid He II (dots) and an ideal gas (dashed line). Excitations in the linear part at small k are phonons whereas excitations close to the relative minimum are called rotons. The dotted-dashed line drawn from the origin is tangent to the dispersion curve near the roton minimum and satisfies Eq.(I.6). Black points correspond to experimental data [8]. Figure taken from the literature [9]

The helium dispersion curve has been determined experimentally by Henshaw and Woods [10], Goble [11], Russell *et al* [8], H. Godfrin *et al.*[12] among others. It is represented in Fig I.4. For low k values it behaves linearly ($\epsilon(k) = \hbar kc$), the slope $c = 238 \text{ ms}^{-1}$ being the speed of ordinary sound (or “first sound” in the liquid helium context). It corresponds to ordinary acoustic waves in a liquid. These excitations are also known as “phonons”, since they are analogous to longitudinal phonons in a solid, for example, vibrations along the length of a bar. At higher values of k , the pattern of $\epsilon(k)$ deviates from linear. Landau introduced another type of excitations based on general thermodynamical properties, in particular the measure of the specific heat. These excitations are called “rotons” and their dispersion relation is assumed to be parabolic $\epsilon(k) = \Delta + \hbar^2(k - k_0)^2/2\mu$ around a certain momentum $\hbar k_0$. The parameters (Δ, k_0, μ) are fitted to experimental results. In the roton region, the minimum slope fixes an $\epsilon(k)$ value corresponds to the Landau critical velocity of Eq. (I.8) equal to $\approx 58 \text{ ms}^{-1}$.

The physical interpretations of the very different motions in the phonon and roton regions are summarized in Fig. I.5. At low momentum a single helium atom couples

strongly to the many-particle condensate. As it moves, the condensate moves rigidly with it, leading to a motion almost like a solid body, and hence a phonon-like energy spectrum. On the other hand, at very high momentum the atom can move relatively independently of the rest of the fluid particles. In contrast, at the intermediate momenta of the roton minimum the moving particle couples strongly to its neighbors. As the atom moves the neighbors must move out of the way. The neighbors must move to the side and end up behind the moving particle, so they actually move in a circular backflow. The net effect is a forward motion of one particle, accompanied by a ring of particles rotating backwards. Feynman has likened the motion to the motion of a smoke-ring! The smoke ring itself moves forward, while the smoke particles themselves move in circular motion constantly rotating backwards around the rim of the smoke ring (Feynman 1972).

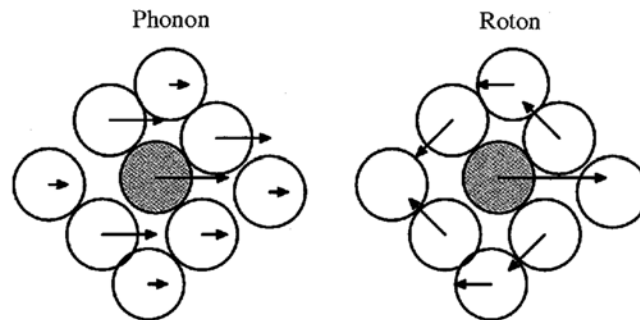


Figure I.5. Physical interpretation of the phonon and roton parts of the quasi-particle spectrum. The phonon motion corresponds to de Broglie wavelengths, $p = h/\lambda$, greater than a single atomic size, and leads to coupled motion of groups of atoms moving together, rather like a phonon in a solid. The roton corresponds to de Broglie wavelengths of order the interparticle separation. It corresponds to a central particle moving forward, while the close packed neighbors must move out of the way in a circular motion. Feynman notes that this combination of linear and circular motion has some nice similarity to a moving smoke-ring. Figure taken from Ref [13]

I-2. Superfluid He droplets

Is superfluidity restricted to bulk liquid? or could it be possible to observe superfluid effects, in finite systems, consisting of a small number of helium atoms? This question was raised at the end of 1950's by E.W. Becker [14]. With this

objective in mind, helium nanodroplets (HND) were produced under controlled conditions. Toennies' group in Göttingen demonstrated that small helium droplets do indeed manifest superfluidity.

The experiment consisted in measuring the rotational spectrum of a single carbonyl sulfide (OCS) molecule embedded in a ^3He droplet (not superfluid at the droplet temperature) and increasing the proportion of ^4He (number of ^4He atoms) which, because of the different mass and hence zero-point energy, replace the ^3He atoms around the OCS molecule (see Fig I.6). For droplets containing about 60 atoms and more, the OCS spectrum looks like that of a free rotor at 0.4 K with its resolved rotational lines. In other words, the OCS molecule appears to rotate freely, with no energy dissipation (albeit with modified rotational constants, see Refs [15, 16] for the original experiment and interpretation).

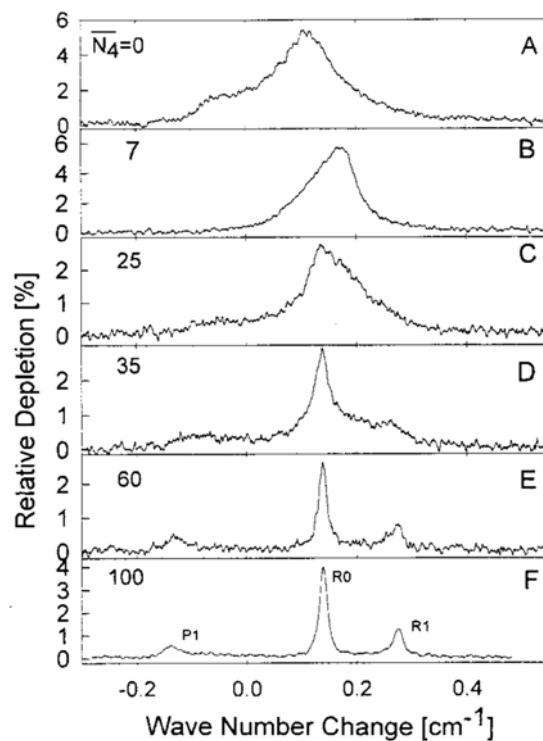


Figure I.6. A series of OCS, embedded in a $^3\text{He}_{12000}$ droplet, IR spectra increasing average numbers \bar{N}_4 of added ^4He atoms [$\bar{N}_4 = 0$ (A), 7(B), 25(C), 35(D), 60(E), and 100(F)]. The change in wave number in the abscissa is with respect to $\nu_0 = 2061.71 \text{ cm}^{-1}$. Figure taken from [15]

A fundamental property of helium droplets is their ability to pick up any species with which they collide. This was demonstrated by Toennies and co-workers in 1990 [17]. In their experimental setup, a HND beam was crossed with beams of foreign atomic or molecular species in various configurations, and fragments emerging from the doped droplets upon ionization were analyzed using a magnetic sector analyzer instrument (MSA) for ion detection. The mass spectra revealed that not only were the foreign gas-phase species captured by the HNDs, but they also coagulated and formed clusters of their own as large as $(\text{H}_2\text{O})_{18}$. These discoveries opened up a plethora of possibilities and applications such as HND isolation spectroscopy, dopant clusters growth and chemical reactions studies inside HNDs. Later, Miller's group [18] studied the formation of small van der Waals clusters of sulfur hexafluoride (SF_6) and mixed SF_6 -rare gas clusters within helium droplets made of ~ 4000 atoms. In all cases a rotational structure was observed, indicating that the embedded species rotated nearly freely, although they had been cooled to a temperature of 0.37 K.

Fast energy dissipation, another superfluid property, has been demonstrated in the clustering of HCCCN (cyanoacetylene) molecules: they formed a long chain (see Fig I.7) rather than a compact cluster, as investigated by Miller *et al* [19]. Upon pick-up, the additional molecule interacts with the electrical field of the dipole moment of the polar chain formed by prior pick-ups. As the molecule comes closer to the polar chain the gradient of the field emanating from the chain attracts the molecule to one end of the chain, where on further approach it is locked into position by strong electrostatic forces. Thus, despite the fact that the global minimum of the potential energy surface corresponds to either cyclic or branched structures, which are indeed observed for complexes formed in seeded beams at somewhat higher temperatures [20], the ultralow temperatures and the mediating effect of the liquid favor the formation of large metastable chains with up to 10 constituent molecules.

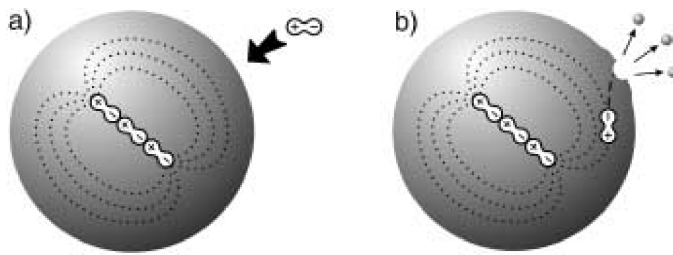


Figure I.7. Schematic representation of the mechanism leading to the formation of chains of polar molecules in ^4He droplets. a) A fourth molecule approaches a droplet containing a chain with three molecules. b) On entering the droplet some ^4He atoms are displaced and the molecule is aligned and attracted by the electric field of the trimer chain. Figure taken from Ref [21]

Most of the dopants reside in the bulk of the droplets (heliophilic dopants). Only the alkali and some alkali earth atoms reside in a dimple at the surface, because their interaction with helium is very weak (heliophobic dopants) [22]. In addition, the liquid helium is transparent to electromagnetic radiation from the far infrared to the vacuum ultraviolet range. These properties combine to make helium droplets ideal spectroscopic matrices.

I-3. Vorticity in superfluid ^4He droplets

Vortices appear in helium as a way to store angular momentum. They are usually called “quantum vortices” because they exhibit specific characteristics that are different from the ones found in classical fluids. For classical vortices each fluid element rotates in the same direction as that of the fluid direction (vorticity¹). The opposite is true for a quantum vortex, see the leaves in Figure I.8 for each case. Also, the tangential velocity [$v(\mathbf{r}) = v_\theta(r)$ obtained for a system rotating around the “z” axis in cylindrical coordinates] increases away from the center (see the length of the horizontal black arrows and the blue curve in Figure I.8). It is given by $\vec{v} = \vec{\Omega} \times \vec{r}$ and its rotational by $\nabla \times \vec{v} = 2\vec{\Omega}$, $\vec{\Omega}$ being the angular velocity. On the other hand, a quantum vortex behaves differently. The rotational of the fluid velocity $\nabla \times \vec{v} = 0$ (thus, it is said to be irrotational or no vorticity, a feature

¹A vector field that gives a microscopic measure of the rotation at any point in the fluid

shared by superfluids and Bose-Einstein condensates) and v_θ is proportional to $1/r$, see Fig I.8 for further details. ⁻

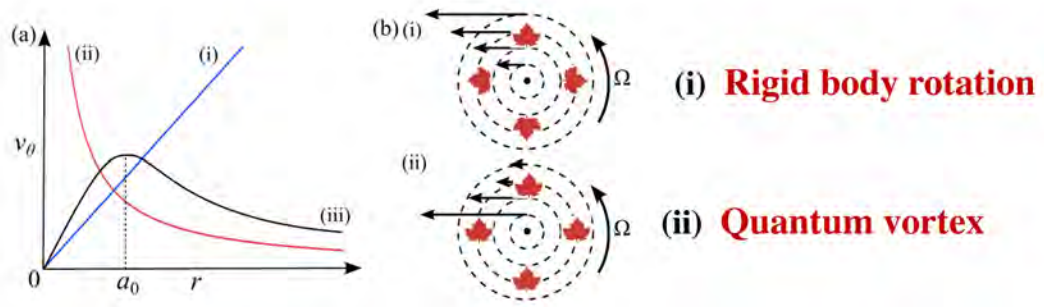


Figure I.8. Rigid body rotation (i), quantum vortex (ii) and a bathtub, “ordinary” vortex (iii). On the left (a): the tangential velocity [$v_\theta(r)$] is displayed as a function of the distance (r) from the center. The width of the core of a quantum vortex is denoted a and is typically 1\AA . The leaves in (b) represent a fluid element around the vortex and its orientation changes if such an element rotates (i) or not (ii). The length of black arrows is proportional to the tangential velocity at distance r . Figure taken from Ref [23]

Besides, the circulation² around a quantum vortex line is quantised, which is contrary to a classical vortex where the circulation can take any value. The core of a quantized vortex is very thin, of the order of the coherence length, which is only about one angstrom in superfluid ^4He : $a \sim 1\text{\AA}$ [22,24], see section II-6.3.

I-4. Energetic balance

In this work it will be made reference to different characteristic energies. We define them here [25-27,28]

- Solvation energy of the impurity X:

$$S_X = E(X@^4\text{He}_N) - E(^4\text{He}_N)$$

- Vortex (V) energy :

$$E_V = E(V@^4\text{He}_N) - E(^4\text{He}_N)$$

²A macroscopic measure of rotation for a finite area of the fluid, defined as the line integral evaluated along the contour of the component of the velocity vector that is locally tangent to the contour.

- Binding energy of the impurity to the vortex, also called “substitution energy”

$$B_X = \{E(X@^4He_N) - E(^4He_N)\} - \{E((X + V)@^4He_N) - E(V@^4He_N)\}$$

I-5. How droplets are obtained in experiments

Superfluid helium droplets are produced by expanding helium into vacuum through a nozzle. Different size distributions are obtained depending on the temperature and pressure in the nozzle as well as on the shape of the nozzle itself. A typical experimental setup is shown in Figure I.9. In that experiment, liquid helium at $T_0 = 5$ K and $P_0 = 20$ bar is expanded into vacuum through a cylindrical nozzle with a nominal diameter $d = 5 \mu\text{m}$ and a channel length of $2 \mu\text{m}$. During the expansion of the fluid through the nozzle, its temperature and pressure drop and the liquid is accelerated to about 170 ms^{-1} [29]. A denser and colder part of the beam is selected by collimating it through a skimmer [30]. The position is placed in such a way that it acts as an effusive source [31] (the mean free path in the jet at the skimmer is larger than the skimmer aperture) about 10 – 15 mm downstream from the nozzle. While reaching the vacuum, a jet is formed that boils vigorously, giving rise to the formation of droplets. Despite the many possible nozzle geometries this only has influence on kinetic phenomena such as relaxation processes and clustering occurring at the nozzle exit [32].

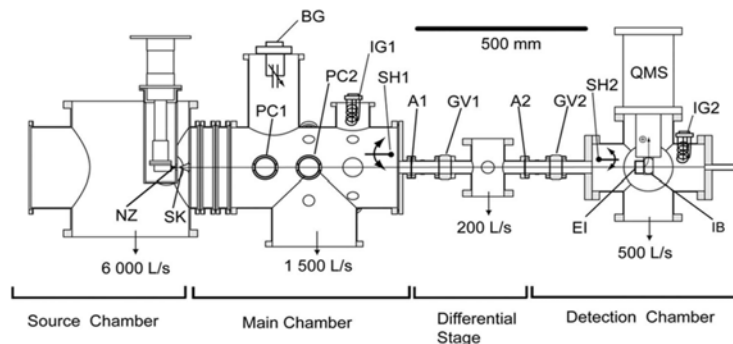


Figure I.9. Typical experimental setup. Schematic of the He droplet beam vacuum apparatus. NZ: cold nozzle, SK: skimmer, PC1 and PC2: pickup cells, BG: Baratron vacuum gauge, IG1 and IG2: ion gauges, SH1 and SH2: beam shutters, A1 and A2: 6 mm diameter apertures, GV1 and GV2: gate valves, EI: electron impact ionizer, IB: ion bender, QMS: quadrupole mass spectrometer. Figure taken from Ref. [29]

The final droplet sizes are determined not only by the growth process, such as droplet coagulation, but also by subsequent cooling by evaporation with a correspondingly large loss of atoms. Evaporation is initially very fast, and decreases exponentially (see Ref [21]) with time. The internal temperature drops with a time constant of about 10^{-11} - 10^{-9} sec until the droplets get so cold that the evaporation rate becomes negligible, see Fig I.10 for droplets get made of $N = 1000$ atoms. After travelling a certain distance (of the order of one meter [29], see Fig I.9), the droplet temperature is 0.4 K. Calculations conducted by Tanyag *et al* [1, 33] have shown that for large droplets ($N = 10^7$, 10^{10} , and 10^{13}) after 10^{-3} sec ($T \approx 0.4$ K) the reduction in size is always about 40% , independently of the droplet size, see Fig I.11. However, it was assumed that the droplet is in equilibrium at shorter times, which is not valid, hence the actual cooling rate will be slower than calculated. In addition, the cooling of the droplets close to the nozzle will be slower than calculated, as the droplets are not in vacuum but surrounded by a helium gas cloud resulting from the fast evaporation.

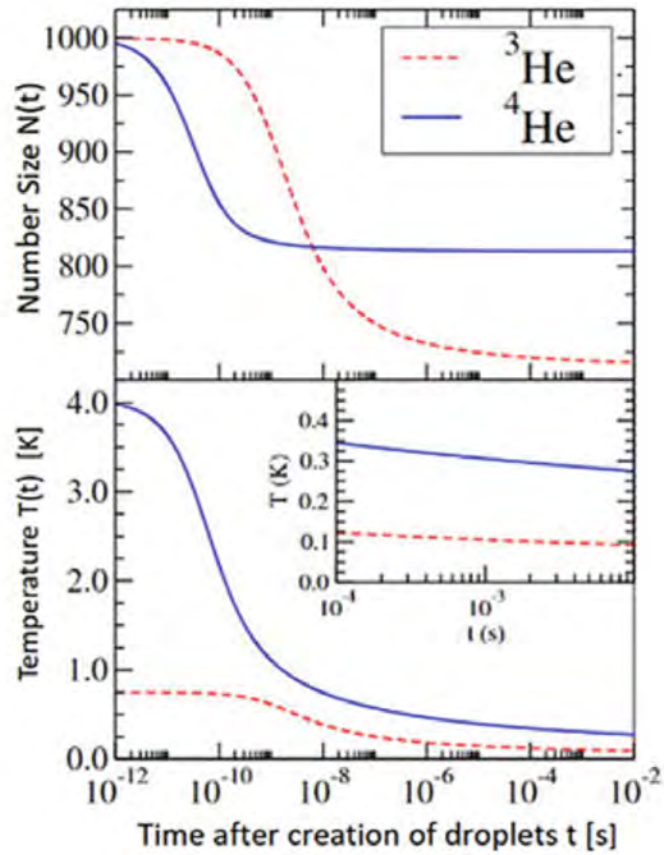


Figure I.10. Calculated time evolution of the mean number sizes and temperatures of ${}^3\text{He}$ and ${}^4\text{He}$ droplets after they have grown to 10^3 atoms. It is assumed that the ${}^4\text{He}$ droplets have initially a temperature of 4.0 K and the ${}^3\text{He}$ droplets 0.8 K. Concomitant with the large evaporative loss the temperatures decrease by about an order of magnitude to below 0.3 K (${}^4\text{He}$) and 0.1 K (${}^3\text{He}$). Figure taken from [1]

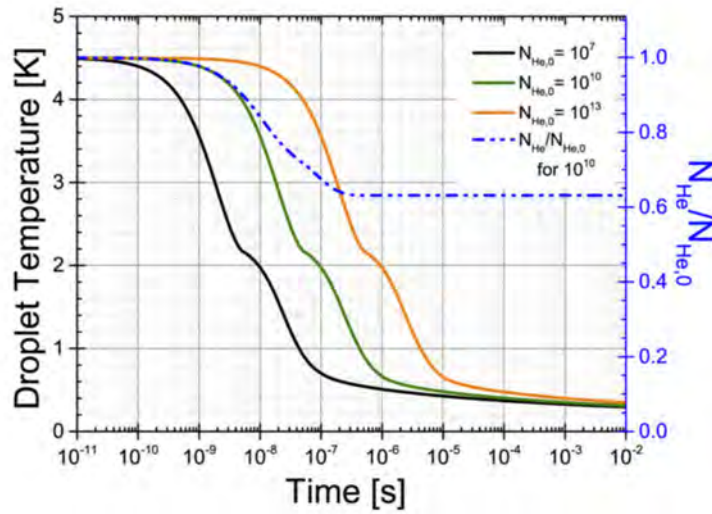


Figure I.11. Helium droplet cooling in an absolute vacuum for droplets with initial diameters of 100 nm ($N_{\text{He},0}=10^7$), 1 μm ($N_{\text{He},0}=10^{10}$), and 10 μm ($N_{\text{He},0}=10^{13}$). The dashed curve shows the fraction of helium atoms remaining in a droplet with initial size of $N_{\text{He},0}=10^{10}$, corresponding to the vertical axis on the right. Figure taken from Ref [33]

The expansion of the gas can be described using the pressure-temperature phase diagram for ^4He , as illustrated in Fig I.12. Changes in the thermodynamic state of helium as it flows through the orifice can be approximated by assuming an adiabatic³ isentropic process in which the gas or liquid is always in thermodynamic equilibrium (Fig. I.12).

³The gas or liquid can adjust adiabatically since it takes only less than about a hundred collisions ($\approx 10^{-12}$ sec) to adapt to a new pressure and temperature. It is supported by the fact both the temperature and density of the gas decrease with increasing distance leading to a fall in the collision rate. Hence, the resulting beam is made of He atoms and droplets.

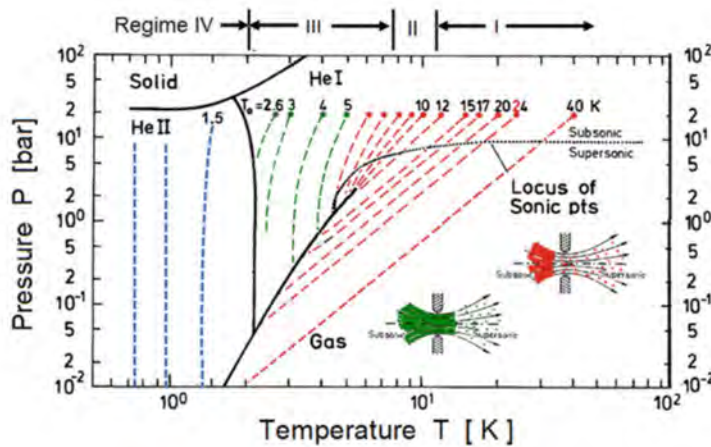


Figure I.12. Pressure-temperature phase diagram for ${}^4\text{He}$ with isentropes (— —) for free jet expansions starting from a stagnation pressure of $P_0 = 20$ bar and a range of temperatures T_0 [34]. Regime I: $T_0 \geq 12$ K, Regime II: $T_0 \approx 8$ -12 K, Regime III: $T_0 \approx 2.8$ -8 K, and Regime IV: $T_0 \leq 2.2$ K. The isentropes are based on data in [8] for different temperatures T_0 and a single initial pressure of $P_0 = 20$ bar. The sonic condition requires that the flow velocity equals the speed of sound at the narrowest point of the orifice and at this point the flow changes from subsonic to supersonic. Figure taken from Ref. [1]

There are several expansion regimes, depending on the source temperature, pressure and nozzle shape, as illustrated in Fig I.13. Droplet sizes increase with decreasing source temperature and increasing pressure [35]. Regime I corresponds to supercritical expansions, in which the nozzle temperature is above the helium critical temperature. Droplets are then formed by gas condensation and are typically of several hundreds up to $\sim 10\,000$ atoms. Larger droplets (up to 10^9 atoms) are produced by expanding liquid helium in critical (Regime II) and subcritical (Regime III) expansions. For nozzle temperatures of about 3 K in the so-called Regime IV, liquid He I leaves the orifice in a cylindrical column which breaks up, because of the surface tension force [36], into a series of nearly uniformly-sized droplets (about 1.89 times the nozzle diameter [37]) with about $10^{10} - 10^{12}$ atoms. That phenomenon is called “Rayleigh break-up”. Droplets produced this way have a narrow size distribution, and the droplet size can be controlled by changing the size of the nozzle diameter [1].

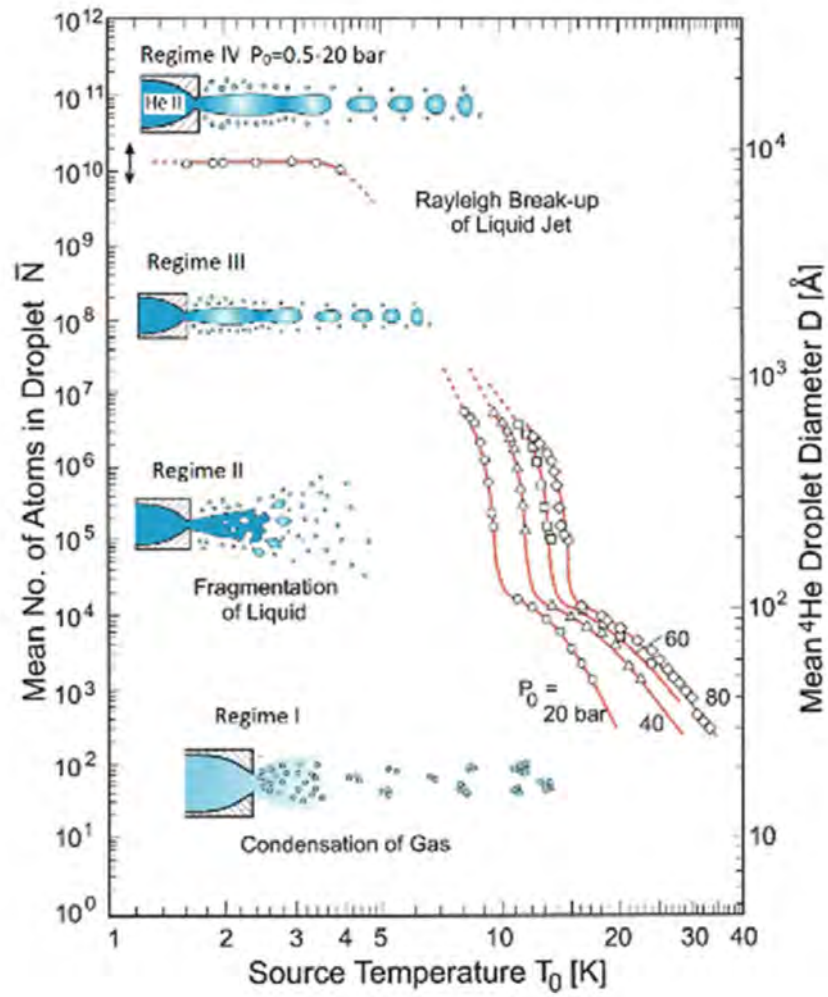


Figure I.13. Droplet size distribution depending on the nozzle temperature and pressure. Figure taken from Ref.[1]

 CHAPTER II

DENSITY FUNCTIONAL THEORY OF LIQUID ^4He AT ZERO TEMPERATURE

The Density Functional Theory (DFT) of liquid helium (^4He -DFT) is similar to electronic DFT but describing helium density instead of electronic density. It constitutes a compromise between the accuracy of *ab initio* methods (like Quantum Monte Carlo (QMC) [38]) and numerical feasibility [39]. In addition, it can be applied to much larger systems than QMC and allows for a time-dependent formulation. Also ^4He -DFT is the only method, up to date, that can successfully reproduce results from a wide range of time-resolved experiments in superfluid helium, for realistic sizes compared to experimental conditions. The ^4He -DFT and its dynamics version (Time-Dependent ^4He -DFT, ^4He -TDDFT) have been tested and corroborated by experimental results in a broad amount of studies involving inhomogeneous ^4He systems like, e.g., liquid-vapor interface [40-41], pure and doped clusters [41-43], layering and prewetting transitions in films [41], alkali atom adsorption on the surface of liquid ^4He and droplets [44] and vortices in ^4He clusters [28].

II-1. Density functional theory for helium

In the ^4He -DFT approach, the total energy $E = \langle \Phi | \mathcal{H} | \Phi \rangle$ of a many-body quantum system, at zero temperature and pressure, is expressed as a functional of the one-particle density $\rho(\mathbf{r}) = \langle \Phi | \sum_i \delta(\mathbf{r} - \mathbf{r}_i) | \Phi \rangle$, where $\Phi(\mathbf{r}_1, \mathbf{r}_2, \dots, \mathbf{r}_N) = \prod_i \phi_0(\mathbf{r}_i)$ and $\phi_0(\mathbf{r}_i)$ is the single-particle orbital

$$E[\rho] = \mathcal{T}[\rho] + \int d\mathbf{r} \mathcal{E}[\rho] \quad (\text{II.1})$$

Eq.(II.1) contains a kinetic energy term \mathcal{T} which is the energy of a fictitious system of non-interacting particles given by

$$\mathcal{T} = \sum_i \mathcal{T}_i = -\frac{\hbar^2}{2m_4} \sum_i \langle \phi_0 | \nabla_i^2 | \phi_0 \rangle = -\frac{\hbar^2}{2m_4} \sum_i \int d\mathbf{r} \phi_0^*(\mathbf{r}_i) \nabla_i^2 \phi_0(\mathbf{r}_i) \quad (\text{II.2})$$

where m_4 is the mass of a single ^4He atom. The difference with the correct kinetic energy is included in the functional $\mathcal{E}[\rho]$, together with exchange and correlations.

The Orsay-Trento functional (section II-2) has been used throughout the calculations performed in this thesis. It has been previously calibrated to reproduce the correct behavior of bulk liquid helium at zero temperature $T=0$ [22].

In the superfluid regime, all ^4He atoms occupy the same single-particle orbital ϕ_0 like in a Bose-Einstein condensate (BEC). The one-dimension density is then

$$\rho(\mathbf{r}) = \sum_i |\phi_i(\mathbf{r})|^2 = N |\phi_0(\mathbf{r})|^2 \quad (\text{II.3})$$

and the kinetic energy is

$$\mathcal{T} = -\frac{\hbar^2}{2m_4} N \langle \phi_0 | \nabla^2 | \phi_0 \rangle = -\frac{\hbar^2}{2m_4} \int d\mathbf{r} \left| \nabla \sqrt{\rho(\mathbf{r})} \right|^2 = -\frac{\hbar^2}{2m_4} \int d\mathbf{r} |\nabla \Psi(\mathbf{r})|^2 \quad (\text{II.4})$$

where $\Psi(r)$ is the so-called ‘‘pseudo wave function’’ or ‘‘order parameter’’ (it represents the phase transition between the normal liquid phase and the superfluid phase), related to $\rho(r)$ by

$$\rho(\mathbf{r}) = \Psi^*(\mathbf{r})\Psi(\mathbf{r}) \quad (\text{II.5})$$

with $\Psi(\mathbf{r}) = \sqrt{N}\phi_0(\mathbf{r})$

II-2. The Orsay-Trento density functional

Stringari and coworkers [45,46] have developed the first and simplest functional for superfluid ^4He . All the terms in $\mathcal{E}[\rho]$ depended only on the local density $\rho(\mathbf{r})$. In recent studies [22], other terms have been included in order to increase the functional accuracy, by fitting bulk liquid properties such as the energy per atom, the equilibrium density, the dispersion relation, and the compressibility at zero temperature and pressure.

The most accurate functional to date is the finite range, non-local Orsay-Trento one (OT) [41]. It is written as

$$\begin{aligned} \mathcal{E}[\rho] = & \frac{1}{2} \int d\mathbf{r}' \rho(\mathbf{r}) V_{LJ}(|\mathbf{r} - \mathbf{r}'|) \rho(\mathbf{r}') \\ & + \frac{1}{2} c_2 \rho(\mathbf{r}) [\bar{\rho}(\mathbf{r})]^2 + \frac{1}{3} c_3 \rho(\mathbf{r}) [\bar{\rho}(\mathbf{r})]^3 \\ & - \frac{\hbar^2}{4m_4} \alpha_s \int d\mathbf{r}' F(|\mathbf{r} - \mathbf{r}'|) [1 - \tilde{\rho}(\mathbf{r})/\rho_{0s}] \nabla \rho(\mathbf{r}) \cdot \nabla' \rho(\mathbf{r}') [1 - \tilde{\rho}(\mathbf{r}')/\rho_{0s}] \\ & - \frac{m_4}{4} \int d\mathbf{r}' V_J(|\mathbf{r} - \mathbf{r}'|) \rho(\mathbf{r}) \rho(\mathbf{r}') [\mathbf{v}(\mathbf{r}) - \mathbf{v}(\mathbf{r}')]^2 \end{aligned} \quad (\text{II.6})$$

The various parameters entering the OT functional are specified in Table B.2, annex B.

The first term corresponds to a classical Lennard-Jones (LJ) interaction between helium atoms. The LJ potential (see Eq.(II.7)) is screened at short distances where the correlation effects start becoming important.

$$\begin{aligned} V_{LJ}(r) &= 4\epsilon_{LJ} \left[\left(\frac{\sigma}{r}\right)^{12} - \left(\frac{\sigma}{r}\right)^6 \right] && \text{if } r > h \\ &= 0 && \text{Otherwise} \end{aligned} \quad (\text{II.7})$$

The second line in Eq.(II.6) accounts for short-range correlation effects. The terms in to c_2 and c_3 correct for short range correlations when $r < h$. Also, two coarse-grained averages of the liquid density, $\bar{\rho}$ (average density over a sphere of radius h) and $\tilde{\rho}$, entering the short-range correlation terms in Eq.(II.6), are given by

$$\bar{\rho}(\mathbf{r}) = \int d\mathbf{r}' \rho(\mathbf{r}') w(|\mathbf{r} - \mathbf{r}'|) \quad (\text{II.8})$$

where

$$\begin{aligned} w(r) &= \frac{3}{4\pi h^3} && \text{if } r < h \\ &= 0 && \text{Otherwise} \end{aligned} \quad (\text{II.9})$$

and

$$\tilde{\rho}(\mathbf{r}) = \int d\mathbf{r}' \rho(\mathbf{r}') F(|\mathbf{r} - \mathbf{r}'|) \quad (\text{II.10})$$

where $F(r)$ is a Gaussian kernel

$$F(r) = \frac{1}{\pi^{3/2} l^3} e^{-r^2/l^2} \quad (\text{II.11})$$

The density $\tilde{\rho}(\mathbf{r})$ is very close to the normal density $\rho(\mathbf{r})$ except in very inhomogeneous situations. For pure helium droplets and free helium surfaces $\tilde{\rho}(\mathbf{r})$ can safely be replaced by $\rho(\mathbf{r})$. Only in the presence of significant short-range density oscillations does the helium density need to be smoothed by the Gaussian kernel F .

The third line (α_s term) is a non-local kinetic energy correction (KC), which partially accounts for the difference $\mathcal{T}[\rho]-T[\rho]$ in the interaction term $\mathcal{E}[\rho]$.

The last term in Eq. (II.6) corresponds to the backflow (BF) contribution, which affects the dynamic response of the functional. The term backflow was introduced by Feynman and Cohen [47] to describe the correlated motion of neighboring particles around a given reference atom. It contains an effective “current”-interaction V_J , whose form has to be guessed and whose parameters are fitted so as to reproduce the dispersion relation.

$$V_J(r) = (\gamma_{11} + \gamma_{12}r^2)e^{-\alpha_1 r^2} + (\gamma_{21} + \gamma_{22}r^2)e^{-\alpha_2 r^2} \quad (\text{II.12})$$

Notice that the BF term only contributes when the order parameter is a complex valued function (e.g. time-dependent problem or vortex state). This will be explained later in section II-6.

When the impurity-helium interaction is strongly attractive, a “solid” energy ($\mathcal{E}_{\text{solid}}$ term) needs to be added to $\mathcal{E}[\rho]$.

$$\mathcal{E}_{\text{solid}} = C \rho(\mathbf{r}) \{1 + \tanh[\beta (\rho(\mathbf{r}) - \rho_m)]\} \quad (\text{II.13})$$

With this correction, unphysical density pile-up (see Ref [22]) are avoided. The model parameters $\{C; \beta; \rho_m\}$ are specified in Table B.2, annex B. The inclusion of this term in the functional does not alter the density distribution. This penalty term was originally developed to account for the liquid-solid phase transition of ^4He [48,49]. It only deviates from zero when the liquid density ρ is comparable to a predefined value ρ_m or larger.

II-3. Time-Independent ^4He -DFT for doped droplets

Impurities/dopants (both terms are used to designate foreign atoms or molecules inside helium droplets) much heavier than helium can be described as classical, point-like particles whereas the others require a quantum mechanical treatment.

In this thesis, we studied helium nanodroplet (HND) doped with alkali atoms ($\text{Ak} \equiv \text{Li, Na, K, Rb, Cs}$) and rare gas atoms such as Ar and Xe. Most of these dopants (except Li and Na) are heavier than helium atoms, hence they are treated as classical particles. The ${}^4\text{He}_N$ -dopant interaction is then treated as an external field (V_X), it is explained in the following page.

The helium-dopant interaction is being approximated as V_X , the total energy is that of the pure droplet [Eq.(II.1)] plus the external potential

$$E[\rho] \rightarrow E[\rho] + \int d\mathbf{r} \rho(\mathbf{r}) V_X(|\mathbf{r} - \mathbf{r}_I|) \quad (\text{II.14})$$

where \mathbf{r}_I is the location of the impurity.

The Euler-Lagrange equation which determine the ground state helium density is given by minimizing $E[\rho]$ with respect to either $\rho(\mathbf{r})$ or $\Psi(\mathbf{r})$, under the constraint of a fixed number of helium atoms ($N = \int d\mathbf{r} \rho(\mathbf{r})$). The Lagrange multiplier is denoted as μ .

$$\delta \left\{ E[\rho] - \mu \int d\mathbf{r} \rho(\mathbf{r}) \right\} = 0 \quad (\text{II.15})$$

The resulting equation

$$\left\{ -\frac{\hbar^2}{2m_4} \nabla^2 + \frac{\delta \mathcal{E}_c}{\delta \rho} + V_X(|\mathbf{r} - \mathbf{r}_I|) \right\} \Psi(\mathbf{r}) = \mu \Psi(\mathbf{r}) \quad (\text{II.16})$$

looks similar to a time-independent Schrödinger equation except for the non-linear term ($\frac{\delta \mathcal{E}_c}{\delta \rho}$). Also, μ is not the energy but the chemical potential.

On the other hand, light impurities, such as Li and Na in this thesis, have to be modelled quantum mechanically. Within a mean field description [from Eq.(II.1)] is modified as

$$E[\rho] \rightarrow E[\rho] + \frac{\hbar^2}{2m_I} \int d\mathbf{r}_I |\nabla_I \phi(\mathbf{r}_I)|^2 + \iint d\mathbf{r} d\mathbf{r}_I \rho(\mathbf{r}) V_X(|\mathbf{r} - \mathbf{r}_I|) |\phi(\mathbf{r}_I)|^2 \quad (\text{II.17})$$

where $\phi(\mathbf{r}_I)$ is the impurity wave function and m_I its mass. This yields two coupled equations, one for the droplet and one for the impurity

$$\begin{aligned} \left\{ -\frac{\hbar^2}{2m_4} \nabla^2 + \frac{\delta \mathcal{E}_c}{\delta \rho} + \int d\mathbf{r}_I V_X(|\mathbf{r} - \mathbf{r}_I|) |\phi(\mathbf{r}_I)|^2 \right\} \Psi(\mathbf{r}) &= \mu \Psi(\mathbf{r}) \\ \left\{ -\frac{\hbar^2}{2m_I} \nabla_I^2 + \int d\mathbf{r} V_X(|\mathbf{r} - \mathbf{r}_I|) \rho(r) \right\} \phi(\mathbf{r}_I) &= \epsilon \phi(\mathbf{r}_I) \end{aligned} \quad (\text{II.18})$$

Equations (II.16) or (II.18) are then solved by iteration in a self-consistent way using the imaginary time propagation method (ITM) [50], see Section II-5 for further technical details.

II-4. Time Dependent DFT (⁴He-TDDFT)

The Runge-Gross theorem [51] makes it possible to extend the ⁴He-DFT theory to its dynamical version, the ⁴He Time-Dependent Density Functional Theory (⁴He-TDDFT).

The functional variation of the associated action [39],

$$A[\Psi] = \int dt d\mathbf{r} \left\{ \xi[\Psi^*, \Psi] - i\hbar \Psi^* \frac{\partial \Psi}{\partial t} \right\} \quad (\text{II.19})$$

where ξ is the energy density ($\int d\mathbf{r} \xi[\Psi^*, \Psi] = E[\rho(\mathbf{r})]$), leads to the following time-dependent Euler-Lagrange (EL) equation, in the case of pure droplets

$$i\hbar \frac{\partial}{\partial t} \Psi(\mathbf{r}, t) = \left\{ -\frac{\hbar^2}{2m_4} \nabla^2 + \frac{\partial \mathcal{E}}{\partial \rho} \right\} \Psi(\mathbf{r}, t) = \mathcal{H}[\rho] \Psi(\mathbf{r}, t) \quad (\text{II.20})$$

This equation is solved by propagation in real time (see section II-5.2). The initial state $\Psi(r, 0)$ is taken as the solution of the static problem, $\Psi(\mathbf{r}, 0) = \sqrt{\rho_{\text{static}}(\mathbf{r})}$, to which a global phase can eventually be added (this is the case in Chapter VI for describing the collision of two droplets). The time evolution of the helium density is then simply $\rho(\mathbf{r}, t) = |\Psi(\mathbf{r}, t)|^2$. Note that $\Psi(\mathbf{r}, t)$ is complex, whereas it was real in the time-independent version (except in the presence of a vortex).

In the case of a doped droplet where the dopant can be treated classically, the total energy is written as:

$$E[\Psi, \mathbf{r}_I] = \int d\mathbf{r} \frac{\hbar^2}{2m_4} |\nabla\Psi|^2 + \frac{p_I^2}{2m_I} + \int d\mathbf{r} \mathcal{E}_c(\rho) + \int d\mathbf{r} \rho(\mathbf{r}) V_X(|\mathbf{r} - \mathbf{r}_I|) \quad (\text{II.21})$$

The time evolution of the helium pseudo wave function $\Psi(\mathbf{r}, t)$ and the impurity position $r_I(t)$ are then governed by two coupled equations

$$\begin{aligned} i\hbar \frac{\partial}{\partial t} \Psi(\mathbf{r}, t) &= \left[-\frac{\hbar^2}{2m_4} \nabla^2 + \frac{\delta\mathcal{E}_c}{\delta\rho} + V_X(|\mathbf{r} - \mathbf{r}_I|) \right] \Psi(\mathbf{r}, t) \\ m_I \ddot{\mathbf{r}}_I &= -\nabla_{\mathbf{r}_I} \left[\int d\mathbf{r} \rho(\mathbf{r}) V_X(|\mathbf{r} - \mathbf{r}_I|) \right] = -\int d\mathbf{r} V_X(|\mathbf{r} - \mathbf{r}_I|) \nabla\rho(\mathbf{r}) \end{aligned} \quad (\text{II.22})$$

The first equation is similar to the time-dependent Schrödinger equation, except that the $\delta\mathcal{E}_c/\delta\rho$ term makes it non-linear. The second equation is the usual Newton equation for a classical particle expressed in Cartesian coordinates.

In the case of a light impurity (requiring a quantum mechanical treatment), the total energy is then written as

$$\begin{aligned} E[\Psi, \mathbf{r}_I] &= \int d\mathbf{r} \frac{\hbar^2}{2m_4} |\nabla\Psi|^2 + \int d\mathbf{r}_I \frac{\hbar^2}{2m_I} |\nabla_{\mathbf{r}_I}\phi|^2 \\ &+ \iint d\mathbf{r} d\mathbf{r}_I \rho(\mathbf{r}, t) V_X(|\mathbf{r} - \mathbf{r}_I|) |\phi(\mathbf{r}_I, \mathbf{t})|^2 \end{aligned} \quad (\text{II.23})$$

where $\phi(\mathbf{r}_I, t)$ is the time-dependent wave function for the impurity. The coupled equations describing the time evolution of the helium pseudo wave function and of the impurity wave function are then

$$\begin{aligned} i\hbar \frac{\partial}{\partial t} \Psi(\mathbf{r}, t) &= \left[-\frac{\hbar^2}{2m_4} \nabla^2 + \frac{\delta\mathcal{E}_c}{\delta\rho} + \int d\mathbf{r}_I V_X(|\mathbf{r} - \mathbf{r}_I|) |\phi(\mathbf{r}_I, t)|^2 \right] \Psi(\mathbf{r}, t) \\ i\hbar \frac{\partial}{\partial t} \phi(\mathbf{r}_I, t) &= \left[-\frac{\hbar^2}{2m_I} \nabla_{\mathbf{r}_I}^2 + \int d\mathbf{r} V_X(|\mathbf{r} - \mathbf{r}_I|) \rho(\mathbf{r}, t) \right] \phi(\mathbf{r}_I, t) \end{aligned} \quad (\text{II.24})$$

Note that this is a mean-field description: the impurity evolves in the mean field created by the helium environment, and vice-versa. As in the case of a classical

impurity, the time evolution equations are solved by propagation. The initial values of $\Psi(\mathbf{r}, 0)$ and $\phi(\mathbf{r}_I, 0)$ are taken as their equilibrium value resulting from the static ^4He -DFT solution.

II-5. Technical details

The calculations are performed in three dimensions without imposing any symmetries. All the quantities are discretised on an evenly spaced Cartesian grid with a step-size that is typically of the order of 0.4 Å. The differential operators are evaluated using a k -point finite difference method where $k = 13$ is sufficiently accurate in most applications. Since the integral terms in OT functional can be expressed as convolutions [41,48,52], they can be evaluated in momentum-space by exploiting the convolution theorem, using highly optimised parallel Fast Fourier Transform algorithms [53].

II-5.1. Imaginary time propagation

The imaginary time propagation method [50] (ITM) yields the ground state of the system provided that the initial guess $\Psi(0)$ used to start the minimization is “reasonable enough”, *i.e.*, that its overlap with the exact pseudo wave function is not negligible.

Let us consider the following time-dependent Schrödinger equation

$$i\hbar \frac{\partial}{\partial t} \Psi = \mathcal{H} \Psi \quad (\text{II.25})$$

It can be formally integrated for a time interval δt yielding

$$\Psi(\delta t) = e^{-i \frac{\delta t}{\hbar} \mathcal{H}} \Psi(0) \quad (\text{II.26})$$

Expanding $\Psi(0)$ in eigenfunctions ψ_k of the Hamiltonian \mathcal{H} , with energy ϵ_k

$$\Psi(0) = \sum_{k=0}^{k=\infty} c_k \psi_k \quad (\text{II.27})$$

Hence,

$$\Psi(\delta t) = \sum_{k=0}^{k=\infty} c_k e^{-i\frac{\delta t}{\hbar}\epsilon_k} \psi_k \quad (\text{II.28})$$

where we have used $e^{-i\frac{\delta t}{\hbar}\mathcal{H}} \approx 1 + \frac{i\delta t}{\hbar}\mathcal{H} + \dots$, giving $e^{-i\frac{\delta t}{\hbar}\mathcal{H}}\psi_k = e^{-i\frac{\delta t}{\hbar}\epsilon_k}\psi_k$ [54].

Any time interval is obtained by setting $t = n\delta t$ and making n as large as needed

$$\Psi(t) = \Psi(n\delta t) = \sum_{k=0}^{k=\infty} c_k e^{-i\frac{n\delta t}{\hbar}\epsilon_k} \psi_k \quad (\text{II.29})$$

By setting $\delta t = -i\hbar\delta\tau$ (τ is called “imaginary time”), it is obtained

$$\Psi(\tau) = \Psi(n\delta\tau) = \sum_{k=0}^{k=\infty} c_k e^{-n\delta\tau\epsilon_k} \psi_k \quad (\text{II.30})$$

For long enough τ , only the component ψ_0 corresponding to the lowest eigenvalue ϵ_0 “survives”

In order to solve the ITM equation, Eq. (II.26) is approximated to the first order in δt (although one could go to higher order, this is not the way it is implemented) writing

$$\Psi(t + \delta t) \approx (1 - \delta\tau\mathcal{H})\Psi(t) = \Psi(t) + \delta\Psi(\tau) \quad (\text{II.31})$$

with

$$\delta\Psi(\tau) = -\frac{\delta t(\mathcal{H} - \mu)}{1 - \delta t(\langle\mathcal{H}\rangle - \mu)} \quad (\text{II.32})$$

and $\mu = \langle\Psi|\mathcal{H}|\Psi\rangle/\langle\Psi|\Psi\rangle$ (the chemical potential of the droplet).

The expression II.31 is iterated until convergence with renormalization of the wave function. Typically, in our statics calculations, energy conservation is imposed to fall below 10^{-6} K.

II-5.2. Predictor-corrector propagator

All equations of motion are solved by time-propagation using a Hamming predictor-modifier-corrector algorithm [55] initiated by a fourth-order Runge-Kutta-Gill algorithm [55] implemented in the BCN-TLS 4He-DFT computing package [56]. Typical time steps range from 0.01 to 0.05 fs.

II-5.3. Absorption box

The time-dependent relaxation of liquid helium affected by the dopant(s) motion usually leads to the creation of sound waves and even shock waves, which induce helium evaporation at the droplet surface. Since we use of a simulation box with periodic boundary conditions (PBC) (imposed by the use of FFT to compute the convolution integrals in the OT functional), evaporated helium density will reach the boundaries and re-enter the box from the opposite side. This can interfere with the system in an unphysical and unpredictable way, and lead to significant errors in the calculations. To avoid such artifacts, absorbing boundaries are implemented by replacing $i \rightarrow i + \Lambda(\mathbf{r})$ into the dynamic equation of the helium [22], with

$$\Lambda(\mathbf{r}) = \Lambda_0 \left[1 + \tanh \left(\frac{b - b_0}{a} \right) \right], \quad b = |\mathbf{r}| \quad (\text{II.33})$$

This is equivalent to adding a purely imaginary potential $i\Lambda(\mathbf{r})$ which has the effect of absorbing helium density in the region where it is non zero. We have fixed $\Lambda_0 = 2$ and $a = 2 \text{ \AA}$. The evolution is damping-free [$\Lambda(\mathbf{r}) \ll 1$] in a sphere of radius $b < b_0 - 2a$.

If for instance, we just include absorption in the “z” direction (equal for all axes), Eq. (II.33) reduces to

$$\Lambda(\mathbf{r}) = \Lambda_0 \left[1 + \tanh \left(\frac{|z| - b_0}{a} \right) \right], \quad b = z \quad (\text{II.34})$$

where the value of b_0 is taken to be 2-3 \AA less than the maximum $|z|$ value in the calculation box.

The absorbing region has to be large enough to remove all the unwanted effects due to the presence of the PBC.

II-6. Vortices within the ^4He -DFT framework

A typical property of superfluids (which is shared with Bose-Einstein condensates) is that the velocity field satisfies $\nabla \times \mathbf{v} = 0$ (thus, it is said to be irrotational). This can be demonstrated by writing the pseudo wave function $\Psi(\mathbf{r})$ as [22]

$$\Psi(\mathbf{r}, t) = R(\mathbf{r}, t)e^{iS(\mathbf{r}, t)} \quad (\text{II.35})$$

where R and S are real functions, with $|\Psi(\mathbf{r}, t)|^2 = \rho(\mathbf{r}, t)$ and $R(\mathbf{r}, t) = \sqrt{\rho(\mathbf{r}, t)}$. The $R(\mathbf{r}, t)$ function is related to the density (diagonal density matrix ρ), while the phase $S(\mathbf{r}, t)$, characterizes the coherence (off-diagonal density matrix) and superfluid phenomena.

II-6.1. Irrotationality within ^4He -TDDFT

Introducing the form (II.35) into the continuity equation of the fluid

$$\frac{\partial \rho}{\partial t} + \nabla \cdot \mathbf{j} = 0 \quad (\text{II.36})$$

where the density current \mathbf{j} is defined as

$$\mathbf{j}(\mathbf{r}, t) = -i \frac{\hbar}{2m_4} [\Psi^*(\mathbf{r}, t) \nabla \Psi(\mathbf{r}, t) - \Psi(\mathbf{r}, t) \nabla \Psi^*(\mathbf{r}, t)] = \rho(\mathbf{r}, t) \frac{\hbar}{m_4} \nabla S(\mathbf{r}, t) \quad (\text{II.37})$$

we obtain the velocity field, given by :

$$\mathbf{v}(\mathbf{r}, t) = \mathbf{j}(\mathbf{r}, t) / \rho(\mathbf{r}, t) = \frac{\hbar}{m_4} \nabla S(\mathbf{r}, t) \quad (\text{II.38})$$

Since the velocity field is the gradient of a function, its rotational is zero ($\nabla \times \nabla S(\mathbf{r}, t) = 0$), which demonstrates the irrotational property of the fluid in the ^4He -TDDFT description.

We can now explain why the backflow (BF) term in Eq.(II.6) only contributes when the pseudo wave function is complex. It contains the term $[\mathbf{v}(\mathbf{r}) - \mathbf{v}(\mathbf{r}')]^2$ with \mathbf{v} coming from the phase term [Eq.(II.38)].

II-6.2. Quantization of the circulation around a vortex line

The circulation of the velocity field over a closed contour (C) is defined as

$$\Gamma_C = \oint_C \vec{v} \cdot d\vec{l} \quad (\text{II.39})$$

Assuming a cylindrical symmetry and a vortex with its axis along the “z” axis, we can calculate the circulation of \vec{v} along a circle (C) around the z axis. In cylindrical coordinates (r, θ, z) , $\vec{\nabla}S = (\partial S/\partial r, \frac{1}{r}\partial S/\partial \theta, \partial S/\partial z)$

the circulation in equation II.39 takes the form

$$\Gamma = \oint_C \vec{v} \cdot d\vec{l} = \int_0^{2\pi} v_\theta r d\theta = \int_0^{2\pi} \left(\frac{\hbar}{m_4} \frac{1}{r} \frac{\partial S}{\partial \theta} \right) r d\theta = \frac{\hbar}{m_4} \int_0^{2\pi} \frac{\partial S}{\partial \theta} d\theta = \frac{\hbar}{m_4} [S(2\pi) - S(0)] \quad (\text{II.40})$$

Since II.35 is single valued : $S(2\pi) = S(0) + 2n\pi$ with $n \in \mathcal{Z}$ ($n = \pm 1, \pm 2, \dots$)

hence,

$$\Gamma_C = n \frac{\hbar}{m_4} \quad (\text{II.41})$$

the circulation is quantized and the sign indicates the orientation of the circulation (positive: counterclockwise and negative: clockwise)

II-6.3. Vortex core

Stokes theorem: the circulation of a vector field around a closed contour (C) is equal to the flux of the curl of this field through any surface enclosed by the contour.

Applied to \vec{v} and the same contour as previous subsection, yields

$$\oint_c \vec{v} \cdot d\vec{l} = \iint_{\xi} \vec{\nabla} \times \vec{v} \cdot d\vec{\xi} \quad (\text{II.42})$$

The result should be zero since \vec{v} is irrotational, except if the contour encloses a point where $\Psi(\mathbf{r}, t) = 0$ the phase $S(\mathbf{r}, t)$ at that point is not defined.

Hence in Eq. (II.41), either $n = 0$ or there is a region (centered on the z-axis because of cylindrical symmetry) where $\Psi(\mathbf{r}, t) = 0$: this is the vortex core, of radius a . In superfluid ^4He , it is about 1 Å in radius ($a \sim 1 \text{ \AA}$).

II-6.4. Velocity field in cylindrical symmetry

In cylindrical symmetry only the azimuthal velocity is non-zero

Since we have shown that $\Gamma_C = n \frac{\hbar}{m_4}$

$$\Gamma_C = \oint_c \vec{v} \cdot d\vec{l} = \int_0^{2\pi} v_{\theta} r d\theta \quad (\text{II.43})$$

with v_{θ} being a constant along the circular contour (C) defined above,

$$\Gamma_C = \oint_c \vec{v} \cdot d\vec{l} = v_{\theta} r \int_0^{2\pi} d\theta = 2\pi r v_{\theta} \quad (\text{II.44})$$

$$2\pi r v_{\theta} = n \frac{\hbar}{m_4} \quad (\text{II.45})$$

so that

$$v_{\theta} = n \frac{\hbar}{m_4} \frac{1}{r} \quad (\text{II.46})$$

with $r \geq a$.

Contrary to a normal fluid, the azimuthal velocity decreases with the distance to the vortex core.

II-6.5. Energy of a linear vortex in cylindrical symmetry

The energy of a vortex is obtained by integrating the kinetic energy density over the droplet volume with an averaged density ρ_0

$$\begin{aligned}
 E_{\text{kin}} &= \frac{1}{2} \int \rho^*(\mathbf{r}) \mathbf{v}^2 dV \quad \text{where} \quad \rho^*(\mathbf{r}) = m_4 \rho(\mathbf{r}) \\
 &= \frac{m_4}{2} \int \rho(\mathbf{r}) v_\theta^2(r) dV \sim \frac{m_4}{2} \int_0^{2\pi} d\theta \int_a^R \rho_0 \left(\frac{n\hbar}{m_4} \right)^2 \frac{dr}{r} \int_0^L dz \\
 E_{\text{kin}}/L &= n^2 \pi \rho_0 \frac{\hbar^2}{m_4} \ln(R/a) \tag{II.47}
 \end{aligned}$$

In practice, only configurations with circulation $n = \pm 1$ are relevant. This is because the kinetic energy of a vortex line is proportional to n^2 and therefore a vortex line with $n = \pm 2$ is energetically less favored than two separate vortex lines with $n = \pm 1$.

II-6.6. Total angular momentum of a linear vortex

Assuming again a cylindrical symmetry

$$\begin{aligned}
 L_z &= \int_0^{2\pi} d\theta \int_a^R \rho_0 (m_4 r v_\theta) r dr \int_0^L dz \\
 &= 2\pi L \rho_0 m_4 \int_a^R \left(\frac{n\hbar}{m_4} \frac{1}{r} r^2 dr \right) \\
 &= \rho_0 (\pi(R^2 - a^2)L) n\hbar = \rho_0 V n\hbar \\
 &= N n\hbar \tag{II.48}
 \end{aligned}$$

II-6.7. How to imprint a vortex line in ^4He -DFT

In the ^4He -Density Functional Theory framework, a vortex line, along the “z” axis can be produced by starting the imaginary-time calculation [50] with the following initial order parameter

$$\Psi(r) = \frac{\rho^{1/2}(\mathbf{r})}{\sqrt{x^2 + y^2}}(x + iy) \quad (\text{II.49})$$

where $\rho(r)$ is the density corresponding to a pure droplet without vortex. That expression is equivalent to $\Psi(r, \theta) = \rho^{1/2}(\mathbf{r})e^{i\theta}$ under cylindrical symmetry with θ being the azimuthal angle.

 CHAPTER IIICLUSTERING IN HELIUM
NANODROPLETS

III-1. Introduction

Since ^4He nanodroplets can be considered as superfluid at the usual experimental temperature ($T \approx 0.4$ K), the formation of bound systems inside them is expected to exhibit the same characteristics as in the gas phase due to negligible viscosity. However, the resulting structures can be different from the ones obtained in the gas phase, due to the very high heat conductivity of the superfluid. These metastable structures result from a kinetic rather than thermodynamical control [21,19-57].

In the pioneering work by Nauta and Miller [19], long-range dipole-dipole interactions were invoked to interpret the self-assembly between HCN (Hydrogen Cyanide) molecules into linear chains. The HCN molecule has a strong electric dipole moment. At long range the dipole-dipole interaction dominates and an additional molecule tends to orient colinearly to the others. When it arrives close to the other molecules already solvated, it is cold and no longer has enough kinetic energy to reorient and form the thermodynamically most stable structure which is compact. The resulting structure inside helium nanodroplets is a long chain (up to 10 molecules). More generally, kinetics is expected to play an important role in the clustering process, especially in the common case of sequential pickup. This is

because the complexes formed early can be stuck into metastable conformations, rearrangement and isomerization under cryogenic conditions being particularly slow [58,59-61].

When multiple pickup chambers are used, this can lead to peculiar structures, such as core-shell clusters [62-63], and nanowires [64]. Experimental studies involving helium clusters and their collision with foreign atoms were addressed by Toennies and coworkers [65,66] in the 1980s. Important results were obtained, among which we can stress that depending on different parameters impact parameter and the strength of the dopant-helium interaction, dopant could be captured, escape or go through the droplet. Upon capture, a significant proportion of the impurity kinetic energy is dissipated into the droplet, which relaxes through multiple evaporation of He atoms [67]. When several dopants are picked up, they eventually meet and form a bond. The superfluid helium environment can interfere in this process, yielding unusual formations such as loosely bound “bubble foam” or “quantum gel” structures for light, weakly attractive impurities, such as Ne [68] or Mg [69]. This was attributed to the formation of a helium shell around the foreign atoms, preventing the formation of a direct bond between them. In addition, the presence of quantized vortices may further influence the cluster morphology, as vortex cores act as nucleation sites and impurities have a tendency to coalesce, forming filaments along them [70-72].

III-2. Method

Coppens *et al.* [73] have studied argon cluster formation in a ${}^4\text{He}_{5000}$ droplet using Time Dependent Density Functional Theory (${}^4\text{He}$ -TDDFT), see Annex G for technical details. They found the production of loosely bound configurations due to the formation of a high density shell of helium around each Ar atom. However, the particular choice of highly symmetric initial conditions could have affected the results. Here we revisit the cluster formation process considering the more realistic case of successive pick-up, in which argon atoms collide with helium droplets doped with argon monomers or small clusters. The interaction potentials are taken from

the literature [74]. Other than ^4He -TDDFT, two approximate atomistic based approaches are also tested: the ring-polymer molecular dynamics (RPMD) [75-77] and the zero-point averaged dynamics (ZPAD) [78-80] methods.

The RPMD method uses a path-integral description of nuclear motion and provides a description at the atomistic level at low but finite temperatures. It has already been employed to address chemical reactions in helium droplets [81], including metastable dimerization [82]. On the other hand, the ZPAD method is based on the frozen Gaussian wavepacket approach by Heller [78] and the equivalent effective potentials by Sterling *et al* [83] to describe the nuclear motion. Zero-point delocalization is described by a frozen wavefunction attached to each He atom, which is equivalent to classical dynamics with effective interaction potentials. In both methods, bosonic exchange effects are ignored. However, the ZPAD method is computationally attractive because the system dynamics can then be treated as classical at the actual helium nanodroplet temperature of 0.4 K, through the use of effective interaction potentials.

The ZPAD method provides a computationally very efficient way of simulating the doped helium droplets, once the effective potentials have been obtained. It is also possible to extend trajectories to the nanosecond time scale or even beyond. The RPMD approach is intermediate between the ^4He -TDDFT and ZPAD methods, at least in terms of computational cost. While the ^4He -TDDFT is, in principle, more realistic or describing superfluid droplets, since it takes into account quantum and exchange-correlation effects, it is significantly more time-consuming than both particle-based approaches. It is also usually limited to zero-temperature simulations.

All three methods used the same Ar-Ar and Ar-He potentials, from [74]. Their references and characteristics are displayed in Table F.10 (annex F).

Only Ar clustering is presented in this thesis because it was my contribution to the following work [84].

III-3. Results

Several simulations were performed to study sequential doping as the collision of one argon atom with a helium nanodroplet composed of 1000 atoms doped with one or several Ar atoms. The simplest case consisted of placing a single Ar atom at the center of the droplet and launching another one toward it from outside the droplet. We label it $\text{Ar}+\text{Ar}@^4\text{He}_{1000}$.

The velocity of the impinging atom was set to 500 ms^{-1} ($5 \text{ \AA}/\text{ps}$) along the z axis, which corresponds approximately to the thermal kinetic energy in the pick up cell at room temperature ($T = 300 \text{ K}$). We also studied the effect of different impact parameters ($b=0,10 \text{ \AA}$), Fig III.1. Another interesting case was the symmetric collision of two outer Ar atoms against one at the middle, with the same initial conditions as the first case (Fig III.2). Finally, we explored the situation where an Ar atom collided with a tetramer (Ar_4) to form the pentamer within the nanodroplet. We include in the analysis the effect of the impact parameter and of different initial positions of the colliding atom with respect to the tetramer. The cluster was initially located with its center of mass at the center of the droplet and with one of its C_3 symmetry axes along the z axis with the base to vertex orientation towards positive z . Two initial positions were tested for each value of the impact parameter: one called “upwards”, where the colliding argon was on the negative side of the z axis with its velocity parallel to it, and the other called “downward” where it was on the positive side of the z axis with its velocity antiparallel to it. See figures III.3 and III.4.

Figures from III.1 to III.4 show the initial (left) and final configuration (right, at the given time highlighted in red) for $\text{Ar}_{n'}+\text{Ar}_n@^4\text{He}_{1000}$ collision ($n'=1,2$ and $n=1,4$).

III-3.1. Formation of Ar dimer

Cases *A* and *B* correspond to an external Ar atom colliding against a helium droplet hosting one Ar atom inside. Collision is tested for an impact parameter of ($b = x = 0$) and $b=10 \text{ \AA}$ respectively. In both cases, an initial velocity ($v_z=5 \text{ \AA/ps}$) is set along the z direction for the outer dopant. The results show a bound dimer for *A* and a loosely bound state for *B*. The latter means there is some helium density in between the argon atoms preventing direct Ar-Ar bond formation.

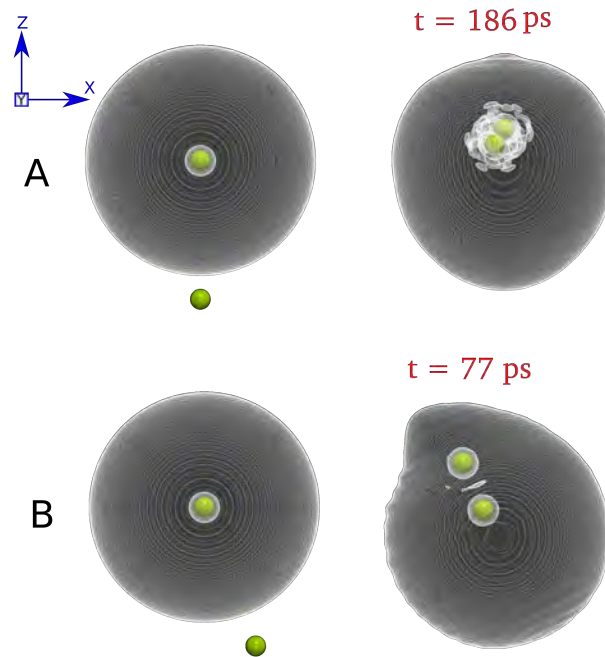


Figure III.1. Ar+Ar@ $^4\text{He}_{1000}$ collision. The initial configuration is shown in the left column at a given time (t). Two impact parameter were explored: $b = 0$ (case A) and $b = 10 \text{ \AA}$ (case B).

III-3.2. Formation of Ar trimer

In case *C*: two impinging Ar atoms collide with one at the center of the droplet. The impact parameter is $b = 0$, and its velocity $v_z=5 \text{ \AA/ps}$ and $v_z=-5 \text{ \AA/ps}$ respectively. A metastable configuration is obtained because the thermodynamically most stable trimer in gas phase corresponds to an equilateral triangle [85] rather than a linear cluster.

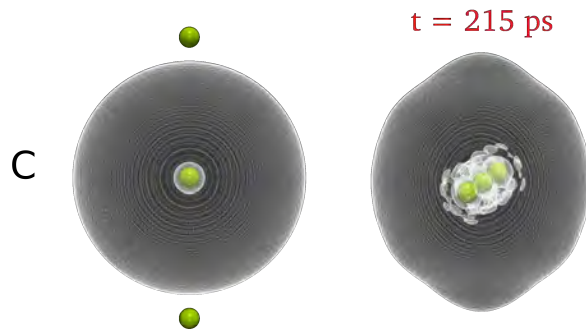


Figure III.2. Ar+Ar+Ar@ ${}^4\text{He}_{1000}$ collision. The initial configuration is shown in the left column and the final one at time t in the right column.

III-3.3. Formation of Ar pentamer

Figures D and E correspond to one Ar atom colliding against the base of an Ar_4 tetramer (triangular basis) embedded in a ${}^4\text{He}_{1000}$ droplet. Case D: $b = 0$, $v_z = 5$ Å/ps (“loosely bound”) whereas E: $b = 10$ Å, $v_z = 5$ Å/ps (metastable configuration, the most stable structure in gas phase is a bipyramid with a triangular basis [85]). On the other hand, Figure III.4 correspond to one Ar atom colliding against the vertex of same tetramer formation as before. Case F: $b = 0$, $v_z = -5$ Å/ps (metastable configuration) and G: $b = 10$ Å, $v_z = -5$ Å/ps (“loosely bound”).

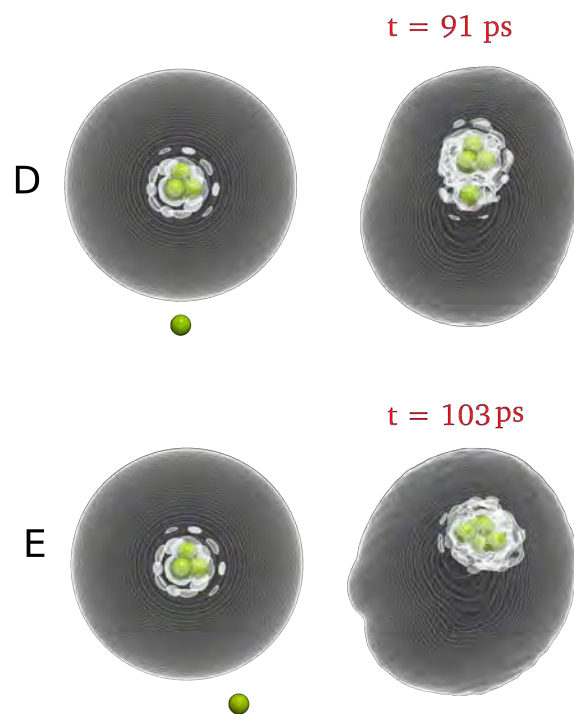


Figure III.3. Ar+Ar₄@⁴He₁₀₀₀ collision. The initial configuration is shown in the left column and the final one at time t in the right column.

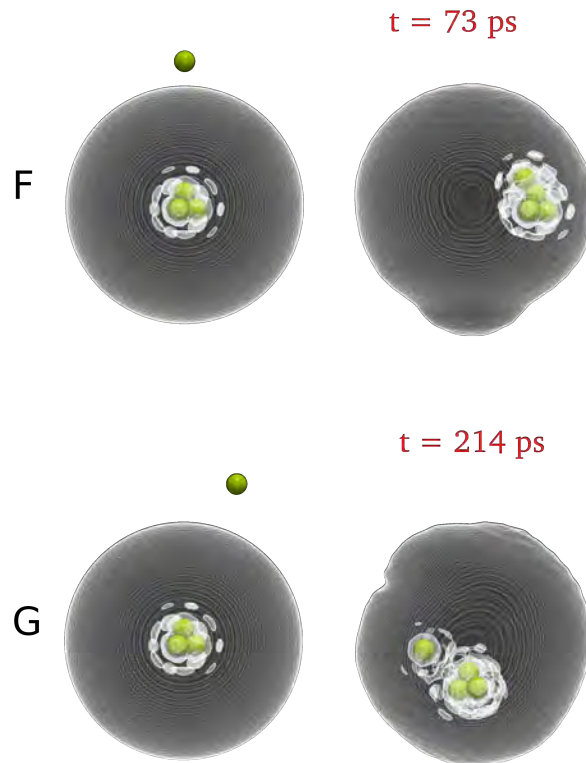


Figure III.4. Ar+Ar₄@⁴He₁₀₀₀ collision. The initial configuration is shown in the left column and the final one at time t in the right column

III-4. Conclusion

The results presented in this chapter are only the ⁴He-TDDFT since they were part of my thesis work. In the published work, they were compared with those of the other two atomistic methods. All three methods predict the helium host droplet plays a role in the formation of Ar cluster. It hinders the chemical bond between dopants, making a shell structure around them. In addition, kinematic effects freeze the growing cluster into metastable configurations. The only dynamics conditions which lead to a bound dimer configuration like in the gas phase was the Ar-Ar@⁴He₁₀₀₀ collision with zero impact parameter.

The ⁴He-TDDFT yielded more dimers at 0 impact parameter than the two approximate, atomistic methods, and more bond although metastable isomers for

the pentamer case. This is presumably due to the superfluid effect of frictionless motion below the Landau critical velocity.

Clustering, collision, and relaxation dynamics in pure and doped helium nanoclusters: Density- vs particle-based approaches

Cite as: J. Chem. Phys. 157, 014106 (2022); doi: 10.1063/5.0091942

Submitted: 18 March 2022 • Accepted: 14 June 2022 •

Published Online: 5 July 2022



View Online



Export Citation



CrossMark

Ernesto García-Alfonso,¹ Manuel Barranco,^{1,2,3} David A. Bonhommeau,⁴ Nadine Halberstadt,¹ Martí Pi,^{2,3} and Florent Calvo^{5,a)}

AFFILIATIONS

¹Laboratoire Collisions, Agrégats, Réactivité (LCAR), Université de Toulouse, CNRS, 31062 Toulouse, France

²Department FQA, Facultat de Física, Universitat de Barcelona, Diagonal 645, 08028 Barcelona, Spain

³Institute of Nanoscience and Nanotechnology (IN2UB), Universitat de Barcelona, Barcelona, Spain

⁴Université de Reims Champagne Ardenne, CNRS, GSMA UMR 7331, 51100 Reims, France

⁵Université Grenoble Alpes, CNRS, LIPHY, F38000 Grenoble, France

^{a)}Author to whom correspondence should be addressed: florent.calvo@univ-grenoble-alpes.fr

ABSTRACT

The clustering, collision, and relaxation dynamics of pristine and doped helium nanodroplets is theoretically investigated in cases of pickup and clustering of heliophilic argon, collision of heliophobic cesium atoms, and coalescence of two droplets brought into contact by their mutual long-range van der Waals interaction. Three approaches are used and compared with each other. The He time-dependent density functional theory method considers the droplet as a continuous medium and accounts for its superfluid character. The ring-polymer molecular dynamics method uses a path-integral description of nuclear motion and incorporates zero-point delocalization while bosonic exchange effects are ignored. Finally, the zero-point averaged dynamics approach is a mixed quantum–classical method in which quantum delocalization is described by attaching a frozen wavefunction to each He atom, equivalent to classical dynamics with effective interaction potentials. All three methods predict that the growth of argon clusters is significantly hindered by the helium host droplet due to the impeding shell structure around the dopants and kinematic effects freezing the growing cluster in metastable configurations. The effects of superfluidity are qualitatively manifested by different collision dynamics of the heliophilic atom at high velocities, as well as quadrupole oscillations that are not seen with particle-based methods, for droplets experiencing a collision with cesium atoms or merging with each other.

Published under an exclusive license by AIP Publishing. <https://doi.org/10.1063/5.0091942>

I. INTRODUCTION

Helium-4 clusters at their usual experimental temperatures ($T \sim 0.37$ K)¹ can be considered as superfluid nanodroplets. As such, they have a negligible viscosity and a large thermal conductivity and readily capture any atom or molecule.²

The extremely weak interactions of helium with most atomic or molecular dopants make helium nanodroplets (HNDs) particularly suitable for spectroscopic studies.^{3–6} The properties of atomic and molecular clusters in ⁴He droplets have been reviewed by several groups.^{1,7–9}

The pickup process used to incorporate the dopant into HNDs is determined by their size and by the conditions in the doping

chamber itself. In particular, more than a single dopant per droplet can be incorporated by varying the vapor pressure.¹ The impurities can then move inside the droplet, eventually meeting each other to form clusters or complexes. Such clustering mechanisms are favored by the negligible viscosity and the small volume of the droplet, which facilitates impurity encounters and also by the large thermal conductivity that helps dissipate the energy released by the clustering process.

Clusters formed in ⁴He droplets do not always show the same structure as in vacuum.^{1,10,11} Such differences can be explained by a number of factors. In the pioneering work by Nauta and Miller,¹⁰ long-range dipole–dipole interactions were invoked to interpret the self-assembly between HCN molecules into linear chains.

More generally, the kinetics is expected to play an important role in the clustering process, especially in the common case of sequential pickup. This is because the complexes formed early might be stuck into metastable conformations, rearrangement and isomerization under cryogenic conditions being particularly slow.^{12–16} When multiple pickup chambers are used, this can lead to peculiar structures, such as core-shell clusters^{17,18} and nanowires.¹⁹ Another interference of helium with the clustering process has been evidenced in the formation of loosely bound “bubble foam” or “quantum gel” structures for light, weakly attractive impurities, such as Ne²⁰ or Mg.^{21,22} This was attributed to the formation of a helium shell around the foreign atoms, preventing the formation of a direct bond between them. In addition, the presence of quantized vortices may further influence the cluster morphology, as vortex cores act as nucleation sites and impurities have a tendency to coalesce, forming filaments along them.^{23–25}

Systematic experimental studies on helium clusters and their collision with foreign atoms started in the 1980s,^{26,27} as reviewed by Toennies.²⁸ The first theoretical study of elastic and inelastic scattering of ⁴He atoms impinging on He clusters was presented by Eichenauer *et al.*, who used a liquid drop plus optical model approach.²⁹ Depending on the collision parameters and the strength of the dopant–helium interaction, a dopant colliding with a droplet was found to be captured, to escape the droplet, or to go right through it. Upon capture, a significant proportion of the impurity kinetic energy is dissipated into the droplet which relaxes through multiple evaporations of He atoms.^{30–32} In addition to the capture of foreign atoms, several groups have recently investigated the soft-landing of helium droplets doped with simple atoms and clusters onto surfaces either experimentally³³ or by means of modeling.^{34–36}

Various efficient methods are available to account for quantum nuclear effects at equilibrium, ranging from vibrational configuration interaction,³⁷ vibrational self-consistent field,³⁸ Gaussian wavepackets,^{39,40} to a broad array of quantum Monte Carlo methods. However, insight into cluster formation and the competition between thermalization and kinetics requires dedicated computational modeling that takes into account the specific nature of the dopants and their interaction with the droplets, in real time. For HNDs that may contain millions of atoms, solving the dynamical problem of capture and subsequent relaxation while accounting for the quantum mechanical nature of ⁴He happens to be a prohibitive task.

In the present article, we have explored three complementary approaches to address the above issues in real time based on different treatments of the helium droplets. Each approach has been successfully used to simulate different processes occurring in helium nanodroplets. They are compared here, for the first time, on the simulation of the same processes. The time-dependent density functional theory (TDDFT) method, thoroughly described in Refs. 41 and 42, is based on the work by Dalfovo and co-workers.⁴³ TDDFT and its static version (DFT) treat the ensemble of ⁴He atoms in an irrotational fluid-like approach at zero temperature, incorporating the peculiarities of the elementary excitation spectrum of ⁴He that makes it superfluid and including an extra term to account for solid–liquid coexistence.⁴⁴ It has recently been applied to the capture and clustering of rare-gas and alkali atoms by He droplets.^{31,32,45–49}

A second approach that is suitable for real-time dynamical studies is the ring-polymer molecular dynamics (RPMD) method

introduced by Craig and Manolopoulos.⁵⁰ It relies on the path-integral framework and provides a description at the atomistic level of details at low but finite temperature, although exchange effects between bosonic ⁴He atoms are not included. The RPMD method has already been employed to address chemical reactions in helium droplets,⁵¹ including metastable dimerization.⁵²

Another atomistic method used here is that of zero-point averaged dynamics (ZPAD), based on the frozen Gaussian wavepacket approach by Heller⁵³ and the equivalent effective potentials by Sterling *et al.*,⁵⁴ which has been successfully used in the dynamical study of rare-gas cluster dissociative ionization inside HNDs.^{55–57} The ZPAD approach associates a frozen wavefunction to each He atom, therefore, incorporating zero-point delocalization effects. As in RPMD, exchange effects are ignored, but the method is computationally attractive because the system dynamics can then be treated as classical at the actual HND temperature of 0.4 K, through the use of effective interaction potentials.

Three different physical situations were covered in our exploration of dynamics and relaxation effects in HNDs. Firstly, impurity clustering was chosen owing to its current experimental interest,⁸ taking here Ar atoms as the model impurities. The argon atom is heliophilic and resides in the bulk of the droplet, being prone to clusterization from successive pickups. In a recent work by some of us employing the TDDFT approach,³² the simultaneous collision of different argon impurities was considered and found to produce loosely bound clusters, but the particular choice of highly symmetric initial conditions in these simulations could have affected the results. Here, we have considered the more realistic case of successive pickup, in which argon atoms collide with helium droplets doped with pre-existing argon monomers or small clusters, and investigated the quantitative influence of the collision conditions, as well as the qualitative roles of the possibly preexisting dopant.

Secondly, the capture of Cs atoms, which are barely bound to the He droplet as their binding energy is only about 10 K,⁴⁵ provides another challenge to theory. Unlike argon, cesium is heliophobic and tends to reside at the droplet surface, unless it is under the form of a larger cluster.^{58–61} In the present work, the collision of a single Cs atom onto a pristine helium droplet was addressed using the three complementary TDDFT, RPMD, and ZPAD approaches, and the effect of collision conditions was assessed.

Finally, we also considered the case of two equivalent droplets merging after being brought into contact. Such a situation has also been already addressed separately earlier by means of TDDFT, both when the two droplets host superfluid vortices⁶² and when they do not.⁶³ Here, the relaxation is caused by the mutual van der Waals attraction between the droplets, in their path toward eventually forming a single double-sized droplet. The droplet-like behavior is highlighted in the merging process, which, thus, constitutes another stringent test on the methodology.

To keep the workload reasonable while still allowing some statistical perspective on the robustness of the results, we have kept the size of the helium droplet to 1000 atoms in our simulations, or two He₅₀₀ droplets experiencing merging. The much larger masses of the argon and cesium atoms relative to helium also justify the usual approximation that their dynamics be considered as classical, only leaving helium atoms to be treated quantum mechanically.

The article is organized as follows: In Sec. II, we outline the three methods used in this work, namely, TDDFT, RPMD, and

ZPAD, in such a way as to provide sufficient insight for the reader who might not be familiar with all of them. In Sec. III, we discuss the results obtained with the three dynamical methods, and some concluding remarks close this paper in Sec. IV. In addition to the main discussion, we provide in the [supplementary material](#) a selection of illustrative real-time dynamics of some clustering or relaxation processes inferred from the three computational approaches, as well as some technical details regarding the effective ZPAD potentials.

II. METHODS

The TDDFT,^{41,42,64} RPMD,^{50,61,65,66} and ZPAD^{55–57} methods applied here to helium nanodroplets have been thoroughly described elsewhere. Hence, we limit our description to their essential features and only describe the few new refinements or the features specific to the present systems in more detail.

In each case, we distinguish the methodology at equilibrium, needed to prepare the systems at time $t = 0$, and the methodology needed to address the real-time dynamics following an excitation corresponding to the collision of an impinging argon or cesium atom, or to the sudden contact between two pre-equilibrated droplets.

A. ⁴He-DFT and TDDFT for liquid helium

Density functional theory for liquid helium is a phenomenological approach constituting a compromise between accuracy and feasibility for realistic size droplets. The parameters of the functional have been adjusted to reproduce various properties of the bulk superfluid liquid, such as equilibrium density, energy per atom, compressibility, as well as the entire dispersion relation of the elementary excitations.

Since their original introduction by Stringari and co-workers (see, e.g., Ref. 67), functionals have been systematically improved and notably now account for the finite range of interatomic interactions.^{43,44} Within He-DFT, the helium droplet is described as a continuous medium at zero temperature. The energy of a N -atom droplet is then written as a functional of the ⁴He atom density $\rho(\mathbf{r})$ as

$$E[\Psi] = \int d\mathbf{r} \frac{\hbar^2}{2m_{\text{He}}} |\nabla\Psi|^2 + \int d\mathbf{r} \mathcal{E}_c(\rho), \quad (1)$$

where $\Psi(\mathbf{r})$ is the effective wavefunction (or order parameter) of the superfluid such that $\rho(\mathbf{r}) = |\Psi(\mathbf{r})|^2$ with $\int d\mathbf{r} |\Psi(\mathbf{r})|^2 = N$, and the functional $\mathcal{E}_c(\rho)$ ⁴⁴ contains the interaction term within the Hartree approximation and additional terms describing nonlocal correlation effects.⁴²

If the droplet carries n atomic impurities A (here, argon or cesium atoms), their effects are taken into account by adding to $E[\Psi]$ in Eq. (1) an external potential under the form $\int d\mathbf{r} \mathcal{V}(\mathbf{r}) \rho(\mathbf{r})$, where $\mathcal{V}(\mathbf{r})$ is the interaction of one single He atom with the cluster calculated by summing He–A interaction potentials as follows:

$$\mathcal{V}(\mathbf{r}) = \sum_{i=1}^n V_{\text{He-A}}(|\mathbf{r} - \mathbf{r}_i|), \quad (2)$$

with \mathbf{r}_i being the position of the i th A atom.

The droplet equilibrium configuration is obtained by solving the Euler–Lagrange equation,

$$\left\{ -\frac{\hbar^2}{2m_{\text{He}}} \nabla^2 + \frac{\delta\mathcal{E}_c}{\delta\rho} + \mathcal{V}(\mathbf{r}) \right\} \Psi = \mu\Psi, \quad (3)$$

where μ is the ⁴He chemical potential corresponding to the number of He atoms in the droplet.

Equation (3) is solved in Cartesian coordinates using a space-step of 0.35 Å in the presence of Ar atoms, 0.4 Å in the presence of a Cs atom, and 0.44 Å for merging He₅₀₀ droplets. In the case of argon clusters, their configuration is kept fixed at the gas phase structure,⁶⁸ since the presence of helium is not expected to introduce any significant change to the structure of the preformed argon cluster^{32,69,70} due to the much weaker He–Ar interaction compared to Ar–Ar.⁷¹

The time evolution equations for the effective wavefunction $\Psi(\mathbf{r})$ and impurity positions \mathbf{r}_i are obtained by minimizing the action,³² which yields

$$i\hbar \frac{\partial}{\partial t} \Psi(\mathbf{r}) = \left[-\frac{\hbar^2}{2m_{\text{He}}} \nabla^2 + \frac{\delta\mathcal{E}_c}{\delta\rho(\mathbf{r})} + \sum_{i=1}^n V_{\text{He-A}}(|\mathbf{r} - \mathbf{r}_i|) \right] \Psi(\mathbf{r}), \quad (4)$$

$$m_A \ddot{\mathbf{r}}_i = - \left\{ \int d\mathbf{r} V_{\text{He-A}}(|\mathbf{r} - \mathbf{r}_i|) \nabla\rho(\mathbf{r}) + \sum_{i \neq j} \left[\frac{\mathbf{r}_i - \mathbf{r}_j}{r_{ij}} \frac{dV_{\text{A-A}}(r)}{dr} \right]_{r=r_{ij}} \right\} \quad (i = 1, \dots, n), \quad (5)$$

where the last term in Eq. (5) is only present for clusters, $r_{ij} = |\mathbf{r}_i - \mathbf{r}_j|$, and the time dependence of the variables has been omitted for clarity.

In order to solve Eqs. (4) and (5), initial values for the $\{\mathbf{r}_i, \dot{\mathbf{r}}_i\}$ variables and the effective wavefunction $\Psi(\mathbf{r})$ have to be specified. When simulating Ar _{n} clustering, they were taken as the He effective wavefunction and the Ar atom positions $\{\mathbf{r}_i(0)\}$, $i = 1, \dots, n - 1$ obtained as the equilibrium configuration of the preformed solvated ($n-1$)-atom cluster by solving Eq. (3), with $\{\dot{\mathbf{r}}_i(0)\} = 0$. When simulating Cs collisions or droplet merging, the He effective wavefunction was taken as that of the pure He₁₀₀₀ or He₅₀₀ droplets, respectively. The values of the remaining variables, $\{\mathbf{r}_n(0), \dot{\mathbf{r}}_n(0)\}$, were chosen to yield the desired impact parameter and kinetic energy of the impinging impurity.

The He–Ar and He–Cs interaction potentials were taken from Tang and Toennies (TT),⁷¹ and from Patil,⁷² respectively. Equations (3)–(5) were solved using the ⁴He-DFT BCN-TLS computing package.⁷³ In particular, Cartesian coordinates were used and a fast Fourier transform⁷⁴ was employed to evaluate the convolution integrals entering the DFT mean-field definition.

The time-dependent equations (4) and (5) were numerically solved using a Hamming predictor–modifier–corrector initiated by a fourth-order Runge–Kutta–Gill algorithm,⁷⁵ with time steps of 0.1 and 0.5 fs in the presence of argon and cesium atoms, respectively, and 1 fs for the merging problem. When needed, absorbing boundary conditions were implemented to prevent evaporated helium atoms from reentering the simulation box (periodic boundary conditions are imposed to use the fast Fourier transform). During the integration of the time evolution equations, the positions of all impurities were free to relax. Reference 64 and references therein

provide more details on how the DFT and TDDFT equations are solved in practice.

B. The RPMD approach

RPMD is an approximate method for solving the time-dependent quantum dynamics problem based on the path-integral formalism, which is exact in the short time and harmonic limits.⁵⁰ Its connections with semiclassical instanton theory⁷⁶ and also with centroid molecular dynamics and Matsubara dynamics have been thoroughly explored by Hele and co-workers.⁷⁷ In the context of real-time dynamics at thermal equilibrium, RPMD has been used to compute vibrational spectra in anharmonic systems^{78–80} to determine transport properties in condensed systems^{81,82} and also to characterize reactive collisions dynamics.^{83,84} The method was also used occasionally to explore various out-of-equilibrium situations induced by a vertical excitation or some momentum impulse^{85,86} and was shown also in this context to be exact in the limit of short times, harmonic potentials, or high temperatures.⁸⁷

Briefly, the method relies on the Feynman formalism of imaginary time path integrals and assimilates the quantum dynamics of the many-body system to an effective classical dynamics of a higher-dimensional system, each particle being described by a ring-polymer of P monomers or beads. In practice, with $\{\mathbf{R}_\alpha, \alpha = 1, \dots, P\}$ denoting the set of positions of these monomers, the dynamics is Hamiltonian and ruled by the effective potential

$$V_{\text{eff}}(\{\mathbf{R}_\alpha\}) = \frac{1}{P} \sum_{\alpha=1}^P V(\mathbf{R}_\alpha) + \sum_{\alpha=1}^P \sum_{i \in \text{atoms}} \frac{m_i P}{2\beta^2 \hbar^2} \|\mathbf{r}_{\alpha,i} - \mathbf{r}_{\alpha,i+1}\|^2, \quad (6)$$

where $\beta = 1/k_B T$ with k_B and \hbar being the Boltzmann and reduced Planck constants, respectively, and T being the temperature. In Eq. (6), $\mathbf{r}_{\alpha,i}$ denotes the position of particle i of replica α with the cyclic condition $\mathbf{r}_{P+1,i} = \mathbf{r}_{1,i}$, the entire set of positions for replica α being referred to as \mathbf{R}_α . In conventional (thermostated) path-integral molecular dynamics (PIMD), each particle with position $\mathbf{r}_{\alpha,i}$ is associated with a momentum $\mathbf{p}_{\alpha,i}$ and a mass $m_{\alpha,i}$ that can be freely adjusted in order to improve sampling efficiency. Within RPMD, the masses are not arbitrary but all set to the physical values, $m_{\alpha,i} = m_i$ for all $\alpha = 1, \dots, P$.

In practice, all variables are transformed into normal modes in order to decouple the harmonic part of the Hamiltonian, which in turn enables the use of the reference system propagation algorithm (RESPA)⁸⁸ to accelerate the integration of the trajectory. The initial conditions of RPMD trajectories need to be properly equilibrated, and each particle was coupled to an individual Nosé–Hoover variable, within conventional PIMD trajectories. Such massive thermostating was used to prepare samples of phase space configurations for the various systems under study, namely, pure helium droplets containing 500 or 1000 atoms and, in the latter case, possibly doped with either one atom, one dimer, or one tetramer of argon.

A ring contraction technique⁸⁹ was also employed to reduce the number of beads needed to describe the heavier atoms. A temperature of $T = 1$ K and a Trotter number of $P = 256$ were chosen to describe the helium atoms, with $P = 16$ beads for argon and cesium atoms. Such a moderately high temperature was necessary to perform PIMD and RPMD simulations within a reasonable amount

of computing time while maintaining a good precision: The binding energy obtained for pure He₁₀₀₀ droplets with 256 beads is in reasonable agreement with reference results.

Efficient Lennard-Jones versions of the TT potential⁷¹ were employed to describe interactions between the rare gases, with corresponding parameters $\epsilon_{\text{He-He}} = 10.76$ K, $\epsilon_{\text{Ar-Ar}} = 143.4$ K, $\epsilon_{\text{He-Ar}} = 29.61$ K, $\sigma_{\text{He-He}} = 2.635$ Å, $\sigma_{\text{Ar-Ar}} = 3.346$ Å, and $\sigma_{\text{He-Ar}} = 3.115$ Å.

In simulating collisions between argon or cesium projectiles onto pure or doped helium droplets, random phase space configurations were borrowed from the PIMD samples for both the projectile and the target cluster and served as initial conditions. Those configurations were randomly rotated and initial positions for the centroid of the projectile were imposed so that the centers of mass between the collision partners are separated initially by 50 Å along the x -axis and by an impact parameter $b = 0$ or $b = 10$ Å along the y -axis. The thermostated PIMD trajectories used for sampling initial conditions used a time step of 0.1 fs, while a longer time step of 0.5 fs could be employed to propagate the RPMD trajectories owing to the RESPA trick. The overall computational load of RPMD trajectories is approximately P times that of classical molecular dynamics.

C. The ZPAD approach

ZPAD is a mixed quantum-classical method designed to model the dynamics of dopants embedded in a quantum environment. It provides an approximate description of the quantum delocalization of helium atoms at almost the same computational cost as classical dynamics. The method originates from the work of Sterling *et al.*⁵⁴ who modeled the dynamics of pure and Li-doped solid parahydrogen by representing H₂ as Gaussian particles. As a result, the H₂ dynamics was similar to the frozen Gaussian approach of Heller⁵³ and can be described as classical dynamics using effective interaction potentials. Slavíček *et al.* later applied this idea to simulate the photodissociation of hydrogen halides in floppy neon clusters.⁹⁰ These authors implemented an iterative procedure to determine neon wavefunctions and were able to rapidly converge accurate effective Ne–Ne potentials. ZPAD, as used in the present work, was introduced as a direct extension of Ref. 90 to the fragmentation dynamics of neon- and argon-doped helium clusters^{55–57,91} by solving the convergence problem due to the extensive delocalization of the helium atom wavefunction.

The ZPAD method relies on the iterative determination of the frozen wavefunction describing the quantum delocalization of the He atoms and of the inferred effective He–He pair potential. The iterative procedure is detailed in Refs. 55–57 and 91; hence, only its essential features are recalled here. At each iteration, a classical simulation of the He_N system at the experimentally relevant temperature of $T = 0.38$ K is performed using the current, iteratively determined He–He pair potential (i.e., the classical He–He potential at the first iteration and an effective, but nonconverged, He–He potential at later iterations). The next He wavefunction is obtained by solving the radial Schrödinger equation for a helium atom in the average environment of the remaining He atoms, assumed to be spherical, using the current effective potential convoluted with the pair distribution function. The classical potential is then doubly convoluted with the squared modulus new He wavefunction to obtain the new effective potential, and the process is repeated until convergence. The final

effective potential is characterized by a much shallower well and a larger equilibrium distance.

In practice, it was necessary to truncate the He wavefunction at $R = 1.6 \text{ \AA}$ in order to reach convergence.⁵⁷ Note that a recent method along the same lines as the ZPAD method does not determine an effective wavefunction for helium atoms but directly the effective potential itself.⁹² Here, the effective potential well depth was found to be 1.81 K at an equilibrium distance of 4.39 \AA .

Because argon atoms are fully solvated in helium droplets, it is relevant to incorporate delocalization effects in the He–Ar interaction as well and, hence, to design a corresponding effective potential. Neglecting any delocalization effect of the Ar atom, the Tang–Toennies Ar–He interaction potential was convoluted with the squared modulus of the He wavefunction obtained previously. The effective Ar–He potential thus obtained has a binding energy of 13.57 K at an equilibrium distance of 4.17 \AA , to be compared with 29.59 K at 3.498 \AA for the original potential.⁷¹ Numerical details of the He–He and Ar–He effective potentials used in this study are given in the [supplementary material](#), and the reader is referred to Refs. 55–57 and 91 for more information about the iterative procedure employed to converge the He–He effective potential. In contrast to argon, heliophobic cesium atoms were treated fully classically in their interaction with helium.

The zero-point averaged dynamics of the doped HND is then carried out by performing classical dynamics for the He and the dopant atoms using as total potential energy the sum of effective He–He interactions, dopant–dopant interactions, and He–dopant interactions (effective for Ar and classical for Cs). All ZPAD trajectories employed a time step of 1 fs.

III. RESULTS

Before addressing the time-dependent processes involving heliophilic or heliophobic impurities or the natural relaxation of droplets merging, and since we need them as initial conditions, it is necessary to consider the equilibrium case of helium nanodroplets themselves. [Figure 1\(a\)](#) shows the radial densities of helium atoms in the He_{1000} droplet determined with respect to the droplet center of mass, as predicted by density-functional theory, path-integral MD at equilibrium, and zero-point averaged MD method at 0, 1, and 0.38 K, respectively. Likewise, [Fig. 1\(b\)](#) depicts the He–Ar radial distributions for He_{1000} droplets doped with a single argon atom lying inside. Overall, the helium density obtained for the pristine helium droplet is extremely smooth with the DFT approach. Such a smooth radial profile is consistent with earlier results, including diffusion Monte Carlo (DMC) simulations.⁴² Within the PIMD description, some minor shell structuration can be perceived, which becomes even more clear with ZPAD. This behavior is a signature of the mostly classical character of ZPAD. In particular, the density at a vanishing distance from the center of mass is extremely small and about 500 times smaller than the first peak at 2.5 \AA , which indicates rigidity near the droplet center, vacant from any atom. Note, however, that the average density profile is reasonable, especially compared to the one obtained from the original He–He potential (not shown).

In the presence of the argon impurity, the helium atoms preferentially localize around it at a distance close to 4 \AA and the three

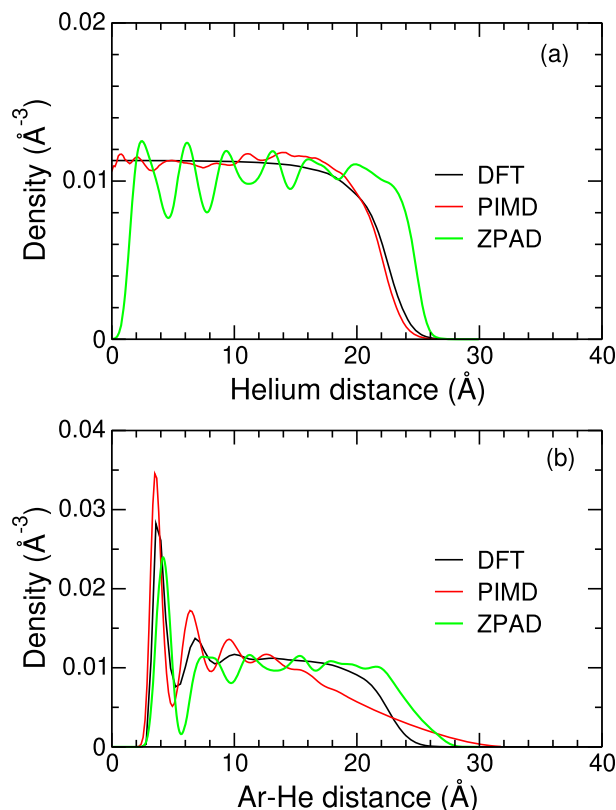


FIG. 1. Equilibrium density profiles of the He_{1000} and ArHe_{1000} droplets obtained with the DFT, PIMD, and ZPAD methods. (a) Pure helium droplets. (b) Droplets doped with a single argon atom.

methods concur in predicting even a second shell, although much less localized than the first one. For such problems of a central heliophilic impurity, DFT was also shown to be robust against DMC calculations.^{93,94} The average radius of the first solvation shell is slightly larger with the ZPAD method and slightly smaller with the RPMD method by a fraction of angström. Interestingly, the decay of the He–Ar radial distribution is much smoother with the PIMD method at equilibrium. Inspection of configurations reveals that this is caused by the argon impurity being rather mobile inside the droplet, exploring a sphere of radius of about 5 \AA around the droplet center. Such a radius is consistent with the extra broadening of the distribution exhibited by the PIMD approach and could also be partly due to the higher temperature of 1 K used with this method. The ZPAD method follows the behavior obtained with DFT, albeit with a first shell that is more marked and a more extended droplet. Thus, in the presence of a very attractive dopant, the more rigid behavior of the ZPAD method makes a smaller difference with the DFT results since the droplet itself is somewhat structured by the dopant.

Besides structural properties, the methods can also be compared with each other on an energetic footing. The binding (virial) energy of the He_{1000} droplet is found to be about -6212 K with

RPMD, or about 20% higher in magnitude than the DFT value (-5396 K), as obtained with the functional of Ref. 44. The corresponding value predicted by the ZPAD method amounts to -9600 K, and it is consistent with the overstructuring of the droplet relative to the DFT reference calculation. This is also the case for RPMD, although to a lesser extent.

A solvation energy E_{solv} of the single argon impurity can also be evaluated from the difference between the total energies of the ArHe_{1000} and pristine He_{1000} systems. With the DFT method, we find $E_{\text{solv}}(\text{Ar}) = 5598 - 5396 = 202$ K, or about seven times the Ar–He well depth at equilibrium. This value is twice as large as that found with the ZPAD method [$E_{\text{solv}}(\text{Ar}) = 9716 - 9615 = 101$ K] and 67% smaller than that found with the PIMD method [$E_{\text{solv}}(\text{Ar}) = 6549 - 6212 = 337$ K]. The apparent underestimation of Ar solvation energy in ZPAD calculations is related to the use of an effective Ar–He potential whose well depth is 2.2 times smaller than that of the Tang–Toennies Ar–He interaction potential (see Fig. 1 in the supplementary material). However, the ZPAD solvation energy is equal to 7.4 times the minimum energy of the effective Ar–He interaction, which is also close to the ratio found in the He–DFT simulation.

A. Heliophilic Ar atoms

In order to evaluate the ability of the three methods to describe the capture and coagulation of Ar atoms, as well as to shed more light on the clustering process inside helium droplets, several simulations were carried out in which an argon atom is projected at fixed velocity onto a He_{1000} droplet doped with a single argon atom or a small Ar_n cluster with $n = 2$ or 4, both being taken in their gas phase equilibrium geometry (regular tetrahedron for the tetramer). In typical experimental conditions (nozzle diameter of $5 \mu\text{m}$ and temperature of 24 K, He pressure of 80 bars), the He droplets' velocity is ~ 480 m/s.⁹⁵ In a pickup cell at 370 K (temperature mentioned by Theisen *et al.*⁹⁶), Cs has an average velocity of 260 m/s randomly oriented with respect to that of the He beam. This yields a range of relative He droplet–Cs velocities between 220 and 740 m/s. The same argument applied to Ar at room temperature (300 K) gives an average Ar velocity of 430 m/s and a range of relative Ar–droplet velocity of 50–910 m/s. Here, we selected velocities of 500 and 1000 m/s for argon projectiles and velocities of 50 and 500 m/s for cesium projectiles. Two different impact parameters were also tested: $b = 0$ or 10 \AA .

The various possible products of the trajectories are depicted in Fig. 2. We first discuss the possible formation of an Ar dimer upon the $\text{Ar} + \text{ArHe}_{1000}$ collision to introduce the main features of the dynamics. Even at thermal velocities of 500 m/s, the capture of impurities such as Ar atoms by weakly bound He droplets appears to be a rather violent process, as particularly illustrated by recent TDDFT simulations.^{32,47} It was notably shown that a sizable fraction of the collision energy of the impinging dopant is transferred to the droplet during the first stages of the collision, producing shock waves and nucleating quantized vortices.^{32,47,48} As a result, a few picoseconds after the projectile enters the droplet, its velocity drops below the Landau critical velocity, which is about 118 m/s for the functional considered here.⁴² At the same time, a high density helium structure builds around the incoming projectile, which, together with the helium solvation shell around the embedded cluster, can hinder the formation of a direct Ar–Ar bond. However, the remaining kinetic

Bound Ar_2			$\text{Ar} + \text{Ar}$		
RPMD	ZPAD	TDDFT	RPMD	ZPAD	TDDFT
6/20	0	1	14/20	21/21	0
6/20	0	0	14/20	21/21	1
12/20	19/21	–	8/20	2/21	–

Bound Ar_3			Saddle Ar_3			$\text{Ar} + \text{Ar}_2$		
RPMD	ZPAD	TDDFT	RPMD	ZPAD	TDDFT	RPMD	ZPAD	TDDFT
2/20	0	–	2/20	0	–	16/20	23/23	–
0	0	–	0	0	–	20/20	23/23	–
4/20	15/23	–	4/20	7/23	–	12/20	1/23	–

Bound Ar_5			Saddle Ar_5			$\text{Ar} + \text{Ar}_4$		
RPMD	ZPAD	TDDFT	RPMD	ZPAD	TDDFT	RPMD	ZPAD	TDDFT
4/20	0	0	2/20	0	1/2	14/20	26/26	1/2
0	0	0	0	0	1/2	20/20	26/26	1/2
6/20	14/26	–	14/20	12/26	–	0	0	–

FIG. 2. Diversity of products obtained upon collisions between an impinging argon atom and He_{1000} droplets doped with an argon monomer, a dimer, or a tetramer, and occurrence statistics of these products for various impact parameters b and collision velocities v . For each of the RPMD, ZPAD, and TDDFT methods, and from top to bottom, the statistics given correspond to collisions at $b = 0$ and $v = 500$ m/s; $b = 10 \text{ \AA}$ and $v = 500$ m/s; $b = 0$ and $v = 1000$ m/s, respectively.

energy of the projectile may be sufficient to enable the formation of a bound cluster with the host atoms inside the droplet. This situation occasionally takes place in our simulations, as illustrated in Fig. 2. However, the propensity for forming Ar–Ar bonds not only depends on the available collision energy but also on the impact parameter, high values of b being necessarily associated with some rotational energy and a concomitantly lower relative translational energy available for breaking the solvation shells and leading to coagulation. At 500 m/s, and within the TDDFT framework, Ar_2 is, thus, formed if the collision takes place at $b = 0$ but not at $b = 10 \text{ \AA}$. This less favorable clustering, also found in the case of Ne,⁴⁹ can be interpreted as the trapping of a significant proportion of the collision energy

into orbital rotation, which makes it difficult to transfer it to relative translation, the only available mechanisms being vortex nucleation and the appearance of surface capillary waves.^{31,97,98}

The cases studied within the RPMD and ZPAD approaches included $b = 0$ and 10 \AA for $v = 500 \text{ m/s}$ and $b = 0$ for $v = 1000 \text{ m/s}$. The latter case was not addressed with TDDFT as it would imply a prohibitively short time step to keep the total energy of the system constant. Within the RPMD approach, 20 independent trajectories were performed for each set of b and v values. Ar_2 is found to be formed in about one-third of the cases, no significant effect of the impact parameter being noticeable. At the much higher collision energy brought by the projectile impinging on the droplet at 1000 m/s , Ar_2 is formed twice as easily. With the ZPAD method, the situation is contrasted, no dimer being produced at 500 m/s but, conversely, most trajectories at 1000 m/s leading to stable Ar_2 products.

We now turn to the coagulation of impinging Ar atoms on a He droplet containing a preformed Ar cluster. RPMD and ZPAD collision simulations were carried out for helium droplets doped with an argon dimer prepared at its equilibrium geometry. As was the case with ArHe_{1000} , and with both methodologies, it is quite difficult to form the expected trimer in its stable geometry (equilateral triangle, denoted as “Bound” in Fig. 2) with an argon atom impinging at 500 m/s . Such a successful coagulation occurs at $b = 0$ in RPMD calculations with 10% probability at 500 m/s and 20% probability at 1000 m/s . With ZPAD, trimers are formed only at the higher collision velocity but with about 65% probability. However, intermediate situations occasionally take place with a cluster having fewer Ar–Ar bonds being formed and occupying higher-order configurations on the potential energy surface instead of the only true minimum, usually close to the linear saddle point. This situation is denoted as “Saddle” in Fig. 2. In the present case, nearly linear trimers are obtained with 20%–35% probability at 1000 m/s

velocity depending on the method, with two such events among 20 trajectories also occurring at 500 m/s and $b = 0$ with RPMD. In the remaining cases, the Ar projectile and the preformed dimer are still roaming inside the droplet at the end of the simulations. They could eventually meet and form a loosely bound trimer, analogous to the loose Ar_6 structure found in Ref. 32, but their low kinetic energy makes it improbable that they could form a trimer in the gas phase configuration.

The three frameworks of TDDFT, RPMD, and ZPAD were used to address the case of Ar projectiles impinging on Ar_4 embedded in He_{1000} , under the same collision conditions as used for the previous systems. Here, again the expected product Ar_5 only has one minimum which is a face-sharing double tetrahedron, although it has a greater diversity of stationary points than Ar_3 . At 500 m/s , and for both $b = 0$ and $b = 10 \text{ \AA}$, two simulations were performed using TDDFT, with the argon atom approaching the target cluster toward an apex atom or oppositely toward a facet. The four resulting simulations lead to the formation of a higher-energy, non-minimum configuration in half of the cases, with the incoming argon binding to two argons from an edge of the tetramer, the other half being associated with unconnected products. With the RPMD approach, low collision velocities usually do not produce larger clusters, but the stable pentamer is obtained in 20% of the cases and higher-order configurations in 10% of the cases, provided that $b = 0$. Such configurations are still denoted as “saddle” in Fig. 2, although no specific attempt was made to characterize the order of the corresponding stationary points. Raising the collision velocity to 1000 m/s always produces connected pentamers, but mostly (2/3) as higher-energy configurations. The ZPAD model is qualitatively consistent with the RPMD description, pentamers being only produced in significant amounts when the collision velocity reaches 1000 m/s .

From a more quantitative perspective, Fig. 3 shows the Ar–Ar distance in collisions between Ar and ArHe_{1000} at the three collision

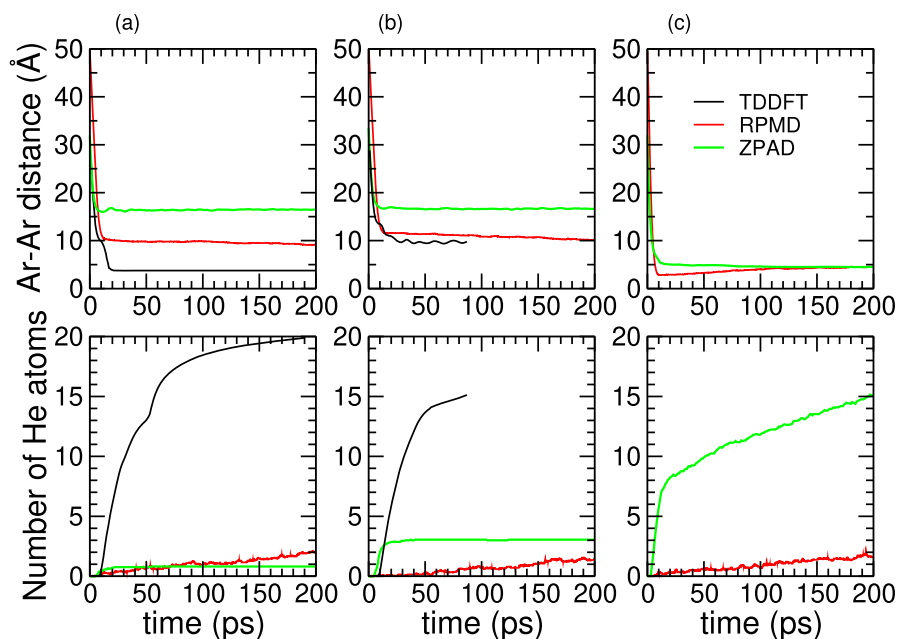


FIG. 3. Ar–Ar distance and number of evaporated helium atoms upon collision of an Ar atom onto ArHe_{1000} droplets, as predicted by the RPMD, ZPAD, and TDDFT methods, at three collision conditions and as a function of time. For RPMD and ZPAD, the results are averaged over 20 and 21 independent trajectories, respectively. (a) $b = 0$ and $v = 500 \text{ m/s}$; (b) $b = 10 \text{ \AA}$ and $v = 500 \text{ m/s}$; (c) $b = 0$ and $v = 1000 \text{ m/s}$.

conditions, as predicted by the three methods and possibly averaged over the independent trajectories in the RPMD and ZPAD cases, as a function of time.

At zero impact parameter, and consistent with the statistics reported in Fig. 2, these distances show that the projectile enters the droplet deeper when modeled with the TDDFT method, then RPMD, relative to ZPAD. Increasing the impact parameter or the collision velocity naturally increases or decreases the average distance, respectively. Interestingly, at 1000 m/s, the average Ar–Ar distance reaches a minimum after about 10 ps and slowly increases later on when the dynamics is described with the RPMD method. This behavior is indicative of some recoil motion once the two argon atoms have connected to each other, such a motion being absent with the ZPAD approach. This contrasted behavior is actually related to the more diffuse character of the argon impurity into the He₁₀₀₀ droplet seen on the radial distribution of Fig. 1(b), which produces some trajectories where the argon projectile connects with the embedded argon atom quite early during the collision, giving it a partial elastic character with the dimer relaxing to its equilibrium distance over shorter time scales.

The TDDFT description predicts straightforward formation of the Ar dimer under $b = 0$ and 500 m/s collision velocity. On a smaller scale, about ten damped oscillations with a period of about 1.1 ps can be seen,³² corresponding to vibrational energy dissipation to the droplet. However, only a loose dimer distant by about 10 Å is formed when $b = 10$ Å. The time oscillations with an approximate period of 10 ps seen in the upper panel of Fig. 3(b) indicate some relative motion between the two embedded impurities that is associated with more global deformations of the droplets but not to vibrations of the dimer, as was the case for $b = 0$. This combined motion that preserves the Ar–Ar distance near 10 Å is best seen directly on the animations provided in the [supplementary material](#).

A direct manifestation of the relaxation dynamics following the clusterization process is found in the emission of helium atoms that is expected as the main pathway to release the excess energy brought by the collision. The average numbers of helium atoms released from the He₁₀₀₀ droplet as a function of time corresponding to the same TDDFT, RPMD, and ZPAD trajectories are shown in the lower panels of Fig. 3. For this property, the TDDFT method predicts that evaporation takes place very quickly and steadily, a kink near 50 ps being indicative of a further ejection of helium matter once the already formed dimer bounces against the droplet surface. The rate of variations of the number of evaporated helium atoms is not linear with TDDFT, and we, thus, expect more atoms to evaporate if the trajectories could be integrated further, and exceed the already significant numbers of 20 or 15 found at $b = 0$ and $b = 10$ Å, respectively. Based on the known energetics of the various processes involved in the dimer formation, we can further predict that about five more helium atoms should evaporate to reach equilibrium again in the TDDFT case. More precisely, at 500 m/s velocity, the energy brought by the collision is about 600 K. The formation of the dimer releases an additional 143.5 K, and the solvation of the projectile atom a further 202 K from the aforementioned data, giving a total of about 950 K to be dissipated. In the present TDDFT simulations, we find that the total energy has decreased by about 765 K after 200 ps, or 80% of this total amount. The remaining 20%, thus, correspond to five atoms that remain to be evaporated.

In contrast, both the RPMD and ZPAD methods significantly underestimate the number of helium atoms emitted by the coagulation process at low collision velocity, between one and three atoms only being evaporated, and this result is a striking manifestation of the different rates at which the energy dissipates in superfluid or non-superfluid systems. Only at 1000 m/s does the ZPAD method predict a copious amount of helium atom evaporations, but still lower in magnitude than what is predicted by TDDFT at 500 m/s only, hence the results reported in the lower panel of Fig. 3(c) are still probably underestimated. At such a higher collision energy, the RPMD method predicts surprisingly robust droplets with a very high propensity for storing the excess energy from the collision and not releasing much of it through evaporative cooling. This points at a possible shortcoming of the path-integral description, which might insufficiently redistribute the excess energy into the intermolecular modes. While the kinetic temperatures inferred from the RPMD trajectories remain very close to the initial imposed value of 1 K, it may well be that the time needed to redistribute the excess energy created by forming the Ar₂ bond into the dissociative mode of an (outer) helium atom is still too long owing to the overstructured nature of the helium droplet within the RPMD model. In addition, inspection of the ZPAD trajectories indicates that several of the helium atoms that are evaporated are actually scattered early during the trajectory after the argon projectile hits the droplet, the slower decay occurring at longer times resulting from the actual bond formation.

One clearly missing ingredient from the RPMD and ZPAD approaches is the role of exchange statistics that is responsible for the superfluid behavior correctly accounted for by the DFT method. Although the superfluid character is expected to favor bond formation due to the low viscosity of the embedding medium, coagulation does not systematically occur either even with the TDDFT approach, and such processes are occasionally found also with the RPMD method in which the helium droplet is treated as a viscous host. The limitations of the ZPAD approach in underestimating the propensity for argon cluster growth can be assigned to the excessive structuration of the liquid, which itself is due to an excessively deep He–He effective potential. This points to a too short truncation distance used in the convergence of the frozen wavefunction.

B. Heliophobic Cs atoms

Crossed-beam experiments involving Cs atoms and either ⁴He or ³He droplets were originally conducted by Gspann and Ries several decades ago²⁷ and subsequently by Lewerenz and co-workers⁹⁵ for droplets containing 10³–10⁴ helium atoms. Cesium binds to helium very weakly, by ~10 K only;⁴⁵ therefore, hoping to get it captured by spontaneous collisions appears as rather challenging. Earlier TDDFT simulations of Cs impinging onto ⁴He₁₀₀₀ superfluid droplets produced a rich phenomenology.⁴⁵ For head-on collisions ($b = 0$), the cesium projectile was found to be captured, to bounce back, or to pierce through the droplet depending on the collision velocity.^{45,47} In the present work, additional TDDFT trajectories were carried out at $b = 10$ Å and the two velocities of $v = 50$ and 500 m/s.

The qualitative outcomes of these trajectories, together with the results obtained using the alternative RPMD and ZPAD methods and their associated statistics, are given in Fig. 4.

Capture			Bounce			Pierce		
RPMD	ZPAD	TDDFT	RPMD	ZPAD	TDDFT	RPMD	ZPAD	TDDFT
20/20	21/23	1	0	2/23	0	0	0	0
20/20	15/23	1	0	8/23	0	0	0	0
20/20	23/23	0	0	0	0	0	0	1
20/20	21/23	0	0	2/23	0	0	0	1

FIG. 4. Three possible outcomes upon collisions between an impinging cesium atom and He_{1000} droplets, and corresponding occurrence statistics of these products for various impact parameters b and collision velocities v . For each of the RPMD, ZPAD, and TDDFT methods, and from top to bottom, the statistics given correspond to collisions at $b = 0$ and $v = 50$ m/s; $b = 10$ Å and $v = 50$ m/s; $b = 0$ and $v = 500$ m/s; $b = 10$ Å and $v = 500$ m/s, respectively.

At the lowest velocity, all methods find that the alkali projectile eventually gets captured by the droplet in all (RPMD) or most (ZPAD) of the cases, and possibly scattered in 1/3 of the cases when $b = 10$ Å with ZPAD. The capture found with TDDFT with $b = 10$ Å consistently completes the results of Ref. 45 using the same methodology (Cs atom being captured for $b = 9$ Å, scattered for $b = 11$ Å).

Qualitative differences between the three methods are found when the collision takes place at 500 m/s, in which case the projectile remains captured when modeled using RPMD or ZPAD, while it pierces through the droplet within the TDDFT framework.

Figure 5 analyzes in more detail the collision process, by showing the distance between the cesium atom and the center of mass of the helium droplet, as a function of time. As shown in this figure, under the conditions leading to its capture, the Cs projectile starts by entering the droplet by a few angstroms before it is eventually pushed back toward the droplet surface and forms a dimple. The penetration depth is about 2 Å with RPMD and ZPAD, but closer to 5 Å with TDDFT, which we explain as due to the much softer nature of the droplet with this method. Another qualitative difference is the orbiting nature of the Cs atom sent toward the droplet with $b > 0$ in TDDFT calculations, whereas the two particle-based methods predict a fast conversion of the rotational energy into internal vibrational modes owing to their description of the helium droplet host as a viscous medium. Such differences are well captured by the movies provided in the supplementary material.

At 500 m/s velocity, the capture of the cesium atom remains the dominant process in ZPAD and RPMD simulations, but the penetration depth is unsurprisingly and significantly larger, even when the impact parameter is taken as 10 Å. However, the TDDFT method predicts that the projectile pierces through the droplet upon head-on collisions, as seen from the distance in Fig. 5(b) reaching the value 0 for $b = 0$. For $b = 10$ Å, this distance reaches a minimum of ~ 12 Å. Inspection of the corresponding movie reveals that the projectile also pierces the droplet, and the turbulences created in the helium host move it by about 2 Å away from the minimum distance of 10 Å corresponding to the impact parameter value.

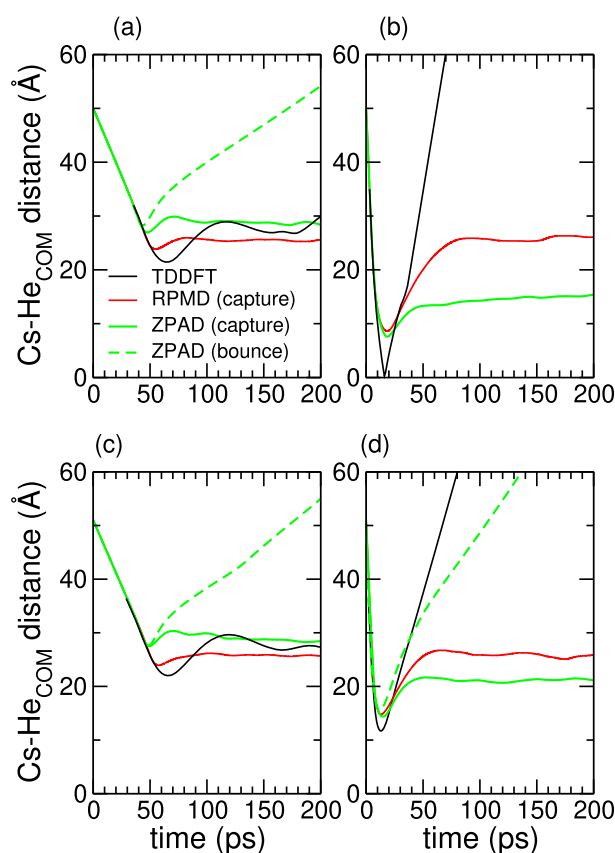


FIG. 5. Average distance between the impinging Cs atom and the center of mass of the He_{1000} droplet as a function of time, as obtained with the RPMD, ZPAD, and TDDFT methods under different collision conditions. The RPMD results are averaged over 20 independent trajectories. The ZPAD results are averaged over subsets of independent trajectories leading to capture or bouncing outcomes. (a) $b = 0$ and $v = 50$ m/s; (b) $b = 10$ Å and $v = 500$ m/s; (c) $b = 10$ Å and $v = 50$ m/s; (d) $b = 10$ Å and $v = 500$ m/s.

A closer inspection of the TDDFT results for $b = 0$ at 500 m/s collision velocity shows that the velocity of the outgoing Cs atom that has pierced through the droplet approaches the Landau velocity for the functional used in this work. The existence of such a limiting velocity has been observed in a combined experimental and ^4He -TDDFT study by Brauer *et al.*⁹⁹ for a silver atom ejected through photoexcitation from inside a helium nanodroplet. This effect cannot be reproduced by the other two methods.

In both cases, the droplet experiences a significant deformation, which can be quantified by computing a normalized quadrupole moment Q_{zz}/R_g^2 along the same direction (noted as z) as the collision velocity vector:

$$Q_{zz} = \frac{1}{N} \int \rho(\mathbf{r})(3z^2 - r^2) d\mathbf{r},$$

$$R_g^2 = \frac{1}{N} \int \rho(\mathbf{r})r^2 d\mathbf{r},$$

where the continuous integration over the fluid density $\rho(\mathbf{r})$ should be replaced by a discrete summation over atoms with ZPAD, or replica beads with RPMD. Figure 6 shows the variations of the quantity Q_{zz}/R_g^2 predicted by the various methods, as a function

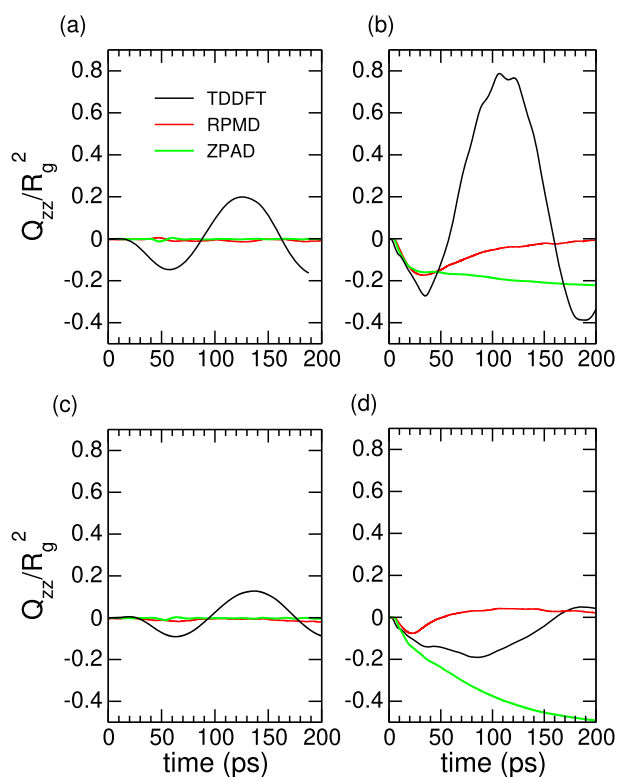


FIG. 6. Average quadrupole moment of the He_{1000} droplet undergoing a collision with a Cs atom as a function of time, as obtained with the RPMD, ZPAD, and TDDFT methods under different collision conditions. The RPMD and ZPAD results are averaged over 20 and 23 independent trajectories, respectively. (a) $b = 0$ and $v = 50$ m/s; (b) $b = 0$ and $v = 500$ m/s; (c) $b = 10$ Å and $v = 50$ m/s; (d) $b = 10$ Å and $v = 500$ m/s.

of time and, for the particle-based methods, after averaging over independent trajectories.

Here, again the influence of the collision velocity on the droplet shape is very significant. While the droplet remains nearly spherical for collisions at 50 m/s, head-on collisions at 500 m/s lead to significant deformations especially when modeled with the TDDFT method, in which piercing occurs.

Under such collision conditions, all methods predict quadrupole deformations of the oblate type, the droplet being compressed along the collision axis. However, within RPMD, the quadrupole deformation index, Q_{zz}/R_g^2 , reaches a minimum after about 20 ps and, subsequently, the droplet relaxes toward a more spherical shape. The TDDFT approach predicts a qualitatively similar behavior for $b = 10$ Å, with the minimum of the quadrupole deformation being reached quite later, after about 100 ps. However, for head-on collisions, the deformation is much stronger with the droplet becoming significantly prolate after 100 ps and entering a seemingly oscillatory phase between the oblate and prolate shapes. With the ZPAD approach, the deformation begins similarly, but the droplet never really relaxes back to the spherical shape within the 200 ps time window, which is consistent with the slower dynamics experienced by these droplets in a more rigid-like state.

C. Merging of two He_{500} droplets

Coalescence¹⁰⁰ and splashing³³ experiments have demonstrated the liquid-like character of helium clusters at the experimental temperatures, a crucial feature to account for the suitability of helium droplets as carrier species in soft-landing processes.^{33,36} Quite remarkably, the sequence of droplet shapes representative of the coalescence of two He droplets has been found to resemble that obtained upon merging of two classical drops,¹⁰¹ and a close analogy has also been undertaken between the coalescence of superfluid He droplets and that of ultradilute quantum droplets, made of mixtures of ultracold ^{39}K atoms in different hyperfine states of a self-bound Bose-Einstein condensate.^{102,103}

The merging, or coalescence, between two He_{500} clusters brought into contact is driven by their mutual van der Waals attraction, without the need for imposing relative velocities to the clusters. This process has been investigated using the density-based TDDFT approach in recent years,^{62,63} and in the present work, we have carried out a complementary exploration of this process using the particle-based RPMD and ZPAD methods. Here also, several independent trajectories were performed, after which the physical properties were determined and averaged.

It is instructive to first consider the qualitative picture that emerges from these simulations. Figure 7 compares the shapes of the merging droplets, as predicted by the TDDFT, RPMD, and ZPAD methods, as a function of time with three snapshots selected at the beginning ($t = 0$) and after 100 or 200 ps. From a more quantitative perspective, the normalized quadrupole deformation parameter Q_{zz}/R_g^2 is also shown in the graph of Fig. 7 as a function of time.

The three approaches predict rather contrasted behaviors, which are nonetheless consistent with the shape analysis performed in the case of collisions with the Cs projectile. With the RPMD method, the merging proceeds in a mostly steady way, the newly formed droplet becoming more and more spherical over time in ~ 200 ps. With ZPAD, merging is hindered due to the individual

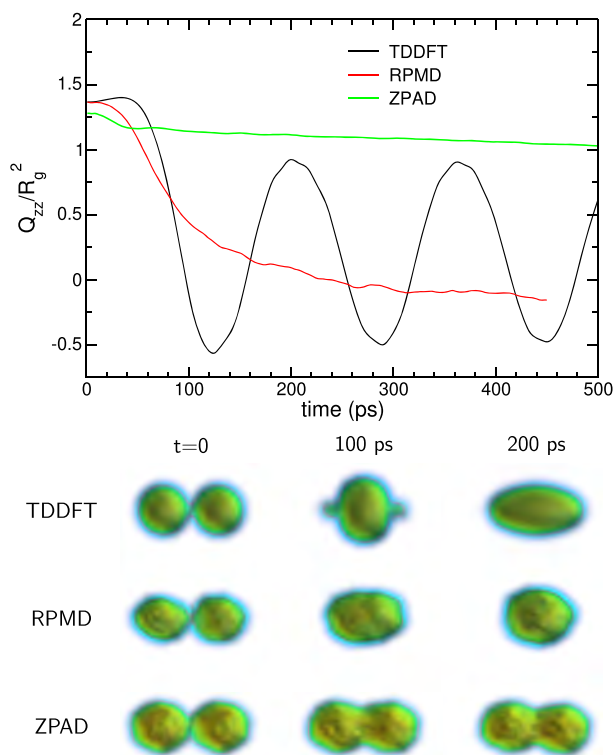


FIG. 7. Upper panel: Quadrupole deformation of the two He_{500} droplets merging upon contact, as predicted by the RPMD, ZPAD, and TDDFT methods, as a function of time. The RPMD and ZPAD results are averaged over 10 and 13 independent trajectories, respectively. Lower panel: Instantaneous shapes of two He_{500} droplets undergoing spontaneous merging upon contact, as predicted by the RPMD, ZPAD, and TDDFT methods, at $t = 0$ and after 100 and 200 ps.

droplets being insufficiently soft and mostly crystalline. Extending the trajectories to time scales reaching 1 ns does not improve the results significantly. The density-based approach predicts deformations that even exceed those found with RPMD, but in the absence of viscous damping, the superfluid droplet that experiences merging actually changes back and forth between oblate and prolate shapes through a slow oscillatory motion with a period of about 150 ps, which roughly corresponds to the quadrupole oscillation period of a He_{1000} droplet.

IV. CONCLUDING REMARKS

The formation of complexes or clusters inside helium nanodroplets is faced with two seemingly contradictory mechanisms. The extreme fluid character of helium itself is expected not to hinder the motion of the atomic or molecular partners much once inside the droplet. However, due to the cryogenic temperatures that are imposed by the droplet itself, rearrangements can be excessively slow and the complexes may also be stuck in metastable structures that are entropically favored, as shown experimentally by a number of studies.^{10,11,15,16} Direct bonds can also be prevented from forming

because of the high density of the helium solvation shell around heliophilic atoms.^{30,22,32}

Because the complexes cannot be entirely explained by equilibrium thermodynamics considerations, it is important that any attempt at modeling complex formation in helium droplets incorporates dynamical effects as much as possible. In the present work, three complementary approaches were employed to address the time-dependent processes of cluster formation through sequential pickup, focusing on the addition of an argon atom on a preformed argon cluster embedded in a He_{1000} , helium droplet a more realistic situation complementary to the very symmetric ones explored in earlier TDDFT studies.³² The same methods were then used to study the contrasted situation of the heliophobic cesium atom impinging on pristine droplets, as well as the spontaneous merging between two smaller He_{500} droplets put into contact and driven by long-range van der Waals forces.

The three methodologies followed here consist of the density-based TDDFT approach, the particle-based ZPAD approach, and the path-integral RPMD method, which also relies on a particle description but lies somewhat in between the two other approaches through the physical extension of the polymer beads associated with each atom. While TDDFT also accounts for the superfluid character of the helium droplets, only zero-point delocalization is incorporated in the two particle-based methods, and in ZPAD, these effects are treated empirically by attaching a frozen wavefunction to each He atom, determined iteratively at the desired temperature of 0.38 K, resulting in classical dynamics of the He atoms with effective potentials.

Regarding the coagulation process between heliophilic argon atoms, the three methods predict qualitatively similar behaviors in regard to various important aspects: The impinging argon always enters the droplet, but most of the time, the thermodynamically most stable isomer is not formed. Instead, metastable structures are formed and prevented to relax to the unique minima by their low kinetic energy associated with a shell structure of helium built around them. The methods differ in that the particle-based methods require a higher impact velocity in order to form a dimer, presumably because of the lack of superfluidity.

In the case of a heliophobic cesium atom impinging on a bare $^4\text{He}_{1000}$ droplet, all three methods find the Cs atom to be captured at the lower collision velocity (50 m/s). Differences arise at the higher velocity of 500 m/s: The density-based approach finds the projectile to pierce through the droplet, whereas both particle-based methods predict that it should be mostly captured or occasionally scattered (ZPAD). This difference could be again attributed to the superfluid behavior, most notably since the velocity of the outgoing Cs atom is found to be similar to the critical Landau velocity for the functional used in this work.

The merging between two small droplets also shows some qualitative differences that shed further light onto the possible importance of superfluidity and delocalization effects in the way they are included (or ignored) from the three methods. In the absence of viscous dissipation, TDDFT predicts large amplitude quadrupole oscillations for the merged He_{1000} droplet, while RPMD predicts a rather continuous process where the merged droplet becomes increasingly spherical. Due to the excessive solid-like character predicted by ZPAD, this process appears particularly slow with this method.

While TDDFT is, in principle, more realistic in describing the superfluid droplets, and even though thermal effects are expected to be limited under the relevant experimental conditions, as a zero temperature method it also ignores the possible fluctuations that, e.g., the doping complexes could experience inside the droplet. The main limitation of TDDFT is that it is significantly more time-consuming than both particle-based approaches, hampering systematic studies as the spatial and temporal resolutions of the TDDFT equations have to be adjusted to the nature of the dopant and the collision velocity. As such, it would not have been thinkable of modeling the collision process onto droplets containing argon clusters that are randomly oriented, only symmetric directions being chosen here for the sake of illustration.

In contrast, the ZPAD method provides a computationally very efficient way of simulating the doped helium droplets, once the effective potentials have been obtained. In particular, accounting for the statistics due to different orientations of the target cluster is straightforward, as well as extending trajectories to the nanosecond time scale or even beyond. It can also predict nonadiabatic transitions in the electronically excited dopant, when used in combination with mixed quantum-classical dynamics for the latter.^{55–57} In addition, the internal temperature is equal to that of the experimental droplets (0.38 K). Its main limitation is its key dependence on the effective potentials (especially the He–He potential), which was found here to be probably too deep as it leads to droplets that are not actually liquid. This points to the need for a specific criterion to fix the truncation distance of the effective He wavefunction.

The RPMD approach is intermediate between the TDDFT and ZPAD methods, at least in terms of computational cost, which increases linearly with the Trotter discretization number. While we do not expect any qualitative improvement of the method with increasing this number (or lowering the temperature down to experimental values), it would be worth considering thermostated versions of the algorithm¹⁰⁴ in the future so even higher numbers of replica beads could be employed. This would notably clarify some of the differences noted with the density-based method, like the motion of argon impurities inside the helium droplet that might be ascribable to the higher temperature of 1 K employed within RPMD. Yet the method can also account for statistics, at least to a reasonable extent, although the trajectories can hardly be as long as those with ZPAD.

To some extent, RPMD can be said to provide information about the importance of superfluidity when compared to TDDFT and about the importance of fluid-like effects in themselves when compared to ZPAD in its current version. The lack of bosonic exchange effects in the particle-based approaches likely explains the qualitative differences found in the high-velocity capture (or absence thereof) of the Cs atom onto the droplets, or the quadrupole oscillations in the merging process, which reveals or stresses what is essentially due to superfluidity in these processes. However, the more approximate methods are suited to address cases where superfluidity may not be essential, especially if the interaction between the dopant and the helium host is strong or when the processes taking place are highly energetic. An extreme case would be that of ionic dopants, where the local crystallization of the solvent in their vicinity (usually referred to as a snowball effect) could be more difficult to address dynamically with density-based methods because of the

numerical constraints on the time and space steps that the rapidly varying densities would practically impose.

SUPPLEMENTARY MATERIAL

See the [supplementary material](#) for the analytical expression of the effective Ar–He and He–He ZPAD potentials, as well as the corresponding parameters, with a figure comparing this potential to the reference interactions. Selected videos showing typical trajectories obtained with the various methods and for the different systems are also provided.

ACKNOWLEDGMENTS

This work has been performed under Grant No. PID2020-114626GB-I00 from the MICIN/AEI/10.13039/501100011033. M.B. acknowledges the Université Fédérale Toulouse Midi-Pyrénées for financial support throughout the “Chaires d’Attractivité 2014” Programme IMDYNHE. E.G.-A. acknowledges financial support from the same program. The authors gratefully acknowledge the regional computer center of Midi-Pyrénées, CALMIP (Grant No. P1039), the regional computer center of Champagne-Ardenne, ROMEO, and the Pôle Scientifique de Modélisation Numérique (PSMN) in Lyon, for providing high performance computer resources.

AUTHOR DECLARATIONS

Conflict of Interest

The authors have no conflicts to disclose.

Author Contributions

Ernesto García-Alfonso: Data curation (equal); Investigation (equal). **Manuel Barranco:** Conceptualization (equal); Data curation (equal); Formal analysis (equal); Investigation (equal); Methodology (equal); Project administration (equal); Supervision (equal); Validation (equal); Writing – original draft (equal); Writing – review and editing (equal). **David A. Bonhommeau:** Conceptualization (equal); Data curation (equal); Investigation (equal); Methodology (equal); Supervision (equal); Validation (equal); Writing – original draft (equal); Writing – review and editing (equal). **Nadine Halberstadt:** Conceptualization (equal); Data curation (equal); Investigation (equal); Methodology (equal); Supervision (equal); Validation (equal); Writing – original draft (equal); Writing – review and editing (equal). **Martí Pi:** Conceptualization (equal); Data curation (equal); Investigation (equal); Supervision (equal); Validation (equal); Writing – original draft (equal); Writing – review and editing (equal). **Florent Calvo:** Conceptualization (equal); Data curation (equal); Investigation (equal); Methodology (equal); Project administration (equal); Supervision (equal); Validation (equal); Writing – original draft (equal); Writing – review and editing (equal).

DATA AVAILABILITY

The data that support the findings of this study are available from the corresponding author upon reasonable request.

REFERENCES

- ¹J. P. Toennies and A. F. Vilesov, *Angew. Chem., Int. Ed.* **43**, 2622 (2004).
- ²A. Scheidemann, J. P. Toennies, and J. A. Northby, *Phys. Rev. Lett.* **64**, 1899 (1990).
- ³K. K. Lehmann and G. Scoles, *Science* **279**, 2065 (1998).
- ⁴M. Y. Choi, G. E. Douberly, T. M. Falconer, W. K. Lewis, C. M. Lindsay, J. M. Merritt, P. L. Stiles, and R. E. Miller, *Int. Rev. Phys. Chem.* **25**, 15 (2006).
- ⁵C. Callegari and W. E. Ernst, in *Handbook of High Resolution Spectroscopy* (Wiley, New York, 2011), Vol. 3, p. 1551.
- ⁶M. Mudrich and F. Stienkemeier, *Int. Rev. Phys. Chem.* **33**, 301 (2014).
- ⁷J. Tiggesbäumker and F. Stienkemeier, *Phys. Chem. Chem. Phys.* **9**, 4748 (2007).
- ⁸A. Mauracher, O. Echt, A. M. Ellis, S. Yang, D. K. Bohme, J. Postler, A. Kaiser, S. Denifl, and P. Scheier, *Phys. Rep.* **751**, 1 (2018).
- ⁹W. E. Ernst and A. W. Hauser, *Phys. Chem. Chem. Phys.* **23**, 7553 (2021).
- ¹⁰K. Nauta and R. E. Miller, *Science* **283**, 1895 (1999).
- ¹¹E. Loginov, L. F. Gomez, N. Chiang, A. Halder, N. Guggemos, V. V. Kresin, and A. F. Vilesov, *Phys. Rev. Lett.* **106**, 233401 (2011).
- ¹²J. D. Pickering, B. Shepperson, L. Christiansen, and H. Stapelfeldt, *J. Chem. Phys.* **149**, 154306 (2018).
- ¹³K. Nauta and R. E. Miller, *Science* **287**, 293 (2000).
- ¹⁴J. Khatri, T. K. Roy, K. Chatterjee, G. Schwaab, and M. Havenith, *J. Phys. Chem. A* **125**, 6954 (2021).
- ¹⁵E.-M. Lottner and A. Slenczka, *J. Phys. Chem. A* **124**, 311 (2020).
- ¹⁶A. M. Ellis, J. A. Davies, E. Yurtsever, and F. Calvo, *J. Chem. Phys.* **156**, 174304 (2022).
- ¹⁷V. Mozhayskiy, M. N. Slipchenko, V. K. Adamchuk, and A. F. Vilesov, *J. Chem. Phys.* **127**, 094701 (2007).
- ¹⁸G. Haberfeiler, P. Thaler, D. Knez, A. Volk, F. Hofer, W. E. Ernst, and G. Kothleitner, *Nat. Commun.* **6**, 8779 (2015).
- ¹⁹A. Volk, P. Thaler, D. Knez, A. W. Hauser, J. Steurer, W. Grogger, F. Hofer, and W. E. Ernst, *Phys. Chem. Chem. Phys.* **18**, 1451 (2016).
- ²⁰J. Eloranta, *Phys. Rev. B* **77**, 134301 (2008).
- ²¹A. Przystawik, S. Göde, T. Döppner, J. Tiggesbäumker, and K.-H. Meiwes-Broer, *Phys. Rev. A* **78**, 021202(R) (2008).
- ²²A. Hernando, M. Barranco, R. Mayol, M. Pi, and F. Ancilotto, *Phys. Rev. B* **78**, 184515 (2008).
- ²³L. F. Gomez, E. Loginov, and A. F. Vilesov, *Phys. Rev. Lett.* **108**, 155302 (2012).
- ²⁴E. Latimer, D. Spence, C. Feng, A. Boatwright, A. M. Ellis, and S. Yang, *Nano Lett.* **14**, 2902 (2014).
- ²⁵P. Thaler, A. Volk, F. Lackner, J. Steurer, D. Knez, W. Grogger, F. Hofer, and W. E. Ernst, *Phys. Rev. B* **90**, 155442 (2014).
- ²⁶J. Gspann and H. Vollmar, *J. Chem. Phys.* **73**, 1657 (1980).
- ²⁷J. Gspann and R. Ries, *Surf. Sci.* **156**, 195 (1985).
- ²⁸J. P. Toennies, The Chemical Physics of Atomic and Molecular Clusters, in *Proceedings of the International School of Physics "Enrico Fermi" Course CVII*, edited by G. Scoles (North Holland, Amsterdam, 1990), p. 597.
- ²⁹D. Eichenauer, A. Scheidemann, and J. P. Toennies, *Z. Phys. D* **8**, 295 (1988).
- ³⁰M. Lewerenz, B. Schilling, and J. P. Toennies, *J. Chem. Phys.* **102**, 8191 (1995).
- ³¹F. Coppens, F. Ancilotto, M. Barranco, N. Halberstadt, and M. Pi, *Phys. Chem. Chem. Phys.* **19**, 24805 (2017).
- ³²F. Coppens, F. Ancilotto, M. Barranco, N. Halberstadt, and M. Pi, *Phys. Chem. Chem. Phys.* **21**, 17423 (2019).
- ³³P. Martini, S. Albertini, F. Laimer, M. Meyer, M. Gatchell, O. Echt, F. Zappa, and P. Scheier, *Phys. Rev. Lett.* **127**, 263401 (2021).
- ³⁴N. F. Aguirre, D. Mateo, A. O. Mitrushchenkov, M. Pi, and M. P. de Lara-Castells, *J. Chem. Phys.* **136**, 124703 (2012).
- ³⁵M. P. de Lara-Castells, N. F. Aguirre, H. Stoll, A. O. Mitrushchenkov, D. Mateo, and M. Pi, *J. Chem. Phys.* **142**, 131101 (2015).
- ³⁶R. Fernández-Perea, L. F. Gómez, C. Cabrillo, M. Pi, A. O. Mitrushchenkov, A. F. Vilesov, and M. P. de Lara-Castells, *J. Phys. Chem. C* **121**, 22248 (2017).
- ³⁷R. B. Gerber and M. A. Ratner, *Adv. Chem. Phys.* **70**, 97 (1988).
- ³⁸J. M. Bowman, K. Christoffel, and F. Tobin, *J. Phys. Chem.* **83**, 905 (1979).
- ³⁹V. Buch, *J. Chem. Phys.* **117**, 4738 (2002).
- ⁴⁰P. A. Frantsuzov and V. A. Mandelshtam, *J. Chem. Phys.* **128**, 094304 (2008).
- ⁴¹M. Barranco, R. Guardiola, S. Hernández, R. Mayol, J. Navarro, and M. Pi, *J. Low Temp. Phys.* **142**, 1 (2006).
- ⁴²F. Ancilotto, M. Barranco, F. Coppens, J. Eloranta, N. Halberstadt, A. Hernando, D. Mateo, and M. Pi, *Int. Rev. Phys. Chem.* **36**, 621 (2017).
- ⁴³F. Dalfovo, A. Lastri, L. Pricaupeenko, S. Stringari, and J. Treiner, *Phys. Rev. B* **52**, 1193 (1995).
- ⁴⁴F. Ancilotto, M. Barranco, F. Caupin, R. Mayol, and M. Pi, *Phys. Rev. B* **72**, 214522 (2005).
- ⁴⁵A. Leal, D. Mateo, A. Hernando, M. Pi, and M. Barranco, *Phys. Chem. Chem. Phys.* **16**, 23206 (2014).
- ⁴⁶A. Vilà and M. González, *Phys. Chem. Chem. Phys.* **18**, 31869 (2016).
- ⁴⁷F. Coppens, A. Leal, M. Barranco, N. Halberstadt, and M. Pi, *J. Low Temp. Phys.* **187**, 439 (2017).
- ⁴⁸M. Blancafort-Jorquera, A. Vilà, and M. González, *Phys. Chem. Chem. Phys.* **20**, 29737 (2018).
- ⁴⁹M. Blancafort-Jorquera, A. Vilà, and M. González, *Phys. Chem. Chem. Phys.* **21**, 24218 (2019).
- ⁵⁰I. R. Craig and D. E. Manolopoulos, *J. Chem. Phys.* **121**, 3368 (2004).
- ⁵¹A. Castillo-García, A. W. Hauser, M. P. de Lara-Castells, and P. Villarreal, *Molecules* **26**, 5783 (2021).
- ⁵²F. Calvo, E. Yurtsever, and Ö. Birer, *J. Phys. Chem. A* **120**, 1727 (2016).
- ⁵³E. J. Heller, *J. Chem. Phys.* **75**, 2923 (1981).
- ⁵⁴M. Sterling, Z. Li, and V. A. Apkarian, *J. Chem. Phys.* **103**, 5679 (1995).
- ⁵⁵D. Bonhommeau, P. T. Lake, Jr., C. Le Quiniou, M. Lewerenz, and N. Halberstadt, *J. Chem. Phys.* **126**, 051104 (2007).
- ⁵⁶D. Bonhommeau, M. Lewerenz, and N. Halberstadt, *J. Chem. Phys.* **128**, 054302 (2008).
- ⁵⁷N. Halberstadt and D. A. Bonhommeau, *J. Chem. Phys.* **152**, 234305 (2020).
- ⁵⁸C. Stark and V. V. Kresin, *Phys. Rev. B* **81**, 085401 (2010).
- ⁵⁹L. A. der Lan, P. Bartl, C. Leidlmair, H. Schöbel, R. Jochum, S. Denifl, T. D. Märk, A. M. Ellis, and P. Scheier, *J. Chem. Phys.* **135**, 044309 (2011).
- ⁶⁰L. A. der Lan, P. Bartl, C. Leidlmair, H. Schöbel, S. Denifl, T. D. Märk, A. M. Ellis, and P. Scheier, *Phys. Rev. B* **85**, 115414 (2012).
- ⁶¹F. Calvo, *Phys. Rev. B* **95**, 035429 (2017).
- ⁶²J. M. Escartín, F. Ancilotto, M. Barranco, and M. Pi, *Phys. Rev. B* **105**, 024511 (2022).
- ⁶³J. M. Escartín, F. Ancilotto, M. Barranco, and M. Pi, *Phys. Rev. B* **99**, 140505(R) (2019).
- ⁶⁴M. Barranco, F. Coppens, N. Halberstadt, A. Hernando, A. Leal, D. Mateo, R. Mayol, and M. Pi, "Zero temperature DFT and TDDFT for ⁴He: A short guide for practitioners," 2017, <https://github.com/bcntls2016/DFT-Guide/blob/master/dft-guide.pdf>.
- ⁶⁵A. Wada, T. Takayanagi, and M. Shiga, *J. Chem. Phys.* **119**, 5478 (2003).
- ⁶⁶T. Takayanagi and M. Shiga, *Phys. Chem. Chem. Phys.* **6**, 3241 (2004).
- ⁶⁷S. Stringari and J. Treiner, *J. Chem. Phys.* **87**, 5021 (1987).
- ⁶⁸D. J. Wales, J. P. K. Doye, A. Dullweber, M. P. Hodges, F. Y. Naumkin, F. Calvo, J. Hernández-Rojas, and T. F. Middleton, The Cambridge Cluster Database, <http://www-wales.ch.cam.ac.uk/CCD.html>.
- ⁶⁹J. Höller, E. Krotscheck, and R. E. Zillich, *Eur. Phys. J. D* **68**, 372 (2014).
- ⁷⁰J. Höller, E. Krotscheck, and R. E. Zillich, *Eur. Phys. J. D* **69**, 198 (2015).
- ⁷¹K. T. Tang and J. P. Toennies, *J. Chem. Phys.* **118**, 4976 (2003).
- ⁷²S. H. Patil, *J. Chem. Phys.* **94**, 8089 (1991).
- ⁷³M. Pi, F. Ancilotto, F. Coppens, N. Halberstadt, A. Hernando, A. Leal, D. Mateo, R. Mayol, and M. Barranco, "⁴He-DFT BCN-TLS: A computer package for simulating structural properties and dynamics of doped liquid helium-4 systems," <https://github.com/bcntls2016/>.
- ⁷⁴M. Frigo and S. G. Johnson, *Proc. IEEE* **93**, 216 (2005).
- ⁷⁵A. Ralston and H. S. Wilf, *Mathematical Methods for Digital Computers* (John Wiley & Sons, New York, 1960).
- ⁷⁶T. J. H. Hele and S. C. Althorpe, *J. Chem. Phys.* **138**, 084108 (2013).
- ⁷⁷T. J. H. Hele, M. J. Willatt, A. Muolo, and S. C. Althorpe, *J. Chem. Phys.* **142**, 191101 (2015).

- ⁷⁸S. Habershon, G. S. Fanourgakis, and D. E. Manolopoulos, *J. Chem. Phys.* **129**, 074501 (2009).
- ⁷⁹M. Shiga and A. Nakayama, *Chem. Phys. Lett.* **451**, 175 (2008).
- ⁸⁰F. Calvo, P. Parneix, and N.-T. Van-Oanh, *J. Chem. Phys.* **132**, 124308 (2010).
- ⁸¹S. Habershon, T. E. Markland, and D. E. Manolopoulos, *J. Chem. Phys.* **131**, 024501 (2009).
- ⁸²F. Calvo and D. Costa, *J. Chem. Theory Comput.* **6**, 508 (2010).
- ⁸³R. Colleparado-Guevara, Y. V. Suleimanov, and D. E. Manolopoulos, *J. Chem. Phys.* **130**, 174713 (2009).
- ⁸⁴A. R. Menzeleev, F. Bell, and T. F. Miller III, *J. Chem. Phys.* **140**, 064103 (2014).
- ⁸⁵A. R. Menzeleev and T. F. Miller III, *J. Chem. Phys.* **132**, 034106 (2010).
- ⁸⁶F. Calvo, C. Falvo, and P. Parneix, *J. Phys. Chem. A* **118**, 5427 (2014).
- ⁸⁷R. Welsch, K. Song, Q. Shi, S. C. Althorpe, and T. F. Miller III, *J. Chem. Phys.* **145**, 204118 (2016).
- ⁸⁸M. Tuckerman, B. J. Berne, and G. J. Martyna, *J. Chem. Phys.* **97**, 1990 (1992).
- ⁸⁹T. E. Markland and D. E. Manolopoulos, *J. Chem. Phys.* **129**, 024105 (2008).
- ⁹⁰P. Slaviček, P. Jungwirth, M. Lewerenz, N. H. Nahler, M. Fárník, and U. Buck, *J. Phys. Chem. A* **107**, 7743 (2003).
- ⁹¹D. A. Bonhommeau, *Chem. Phys.* **550**, 111307 (2021).
- ⁹²R. Panzou and M. Lewerenz, *Mol. Phys.* **119**, e1977862 (2021).
- ⁹³F. Ancilotto, M. Pi, R. Mayol, M. Barranco, and K. K. Lehmann, *J. Phys. Chem. A* **111**, 12695 (2007).
- ⁹⁴A. Leal, D. Mateo, A. Hernando, M. Pi, M. Barranco, A. Ponti, F. Cargnoni, and M. Drabbels, *Phys. Rev. B* **90**, 224518 (2014).
- ⁹⁵M. Lewerenz, B. Schilling, and J. P. Toennies, *Chem. Phys. Lett.* **206**, 381 (1993).
- ⁹⁶M. Theisen, F. Lackner, and W. E. Ernst, *J. Chem. Phys.* **135**, 074306 (2011).
- ⁹⁷S. M. O. O'Connell, R. M. P. Tanyag, D. Verma, C. Bernando, W. Pang, C. Bacellar, C. A. Saldrigas, J. Mahl, B. W. Toulson, Y. Kumagai, P. Walter, F. Ancilotto, M. Barranco, M. Pi, C. Bostedt, O. Gessner, and A. F. Vilesov, *Phys. Rev. Lett.* **124**, 215301 (2020).
- ⁹⁸M. Pi, J. M. Escartin, F. Ancilotto, and M. Barranco, *Phys. Rev. B* **104**, 094509 (2021).
- ⁹⁹N. B. Brauer, S. Smolarek, E. Loginov, D. Mateo, A. Hernando, M. Pi, M. Barranco, W. J. Buma, and M. Drabbels, *Phys. Rev. Lett.* **111**, 153002 (2013).
- ¹⁰⁰C. L. Vicente, C. Kim, H. J. Maris, and G. M. Seidel, *J. Low Temp. Phys.* **121**, 627 (2000).
- ¹⁰¹J. Qian and C. K. Law, *J. Fluid Mech.* **331**, 59 (1997).
- ¹⁰²G. Ferioli, G. Semeghini, L. Masi, G. Giusti, G. Modugno, M. Inguscio, A. Gallemí, A. Recati, and M. Fattori, *Phys. Rev. Lett.* **122**, 090401 (2019).
- ¹⁰³V. Cikojević, L. V. Markić, M. Pi, M. Barranco, F. Ancilotto, and J. Boronat, *Phys. Rev. Res.* **3**, 043139 (2021).
- ¹⁰⁴M. Ceriotti, M. Parrinello, T. E. Markland, and D. E. Manolopoulos, *J. Chem. Phys.* **133**, 124104 (2010).

**Supplementary Material for “Clustering, Collision, and
Relaxation dynamics in pure and doped Helium nanoclusters:
density- versus particle-based approaches”**

Ernesto García-Alfonso,¹ Manuel Barranco,^{1,2,3} David A.
Bonhommeau,⁴ Nadine Halberstadt,¹ Martí Pi,^{2,3} and Florent Calvo^{5,*}

¹*Laboratoire Collisions, Agrégats, Réactivité (LCAR), Fédération FeRMI,
Université de Toulouse, CNRS, 31062, Toulouse, France*

²*Departament FQA, Facultat de Física,
Universitat de Barcelona. Diagonal 645, 08028 Barcelona, Spain*

³*Institute of Nanoscience and Nanotechnology (IN2UB),
Universitat de Barcelona, Barcelona, Spain.*

⁴*Université de Reims Champagne Ardenne,
CNRS, GSMA UMR 7331, 51097 Reims, France*

⁵*Université Grenoble Alpes, LIPHY, F-38000 Grenoble,
France and CNRS, LIPHY, F-38000 Grenoble, France*

CONTENTS

1. Effective Ar-He interaction potential used in ZPAD simulations
2. List of typical animations of the various dynamical processes obtained by the different methods

I. EFFECTIVE Ar-He INTERACTION POTENTIAL USED IN ZPAD SIMULATIONS

As mentioned in Section II of the main manuscript, the effective Ar-He interaction potential used in ZPAD simulations is converged iteratively. Then, the subsequent set of data points is fitted on the analytical form^{1,2}

$$V_{\text{He-Ar}}^{\text{eff}}(R) = V_{\text{short}}(R) + T(R)[V_{\text{long}}(R) - V_{\text{short}}(R)], \quad (1)$$

where

$$V_{\text{short}}(R) = A \exp[-\alpha_1 R/R_e - \alpha_2 (R/R_e)^2] \quad (2)$$

$$V_{\text{long}}(R) = \sum_{i=3}^8 c_{2i} (R/R_e)^{-2i} \quad (3)$$

$$T(R) = 0.5 (1 + \tanh[a(R - b)]). \quad (4)$$

The parameters of the short-range function $V_{\text{short}}(R)$, long-range function $V_{\text{long}}(R)$, and switching function $T(R)$ are collected in Table I. The original Tang-Toennies potential³ for Ar-He and the effective potential presently used in ZPAD simulations are also depicted in Figure 1 for the sake of comparison. Similar figures for He-He interaction potential are available in our recent publication on the fragmentation of $\text{Ar}_n^+\text{He}_{1000}$ clusters, the corresponding data and graph are shown as well for consistency.²

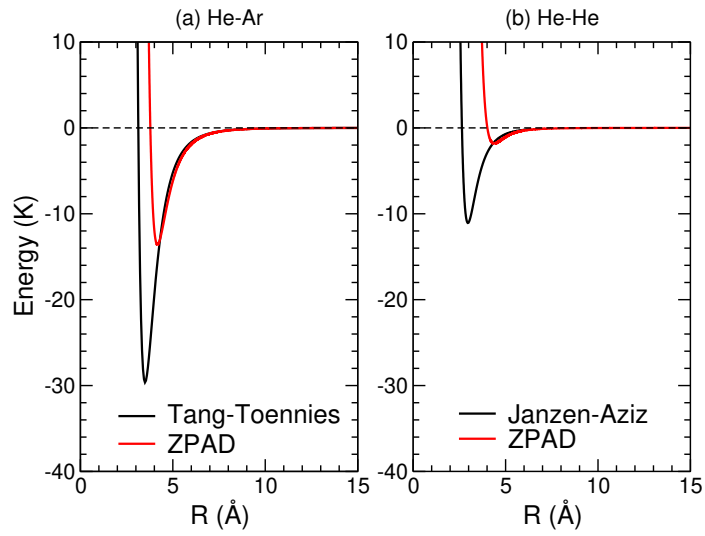


FIG. 1. Original and effective ZPAD potentials for the Ar-He and He-He interactions, shown with common scales. (a) Ar-He potentials; (b) He-He potentials. The original potentials for Ar-He and He-He are from Tang and Toennies³ and Janzen and Aziz⁴ (SAPT2), respectively.

TABLE I. Parameters of $V_{\text{He-He}}^{\text{eff}}(R)$ and $V_{\text{He-Ar}}^{\text{eff}}(R)$ for a cutoff radius $R_{\text{cut}} = 1.6 \text{ \AA}$. The standard deviations between the fitted curve and the original data points for the regions of positive and negative energies are denoted SD^+ and SD^- , respectively. The parameters for the He-He diatomic are adapted from Ref. 2.

Parameter (unit)	He-He	He-Ar
R_e (\AA)	4.401 36	4.199 29
A (10^4 K)	6.167 19	2289.97
α_1	-0.922 778	10.461
α_2	13.021	5.394 25
c_6 (K)	-3.474 56	-11.3992
c_8 (K)	11.1168	-17.7762
c_{10} (K)	-22.4079	58.9441
c_{12} (K)	12.9490	-143.684
c_{14} (K)	0	135.542
c_{16} (K)	0	-35.1591
a (\AA^{-1})	41.7872	7.202 81
b (\AA)	3.561 43	3.246 32
SD^- (10^{-3} K)	3.6	1.6
SD^+ (K)	0.30	5.12

II. LIST OF ANIMATIONS

- TDDFT simulation of the capture of an Ar atom at 500 m/s and impact parameter $b = 0$ by a $\text{Ar}@^4\text{He}_{1000}$ droplet
- TDDFT simulation of the capture of an Ar atom at 500 m/s and impact parameter $b = 10 \text{ \AA}$ by a $\text{Ar}@^4\text{He}_{1000}$ droplet
- RPMD simulation of an Ar atom impinging on a $\text{Ar}@^4\text{He}_{1000}$ droplet at 500 m/s and $b = 0$, without forming an argon dimer
- ZPAD simulation of the (late) formation of the nearly linear Ar_3 by capture of one Ar atom at 1000 m/s and zero impact parameter by an $\text{Ar}_2@^4\text{He}_{1000}$ droplet.
- RPMD simulation of the formation of the linear Ar_3 by capture of one Ar atom at 500 m/s and zero impact parameter by an $\text{Ar}_2@^4\text{He}_{1000}$ droplet.
- TDDFT simulation of the capture of an Ar atom at 500 m/s and impact parameter $b = 0$ by a $\text{Ar}_4@^4\text{He}_{1000}$ droplet, the Ar projectile being sent towards an apex atom and leading to a higher order stationary configuration with a single bond
- TDDFT simulation of an Ar atom impinging at 500 m/s and impact parameter $b = 0$ on a $\text{Ar}_4@^4\text{He}_{1000}$ droplet, the Ar projectile being sent towards a facet
- TDDFT simulation of an Ar atom impinging at 500 m/s and impact parameter $b = 10 \text{ \AA}$ on a $\text{Ar}_4@^4\text{He}_{1000}$ droplet, the Ar projectile being sent towards a facet
- TDDFT simulation of the capture of an Ar atom at 500 m/s and impact parameter $b = 10 \text{ \AA}$ by a $\text{Ar}_4@^4\text{He}_{1000}$ droplet, the Ar projectile being sent towards an apex atom and leading to a high order configuration with two extra bonds
- Two RPMD simulations of an Ar atom impinging at 500 m/s and impact parameter $b = 0$ on a $\text{Ar}_4@^4\text{He}_{1000}$ droplet, leading to high-energy configurations
- RPMD simulation of the capture of a Cs atom at 500 m/s and impact parameter $b = 10 \text{ \AA}$ by a $^4\text{He}_{1000}$ droplet
- ZPAD simulation of the bouncing of an impinging Cs atom onto a $^4\text{He}_{1000}$ droplet at $b = 0$ and $v = 50 \text{ m/s}$

- TDDFT simulation of the capture of a Cs atom at 50 m/s and impact parameter $b = 10 \text{ \AA}$ by a ${}^4\text{He}_{1000}$ droplet
- TDDFT simulation of Cs atom piercing through a ${}^4\text{He}_{1000}$ droplet at impact parameter $b = 10 \text{ \AA}$ and 500 m/s velocity
- Three simulations of the merging process between two ${}^4\text{He}_{500}$ droplets obtained with the TDDFT, RPMD, and ZPAD methods

* florent.calvo@univ-grenoble-alpes.fr

¹ N. Halberstadt and D. A. Bonhommeau, *J. Chem. Phys.* **152**, 234305 (2020).

² D. A. Bonhommeau, *Chem. Phys.* **550**, 111307 (2021).

³ K. T. Tang and J. P. Toennies, *J. Chem. Phys.* **118**, 4976 (2003).

⁴ A. R. Janzen and R. A. Aziz, *J. Chem. Phys.* **107**, 914 (1997).

 CHAPTER IVALKALI ION SOLVATION INTO A
 ${}^4\text{He}_{2000}$ DROPLET

IV-1. Introduction

The interaction of a He atom with a cation is very strong compared to that with a neutral atom. This leads to the appearance of a high density -some times solid-like- solvation shell around the cation, inside a helium droplet or the bulk liquid: the so-called “snowball” [22]. Often, several additional high density solvation shells can be distinguished. For very strong interactions, the first shell is nearly isolated, hampering bosonic exchanges with the rest of the superfluid. Note that the term of “snowball” can have different meanings in the literature, so that it is somewhat ill-defined [86]. Here, it will refer to the first, high density shell of helium appearing around the cation.

Neutral alkali (Ak) atoms have the peculiar property of remaining outside, in a dimple of the droplet surface [87]. Upon ionization, the resulting Ak^+ cation sinks into the droplet [88]. At variance with the situation in bulk liquid He, this motion does not require the application of any external electric field to proceed.

In a recent experiment, Albrechtsen *et al* [89] have used this process as a model to unveil the primary steps of ion solvation in helium droplets. This is a remarkable

achievement, especially considering the recent quote from Markus [90] “*It is impossible to follow by measurements an actual experimental process of the transfer of a single ion from its isolated state in the gas phase to its fully solvated state in a solution. Such a process, however, may be dealt with as a thought process and theoretical considerations may be applied to it*”. To accomplish this goal, a He nanodroplet doped with a Xe atom inside and a Na atom on the surface was interrogated in a laser pump-probe experiment.

The pump pulse ionized the Na atom, thereby initiating the ion solvation process. After a variable time delay, the probe pulse ionized the Xe atom, triggering Coulomb repulsion between the Xe⁺ and Na⁺ ions. This led to the ejection of Na⁺ along with a number n of He atoms. The resulting Na⁺-⁴He _{n} complexes were detected and characterized by velocity map imaging. By carefully analyzing the Na⁺-⁴He _{n} ion yields as a function of time delay, the authors concluded that the process was Poissonian up to $n = 5$: the first He atoms attached to the Na⁺ ion independently of each other with a constant time rate, as shown by the linear time-dependence of the probability distribution peaks $n(t) = At$. This was confirmed by a theoretical simulation based on the ⁴He-TDDFT approach [89].

IV-2. Method

We have investigated the sinking of alkali cations (Li⁺, Na⁺, K⁺, Rb⁺ and Cs⁺) in superfluid ⁴He nanodroplets using ⁴He time-dependent density functional theory at zero temperature. The use of ⁴He-TDDFT here is important because the ions are moving inside the droplet, and the sinking process creates important excitations in the droplet. Hence, superfluidity and its frictionless motion below Landau critical velocity needs to be taken into account, and the excitations modes need to be correctly described. On the other hand, some of the polarization effects such as induced dipole-induced dipole interactions cannot be described (see details on page 5 of the accompanying article, last paragraph).

The equilibrium configuration of neutral Ak on a ⁴He₂₀₀₀ droplet is determined using static simulations as described in chapter II. The dynamics is triggered by substituting the Ak atom by its cation Ak⁺. The latter is equivalent to a sudden ionization. Upon ionization, the Ak⁺ cation sinks towards its equilibrium position at the center of the droplet. All alkali ions were treated as classical particles.

In order to compare with experiment, it was assumed in the Na⁺ case that the first n He atoms attached to the ion during the sinking process would remain tightly bound to it during the Coulomb repulsion process and lead to the detection of Ak⁺-⁴He _{n} . This was justified by the strength of the Ak⁺-He interaction. Here we used the same assumption, and for each alkali cation, $n(t)$ is fitted to a linear form $n(t) = At$ for n up to 5; the parameter A can be identified with the binding rate.

IV-3. Results

Figure IV.1 displays the sinking process of the Rb⁺ evolving into a ⁴He₂₀₀₀ droplet as snapshots at different times of the simulation ($t=0, 2, 6, 10, 30, 60, 80$ and 100.8 ps). As can be seen in that figure, a high density shell is rapidly formed around the ion, almost as soon as it enters the droplet. In addition, the motion of the ion and its solvation complex towards the droplet center creates a lot of excitation inside the helium.

At the same time, we determined the spherically averaged helium density profile around each ion as the systems evolve, as displayed in Figure IV.2 for Rb⁺ solvation. It can be seen that the solvation structure is stable at about 30 ps, although it keeps gaining some more helium.

In order to quantify the solvation process, we have determined the spherical average of the helium density as a function of the distance to the ion. It is presented in Fig IV.2 for Rb⁺ solvation at the same values of the time as the snapshots of Fig IV.1. The number of helium atoms in the first or second solvation shell are also shown. They were obtained by first determining the radius of the solvation shells

r_1 and r_2 in a separate, static calculation of Rb⁺@He₂₀₀₀, and then integrating the helium density around Rb⁺ from 0 to r_1 and r_2 , respectively.

We report in Fig IV.3 the two-dimensional cut through the helium density side-by-side with the spherical averaged density around the cation position at the end of the simulation for each alkali ion studied. In each case the solvation structure is stabilized. Note that for the most attractive ions, Li⁺ and Na⁺ (the characteristics of the interaction potentials are collected in Table F.10 of annex E), the first solvation shell is well separated from the second one, preventing exchange between the two.

The spherical average is used to compute the He atoms content n_1 in the first (black lines in Fig IV.2) solvation shell by integrating the He density profile from the location of the Ak⁺ ion equilibrium position, $r = 0$, to $r = r_1$. Those distances are obtained in a preliminary static calculation and are drawn as blue vertical dashed lines in Figure IV.2. The blue horizontal line shows the number n_1/n_2 of helium atoms in the first/second solvation shell. See Figure IV.2 for the Rb⁺ sinking and Figure IV.3 where two dimensional cut and spherical average at the end of each simulation are shown one next to other.

In order to relate our findings to the experiment of Albrechtsen *et al.* [89] we have determined the number of He atoms (n) in the first solvation shell as a function of time. We have then fitted $n(t)$ to a linear form, $n(t) = At$. Each fit was performed twice, once for each of the following definitions of $n(t)$. The first definition corresponds to the first time the integrated density in the solvation sphere reaches n ; the second one first time it reaches n with no more fluctuations back to $n - 1$. The first definition yields a larger value of A than the second one. The shadowed regions between the two lines in the panels of Fig IV.4 give an idea of the uncertainty on the rates obtained within the ⁴He-TDDFT approach.

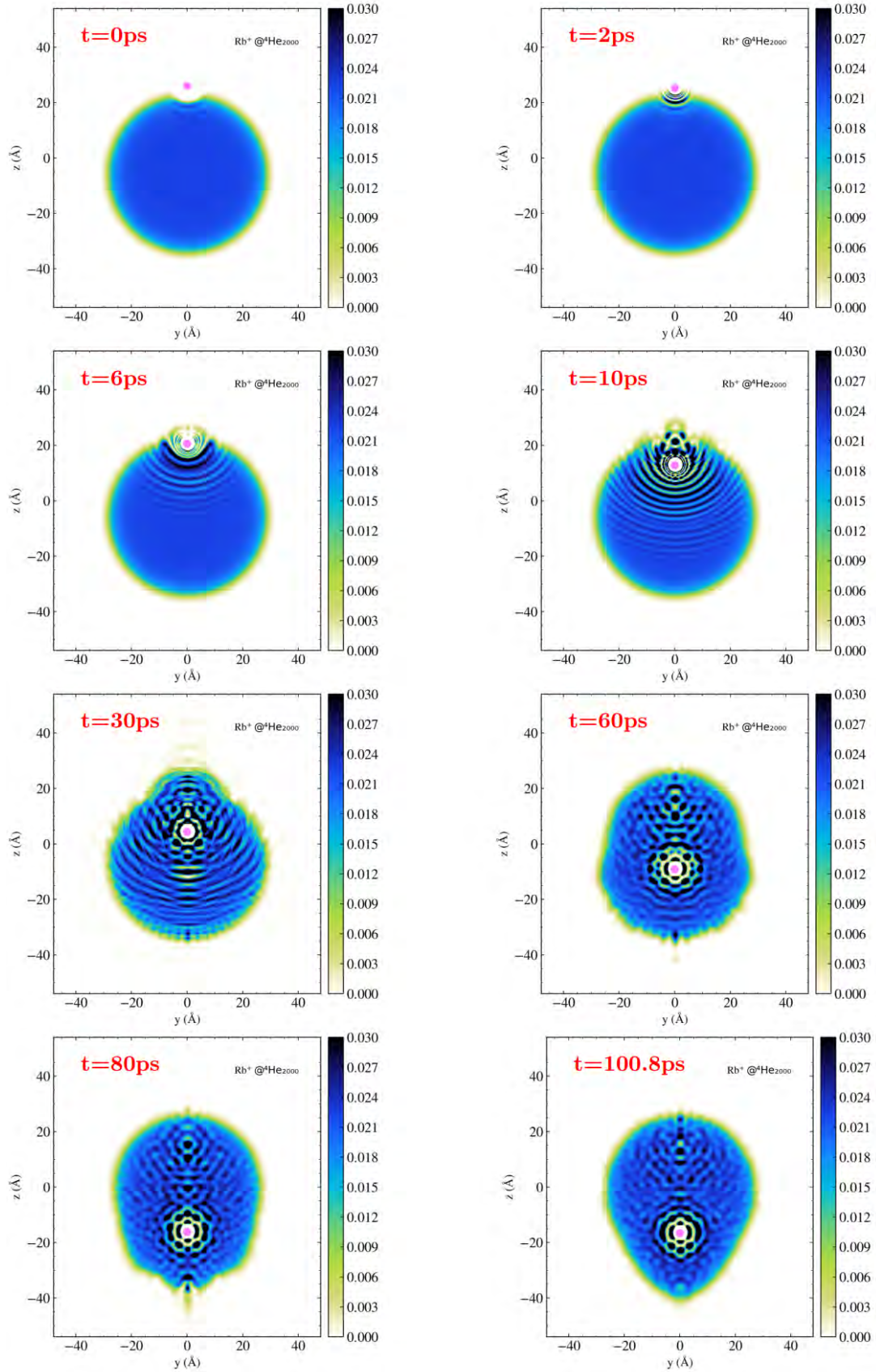


Figure IV.1. Two-dimensional cut of the helium density in a symmetry plane and ion position for Rb^+ solvation at $t=0, 2, 6, 10, 30, 60, 80$ and 100.8 ps. The color scale to the right of each panel corresponds to the superfluid helium density given in \AA^{-3} bulk superfluid helium density 0.0218\AA^{-3} at $T = P = 0$; freezing density 0.026\AA^{-3}).

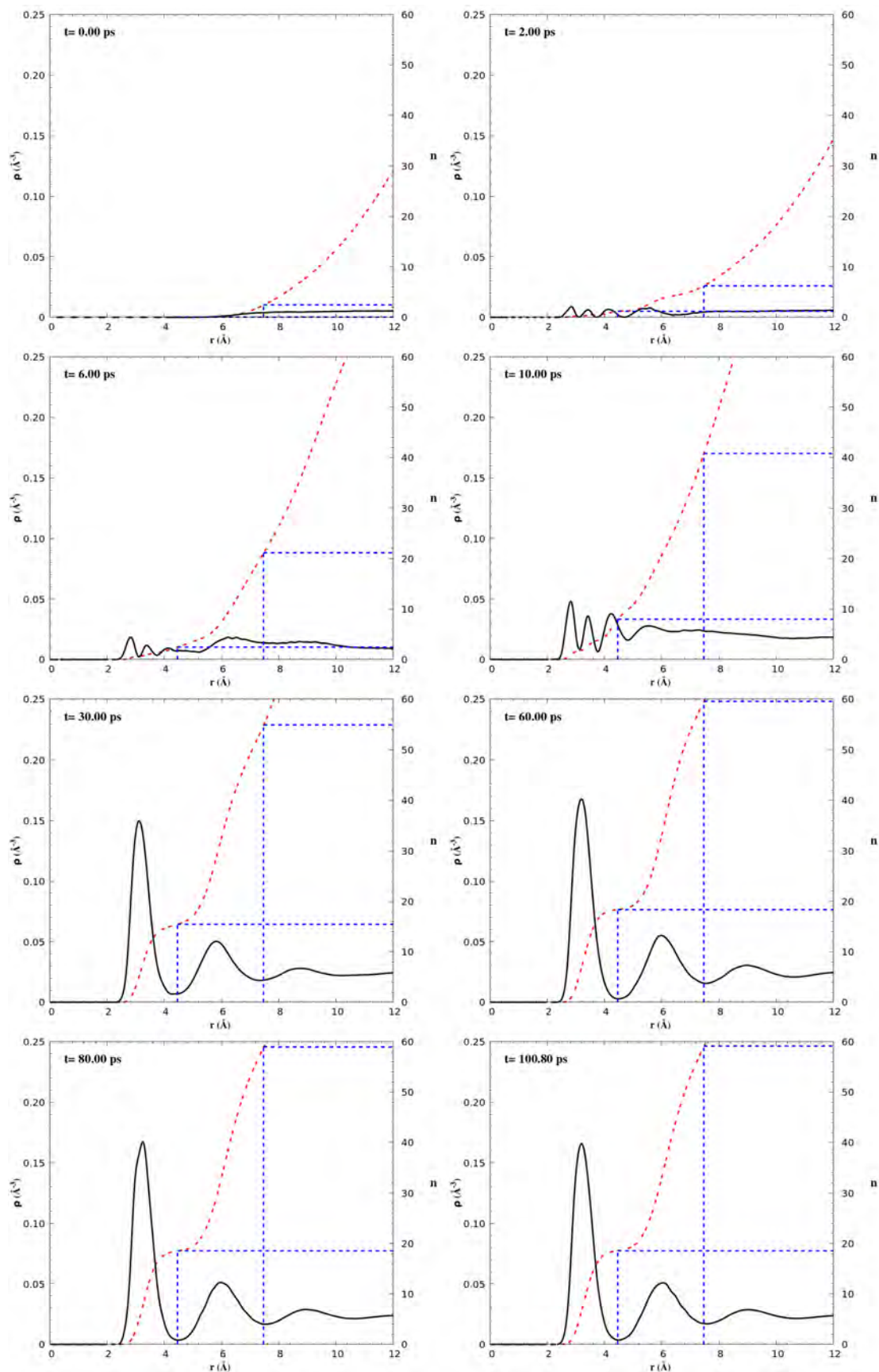


Figure IV.2. Spherical average (solid black curve) (at $t=0, 2, 6, 10, 30, 60, 80$ and 100.8 ps) of the helium density as a function of the distance from the Rb^+ position, number of He atoms n (red dashed line). The blue dashed vertical lines show the radius of the first and second solvation shell, and the blue dashed horizontal lines the integrated density within the corresponding shell.

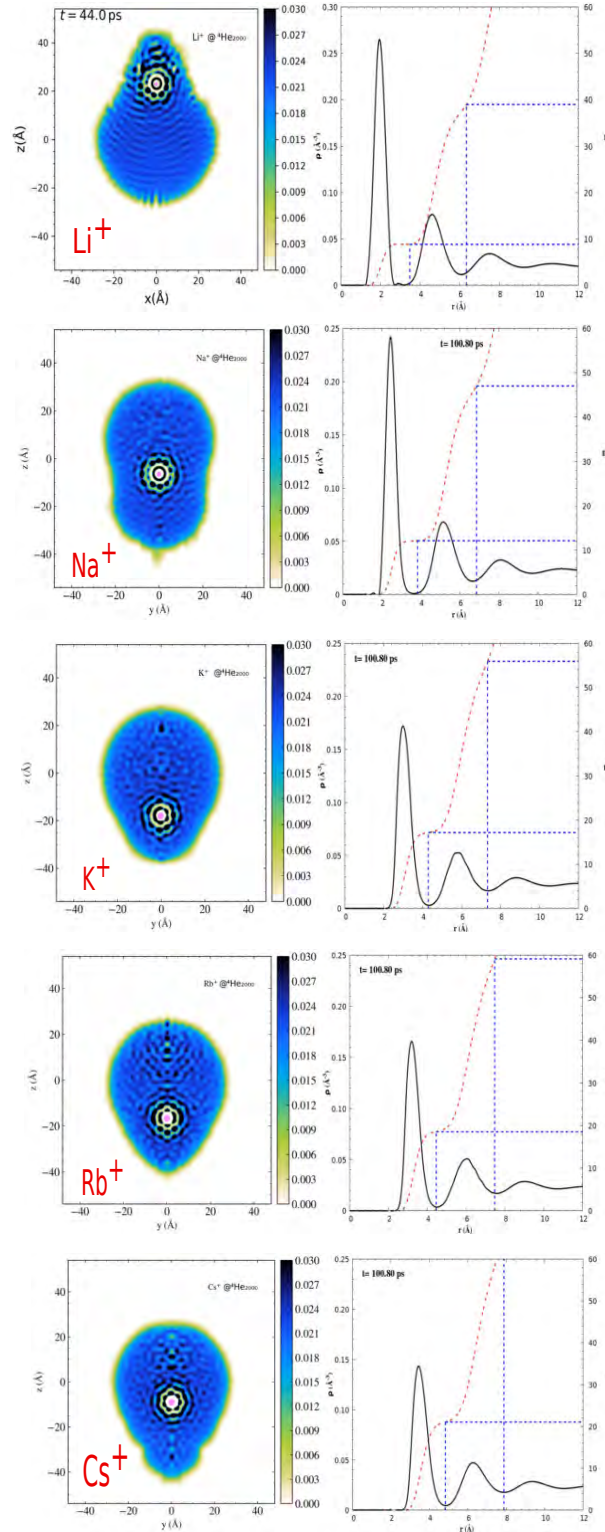


Figure IV.3. Solvation of Ak cation into a ${}^4\text{He}_{2000}$ droplet at $t=44, 100.8, 100.8, 100.8, 100.8$ ps for Li^+ , Na^+ , K^+ , Rb^+ and Cs^+ respectively. Each illustration is composed of two panels. Left panel: two-dimensional cut through the helium density in a symmetry plane and ion position; right panel: spherical average helium density as a function of the distance to Ak^+ .

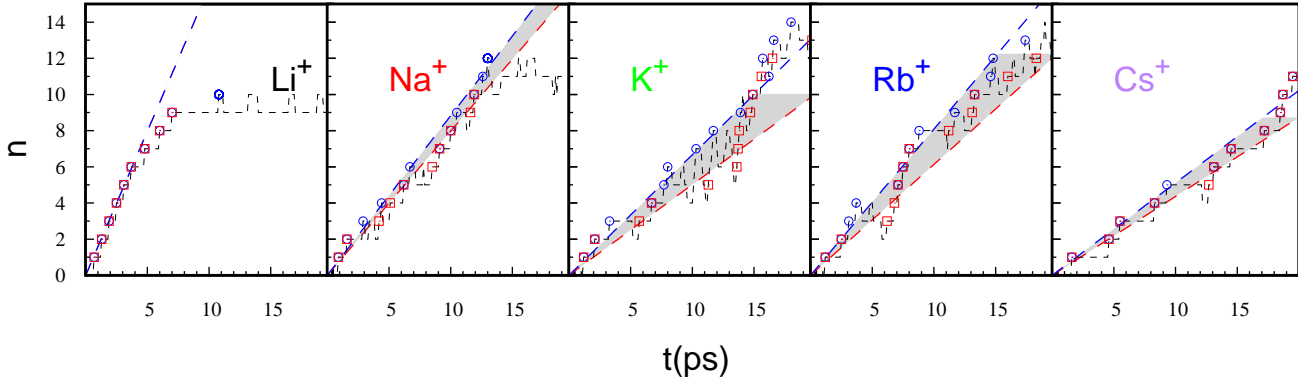


Figure IV.4. Number of He atoms n around the Ak⁺ ions as a function of t for Ak⁺@⁴He₂₀₀₀. The blue empty circles or the red empty squares correspond to the first or second definition, respectively, of $n(t)$ explained in the text. The lines are the best fit to the law $n(t) = At$ for the Ak⁺@⁴He _{n} complexes up to $n = 5$, see text for explanation.

IV-4. Conclusions

As can be seen in Fig IV.3, the droplets are still rather excited at the end of the simulations. They are far from their final equilibrium configuration, which corresponds to an Ak⁺ ion at rest at the center of the remaining ⁴He _{M} spherical droplet (with $M < 2000$). A sizeable part of the excitation energy remains in the droplet in the form of density waves and large amplitude surface modes, plus some kinetic energy in the ion and in the droplet itself.

The simulations show the progressive build up of the first solvation shell around the cations [91]. The number of helium atoms in this shell is found to linearly increase with time during the first stages of the dynamics. This points to a Poissonian capture process, as concluded in the work of Albrechtsen *et al* [89].

A more demanding simulation is underway, that of the full pump-probe process. It consists in adding a neutral Xe atom at the center of the helium droplet during the pump process (ionization of the alkali at the droplet surface followed by its solvation) and in a second step (probe) in suddenly ionizing the Xe atom, the same way as we did for the ionization of Ak. The probe step will trigger a Coulomb explosion between Ak⁺ and Xe⁺. The simulations should provide a direct measure of the kinetics of Ak⁺ ejection and of the number of He atoms attached to it, and

also whether the ejected Ak⁺-He_n complex is stable or whether it can still lose He atoms in its way to detection.

Time-resolved solvation of alkali ions in superfluid helium nanodroplets

Cite as: J. Chem. Phys. **160**, 164308 (2024); doi: 10.1063/5.0205951

Submitted: 28 February 2024 • Accepted: 29 March 2024 •

Published Online: 23 April 2024



View Online



Export Citation



CrossMark

Ernesto García-Alfonso,¹  Manuel Barranco,^{2,3}  Nadine Halberstadt,^{1,a)}  and Martí Pi^{2,3} 

AFFILIATIONS

¹Laboratoire Collisions, Agrégats, Réactivité (LCAR), Université de Toulouse, CNRS, 31062 Toulouse, France²Departament FQA, Facultat de Física, Universitat de Barcelona, Av. Diagonal 645, 08028 Barcelona, Spain³Institute of Nanoscience and Nanotechnology (IN2UB), Universitat de Barcelona, Barcelona, Spain^{a)}Author to whom correspondence should be addressed: nadine.halberstadt@irsamc.ups-tlse.fr

ABSTRACT

The sinking of alkali cations in superfluid ⁴He nanodroplets is investigated theoretically using liquid ⁴He time-dependent density functional theory at zero temperature. The simulations illustrate the dynamics of the buildup of the first solvation shell around the ions. The number of helium atoms in this shell is found to linearly increase with time during the first stages of the dynamics. This points to a Poissonian capture process, as concluded in the work of Albrechtsen *et al.* on the primary steps of Na⁺ solvation in helium droplets [Albrechtsen *et al.*, *Nature* **623**, 319 (2023)]. The energy dissipation rate by helium atom ejection is found to be quite similar between all alkalis, the main difference being a larger energy dissipated per atom for the lighter alkalis at the beginning of the dynamics. In addition, the number of helium atoms in the first solvation shell is found to be lower at the end of the dynamics than at equilibrium for both Li⁺ and Na⁺, pointing to a kinetic rather than thermodynamical control of the snowball size for small and strongly attractive ions.

Published under an exclusive license by AIP Publishing. <https://doi.org/10.1063/5.0205951>

I. INTRODUCTION

The study of ion motion in liquid helium has been used to investigate some of the peculiar properties of this unique quantum fluid. In particular, many experimental and theoretical studies have aimed at characterizing ion mobilities inside superfluid helium by drifting the ions through the liquid by means of an external electric field and measuring their time of flight spectrum; see, e.g., Refs. 1–3 and references therein. Most of these experiments were designed to study the response of bulk superfluid helium at the atomic scale.

The interaction of a He atom with a cation is very strong compared to that with a neutral atom. This leads to the appearance of a high density—sometimes solid-like—solvation shell around the cation: the so-called “snowball.” Often, several additional high density solvation shells can be distinguished. For very strong interactions, the first shell is nearly isolated, hampering bosonic exchanges with the rest of the superfluid. Note that the term of “snowball” can have different meanings in the literature so that it is somewhat ill-defined.⁴ Here, it will refer to the first, high density shell of helium appearing around the ion.

Studies of ions in helium drops are less common. They have been comprehensively reviewed in a recent paper.⁴ Cations, as most of the neutral impurities, reside in the bulk of the drops. This leads to an interesting effect in the case of alkali (Ak) atoms ionization. Ak atoms have the peculiar property of remaining outside, in a dimple of the droplet surface. Upon Ak ionization, the resulting Ak⁺ ion sinks into the droplet.⁵ At variance with the situation in bulk liquid He, this motion does not require the application of any external electric field to proceed. It has been found that cation sinking can yield quantized vortex rings, as seen for the alkaline-earth Ba⁺ ions⁶ (Ba atoms also reside on the drop surface), or vortex loops nucleation as in the case of Rb⁺ and Cs⁺ cations.⁵

The sinking of Ba⁺ had been monitored in real time through its absorption spectrum. The latter reflected the location of Ba⁺: initially at the droplet surface, it gradually moved inside, where the spectrum characteristics were very similar to the ones in bulk liquid helium.⁷ The experiment was accurately reproduced in a ⁴He-TDDFT analysis.⁶ No similar study of the time-resolved absorption spectrum has been carried out for other sinking cations.

An extensive experimental study on the formation and stability of snowball complexes upon photoionization of Na, K, Rb, and Cs

alkali metal clusters on He nanodroplets has been conducted by Müller *et al.*⁸ using femtosecond laser pulses (multiphoton ionization). Relevant theoretical activity on ions in He drops carried out before 2009 is summarized in Refs. 8 and 9. As already mentioned, alkali atoms are weakly bound to the helium droplet surface:¹⁰ this is due to the extremely weak attractive interaction between Ak and He atoms. Above-threshold laser ionization then leads to massive He atoms evaporation as well as to the expulsion of the ionized dopant, which carries along He atoms forming a snowball structure. The Ak⁺@He_n ion abundances in experimental mass spectra are compared to theoretical predictions and are found to agree on the first He shell closure for Rb and Cs snowballs within experimental error. The number of He atoms found for the Rb⁺ and Cs⁺ snowballs is of 14 and 16, respectively.⁸ No differential mass spectra of snowballs similar to those of Rb⁺ and Cs⁺ are provided for Na⁺ and K⁺. In contrast to the heavier Rb and Cs alkali metals, the lighter Na and K species show only very limited snowball progressions in these experiments (Ak⁺@⁴He_n complexes with $n > 8$ were not observed), and the completion of the first solvation shell is not achieved.

The most recent experimental results are from Scheier's group and co-workers; see especially Refs. 4 and 11. In particular, high-resolution mass spectrometry experiments conducted on Na⁺@⁴He_n and K⁺@⁴He_n complexes formed by electron ionization of doped He droplets¹¹ gave a snowball size slightly smaller than the calculated one.

A related experimental work was conducted by Theisen *et al.* on the sinking of Rb⁺ ions¹² and Cs⁺ ions.¹³ The Ak atom was excited to the $n^2P_{1/2}$ ($^2\Pi_{1/2}$) state ($n = 5$ or 6 for Rb or Cs, respectively) and remained on the droplet surface for a time much longer than needed for the droplet to relax around the excited Ak atom. Subsequently, the excited Ak atom was ionized, and eventually, the Ak⁺ ion sank into the droplet. The size of the snowball was not determined.

In a recent experiment, Albrechtsen *et al.*¹⁴ have been able to unveil the primary steps of ion solvation in helium droplets. This is a remarkable achievement, all the more so considering the recent quote from Markus:¹⁵ "It is impossible to follow by measurements an actual experimental process of the transfer of a single ion from its isolated state in the gas phase to its fully solvated state in a solution. Such a process, however, may be dealt with as a thought process and theoretical considerations may be applied to it." To accomplish this goal, a He nanodroplet doped with a Xe atom inside and a Na atom on the surface was interrogated in a laser pump-probe experiment. The pump pulse ionized the Na atom, thereby initiating the ion solvation process. After a variable time delay, the probe pulse ionized the Xe atom, triggering Coulomb repulsion between the Xe⁺ and Na⁺ ions. This led to the ejection of Na⁺ along with a number n of He atoms. The resulting Na⁺@⁴He_n complexes were detected and characterized by velocity map imaging. By carefully analyzing the Na⁺@⁴He_n ion yields as a function of time delay, the authors concluded that the process was Poissonian up to $n = 5$: the first He atoms attached to the Na⁺ ion independently of each other with a constant time rate, as shown by the linear time-dependence of the probability distribution peaks $n(t) = At$. This was confirmed by a theoretical simulation based on the ⁴He-TDDFT approach included in the same publication.

In this work, we extend the theoretical part of the study on Ak⁺ cation sinking carried out for Na⁺ in Ref. 14, as well as the theoretical

study on Rb⁺ and Cs⁺,⁵ to the whole series of alkali atoms, studied under the same conditions. Special attention is paid to the first picoseconds of the process and to determining how the first solvation shell is being filled. To this end, we apply the density functional theory approach for superfluid helium at zero temperature (⁴He-TDDFT approach, thoroughly exposed in Ref. 16) to a larger, more realistic He droplet made of 2000 He atoms, using a more accurate version of the computing codes.¹⁷

This work is organized as follows. The ⁴He-DFT method is briefly described in Sec. II. We present the results in Sec. III, and a summary is given in Sec. IV. We also provide in the supplementary material movies illustrating the real-time simulations of the sinking of Ak⁺ ions addressed in this work. This multimedia material helps capture physical details that would be difficult to present and thoroughly describe in the main text.

II. THE ⁴He-DFT APPROACH

The helium density functional (⁴He-DFT) method and its time-dependent version (⁴He-TDDFT) have proven to be very powerful numerical tools to investigate superfluid ⁴He droplets. They derive from a phenomenological approach and constitute a good compromise between accuracy and feasibility. The parameters of the functional have been adjusted to reproduce various properties of bulk superfluid helium, such as its equilibrium density, energy per atom, and compressibility, as well as the main features of the dispersion relation of its elementary excitations.¹⁸ A detailed description of the method can be found in Refs. 16, and 18–20. In this work, we have treated Ak impurities as an external field in the statics calculations carried out to obtain the Ak@He₂₀₀₀ equilibrium configurations and Ak⁺ ions as classical particles in the dynamics simulations of Ak⁺ sinking inside a He₂₀₀₀ droplet.¹⁶

A. Statics

Within the ⁴He-DFT approach at zero temperature, the energy of a N -atom helium droplet ⁴He _{N} doped with an Ak atom, taken as an external field, is written as a functional of the ⁴He atom density $\rho(\mathbf{r})$ as

$$E[\Psi] = \int d\mathbf{r} \frac{\hbar^2}{2m_{\text{He}}} |\nabla\Psi|^2 + \int d\mathbf{r} \mathcal{E}_c(\rho) + \int d\mathbf{r} \mathcal{V}_{\text{He-Ak}}(|\mathbf{r} - \mathbf{r}_{\text{Ak}}|) \rho(\mathbf{r}), \quad (1)$$

where the first term is the kinetic energy of the superfluid, m_{He} is the mass of the ⁴He atom, and $\Psi(\mathbf{r})$ is the effective wave function (or order parameter) of the superfluid such that $\rho(\mathbf{r}) = |\Psi(\mathbf{r})|^2$ with $\int d\mathbf{r} |\Psi(\mathbf{r})|^2 = N$. The functional $\mathcal{E}_c(\rho)$ we have used contains the He-He interaction term within the Hartree approximation and additional terms describing non-local correlation effects.²¹ It is a modification of the Orsay-Trento functional,¹⁸ which makes it stable even in the presence of very attractive impurities. The interaction of one single He atom with the Ak impurity is represented by the pair potential $\mathcal{V}_{\text{He-Ak}}(|\mathbf{r} - \mathbf{r}_{\text{Ak}}|)$ taken from the work of Patil.²² In the calculations involving Ak⁺ ions, we have used the $\mathcal{V}_{\text{He-Ak}^+}(|\mathbf{r} - \mathbf{r}_{\text{Ak}^+}|)$ pair potentials by Koutselos *et al.*²³ Although there are more recent potentials, the ones by Koutselos *et al.* have been chosen in order to keep a consistent level of accuracy for all alkali ions.

The droplet equilibrium configuration is obtained by solving the Euler–Lagrange (EL) equation arising from functional variation of Eq. (1),

$$\left\{ -\frac{\hbar^2}{2m_{\text{He}}} \nabla^2 + \frac{\delta \mathcal{E}_c}{\delta \rho} + \mathcal{V}_{\text{He-Ak}}(|\mathbf{r} - \mathbf{r}_{\text{Ak}}|) \right\} \Psi \equiv \mathcal{H}[\rho] \Psi = \mu \Psi, \quad (2)$$

where μ is the ⁴He chemical potential corresponding to the number of He atoms in the droplet ($N = 2000$ in this work, corresponding to a droplet of $R = 28 \text{ \AA}$ radius¹⁹) and \mathcal{H} is the DFT Hamiltonian,

$$\mathcal{H} = -\frac{\hbar^2}{2m_{\text{He}}} \nabla^2 + \frac{\delta \mathcal{E}_c}{\delta \rho(\mathbf{r})} + \mathcal{V}_{\text{He-Ak}}(|\mathbf{r} - \mathbf{r}_{\text{Ak}}|). \quad (3)$$

The EL equation has been solved by a relaxation (imaginary time) method using the ⁴He-DFT BCN-TLS computing package;¹⁷ see Refs. 16 and 20 and references therein for additional details. We work in Cartesian coordinates, with the effective wave function $\Psi(\mathbf{r}, t)$ defined at the nodes of a 3D grid inside a calculation box discretized using a 0.3 \AA space step. Periodic boundary conditions (PBCs) are imposed, which allow us to use the Fast Fourier Transform (FFT)²⁴ to efficiently compute the convolutions needed to obtain the DFT mean field $\mathcal{H}[\rho]$. The differential operators in $\mathcal{H}[\rho]$ are approximated by 13-point formulas.

B. Dynamics

The dynamics is triggered by substituting the Ak atom by its ion Ak⁺. Treating the Ak⁺ ions as classical particles, the total energy of the system can be written as

$$E[\Psi, \mathbf{r}_{\text{Ak}^+}] = \int d\mathbf{r} \frac{\hbar^2}{2m_{\text{He}}} |\nabla \Psi|^2 + \int d\mathbf{r} \mathcal{E}_c(\rho) + \int d\mathbf{r} \rho(\mathbf{r}) \mathcal{V}_{\text{He-Ak}^+}(|\mathbf{r} - \mathbf{r}_{\text{Ak}^+}|) + \frac{1}{2} m_{\text{Ak}^+} \dot{\mathbf{r}}_{\text{Ak}^+}^2. \quad (4)$$

The equations describing the dynamics of the system are obtained by minimizing the action²⁵

$$\mathcal{A}[\Psi, \mathbf{r}_{\text{Ak}^+}] = \int dt \left\{ i\hbar \int d\mathbf{r} \Psi^*(\mathbf{r}, t) \frac{\partial}{\partial t} \Psi(\mathbf{r}, t) + m_{\text{Ak}^+} \dot{\mathbf{r}}_{\text{Ak}^+}^2 - E[\Psi, \mathbf{r}_{\text{Ak}^+}] \right\}. \quad (5)$$

Variation of \mathcal{A} with respect to Ψ^* and \mathbf{r}_{Ak^+} yields

$$i\hbar \frac{\partial}{\partial t} \Psi = \left\{ -\frac{\hbar^2}{2m_{\text{He}}} \nabla^2 + \frac{\delta \mathcal{E}_c}{\delta \rho(\mathbf{r})} + V_{\text{Ak}^+\text{He}}(|\mathbf{r} - \mathbf{r}_{\text{Ak}^+}|) \right\} \Psi, \quad (6)$$

$$m_{\text{Ak}^+} \ddot{\mathbf{r}}_{\text{Ak}^+} = - \int d\mathbf{r} V_{\text{Ak}^+\text{He}}(|\mathbf{r} - \mathbf{r}_{\text{Ak}^+}|) \nabla \rho(\mathbf{r}),$$

where the time dependence of the variables has been omitted for clarity. Initial values for the $\{\mathbf{r}_{\text{Ak}^+}, \dot{\mathbf{r}}_{\text{Ak}^+}\}$ variables and the effective wave function $\Psi(\mathbf{r})$ have to be specified. $\Psi(\mathbf{r})$ is taken as the effective wave function corresponding to the equilibrium configuration of Ak@He₂₀₀₀, the ion position \mathbf{r}_{Ak^+} is taken as the equilibrium position of neutral Ak in the dimple, and the ion velocity $\dot{\mathbf{r}}_{\text{Ak}^+}$ is set to zero.

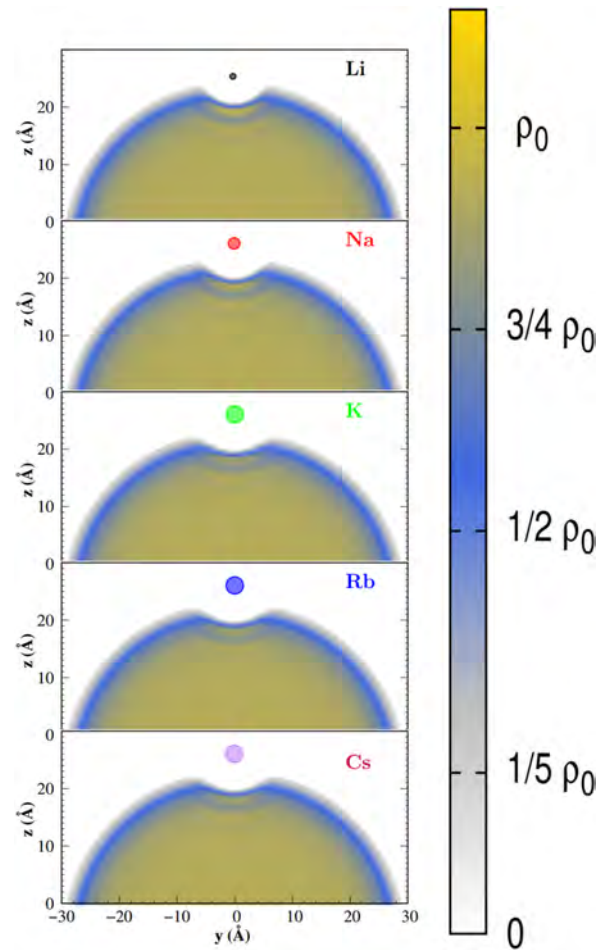


FIG. 1. Equilibrium configuration of Ak@⁴He₂₀₀₀ droplets (two-dimensional cuts). The density scale on the right is given in units of ρ_0 , the bulk superfluid helium density at zero temperature and pressure ($\rho_0 = 0.0218 \text{ \AA}^{-3}$). The sharp density radius of He₂₀₀₀ is 28.0 \AA .

Equations (6) are solved using the same simulation box and space step as in the statics. They have been numerically integrated using a Hamming predictor–modifier–corrector algorithm²⁶ initiated by a fourth-order Runge–Kutta–Gill algorithm²⁶ implemented in the ⁴He-DFT BCN-TLS computing package. We have employed a time step of 0.05 fs except in the case of Li⁺, where a time step of 0.01 fs has been needed to keep the simulation stable.

Due to the large energy available in the sinking process, very energetic excitations are expected to be produced in the droplet, such as phonons, rotons, and ripplons. Eventually, this energy is dissipated by He atom ejection. These atoms reach the simulation box boundaries and re-enter the box from the opposite side due to the imposed PBCs, interfering with the droplet in an unphysical and unpredictable way. In order to avoid this, an absorption potential is added inside a buffer located near the borders of the simulation

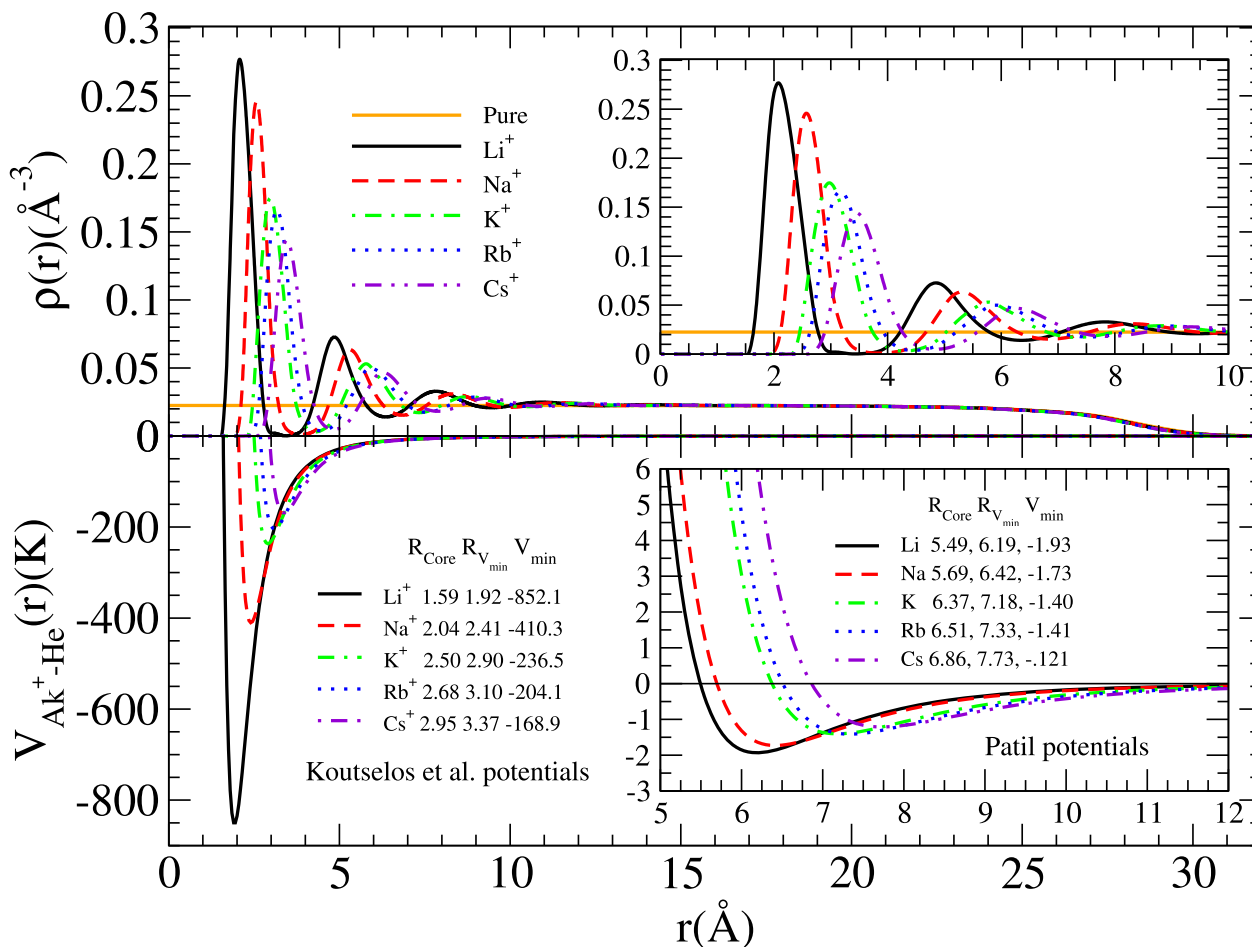


FIG. 2. Top: Spherically averaged helium density profiles of the equilibrium configuration of Ak⁺@⁴He₂₀₀₀ droplets as a function of the distance r to the cation, located at the droplet center. Also shown is the density profile of the pure ⁴He₂₀₀₀ (orange solid line). The inset zooms in on the density profiles in the region $r \leq 10$ Å. Bottom: Ak⁺-He pair potentials.²³ The inset displays the corresponding neutral Ak-He pair potentials.²²

box and gradually drives to zero the density corresponding to the evaporated He atoms.²⁷

III. RESULTS

A. Statics

Figure 1 shows the equilibrium configuration for each Ak atom in a ⁴He₂₀₀₀ droplet, which is the starting configuration for the sinking dynamics. The dimple in which the Ak atom resides is clearly visible. From the Ak-He pair potentials drawn in Fig. 2 (bottom inset), it can be noticed that the stronger the Ak-He interaction and the shorter its equilibrium distance, the deeper the dimple and the closer the Ak atom to the distorted droplet surface. This was also the case in the ⁴He-DFT study of Ak@He₁₀₀₀ absorption spectra (see Ref. 10 and Table I in Ref. 28).

Upon ionization, the Ak⁺ ion sinks toward its equilibrium position at the center of the droplet. The spherically averaged density

profile of Ak⁺@⁴He₂₀₀₀ complexes at equilibrium is shown in the top panel of Fig. 2 as a function of the distance to the cation. The bottom panel of Fig. 2 shows the Ak⁺-He pair potentials.²³ The neutral Ak-He pair potentials²² are also displayed as an inset. It can be seen from Fig. 2 that the effect of the impurity (Ak or Ak⁺) on the He droplet, even if sizable, remains local.

A well-defined inner (solvation) shell of He atoms around the Ak⁺ cation can be clearly seen in the inset in the top panel of Fig. 2, showing a focus on the helium density around the cation ($r \leq 10$ Å); see also Refs. 5 and 29. Note also that for a large drop, such as ⁴He₂₀₀₀, two additional shells are distinguishable. However, the concept of shell is rather approximate in this case since, in contrast with the first solvation shell which is well separated from the others, the helium density in between shells is significant. The average density in the first shell is well-above the freezing density of bulk liquid ⁴He (0.026 Å⁻³). Although this might be considered as an indication of a helium solid-like structure in the first solvation shell,

TABLE I. Solvation energies of Ak atoms and ions, sinking energy of the Ak⁺ ion, and radius of the first solvation shell corresponding to the ⁴He₂₀₀₀ droplet; see Eqs. (7) and (8) and the related text for definitions.

	S _{Ak} (K)	S _{Ak⁺} (K)	E _{sink} (K)	r ₁ (Å)
Li	-10.1	-7188.9	7007.7	3.5
Na	-9.6	-4627.4	4461.2	3.8
K	-10.4	-3465.6	3329.4	4.3
Rb	-11.4	-3254.9	3119.7	4.5
Cs	-10.8	-3013.4	2980.8	4.8

to clearly assess the solid-like or liquid-like character of the structure around the cation, one should also consider the dynamical behavior of the helium atoms. This is beyond the capabilities of the ⁴He-DFT approach, but could be addressed by more fundamental methods, such as path integral Monte Carlo (PIMC).^{30,31}

As will be discussed below, density functional calculations of ⁴He samples hosting very attractive impurities, such as cations, yield very structured helium densities displaying high density “blobs” in the vicinity of the cation; depending on the impurity, these blobs have a clearly identifiable symmetry, e.g., icosahedral for the case of Be⁺.²⁹ Although one might be tempted to interpret these blobs as representing actual helium atoms, it should be kept in mind that what ⁴He-DFT yields is the helium density $\rho(\mathbf{r})$, i.e., the squared order parameter $|\Psi(\mathbf{r})|^2$. It would be misleading to associate a helium atom with each blob in the structure. However, to the extent that these density blobs are separated by quasi-zero helium density regions, they can be taken as an indication that the corresponding shell is quasi-rigid, i.e., solid-like.

Several quantities of interest can be obtained from the static ⁴He-DFT calculations. In particular, the energy available in the sinking process, i.e., the difference between the initial total energy at the ionization time and the one at Ak⁺@⁴He_N equilibrium, is

$$E_{\text{sink}}(\text{Ak}^+ @ ^4\text{He}_N) = E_{\text{dim}}(\text{Ak}^+ @ ^4\text{He}_N) - E_{\text{bulk}}(\text{Ak}^+ @ ^4\text{He}_N), \quad (7)$$

where E_{dim} is the energy of the initial Ak⁺@⁴He_N complex where the ion just replaced the neutral atom at the dimple position and E_{bulk} is the energy of the relaxed Ak⁺@⁴He_N system. These energies are collected in Table I for all Ak cations and $N = 2000$. They are very high, increasing from 2981 K for Cs⁺ to 7008 K for Li⁺. This shows that ion sinking is a very energetic process, which will generate

strong excitations in the helium droplet. Another relevant quantity, also collected in Table I, is the solvation energy S_X of the Ak atoms and of the Ak⁺ ions into a ⁴He_N droplet, defined as

$$S_X = E(X @ ^4\text{He}_N) - E(^4\text{He}_N). \quad (8)$$

All these quantities depend on N and on the functional used to obtain them, so minor differences may be found with former published values. As an illustration of the size dependence, we have obtained $S_{\text{Na}} = -10.4$ K, $S_{\text{Na}^+} = -4673.5$ K, and $E_{\text{sink}} = 4496.2$ K for a Na⁺@⁴He₅₀₀₀ droplet to be compared to the values in Table I for $N = 2000$. We have also calculated the value of S_{Na} for the free surface of superfluid helium, which corresponds to the asymptotic $N \rightarrow \infty$ limit: $S_{\text{Na}} = -10.7$ K.

Also shown in Table I is the radius of the first solvation shell, r_1 , defined as the location of the first minimum of the density profile when the cation is at the droplet center. It is used to compute the He atom content n_1 of the first (spherically averaged) solvation shell by integrating the He density profile from the location of the Ak⁺ ion equilibrium position, $r = 0$, to $r = r_1$.

An extensive compilation of the size of snowballs and other energetically favorable structures around a wide variety of ions can be found in Tables I and II of Ref. 4. Table II here compares the values for Ak⁺ cations obtained in the present work with the ones calculated by different authors using other approaches: These may refer to anomalies in computed dissociation energies or to sizes at which radial distribution functions or other measures indicate closure of a solvation shell.⁴ As can be seen in Table II, ⁴He-DFT tends to overestimate the number of ⁴He atoms in the first solvation shell.

Let us comment some of the results displayed in Table II. The helium-Ak⁺ interaction is usually taken as a sum of pairwise potentials.^{5,30,32-40} The attractive part of this two-body (2B) interaction is dominated by the interaction between the ion charge and the induced dipole in the He atom, $V_{qd}(r) = -q^2\alpha_{\text{He}}/(2r^4)$ (in atomic units), with q being the ion charge and α_{He} being the He atom polarizability. However, several studies⁴¹⁻⁴⁴ have also taken into account non pairwise additive interactions—denoted here as three-body (3B) contributions—arising from induced dipoles interacting between themselves. It has been argued⁴¹ that these 3B interactions could be responsible for the overestimation of the size of the Na⁺ first solvation shell by simulations including only 2B interactions, compared to the experimental results of An der Lan *et al.*¹¹ This

TABLE II. Number of He atoms in the first solvation shell n_1 and of other energetically favorable structures around Ak⁺ ions obtained with different *static* theoretical approaches in the indicated references (p.w.: present work). PIMC: path integral Monte Carlo; PIGSMC: path integral ground-state Monte Carlo; SWF-VMC: shadow wave function variational Monte Carlo; DMC: diffusion Monte Carlo; DFT: ⁴He-DFT; Class-sim.: classical simulation method; and BH-DMC/PIMC: basin-hopping DMC/PIMC.

	PIMC	PIGSMC ³⁰	SWF-VMC	DMC ³³	DFT	Class-sim. ³⁶	BH-DMC/PIMC
Li ⁺		8.2		6, 10	12 ^(p.w.)		4, 6, 8; ⁴² 5, 6, 8, 10 ⁴⁴
Na ⁺	12; ³² 16; ³⁴ 10 ⁴¹	12	9; ³⁸ 12 ³⁵		14 ¹⁴ (p.w.)		12 ⁴⁴
K ⁺	15 ³²		12; ³⁸ 15 ³⁵		17 ^(p.w.)	15	15 ⁴⁴
Rb ⁺					19; ⁵ 18 ^(p.w.)		
Cs ⁺	18 ³²		17.5 ³⁵		21 ⁵ (p.w.)		12, 17 ³⁷

claim is disputed by other theorists. While it is acknowledged that including 3B effects usually decreases the binding energy of the system and, consequently, the evaporation energies, it has been found that it does not alter the general picture, i.e., the relative stability of the configurations appears to be unchanged.^{42,43} In particular, the first shell closure was found at the same number of helium atoms (see, e.g., Fig. 7 of Ref. 42 for Li⁺ and Fig. 4, left, of Ref. 43 for Pb²⁺). It was also concluded⁴⁴ that the structural observables are essentially unaffected by 3B corrections, and therefore, the results on cluster structuring evolution remained reliable when one only uses the 2B potential.

An interesting point discussed by Galli *et al.*³² is the influence of Bose statistics on the structure of X⁺@He_N systems. They have compared PIMC simulations of doped droplets with or without sampling permutations between ⁴He atoms in the X⁺@⁴He₆₄ system with X = Na or Mg. While the effect of bosonic exchange on energies was found to be significant, the density profile around Na⁺ and Mg⁺ remained unaffected (see Fig. 3 in that reference) and not only in the first solvation shell where it might have been expected due to its solid-like character. It is worth mentioning that boson exchanges are not considered in the PIMC calculations of Ref. 41 and that when only 2B interactions are considered, they find the same size for the first solvation shell of Na⁺ as the PIMC calculations, which include them.³² Unfortunately, we cannot determine the relative importance of 3B and permutation statistics effects on the energetics and morphology of these systems from the published results.

Two different strategies are usually applied by theoreticians to determine the size of snowballs: either simulate ionic systems with a number of ⁴He atoms substantially larger than the snowball^{30,32} and deduce snowball sizes from integrated densities or add ⁴He atoms “one by one” to the ion^{36,41–43} and deduce them from the relative stability of the Ak⁺-He_n complexes. For some Ak⁺, a number of the latter calculations have been stopped before reaching the first solvation shell closure.^{39,40}

TABLE III. Total energy E_n , dissociation energy D_n , and second energy difference Δ_2 of some Na⁺@⁴He_n complexes; see Eqs. (9) and (10) and the related text.

n	E_n (K)	D_n (K)	Δ_2 (K)
2	-648.49		
3	-972.64	324.2	1.9
4	-1294.92	322.3	8.4
5	-1612.56	317.6	8.4
6	-1921.77	309.2	13.4
7	-2217.55	295.8	21.2
8	-2492.14	274.6	23.8
9	-2742.92	250.8	32.4
10	-2961.35	218.4	38.3
11	-3141.45	180.1	42.2
12	-3279.34	137.9	44.0
13	-3373.23	93.9	43.6
14	-3423.51	50.3	24.1
15	-3449.73	26.2	1.1
16	-3474.87	25.1	

The ⁴He-DFT method used in this work pertains to the first strategy. In order to compare with the second one, we have also carried out static calculations for Na⁺@⁴He_n complexes, $n = 2$ to 16. The resulting total energies $E_n = E(\text{Ak}^+@^4\text{He}_n)$ are collected in Table III, together with the dissociation (or evaporation) energies D_n and second energy differences $\Delta_2(n)$ defined as

$$D_n = E_{n-1} - E_n, \quad (9)$$

$$\Delta_2(n) = D_n - D_{n+1} = E_{n+1} - 2E_n + E_{n-1}. \quad (10)$$

Local maxima of $\Delta_2(n)$ are expected to characterize the most stable configurations, some of them corresponding to solvation shell closures. The results in Table III illustrate the difficulties in using a single criterion for determining the closure of the first solvation shell. The maximum of the second energy difference Δ_2 points to $n = 12$ –13 as the maximum number of He atoms in the first solvation shell, with a strong decrease for $n = 14$ down to a very small Δ_2 value for $n = 15$. At variance, direct integration of the spherically averaged density up to r_1 yields $n_1 = 14$, as in Ref. 14. Hence, the two criteria (energetics and density integration) fairly agree but not necessarily coincide.

Table II also reveals that no structure is particularly stable below n_1 within the ⁴He-DFT approach. This is due to the fluid-like character of the ⁴He-DFT description of the system. Yet, a plot of Δ_2 vs n exhibits some anomalies around $n = 4$ –5 and around $n = 7$ –8, indicating that energetically favorable structures might show up around these n values. Atomic resolved calculations, such as the ones referred to above, are inherently well suited to handle these structures and determine the most stable complexes. Experimentally, they can be determined as local anomalies in the Ak⁺He_n ion yields in mass spectrometry experiments.¹¹

B. Dynamics

The sinking dynamics was triggered by substituting the Ak-He pair potential with that of the Ak⁺-He pair in the Ak@⁴He₂₀₀₀ equilibrium configuration of Fig. 1.⁵ The simulations then proceeded as explained in Sec. II and were conducted for about $t_{\text{sim}} = 100$ ps; see Table IV. Note that the simulation time is shorter for Li⁺ than for the other ions. The much stronger He-Li⁺ attraction (the He-Li⁺ well depth is more than double the one of the next largest well depth, that of He-Na⁺; see Fig. 2), combined with the light mass of the cation, required a much smaller time step for the dynamics, which

TABLE IV. Number of emitted He atoms ΔN for the duration t_{sim} of the dynamics simulation of Ak⁺ ions sinking in a ⁴He₂₀₀₀ droplet. Also given is the slope of the $n(t) = At$ law; see the text for explanation.

	t_{sim} (ps)	ΔN	A (ps ⁻¹)
Li ⁺	44	40	[1.46, 1.46]
Na ⁺	100.8	63	[0.79, 0.74]
K ⁺	100.8	63	[0.67, 0.50]
Rb ⁺	100.8	80	[0.81, 0.61]
Cs ⁺	100.8	75	[0.74, 0.67]

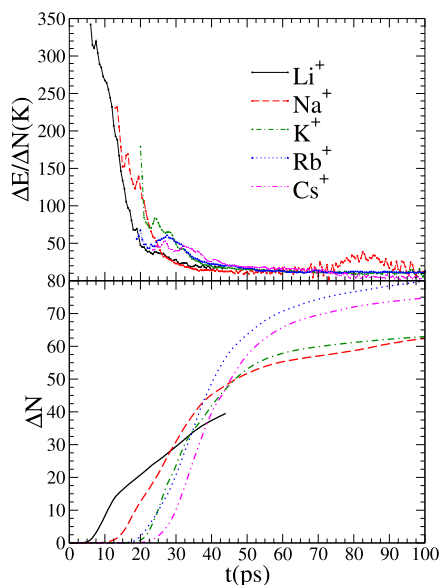


FIG. 3. Droplet relaxation by helium atom ejection during the sinking dynamics of Ak⁺@⁴He₂₀₀₀. Top plot: Time evolution of the average energy dissipated per ejected atom, $\Delta E/\Delta N$ (see the text for definition). Bottom plot: Number ΔN of ejected He atoms as a function of time.

could not be run for much longer times within reasonable computing time cost. Yet, the simulation time is long enough to observe its sinking.

As mentioned in Sec. III A, the available energy during the sinking process (E_{sink} in Table I) is very high. Therefore, extensive helium atom ejection (the only energy dissipation mechanism by the droplet in our approach) is expected. The number of ejected atoms ΔN as

well as the average dissipated energy per ejected atom $\Delta E/\Delta N$ are calculated as a function of time as follows:

$$\Delta N(t) = N - \langle |\Psi(\mathbf{r}, t)|^2 \rangle, \quad (11a)$$

$$\frac{\Delta E}{\Delta N} = - \frac{(\Delta E/\Delta t)}{(\Delta N/\Delta t)}. \quad (11b)$$

They are represented in Fig. 3 for all alkali ions. The time interval Δt was set at 0.5 ps, and a three-point formula was used to calculate $\Delta E/\Delta t$ and $\Delta N/\Delta t$ in order to minimize unavoidable fluctuations. The $\Delta E/\Delta N$ curves start at the time at which about one atom has been emitted. It is worth noting that because of the way $\Delta N(t)$ is calculated [by subtracting the integrated helium density remaining in the simulation box from the initial number of atoms, first Eq. (11a)], emitted helium atoms (or rather, density) are only accounted for when they reach the absorption buffer of the box, which inevitably adds a delay. The numbers of emitted He atoms ΔN at the end of each simulation are collected in Table IV.

As can be seen in Fig. 3, the time evolution of the number of emitted atoms follows the same behavior for all alkalis: first a fast increase after a variable time delay and then a slower increase. In addition, despite the large differences in He–Ak⁺ interactions (well depth V_{min} and equilibrium distance $R_{V_{min}}$; see the inset in Fig. 2), the time evolution of $\Delta E/\Delta N$ is remarkably similar for all alkalis. The first emitted atoms, $t \lesssim 20$ ps, have a rather high kinetic energy, up to 300–350 K for Li⁺ in the first 10 ps. This is much higher than 7 K corresponding approximately to the extraction energy of one helium atom in bulk liquid helium in thermodynamic equilibrium at zero temperature and pressure. These highly energetic and promptly emitted atoms constitute a significant proportion of the emitted helium atoms. This shows that estimating the number of emitted atoms by dividing the overall excitation energy by 7 K can give a very rough result: promptly emitted helium atoms can be, and usually are, very energetic. The energy dissipated per atom

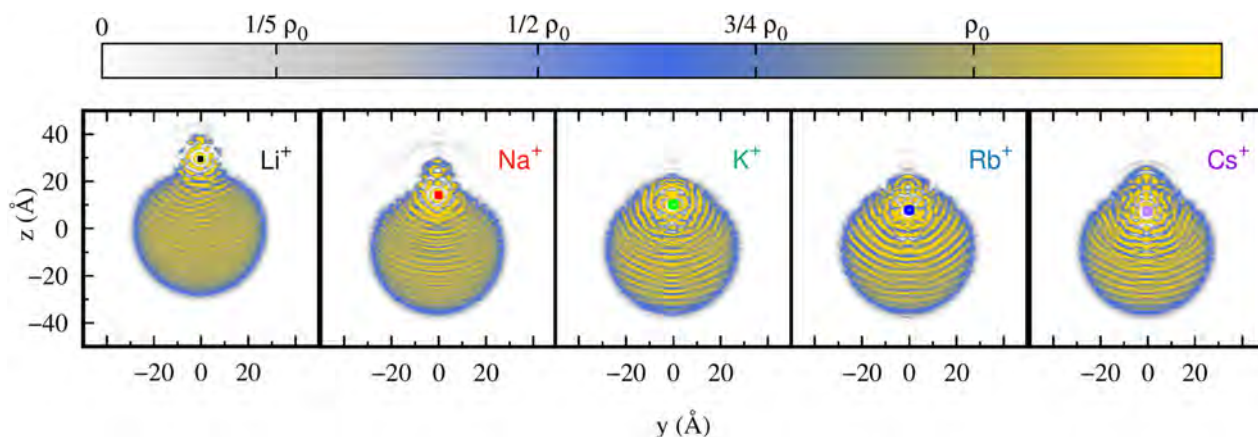


FIG. 4. Ion location and helium density (two-dimensional cut in a symmetry plane) after $t = 20$ ps of Ak⁺ sinking in a ⁴He₂₀₀₀ nanodroplet. The density scale on top is given in units of ρ_0 , which is the bulk superfluid density at zero temperature and pressure ($\rho_0 = 0.0218 \text{ \AA}^{-3}$). Individual movies presenting the time evolution of the 2D cuts side by side with that of the spherically averaged density profile (see Fig. 5) are presented as the supplementary material for each Ak⁺.

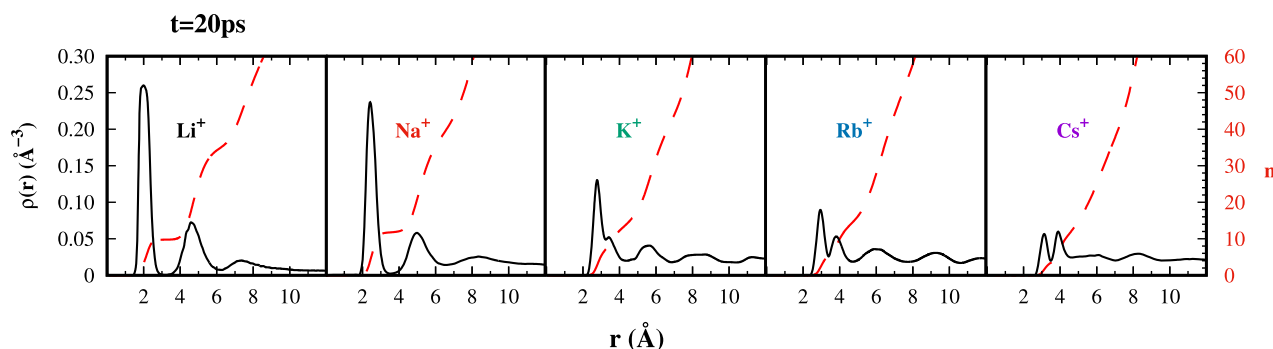


FIG. 5. Spherically averaged density profile (black solid line, left vertical scale) and the number of He atoms $n(r)$ as a function of the distance to the ion (red dashed line, right vertical scale) after $t = 20$ ps of Ak⁺ sinking in a ⁴He₂₀₀₀ nanodroplet. Individual movies presenting the time evolution of the spherically averaged density profile side by side with that of 2D cuts (see Fig. 4) are presented as the supplementary material for each Ak⁺.

then slowly decreases to about 10 K or below for $40 \lesssim t \lesssim 100$ ps. This common asymptotic behavior is expected since it is close to the helium atom evaporation regime where each atom dissipates the equivalent of its binding energy to the droplet, about 7 K. It is remarkable that an evaporation-like regime can be attained in several tens of picoseconds, given the amount of energy initially present in the system. The only notable difference between alkalis is the value of $\Delta E/\Delta N$ at the beginning of the solvation dynamics and the time it takes for the equivalent of the first atom to be emitted. The lighter alkalis, especially Li⁺, give rise to very energetic helium atoms, which appear earlier, presumably because they are faster in reaching the absorption buffer of the simulation box where they are detected.

Finally, there is a peculiar oscillation between 75 and 90 ps for Na⁺. Examination of the movies introduced in the next paragraph shows that this oscillation coincides with the eruption of energetic helium atoms on the opposite side of the sinking: this usually results from the creation of a traveling surface wave at the

sinking point, which propagates on the droplet surface until collapsing at the opposite point from its creation, then producing a helium atom burst.

Movies illustrating the sinking dynamics for each Ak⁺ cation are provided in the supplementary material. Two panels are displayed. The one on the left hand side shows the time evolution of the ion position inside the helium droplet, represented as a two-dimensional (2D) cut of the density in a symmetry plane. The one on the right hand side depicts the time evolution of the spherically averaged helium density profile around Ak⁺ as a function of the distance r to the cation. The latter movie is particularly appealing as it shows the dynamical formation of the solvation shells and their contents.

The snapshots corresponding to $t = 20$ ps are shown in Fig. 4 (Ak⁺ position in a 2D-cut through the helium density) and Fig. 5 (spherically averaged density profile around Ak⁺). At that time, the first solvation shell is already well in place for the lighter alkalis (Li⁺, Na⁺), but not for the heavier ones (K⁺, Rb⁺ and Cs⁺), as can be

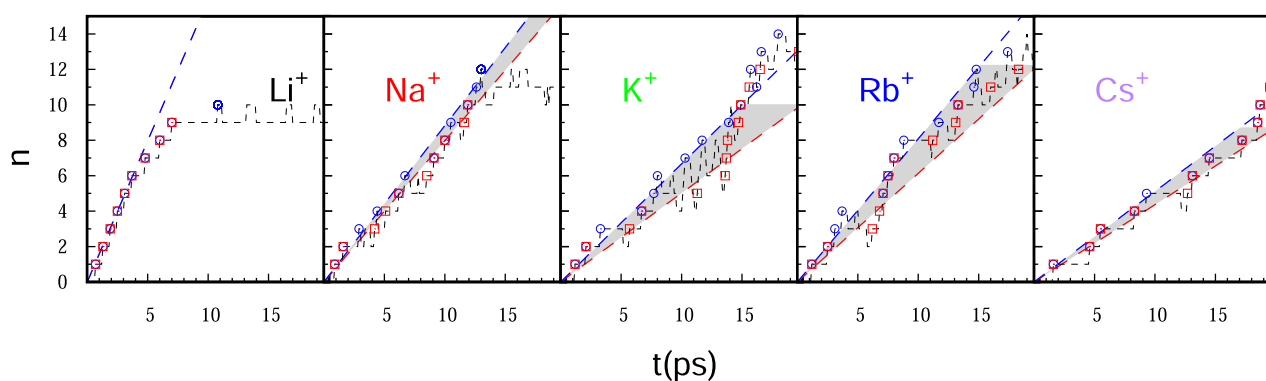


FIG. 6. Number of He atoms n around the Ak⁺ ions as a function of t for Ak⁺@⁴He₂₀₀₀. Open blue circles correspond to the first time at which the number of He atoms is equal to the integer value n , whereas open red squares mark the first time it reaches n with no more fluctuations back to $(n-1)$. The lines are the best linear fits $n(t) = At$ (a hint pointing to a Poissonian capture process) for the Ak⁺@He _{n} complexes up to $n = 5$ for each definition. The shadowed regions between the two lines give an idea of the uncertainty on the rates obtained within the ⁴He-TDDFT approach. See the text for more details.

seen by the separation of the first density peak from the rest of the spherically averaged density. This is remarkable since as can be seen in Fig. 4, the ions are already well within the bulk of the droplet. This difference is presumably due to the much deeper He–Li⁺ and He–Na⁺ interaction potential well.

As can be seen from the movies, the droplets are still rather excited at the end of the simulations. They are far from their final equilibrium configuration, which corresponds to an Ak⁺ ion at rest at the center of the remaining ⁴He_M spherical droplet (with $M < 2000$). A sizable part of the excitation energy remains in the droplet in the form of density waves and large amplitude surface modes, plus some kinetic energy in the ion and in the droplet itself. The absence of viscosity implies that the excitation energy can only be dissipated by atom evaporation.

C. Comparison with experiment

In the experiment by Albrechtsen *et al.* recalled in the Introduction,¹⁴ the first step consists in ionizing the Ak atom attached to a helium droplet doped with a xenon atom. In the work presented here, there is no xenon atom at the droplet center. However, due to the droplet size, the interaction of the sinking Ak⁺ ion with a neutral impurity residing in the bulk of the droplet is very small during the first picoseconds of the pump process and can be neglected. Hence, our simulations sensibly represent the pump process. Even though we have not yet conducted the more demanding simulation of the whole pump–probe process, the comparison of the ion solvation rate $n(t)$ reported in Fig. 6 and Table IV with experimental results should already be meaningful, at least at short times.

Due to the strong Ak⁺–He interaction, the first n He atoms attached to the ion during the first stages of the sinking process are expected to remain tightly bound to it during the Coulomb repulsion process and lead to the detection of Ak⁺@⁴He_{*n*}, as explicitly shown in the Na⁺ case.¹⁴ Within the ⁴He–DFT approach, this number has been obtained by integrating the spherically averaged helium density profile inside the first solvation sphere of radius r_1 around the Ak⁺ ion. Figure 6 displays the time-dependence of n for all alkalis. This number sometimes fluctuates back and forth by ± 1 with time. Open blue circles correspond to the first time at which an integer number of atoms $n = 1, 2, 3, \dots$ is attached to the cation. Open red squares correspond to the time starting from which this number no longer fluctuates back to $n - 1$. As can be seen from Fig. 6, the time-dependence of n is linear during the first picoseconds, pointing to a Poissonian capture process in which the helium atoms bind independently of each other and with a constant rate.¹⁴ This is especially true for the more attractive Li⁺ and Na⁺ cations.

For each alkali ion, we have fitted $n(t)$ to a linear form $n(t) = At$ for n up to 5; the parameter A can be identified with the binding rate. Each fit was performed twice, once for each definition of $n(t)$ discussed in the preceding paragraph, the first definition (the first time the integrated density in the solvation sphere reaches n) yielding a larger value of A than the second one (the first time it reaches n with no more fluctuations back to $n - 1$). Both A values are reported in between brackets in Table IV and plotted as straight, dashed lines in Fig. 6 (blue or red for the first or second definition, respectively). The shadowed regions between the two lines in the panels of Fig. 6 give an idea of the uncertainty on the rates obtained

within the ⁴He–TDDFT approach. Table IV shows that the binding rate A is very similar for all alkalis, except for Li⁺ for which it is much larger. This is due to the combination of two effects, namely, a deeper dimple for neutral Li together with a stronger Li⁺–He attraction.

An interesting kinetic effect was found for the lighter alkalis: the ... number of He atoms in the first solvation shell at the end of the simulation is smaller than the one obtained from the static calculation (9 instead of 12 for Li⁺ and 12 instead of 14 for Na⁺). For the heavier alkalis, it is equal (17 for K⁺, 18 for Rb⁺, and 21 for Cs⁺). The reason why this occurs for the lighter alkalis and not for the heavier ones is unclear. It could be due to the fact that the first solvation shell is more rigid for the lighter alkalis, as can be seen by scrutinizing the density profiles at the end of the dynamics: the helium density does not go quite to zero between the first and the second solvation shell for the heavier alkalis. This is also true for the equilibrium structures shown in Fig. 2. This allows for continuous equilibration of the density between the first and the second shell. In contrast, the two shells are clearly separated in the equilibrium structure of the lighter alkali ions, and the isolation of the first density shells occurs before the end of the dynamics, around 20 ps for Li⁺ and 25–30 ps for Na⁺. After that, the integrated density (or number of helium atoms) inside the first solvation shells no longer varies.

IV. SUMMARY AND OUTLOOK

We have described the sinking of alkali ions Ak⁺ in a He droplet containing 2000 atoms using the ⁴He–TDDFT approach. The movies in the supplementary material as well as the energetics of the process (excitation energy) show that this corresponds to a rather violent dynamics for the droplet. This is confirmed by the high energy dissipated per ejected helium atom, especially in the first 10–20 ps. The time evolution of the droplet energy relaxation by helium atom emission is found to be remarkably similar between all alkalis, the most notable difference being the amount of energy dissipated per helium atom at the beginning of the dynamics, which is highest for the lightest alkali ions, Li⁺, followed by Na⁺, following the strength of decreasing He–Ak⁺ interaction. The first emitted helium atoms also appear earlier for Li⁺, which makes sense since they are also faster.

In order to relate our findings to the first experiment designed to unravel the primary steps of ion solvation in helium nanodroplets,¹⁴ we have determined the number of He atoms in the first solvation shell as a function of time. Our simulations show how these shells are dynamically built around the cation. The number of helium atoms inside the first solvation shell is found to linearly increase with time during the first stages of the process, in agreement with the linear behavior observed in the experiment on Na⁺,¹⁴ pointing to a Poissonian capture process.

Remarkably, we have found that the number of helium atoms in the first solvation shell is lower at the end of the (limited) dynamics than obtained at equilibrium for Li⁺ and Na⁺. This points to kinetic rather than thermodynamical control of the snowball size for small and strongly attractive ions.

The more demanding simulations of the full pump–probe processes are under progress.

SUPPLEMENTARY MATERIAL

We provide as the supplementary material one movie for each alkali ion, Ak⁺ ≡ Li⁺, Na⁺, K⁺, Rb⁺, and Cs⁺, illustrating the real-time simulations of the sinking of Ak⁺ ions addressed in this work. This multimedia material helps capture physical details that would be difficult to present and thoroughly describe in the main text. Two panels are displayed in each movie. The one on the left hand side shows the time evolution of the ion position inside the helium droplet, represented as a two-dimensional (2D) cut of the density in a symmetry plane, as shown in the snapshots of Fig. 4. The one on the right hand side depicts the time evolution of the spherically averaged helium density profile around Ak⁺ as a function of the distance *r* to the cation, as shown in the snapshots of Fig. 5. It is particularly appealing as it shows the dynamical formation of the solvation shells and their contents.

ACKNOWLEDGMENTS

A computer grant from the CALMIP high performance computer center (Grant No. P1039) is gratefully acknowledged. This work was performed under Grant No. PID2020-114626GB-I00 from MICIN/AEI/10.13039/501100011033 and benefited from COST Action CA21101 “Confined molecular systems: from a new generation of materials to the stars” (COSY) supported by COST (European Cooperation in Science and Technology).

AUTHOR DECLARATIONS

Conflict of Interest

The authors have no conflicts to disclose.

Author Contributions

Ernesto García-Alfonso: Conceptualization (equal); Data curation (lead); Formal analysis (equal); Funding acquisition (supporting); Investigation (equal); Methodology (equal); Project administration (supporting); Resources (equal); Software (equal); Supervision (supporting); Validation (equal); Visualization (lead); Writing – original draft (equal); Writing – review & editing (equal). **Manuel Barranco:** Conceptualization (equal); Data curation (supporting); Formal analysis (equal); Funding acquisition (equal); Investigation (equal); Methodology (equal); Project administration (equal); Resources (equal); Software (equal); Supervision (equal); Validation (equal); Visualization (supporting); Writing – original draft (equal); Writing – review & editing (equal). **Nadine Halberstadt:** Conceptualization (equal); Data curation (supporting); Formal analysis (equal); Funding acquisition (equal); Investigation (equal); Methodology (equal); Project administration (equal); Resources (equal); Software (equal); Supervision (equal); Validation (equal); Visualization (supporting); Writing – original draft (equal); Writing – review & editing (equal). **Martí Pi:** Conceptualization (equal); Data curation (supporting); Formal analysis (equal); Funding acquisition (equal); Investigation (equal); Methodology (equal); Project administration (equal); Resources (equal); Software (equal); Supervision (equal); Validation (equal); Visualization (supporting); Writing – original draft (equal); Writing – review & editing (equal).

DATA AVAILABILITY

The data that support the findings of this study are available from the corresponding author upon reasonable request.

REFERENCES

- B. Tabbert, H. Günther, and G. zu Putlitz, *J. Low Temp. Phys.* **109**, 653 (1997).
- S. L. Fiedler, D. Mateo, T. Aleksanyan, and J. Eloranta, *Phys. Rev. B* **86**, 144522 (2012).
- W. Wei, Z. Xie, L. N. Cooper, G. M. Seidel, and H. J. Maris, *J. Low Temp. Phys.* **178**, 78 (2015).
- T. González-Lezana, O. Echt, M. Gatchell, M. Bartolomei, J. Campos-Martínez, and P. Scheier, *Int. Rev. Phys. Chem.* **39**, 465 (2020).
- A. Leal, D. Mateo, A. Hernando, M. Pi, M. Barranco, A. Ponti, F. Cargnoni, and M. Drabbels, *Phys. Rev. B* **90**, 224518 (2014).
- D. Mateo, A. Leal, A. Hernando, M. Barranco, M. Pi, F. Cargnoni, M. Mella, X. Zhang, and M. Drabbels, *J. Chem. Phys.* **140**, 131101 (2014).
- X. Zhang and M. Drabbels, *J. Chem. Phys.* **137**, 051102 (2012).
- S. Müller, M. Mudrich, and F. Stienkemeier, *J. Chem. Phys.* **131**, 044319 (2009).
- J. Tiggesbäumker and F. Stienkemeier, *Phys. Chem. Chem. Phys.* **9**, 4748 (2007).
- O. Bünermann, G. Droppelmann, A. Hernando, R. Mayol, and F. Stienkemeier, *J. Phys. Chem. A* **111**, 12684 (2007).
- L. An der Lan, P. Bartl, C. Leidlmair, R. Jochum, S. Denifl, O. Echt, and P. Scheier, *Chem. – Eur. J.* **18**, 4411 (2012).
- M. Theisen, F. Lackner, and W. E. Ernst, *Phys. Chem. Chem. Phys.* **12**, 14861 (2010).
- M. Theisen, F. Lackner, and W. E. Ernst, *J. Chem. Phys.* **135**, 014861 (2011).
- S. H. Albrechtsen, C. A. Schouder, A. Viñas-Muñoz, J. K. Christensen, C. Engelbrecht Petersen, M. Pi, M. Barranco, and H. Stapelfeldt, *Nature* **623**, 319 (2023).
- Y. Markus, *Ions in Solution and Their Solvation* (Wiley, 2015), Chap. 4, p. 107.
- F. Ancilotto, M. Barranco, F. Coppens, J. Eloranta, N. Halberstadt, A. Hernando, D. Mateo, and M. Pi, *Int. Rev. Phys. Chem.* **36**, 621 (2017).
- M. Pi, F. Ancilotto, F. Coppens, N. Halberstadt, A. Hernando, A. Leal, D. Mateo, R. Mayol, and M. Barranco, ⁴He-DFT BCN-TLS: A computer package for simulating structural properties and dynamics of doped liquid helium-4 systems, <https://github.com/bcntls2016/>.
- F. Dalfovo, A. Lastrì, L. Pricaupeko, S. Stringari, and J. Treiner, *Phys. Rev. B* **52**, 1193 (1995).
- M. Barranco, R. Guardiola, S. Hernández, R. Mayol, J. Navarro, and M. Pi, *J. Low Temp. Phys.* **142**, 1 (2006).
- M. Barranco, F. Coppens, N. Halberstadt, A. Hernando, A. Leal, D. Mateo, R. Mayol, and M. Pi, Zero temperature DFT and TDDFT for ⁴He: A short guide for practitioners, <https://github.com/bcntls2016/DFT-Guide/blob/master/dft-guide.pdf>.
- F. Ancilotto, M. Barranco, F. Caupin, R. Mayol, and M. Pi, *Phys. Rev. B* **72**, 214522 (2005).
- S. H. Patil, *J. Chem. Phys.* **94**, 8089 (1991).
- A. D. Koutselos, E. A. Mason, and L. A. Viehland, *J. Chem. Phys.* **93**, 7125 (1990).
- M. Frigo and S. G. Johnson, *Proc. IEEE* **93**, 216 (2005).
- F. Coppens, F. Ancilotto, M. Barranco, N. Halberstadt, and M. Pi, *Phys. Chem. Chem. Phys.* **21**, 17423 (2019).
- A. Ralston and H. S. Wilf, *Mathematical Methods for Digital Computers* (John Wiley and Sons, New York, 1960).
- D. Mateo, D. Jin, M. Barranco, and M. Pi, *J. Chem. Phys.* **134**, 044507 (2011).
- E. García-Alfonso, F. Coppens, M. Barranco, M. Pi, F. Stienkemeier, and N. Halberstadt, *J. Chem. Phys.* **152**, 194109 (2020).
- F. Ancilotto, M. Pi, R. Mayol, M. Barranco, and K. K. Lehmann, *J. Phys. Chem. A* **111**, 12695 (2007).

- ³⁰S. Paolini, F. Ancilotto, and F. Toigo, *J. Chem. Phys.* **126**, 124317 (2007).
- ³¹F. Briec, C. Schran, and D. Marx, *Phys. Rev. Res.* **5**, 043083 (2023).
- ³²D. E. Galli, D. M. Ceperley, and L. Reatto, *J. Phys. Chem. A* **115**, 7300 (2011).
- ³³C. Di Paola, F. Sebastianelli, E. Bodo, I. Baccarelli, F. A. Gianturco, and M. Yurtsever, *J. Chem. Theory Comput.* **1**, 1045 (2005).
- ³⁴A. Nakayama and K. Yamashita, *J. Chem. Phys.* **112**, 10966 (2000).
- ³⁵M. Rossi, M. Verona, D. E. Galli, and L. Reatto, *Phys. Rev. B* **69**, 212510 (2004).
- ³⁶E. Yurtsever, E. Yildirim, M. Yurtsever, E. Bodo, and F. A. Gianturco, *Eur. Phys. J. D* **43**, 105 (2007).
- ³⁷R. Pérez de Tudela, P. Martini, M. Goulart, P. Scheier, F. Pirani, J. Hernández-Rojas, J. Bretón, J. Ortiz de Zárate, M. Bartolomei, T. González-Lezana, M. I. Hernández, J. Campos-Martínez, and P. Villarreal, *J. Chem. Phys.* **150**, 154304 (2019).
- ³⁸D. E. Galli, M. Buzzacchi, and L. Reatto, *J. Chem. Phys.* **115**, 10239 (2001).
- ³⁹F. Sebastianelli, E. Bodo, I. Baccarelli, C. Di Paola, F. A. Gianturco, and M. Yurtsever, *Comput. Mater. Sci.* **35**, 261 (2006).
- ⁴⁰E. Coccia, E. Bodo, F. Marinetti, F. A. Gianturco, E. Yildirim, M. Yurtsever, and E. Yurtsever, *J. Chem. Phys.* **126**, 124319 (2007).
- ⁴¹N. Issaoui, K. Abdessalem, H. Ghalla, S. J. Yaghmour, F. Calvo, and B. Oujia, *J. Chem. Phys.* **141**, 174316 (2014).
- ⁴²M. Rastogi, C. Leidlmair, L. An der Lan, J. Ortiz de Zárate, R. Pérez de Tudela, M. Bartolomei, M. I. Hernández, J. Campos-Martínez, T. González-Lezana, J. Hernández-Rojas, J. Bretón, P. Scheier, and M. Gatchell, *Phys. Chem. Chem. Phys.* **20**, 25569 (2018).
- ⁴³P. Slavíček and M. Lewerenz, *Phys. Chem. Chem. Phys.* **12**, 1152 (2010).
- ⁴⁴F. Marinetti, E. Coccia, E. Bodo, F. A. Gianturco, E. Yurtsever, M. Yurtsever, and E. Yildirim, *Theor. Chem. Acc.* **118**, 53 (2007).

 CHAPTER V

AK₂ COULOMB EXPLOSION ON A ⁴HE NANODROPLET

V-1. Introduction

Previous studies have shown that alkali (Ak) atoms remain at the surface of helium nanodroplets (HNDs) [87] causing a small depression in the smooth density profile of the helium surface known as “dimple” as also mentioned in the preceding chapter. Ak dimers [92-95] and trimers [92,96,97] on helium drops have also been the focus of many researches since 1995 when they were first reported by Stienkemeier *et al.* [92]. After impacting the drop, Ak atoms eventually meet on their surface and form the diatomic Ak₂ molecule. Depending on the initial relative orientation of the electronic spins of the atoms, either the singlet (antiparallel) or the triplet (parallel) ground state is formed. Statistically, the triplet to singlet ratio should be 3 : 1 (from spin statistics). However, a ratio of 90 : 1 has been detected in Ref [98] for a mean droplet size between 5000 and 20 000 and a ratio of 50 : 1 for larger ⁴He droplets. The difference with the expected statistical ratio was attributed to the mechanism of cluster stabilization in HNDs. Dissipation of the binding energy of the dimer induces evaporation of helium atoms, until the doped droplet temperature has re-equilibrated to 0.4 K. The larger binding energy

of the singlet state (232.07 K and 8490.94 K for Na₂ triplet and singlet state, respectively) may cause the desorption of the alkali molecule or the deviation of the droplet off the beam axis, or even the complete evaporation of the smaller droplets. Hence, droplets doped with Ak₂ in the triplet state would be more likely to be detected than those with Ak₂ in the singlet state.

V-1.1. Coulomb explosion as a tool to differentiate singlet from triplet Ak₂

Stapelfeldt's group estimated the abundance ratio of triplet to singlet state Ak₂ [99] formed on the surface of a helium nanodroplet for Ak=Li, Na, Rb and Cs using Coulomb explosion. Coulomb explosion is an ideal technique for studying the structure of small molecules [100,101], and thus to measure the bond length distribution of the diatomics, and to be able to differentiate the triplet from singlet state Ak₂ based on the difference in equilibrium distance ($r_{\text{eq}} = 5.2$ and 3.072 Å for Na₂ triplet and singlet state respectively, see Annex D, Table D.3).

Coulomb explosion is ignited by doubly ionizing Ak₂@⁴He_N using an intense femtosecond laser pulse [102]. The Ak⁺ ions fly away from each other, their initial Coulomb potential energy turning into kinetic energy. The initial Ak₂ interatomic distance can be deduced from their final kinetic energy recorded when hitting the detector. Since the Ak₂ equilibrium distance is shorter in the singlet than in the triplet state, the final kinetic energy is expected to be higher for the former than for the latter. A kinetic energy distribution $P(E_{\text{kin}})$ was measured for each Ak⁺ fragment ions [100,101]. In a more recent publication [102] Stapelfeldt's group compared the internuclear distances distribution $P(r)$, retrieved by a transformation of the kinetic energy distributions $P(E_{\text{kin}})$, with the wave function density $|\Psi(r)|^2$ of the isolated dimer in its ground (singlet or triplet) electronic state. The wave function $\Psi(r)$ was computed theoretically by solving the Schrödinger equation. For the singlet and triplet states of Li₂, K₂ and Rb₂ the center of the $P(r)$ distribution was found to be displaced from the $|\Psi(r)|^2$ center, whereas in the case

Na₂ and Cs₂, only a small shift was observed. In all cases the P(r) distribution was significantly broader than $|\Psi(r)|^2$.

V-1.2. Dynamics simulation upon double ionization of Ak₂@⁴He_N

We have used ⁴He TD-DFT to conduct Coulomb explosion simulations in order to understand the effect of the HND over the Ak₂⁺⁺ (Li, Na, K, Rb, Cs) fragmentation dynamics. Here the use of ⁴He-TDDFT was required since the Coulomb explosion process was expected to transfer energy to the droplet modes, which need to be correctly described. In addition, the dimple in which Ak₂ is sitting previous to ionization is found to be important in the angular deviation, see section V-4.

In particular, we wanted to compare the importance of the shift and width of the kinetic energy distribution due to the presence of the droplet. Several parameters were examined such as: the droplet size effect (N=1000, 5000, up to 50 000 in one case), the zero point motion of the isolated Ak₂ in gas phase and the zero point orientational distribution of Ak₂ (φ) on the droplet surface. We also designed a model to estimate the influence of much larger droplets on the Coulomb explosion process.

Our simulations have revealed an interesting consequence of the presence of HND: the ions trajectories are bent because of the interaction with helium. This angular deviation is measurable and depends on several factors such as the Ak⁺- ⁴He_N interaction strength and the time of flight of the dopants, itself related to the initial bond length of the diatomic and to the ion mass. We are collaborating with the group of Stapelfeldt in order to verify if this serendipity result could be used to measure individual droplet sizes. Droplet size measurement has only been possible so far for very large droplets that can be visualized in single object X-ray diffraction (typically 10⁹ atoms or more). If this works, it would be the first possibility to measure droplet sizes from a few hundred atoms to several hundred thousand atoms.

V-1.3. An Experimental setup

The principle of Stapelfeldt's method, reported in Ref [99], consists in doubly ionizing alkali dimers by multiphoton absorption from an intense femtosecond laser pulse as illustrated in Fig. V.1 for Rb₂ in both equilibrium configurations: singlet ($X^1\Sigma_g^+$) or triplet ($a^3\Sigma_u^+$) state. The corresponding equilibrium distance, R_{eq} is 4.21 Å or 6.06 Å, respectively (see Annex D, Table D.3). Upon double ionization, the vibrational wave function of Rb₂ is projected onto the potential curve of Rb₂²⁺, thereby acquiring a potential energy $V_{\text{Coul}}(R_{\text{eq}}) = 3.42$ eV or 2.38 eV. The internal electrostatic repulsion of Rb₂²⁺ results in Coulomb explosion and conversion of $V_{\text{Coul}}(R_{\text{eq}})$ into kinetic energy, E_{kin} , of the Rb⁺ ion fragments, i.e. each Rb⁺ ion acquires a final kinetic energy E_{kin} equal to $\frac{1}{2}V_{\text{Coul}}(R_{\text{eq}})$. Experimentally, two distinct peaks were observed for E_{kin} , each one centered at a value close to that expected for the singlet or the triplet state, using a 2D velocity map imaging. See Figure V.2(ai)-(ei).

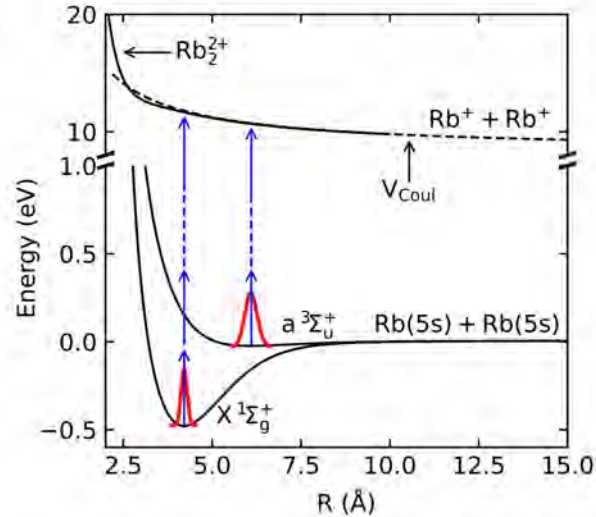


Figure V.1. Energy diagram of the Rb dimer showing the potential curves for the $X^1\Sigma_g^+$ and $a^3\Sigma_u^+$ states [27] and for Rb_2^{2+} [28]. The dashed curve depicts the Coulomb potential. The red shapes show the square of the wavefunction of the vibrational ground state in the X and a potentials. The blue vertical arrows represent the laser photons (not to scale) to illustrate the double ionization process that leads to Coulomb explosion into a pair of Rb⁺ ions. Figure taken from Ref [99].

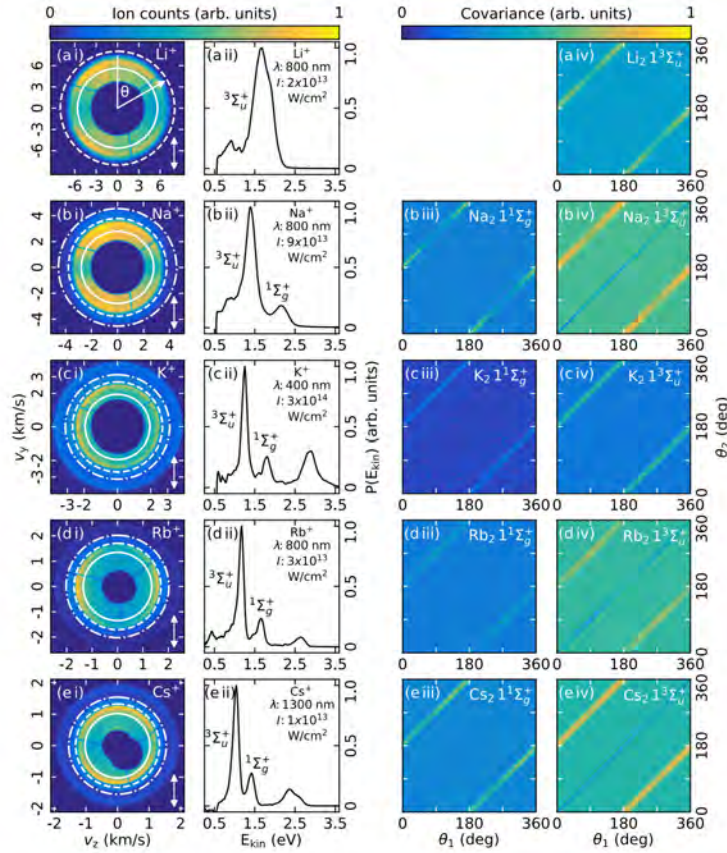


Figure V.2. (ai)-(ei) Two-dimensional velocity images of Ak⁺ ions. The white arrows in the bottom right corners indicate the polarization axis of the laser pulses. The annotated white rings designate the regions of the $1^3\Sigma_u^+$ and $1^1\Sigma_g^+$ channels. (a(ii)-(eii) Kinetic energy spectra of the respective Ak⁺ ions. Angular covariance maps are shown for the (b(iii)-(eiii) $1^1\Sigma_g^+$ and (a(iv)-(eiv) $1^3\Sigma_u^+$ channels. The T_{nozzle} was 11 K for the data in (a) and (b) and 12 K for the data in (c)-(e). Figure taken from Ref. [102]

The setup is similar to the typical setup described in chapter I, section I-5, with 5 μm diameter nozzle and background pressure $P_0=25$ bar and temperature $T_0=11$ -16K. The droplets travel through a pickup cell containing a gas of Rb atoms, see Fig. V.3(a). The Rb vapor pressure is adjusted such that some of the droplets pick up two Rb atoms, which leads to formation of Rb dimers on the droplet surfaces. Further downstream, inside a velocity map imaging (VMI) spectrometer, the doped droplet beam is crossed by a pulsed linearly polarized, focused laser beam. The Rb⁺ ions created by the laser pulses are projected by the VMI spectrometer onto a 2D imaging detector backed by a Charge-coupled device (CCD) camera.

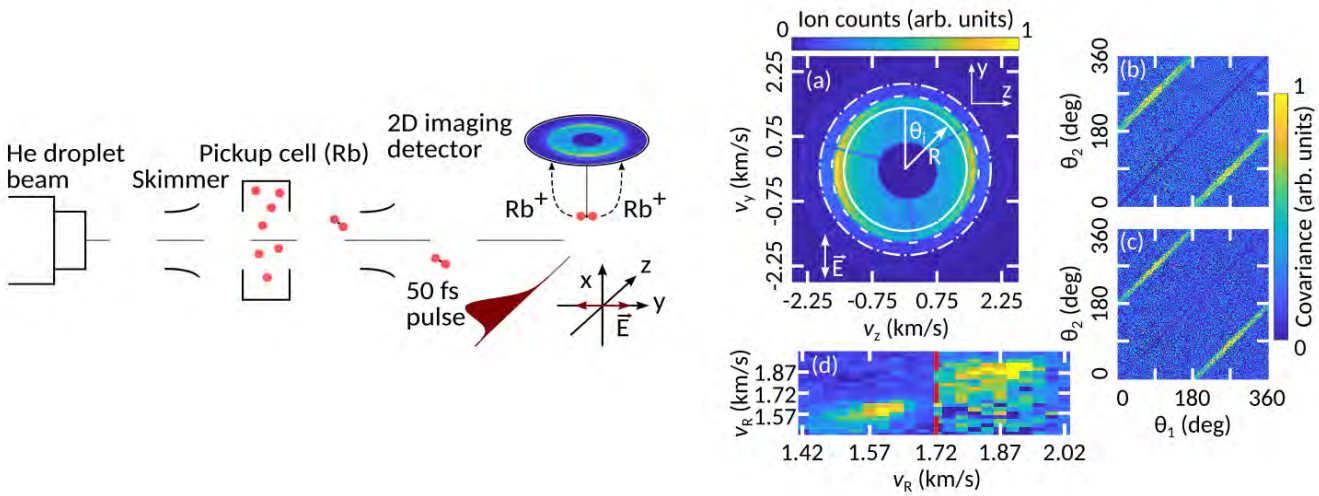


Figure V.3. Schematic of the key elements in the experiment (left). (a) 2D-velocity image of $^{85}\text{Rb}^+$ ions for $T_{\text{nozzle}} = 12$ K (right). The annotated white circles mark the regions of the inner and outer channel, see text. The polarization direction of the laser pulse is displayed in the bottom left corner. (c), (d) Angular covariance maps for the inner and the outer channels respectively. (e) Radial covariance map. The region after the red dashed line ($1.72\text{-}2.02$ km s^{-1}) has been saturated to highlight the presence of the outer channel. The color bar to the right applies to (c), (d) and (e). Courtesy of Henrik Høj Kristensen [99]

V-2. Method

We introduce here the details specific to the simulation of the Coulomb explosion of Ak₂ on a HND. In all the dynamics described in this chapter, double ionization is assumed to be instantaneous. The Ak₂@⁴He_N system is initially set at its equilibrium configuration obtained in the static simulations. The initial conditions (either singlet or triplet state) were deduced from the following Potential Energy Surface (PES): Li₂ [103], Na₂ [104], K₂ [105,106], Rb₂ [107,108] and Cs₂ [104].

V-2.1. ⁴He-TDDFT applied to Coulomb explosion

Coulomb explosion is triggered at time $t = 0$ by substituting each Ak atom by the corresponding Ak⁺ ion. The total energy of the system at zero temperature can then be written as

$$\begin{aligned}
E[\Psi, \mathbf{r}_{Ak_a^+}, \mathbf{r}_{Ak_b^+}] &= \int d\mathbf{r} \frac{\hbar^2}{2m_{\text{He}}} |\nabla \Psi|^2 + \int d\mathbf{r} \mathcal{E}_c(\rho) \\
&+ \sum_{\alpha=a}^b \left[\int d\mathbf{r} \rho(\mathbf{r}) V_{\text{He-Ak}^+}(|\mathbf{r} - \mathbf{r}_{Ak_\alpha^+}|) + \frac{1}{2} m_{\text{Ak}^+} \dot{\mathbf{r}}_{\text{Ak}_\alpha^+}^2 \right] \\
&+ V_{\text{Cb}}(|\mathbf{r}_{\text{Ak}_b^+} - \mathbf{r}_{\text{Ak}_a^+}|).
\end{aligned} \tag{V.1}$$

where both ions are treated classically.

The equations describing the dynamics of the system couple the equation for the time evolution the helium density with that for the (classical) alkali ions Ak_α^+ , $\alpha = a$ or b , like in Eq. II.22. The Ak^+ -He interaction $V_{\text{He-Ak}^+}$ is taken from Koutselos [109] and the Ak^+ - Ak^+ potential is taken as the charge-charge Coulombic interaction. The latter is modified by adding a volume effect term in order to take into account the overlap of the singly charged ion cores. Details are given in annex D, subsection D.4.2. Although there are more recent potential energy curves, these curves were chosen in order to provide a consistent level of accuracy for all alkalis. Equations have been solved using the same box and space step as in the statics, see Annex G for further details.

The Ak_2 dimer is initially set parallel to the droplet surface. We have checked that it is the preferred orientation for the Rb_2 and Cs_2 : the difference with the “erect” diatomic is 8.8 K and 9.1 K for Rb_2 in the singlet and triplet state, respectively, and 8.4 K and 8.0 K for Cs_2 in the singlet and triplet state, respectively. This is in agreement with the work by Ancilotto *et al.* [110, 111] on Na_2 at the surface of bulk liquid helium, where the binding energy for the “erect” dimer was found to be higher by 1 K than that of the “flat” dimer. However, we find a more important difference between the two configurations on the surface of a $N=1000$ atom droplet, likely due to curvature effects. Guillon *et al.* [112] also found Rb_2 triplet to be parallel to a flat ^4He surface. Notice that the effect of the diatomic orientation with respect to the droplet surface is studied in section V-2.3 below.

V-2.2. *Width due to the diatomic vibrational amplitude*

The influence of Ak₂ vibrational amplitude in its zero-point level has been estimated by running simulations from the interatomic Ak-Ak distances corresponding to the full width at half maximum (FWHM) of the bond length distribution in the ground vibrational state.

The Ak₂ ($v=0$) vibrational wave function was computed from available potential energy curves of the singlet or triplet electronic states (see Annex D, subsection D.4.1). The FWHM of the corresponding probability distribution function was characterized by the two points denoted by R_- and R_+ for which the square of the ($v=0$) vibrational wave function was equal to half the value of its maximum. The values for these points are collected in Table D.3. For each of these points, the Ak₂@⁴He_N system was re-equilibrated and a double ionization simulation was launched. The differences between the observables obtained for these bond lengths were taken as the width of these observables due to Ak₂ vibration.

V-2.3. *Width due to the diatomic angular distribution on the droplet surface*

Although Ak₂ is parallel to the surface in the most stable configuration, it can access different orientations due to zero-point motion. We have examined the influence of this angular distribution on the Coulomb explosion process. We use (x, y, z) axes with the origin O at the center of mass of the system, and the z axis parallel to the symmetry axis (from O to the Ak₂ center of mass g). Ak₂ being considered as a rigid rotor, its coordinates are z_g , the position of its center of mass, and the orientation angles of the molecular axis in the fixed frame. Azimuthal angle rotation around the z axis is akin to free rotation and is not considered here. The polar angle is denoted by φ (see schematic at the top of Fig. V.4). The zero-point motion associated with this angle has been investigated by Guillon *et al.*[112] for Rb₂ a³Σ_u⁺ and by Kranabetter *et al.*[102] for Na₂. In the latter case, the angular distribution peaked at 90° (Na₂ axis parallel to the surface) and died

out for $\varphi = 45^\circ$. However, we have found that this angular motion was significantly coupled to the vertical position of the Ak₂ center of mass z_g , as expected since upon increasing φ one of the Ak atoms is getting much closer to the helium surface.

Hence we have designed a two-dimensional model as follows. In the adiabatic approximation where the helium density instantly adapts to the Na₂ position and orientation, the Hamiltonian is equivalent to that of a pseudo-triatomic complex in which the droplet plays the role of a super-atom:

$$H = -\frac{\hbar^2}{2m} \frac{\partial^2}{\partial \mathcal{R}^2} + \frac{\hat{j}^2}{2\mu R^2} + \frac{\hat{\ell}^2}{2MR^2} + W(\mathcal{R}, \varphi) \quad (\text{V.2})$$

where \mathcal{R} is the distance between the center of mass of the droplet and the center of mass of Na₂, with $m = M_{\text{He}_{1000}} M_{\text{Na}_2} / [M_{\text{He}_{1000}} + M_{\text{Na}_2}]$ its associated reduced mass and $\hat{\ell}$ its associated angular momentum. R is the (frozen) Na₂ distance, with $\mu = M_{\text{Na}}/2$ its associated reduced mass and \hat{j} its associated angular momentum. We can thus use the method developed for triatomic van der Waals complexes, see e.g. Refs. [113, 114]. Here it is very simplified since we assume that the total angular momentum $\mathbf{j} + \mathbf{\ell}$ is zero, and R is frozen. We have determined the total energy $W(\mathcal{R}, \varphi)$ of Na₂ a³Σ_u⁺ @He₁₀₀₀ for a range of (\mathcal{R}, φ) values. The interpolated values served as the potential energy surface to obtain the ground state wave function.

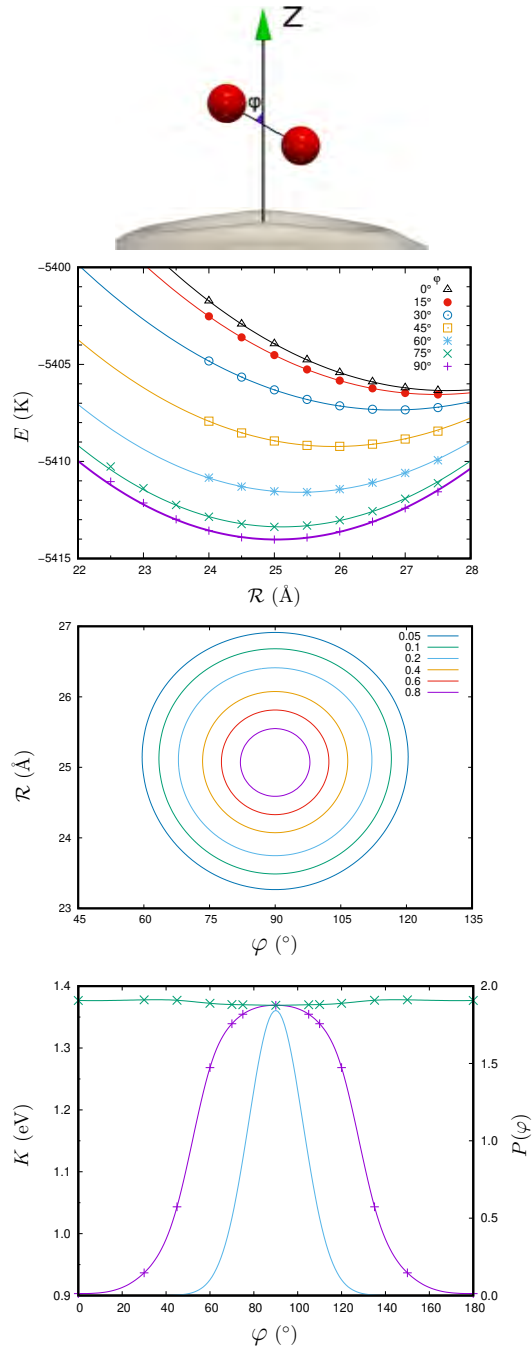


Figure V.4. From top to bottom: Schematic view: Definition of the angle φ (between the Na₂ interatomic axis and the line connecting the centers of mass of the droplet and of the diatomic). Top panel: Total energy of Na₂ $^1\Sigma_g^+$ @He₁₀₀₀ as a function of the distance of Na₂ center of mass to the center of mass of the droplet, for several values of the angle φ . Middle panel: two-dimension probability distribution (square of the two-dimension wave function multiplied by $\sin \varphi$) in \mathcal{R} (distance between the center of mass of the droplet and that of the diatomic) and φ ; Bottom panel: asymptotic kinetic energy of the Na⁺ ion going towards (purple line, + markers) or away from (green line, × markers) the helium droplet, and φ probability distribution integrated over \mathcal{R} (cyan line, no marker)

V-3. Results of the Coulomb explosion dynamics

The characteristics of the Ak₂@⁴He_N equilibrium configurations (results of the static simulations) are collected in Annex E, table E.5. Here we present the result of the Coulomb explosion dynamics.

Let us focus first on the case of Na₂ X¹Σ_g⁺ @He₁₀₀₀. As previously mentioned (Section V-1), the dynamics following double ionization at time $t=0$ is simulated by suddenly switching on ionic interactions at $t = 0$ starting from the equilibrium Ak₂@He_N configuration. It is illustrated in Fig. V.5, which shows a snapshot of the trajectory every 0.2 ps for Na₂@⁴He₁₀₀₀. The newly formed ions strongly accelerate away from each other, as they would in the gas phase. At the same time the droplet feels the attraction by the positive charges and two chunks of helium density detach from its surface and move towards them. But the ions are too fast and the helium cannot follow their motion and remains above the droplet, eventually being reabsorbed. This is quite a remarkable result, since helium is very light and the helium-positive charge attraction is very strong. One might have expected some helium density to rapidly surround the positively charged ions, and therefore slow them down. But acceleration due to charge-charge repulsion is so strong that the ions are already too far when helium moves, and they end up as bare ions, which is consistent with the experimental result [99, 102].

The dissociation dynamics of Na₂⁺⁺ upon double ionization of Na₂ in its triplet state is very similar to that of the singlet state, but it is slower. This is due to the longer Na₂ bond length in the a³Σ_u⁺ state, 5.2 Å instead of 3.072 Å (see Table E.5), hence Coulomb repulsion is not as strong: 2.769 eV instead of 4.689 eV. This is visualized by comparing the ions positions in the snapshots at 1 ps at the bottom of Fig. V.5. The Na⁺ ions are more than 80 Å away from each other for the singlet state and about 60 Å away for the triplet state.

This result is in good agreement with the experimental observations that the kinetic energy peaks of ions originating from Na₂ singlet and triplet can be straightforwardly identified even when they were formed on the surface of a helium nanodroplet.

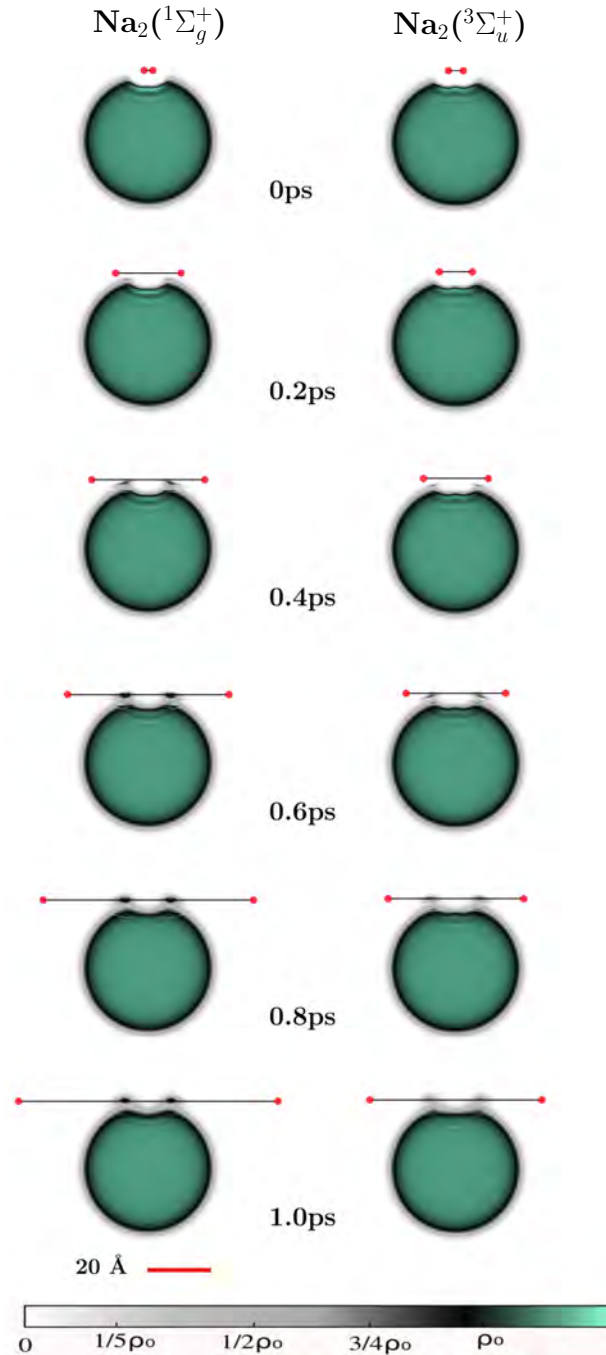


Figure V.5. Snapshots every 0,2 ps following double ionization of Na₂ on a ⁴He₁₀₀₀ nanodroplet. Left: from Na₂ singlet state $^1\Sigma_g^+$; Right: from Na₂ triplet state $^3\Sigma_u^+$. The helium nanodroplet is represented by its two-dimensional cut in the plane containing the ions. The density scale is given at the bottom in units of the bulk superfluid helium density, $\rho_0=0.0218 \text{ \AA}^{-3}$. The ions are represented as red disks with a black, horizontal line to materialize their distance (and not their trajectory, which is actually bent, see Fig. V.8). Note the faster dynamics for the singlet state than for the triplet state.

V-3.1. Kinetic energy distribution of the ions

The results displayed in Fig. V.6 provide a more detailed view of the double ionization dynamics of Na₂ X¹Σ_g⁺ @He₁₀₀₀ as an example. By 1.6 ps, the two ions are over 140 Å apart (top left plot). In addition, the bottom left plot shows that each ion is more than 70 Å away from the droplet center of mass (COM). At that distance the Na⁺-droplet interaction energy is negligible, which justifies stopping the propagation.

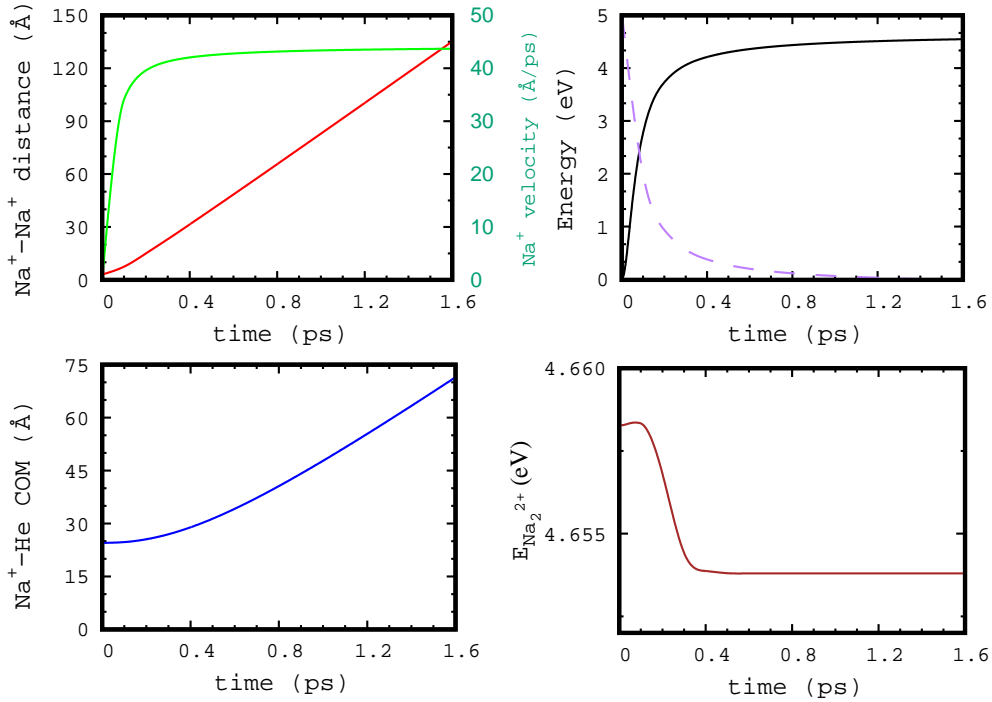


Figure V.6. Details of the dynamics following the double ionization of Na₂ X¹Σ_g⁺ @He₁₀₀₀. Top left panel: Na⁺-Na⁺ distance (red line, left axis) and Na⁺ velocity (green line, right axis) as a function of time. Top right panel: Total kinetic energy for Na₂²⁺ (black, solid line) and Na⁺-Na⁺ potential energy (V_{Cb} , purple dashed curve) as a function of time. The total kinetic energy at $t=1.6$ ps is $K_{Na_2^{2+}}=4.547$ eV and $V_{Cb}=0.107$ eV. Hence the total asymptotic kinetic energy (when $V_{Cb}=0$) is $K_{asym}=4.654$ eV, so that each Na⁺ has a kinetic energy of 2.327 eV. Bottom left panel: Distance between Na⁺ and the helium center of mass (COM) *vs* time (the distances are the same for both impurities); Bottom right panel: Total impurity energy as a function of time.

The kinetic energy is then $K_{\text{Na}_2^+} = 4.547$ eV and the inter-ion potential energy is $V_{\text{Cb}} = 0.107$ eV (top right plot). This predicts an asymptotic value of the Na⁺ kinetic energy of 2.327 eV $[(K_{\text{Na}_2^+} + V_{\text{Cb}})/2]$, to compare with the result in vacuum (obtained using the same inter-ion potential): $4.689/2 = 2.344$ eV. Hence the presence of the droplet shifts the asymptotic kinetic energy of each Na⁺ ion by 17 meV, *i.e.*, 35 meV in total, with respect to gas phase. The most important contribution is due to the interaction energy of the double ion with the surrounding helium, 31 meV (note that it is much less than the solvation energy of two Na⁺ ions since the surrounding helium configuration is that of neutral Na₂). The total energy of Na₂⁺⁺ on the droplet at $t = 0$ is thus lower by 31 meV than that in the gas phase, hence the asymptotic kinetic energy is lower by at least the same amount. Additionally, there is some kinetic energy transferred to helium during the dissociation dynamics. It is equal to the difference of the Na₂⁺⁺ total (potential + kinetic) energy between its $t = 0$ and its asymptotic values. In the case of Na₂ X¹Σ_g⁺ @He₁₀₀₀ depicted in Fig. V.6, this additional energy transferred to helium amounts to ~ 4 meV, as can be deduced from the decrease in the total (potential + kinetic) energy of Na₂⁺⁺ in the bottom right plot of the figure.

V-3.2. Influence of the droplet size

The experiments by Kristensen *et al.* [99] were conducted using a droplet size distribution with an average value of $N = 5000$ to 15 000 depending on the nozzle temperature. In order to address the question of the role of the droplet size on the final kinetic energy distribution of the ions, we have repeated the simulations for droplets of 5000 atoms instead of 1000. In the case of Na₂ in the triplet state we have also considered much larger droplet sizes: 10 000, 20 000 and 50 000. The change in droplet radius is significant: it increases from 22.2 Å for $N = 1000$ to 38.0 Å for $N = 5000$ and 81.8 Å for $N = 50000$. For droplets with $N \geq 10000$, the simulation was possible at the expense of freezing the helium density during the dynamics (but not during the static). This was justified in our opinion since the changes in the droplet density appear when the ions are already far, as could

be seen in Fig. V.5. However, the error made in using this approximation should increase with droplet size. We have therefore introduced a correction, as detailed below (see also subsection V-4.2).

The asymptotic kinetic energies of the Ak⁺ ions are displayed in Table V.1 for all the droplet size values considered in this work. They show that the red shift of the Ak⁺ ions kinetic energy increases (*i.e.*, their kinetic energy decreases) with droplet size, as expected since the interaction time of the ions with the droplet increases. For instance for Na₂ triplet state the red shift increases from 16 meV to 22 meV for a droplet size increase from 1000 to 5000 atoms: their final kinetic energy is 1.369 eV for $N=1000$, compared to 1.363 eV for $N=5000$. Part of this increase is due to the interaction energy of the double ion with helium at $t = 0$, denoted as S_D^{++} , which increases (in absolute value) by 7 meV (contributing -3.5 meV for each ion). This is illustrated in Fig. V.7 showing $S_D^{++}/2$ as a function of droplet size. But the energy transferred to the droplet also increases, from 3 to 9 meV, contributing an additional 3 meV difference for each ion. This can be seen in Fig. V.7 as the increasing difference between the kinetic energy shift ΔK of each ion with respect to gas phase and $S_D^{++}/2$. For droplet sizes $N > 10\,000$, ΔK is equal to $S_D^{++}/2$, since the helium density was maintained frozen during the dynamics (rows marked as N^* in Table V.1, column 4). The corrected energy shift ΔK_{corr} in Fig. V.7 is obtained using a rough estimate of the missing energy transfer to the droplet by assuming a linear dependence with the droplet radius.

The total expected shift of the kinetic energy peak of the Na⁺ ions compared to gas phase would be ~ 25 meV for a droplet of 15 000 atoms, the average droplet size in the experiments.

Also, since there is a droplet size distribution in the experiment, the results displayed in Table V.1 can be used to estimate its contribution to the width of the kinetic energy peaks. The difference between $N = 1000$ and 5000 is about 10 meV or less. Taking into account the larger droplet sizes (using frozen helium dynamics) would increase the width by about 20 meV, based on the Na₂ results for the triplet state.

Table V.1 shows that the agreement between experimental and theoretical shifts of the kinetic energy peak positions with respect to gas phase is very good for Rb₂ triplet and Cs₂ triplet, and very reasonable for Na₂ triplet, K₂ (singlet and triplet), and Rb₂ singlet. The main difference is for Na₂ ¹Σ_g⁺, where the experimental shift is much larger than the simulated one, even for the larger droplets: ~ 190 meV instead of 23 meV. Possible origins for this large experimental shift have been discussed [102]. It could be due to some dynamics that might have already started during the multi-photon ionization process, presumably due to resonance with an intermediate Na₂ excited state.

		X ¹ Σ _g ⁺	a ³ Σ _u ⁺	corr*
Li ₂	gas phase	2.709	1.742	—
	N=1000	2.690	1.725	—
	N=5000	2.683	1.719	—
	experiment	—	1.69	—
Na ₂	gas phase	2.344	1.385	—
	N=1000	2.327	1.369	—
	N=5000	2.321	1.363	1.368
	N*=10 000	—	1.367	1.361
	N*=20 000	—	1.366	1.359
	N*=50 000	—	1.365	1.356
	experiment	2.15	1.39	—
K ₂	gas phase	1.841	1.247	—
	N=1000	1.822	1.235	—
	N=5000	1.816	1.230	—
	experiment	1.80	1.25	—
Rb ₂	gas phase	1.703	1.178	—
	N=1000	1.689	1.164	—
	N=5000	1.681	1.157	—
	experiment	1.65	1.16	—
Cs ₂	gas phase	1.549	1.133	—
	N=1000	1.539	1.121	—
	N=5000	1.531	1.113	—
	experiment	1.41	1.03	—

Table V.1. Final (asymptotic) kinetic energy of the ions (in eV) following double ionization of the singlet or triplet state in our ⁴He-TDDFT simulations for a 1000 or 5000-atom droplet, compared to experiment and to gas phase values. In the case of Na₂ ³Σ_u⁺, N* values correspond to frozen density simulations, and the extra column (corr*) to the value including a correction to take into account additional energy transferred to helium (see text). Gas phase values are obtained from the value of the Ak⁺-Ak⁺ interaction at t=0; Experimental values are from Kristensen *et al.*, [99, 102] for mean droplet sizes around 15 000 He atoms.

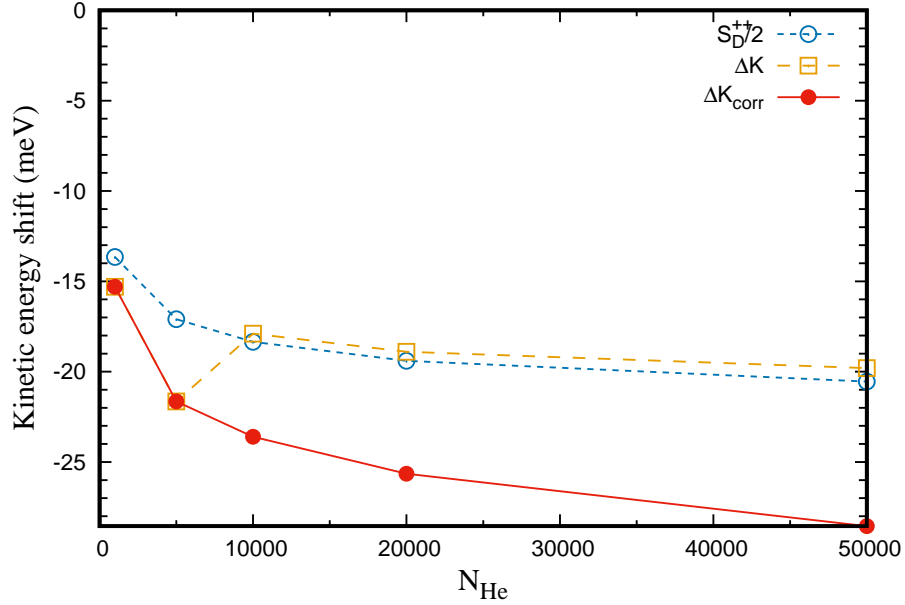


Figure V.7. Na⁺ kinetic energy shift with respect to gas phase for Na₂ ³Σ_u⁺ double ionization as a function of the droplet size. Blue dotted line with circles ($S_D^{++}/2$): contribution of the Na₂⁺⁺ interaction energy with helium at $t = 0$; Orange, dashed line with empty squares (ΔK): result of the dynamics simulation, complete for $N_{\text{He}} = 1000, 5000$, or with frozen helium density for $N \geq 10000$; Red line with disks (ΔK_{corr}): result of the dynamics simulation, including a correction for energy transfer to the droplet if $N \geq 10000$ (see text)

V-3.3. Widths of the ions kinetic energy distribution due to vibration

As explained in section V-2.2, we have determined the contribution of the bond length distribution of the dialkali molecules in their ($v=0$) vibrational level to the width of the kinetic energy peaks. Table V.2 displays the corresponding FWHM compared to the experimental values of Kristensen *et al.* [99, 102], found by fits to the published data [116].

For all alkali dimers this width is basically the same one as that of Ak₂($v = 0$) in the gas phase. Although the position of the ion kinetic energy peaks does depend on the droplet size, as discussed in the previous section, their width does not vary within the range tested. Depending on the alkalis and on the initial electronic state, the width of vibrational origin represents between one third to one half of the experimental width.

Taking into account the additional width of about 20 meV due to droplet size distribution (see section V-3.2) gives a slightly better agreement but not enough to recover the experimental values.

Table V.2. FWHM of the ions kinetic energy distributions following Ak₂ double ionization on ⁴He_N from the singlet or triplet electronic state resulting from Ak₂(*v* = 0) bond length distribution (see text). Experimental values from Kristensen *et al.* [99, 102].

Ak ₂		X ¹ Σ _g ⁺		a ³ Σ _u ⁺	
		Δ <i>K</i> _{vib} (eV)	expt. (eV)	Δ <i>K</i> _{vib} (eV)	expt. (eV)
Li ₂	gas phase	0.281		0.264	
	<i>N</i> =1000	0.280	--	0.264	0.53
	<i>N</i> =5000	0.280		0.266	
Na ₂	gas phase	0.176		0.156	
	<i>N</i> =1000	0.176	0.42	0.155	0.33
	<i>N</i> =5000	0.176		0.155	
K ₂	gas phase	0.110		0.101	
	<i>N</i> =1000	0.106	0.25	0.101	0.18
	<i>N</i> =5000	0.107		0.101	
Rb ₂	gas phase	0.080		0.079	
	<i>N</i> =1000	0.080	0.21	0.079	0.16
	<i>N</i> =5000	0.080		0.079	
Cs ₂	gas phase	0.062		0.063	
	<i>N</i> =1000	0.064	0.20	0.063	0.18
	<i>N</i> =5000	0.063		0.066	

It is interesting to note that the gas phase FWHM are very similar for the singlet and triplet states. This results from the compensation of two opposite effects. The width of the vibrational wave function is larger for the triplet state but the slope

of the Coulomb repulsive curve is smaller at the equilibrium distance of the triplet state.

As mentioned above, Kristensen *et al.*[102] have retrieved the initial distribution of internuclear distances $P(R)$ for the alkali dimers from the $P(E_{kin})$ kinetic energy distribution of the Ak⁺ fragments, by inverting the Coulomb potential governing the kinetic energy release as a function of the interatomic distance. Comparing the internuclear distance distribution obtained from this inversion to the one obtained as the Ak₂ squared wave function, they concluded that the experiment gave broader peaks than expected, and for some of the alkalis the peaks were shifted. This is in agreement with our finding that the experimental kinetic energy distribution peaks are broader than predicted by the $v = 0$ bond length distribution, and that some peaks are shifted, in particular for Na₂: the kinetic energy shift is smaller than the experimental one for the singlet state, and slightly too large for the triplet state, see Table V.1.

V-3.4. Effect of the angle of the diatomic molecule with the surface of the droplet

As already mentioned before, the equilibrium configuration of the dialkali molecule is parallel to the droplet surface, but other orientations are permitted by zero-point angular motion. In that case, one of the two ions is initially closer to the surface and can interact more strongly with the droplet. This could lead to an additional width of the energy peaks.

We have performed simulations for Na₂ a³Σ_u⁺ @He₁₀₀₀ as a test case, using the method described in section V-2.3. The total energies of Na₂ a³Σ_u⁺ @He₁₀₀₀ obtained from static ⁴HeDFT simulations for a number of R and φ values are displayed in the top panel of Fig. V.4. The minimum is -5414.0 K at $R = 25.0$ Å for $\varphi = 90^\circ$. The ground state wave function is represented in the middle panel of Fig. V.4. Its energy is -5412.7 K, i.e. 1.3 K above the minimum energy. The stretching and

bending frequencies were estimated to be 1.0 K and 1.6 K respectively, so that no excited state can be populated at the droplet temperature of 0.37 K.

Kranabetter *et al.*[102] have also calculated the angular distribution of the triplet Na₂ dimers in the effective potential from the droplet, modeled as a helium film. Their distribution has a maximum for $\varphi=90^\circ$, and extends to $\sim 45^\circ$. Our distribution seems to be slightly narrower, which could be a result of the curvature of the surface droplet.

As shown in the bottom panel of Fig. V.4, the ion kinetic energy (see Table E.7 for numerical values) curve as a function of the initial orientation angle φ is rather flat around $\varphi = 90^\circ$. By viewing the movies corresponding to each angle tested, we have seen that starting from $\varphi = 60^\circ$, one of the ions enters the droplet and a portion of its trajectory is therefore strongly hindered. Amazingly, even though part of its trajectory is then inside the droplet, this ion emerges without any helium attached. This is probably due to its high velocity, since its kinetic energy is still 1.268 eV. The other ion is escaping freely and its kinetic energy is basically not affected (it is only slightly increased for $\varphi \leq 60^\circ$, because the ion entering the droplet is slowed down hence the inter-ion distance does not increase as fast: as a result the Coulomb repulsion acts a little longer).

The angle at which the angular distribution is about half its maximum is 75° (from the bottom panel in Fig. V.4). The probability distribution resulting from the two-dimension wave function was integrated over \mathcal{R} and used to weight the kinetic energy distribution of the Na⁺ ions. The averaged kinetic energy value for each ion is 1.356 eV and 1.370 eV. This would correspond to an additional width of ~ 14 meV in the kinetic energy distribution.

It was not feasible to perform a systematic study of the effect of the zero-point angular motion on the Coulomb explosion of Ak₂. However, a simple model in which the droplet is assumed to be a sphere of radius R_N , and the center of mass of Ak₂ is initially sitting at a distance h above the sphere surface, gives the limiting angles φ_l above and below which one of the alkali atoms hits the droplet:

$$|\sin \varphi_l| = \frac{R_N}{R_N + h} \quad (\text{V.3})$$

This result was derived assuming a rigid sphere and no deviation of the Ak⁺ ion away from its initial orientation. For $h = 3 \text{ \AA}$ [the value for Na₂ a³Σ_u⁺] and $N = 1000$, $R_{1000} = 22.2 \text{ \AA}$ and the resulting value is $\varphi_l = 62^\circ$, which is very close to the 60° value at which the simulations show one ion hitting the droplet. For $h = 3 \text{ \AA}$ and $N = 15\,000$, $R_{15000} = 54.8 \text{ \AA}$ and the resulting value is $\varphi_l = 71^\circ$. This value is close to the angle corresponding to the FWHM of the angular distribution in the bottom plot of Fig. V.4. Assuming that the angular distribution of the Na₂ axis is only slightly modified by the droplet size (from the comparison with Kranabetter *et al.*[102]), it can be expected that for $N \geq 15\,000$, a significant proportion of ions will hit the droplet. The effect on the kinetic energy of the inward ion should be significant. For instance, the shift is about 100 meV for a 1000-atom droplet when one of the ions hits the droplet at $\varphi = 60^\circ$.

It is not clear what the result would be for Li₂: the width of the angular distribution of Ak₂ around its equilibrium configuration is governed by the ratio of Ak₂ rotational constant to the anisotropy of the Ak₂-droplet interaction. Because of its lighter mass and smaller interatomic distance, Li₂ rotational constant is larger than that of Na₂, which makes it less sensitive to the anisotropy of the Ak₂-droplet interaction and hence less localized in angle around the equilibrium configuration.

The effect should be more pronounced for the singlet state of Na₂, because the Ak₂ bonding distance is smaller, hence the rotational constant is larger so that the angular wave function should be less localized.

V-4. Ions trajectory deviation by the helium droplet

Our simulations have revealed an interesting effect: due to the He-Ak⁺ attraction, the presence of the helium nanodroplet slightly bends the trajectories of the departing ions towards it. This effect is small, but significant enough to be measurable. It is illustrated in Fig. V.8 for Rb₂ X¹Σ_g⁺ @He₁₀₀₀.

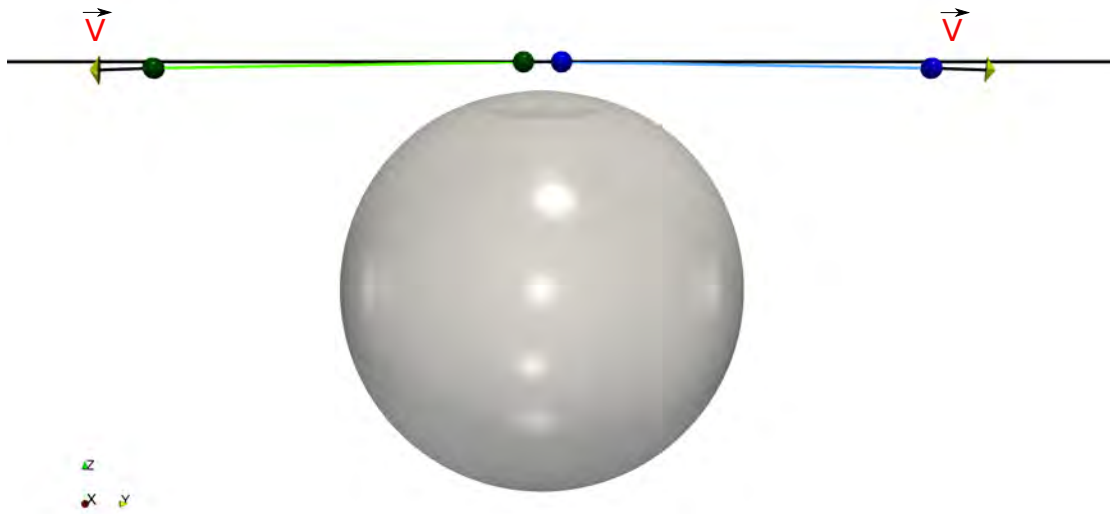


Figure V.8. Trajectory of the Rb⁺ ions (blue and green lines) upon Rb₂ X¹Σ_g⁺ @He₁₀₀₀ double ionization. The velocity vectors \vec{v} form an angle θ different from 180°, the value expected in the absence of the helium droplet.

V-4.1. Simulation results

The final values of the angle θ between velocity vectors, for all Ak, are collected in Table V-4.1 for equilibrium distance, Table E.6 (in annex E) for the distances corresponding to the FWHM and in Table E.7 for Na₂ ³Σ_u⁺ @⁴He₁₀₀₀ as a function of the angle φ .

We have also checked the effect of using the 3-body potential from Guillon *et al.*[117] rather than the sum of 2-body Rb-He interactions from Patil [118] on the equilibrium properties, final ions kinetic energy K and the bending angle (θ) between the ions velocity vectors. The results show a small effect and are summarized in Tables E.8 and E.9 in Annex E, subsection E.5.3.

The deviation from 180° is more important for a 5000-He droplet than for a 1000 one, as could be expected. For Na₂ ³Σ_u⁺ on larger (frozen) droplets the deviation can reach 10° for the largest size studied ($N = 50\,000$). For the average size droplet of $N = 15\,000$ the angle (θ) between velocity vectors is 172.6°.

The deviation is more important for the triplet than for the singlet state. This is because the diatomic bond length is longer in the triplet state, which makes the Coulomb repulsion weaker. This has two consequences which work in the same direction. Since the droplet attraction is only slightly weaker in the triplet state than in the singlet one (because of the slightly longer Ak distance to the center of mass of the droplet), the relative effect of the attraction compared to Coulomb repulsion is stronger and the deviation angle is larger. In addition, the ions feel the droplet attraction during a longer time because of the slower Coulomb explosion.

Remarkably, there is no significant variation of this angle with the nature of the alkali, except for the lightest one(s). When Ak₂ is initially in the singlet state, only Li₂ exhibits a larger deviation (by about 1° for the larger droplets). When it is in its triplet state, both Na₂ and Li₂ exhibit a larger deviation, but again only by about 1°. Both the mass and the equilibrium distance increase with atomic number, making the Coulomb explosion dynamics slower: this should increase the deviation angle since the droplet-ion attraction is exerted during a longer time. On the other hand, the helium-ion attraction decreases with atomic number (see Table D.3), which makes the droplet-ion attraction weaker.

Ak ₂	Final velocity angle θ (°)			
	$^1\Sigma_g^+$		$^3\Sigma_u^+$	
	$N = 1000$	$N = 5000$	$N = 1000$	$N = 5000$
Li ₂	177.3	175.7	176.4	174.2
Na ₂	177.6	176.5	176.5	174.5
K ₂	177.8	176.6	177.1	175.2
Rb ₂	177.7	176.8	176.9	175.2
Cs ₂	177.8	176.5	177.1	175.4
Na ₂	$N^* = 10\,000$	$N^* = 15\,000$	$N^* = 20\,000$	$N^* = 50\,000$
$^3\Sigma_u^+$	173.3	172.6	172.1	170.1

Table V.3. Angle θ between the ion velocity vectors at the end of the Ak₂ $^1\Sigma_g^+$ or $^3\Sigma_u^+$ Coulomb explosion on a He_N droplet for $N = 1000$ and 5000 for all alkalis. The last row gives the result for Na₂ $^3\Sigma_u^+$ on additional, larger droplets $N^* = 10000$ to 50000 , where the asterisk indicates that the helium density was maintained frozen during the dynamics. We have checked in the case of $N = 5000$ that the difference between frozen and non-frozen dynamics is less than 0.1° .

V-4.2. A model to estimate the ions trajectory deflection for large droplets

As shown in the preceding section, the ions do not follow a rectilinear trajectory as they do in the gas phase: their trajectory is curved towards the droplet because of the helium-cation attractive interaction. This has been confirmed by experiments conducted by Kristensen *et al.* [116]. However, in order to confirm their experimental results, they would need the deviation angle for the whole range of the droplet size distribution.

With the ^4He -TDDFT method we could simulate Coulomb explosion dynamics and determine the final angle between the ion velocity vectors, hence the deflection angle from linearity, up to $N = 15\,000$ atoms. This range could be extended up

to $N = 50\,000$ when freezing the helium density during the dynamics: the limit was set by the requirement of obtaining the $\text{Ak}_2@He_N$ equilibrium configuration which was very CPU time and storage space expensive. The goal of this work is to extrapolate the ^4He -TDDFT results for the deflection angle to much larger droplet sizes. In addition, we would like an estimate of the maximum size N_{max} for which the Ak^+ ions can escape the droplet: above this, they should fall into the droplet and get solvated. In order to achieve this goal, we have designed a model to estimate the deflection angle between the ions velocity vectors as a function of N for large to very large droplets, up to N_{max} .

V-4.2.1. The Rigid Sphere Model

The idea is that Coulomb explosion is so energetic that apart from a small time interval at the beginning of the dynamics, the ions are soon far enough away from the droplet to feel its attraction as that of a rigid and homogeneous helium sphere. The main advantage is that only the Van der Waals attraction needs then to be taken into account, as shown in Fig. V.9, and that its integration over the whole sphere is analytic.

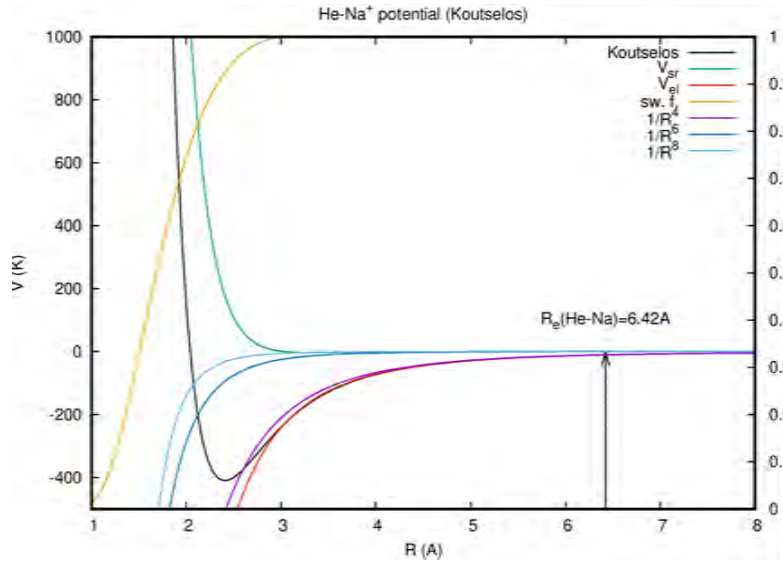


Figure V.9. He-Na⁺ Koutselos interaction potential ([109], black curve) and its components: short range V_{sr} , green curve; long range (electrostatic) V_{el} (red curve); and switching function (sw. f., yellow curve, right vertical axis) between the two. The He-Na equilibrium distance $R_e(\text{He-Na})$ is denoted by a vertical arrow, to show that at that distance, only the electrostatic interaction V_{el} is important and that it is largely dominated by the term in $1/R^4$ (charge-induced dipole interaction, purple curve).

The interaction of the ions with the N -atom droplet is thus approximated by integrating the $-C_4/R^4 - C_6/R^6$ helium-ion interaction over the whole droplet, taken as a sphere with constant density ρ_0 :

$$\begin{aligned} V_{HeN-Ak_2^{++}}(R_j) &= -\rho_0 \sum_{j=1}^2 \int_{\text{sphere}} \left(\frac{C_4}{|\vec{R}_j - \vec{r}_{\text{He}}|^4} + \frac{C_6}{|\vec{R}_j - \vec{r}_{\text{He}}|^6} \right) dr_{\text{He}}^3 \\ &= -\sum_{j=1}^2 \left\{ \frac{\pi C_4 \rho_0}{R_j} \left[\frac{2R_N R_j}{R_j^2 - R_N^2} + \ln \left(\frac{R_j - R_N}{R_j + R_N} \right) \right] + N \frac{C_6}{(R_j^2 - R_N^2)^3} \right\} \quad (\text{V.4}) \end{aligned}$$

where \vec{R}_j is the distance vector of ion j ($j=1,2$), to the droplet center of mass, see Figure V.10; \vec{r}_{He} denotes the position of the helium volume element (integration variable). The droplet is approximated as a rigid sphere with constant density $\rho_0 = 0.021836 \text{ \AA}^{-3}$ corresponding to the bulk superfluid Helium density at zero temperature [22]. Its radius is thus given as $R_N = (3/4\pi\rho_0)^{1/3} N^{1/3} (\simeq 2.22N^{1/3})$. The dispersion coefficients C_4 and C_6 are taken from the He-Ak⁺ pair potential [109]. Note that all the equations are written in atomic units.

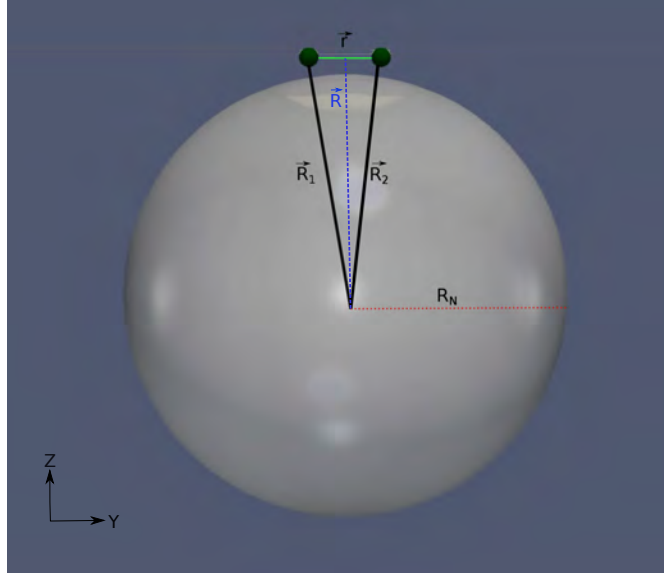


Figure V.10. 3D representation of the rigid sphere model and its coordinates. The two Ak ions are represented as small green spheres and the ${}^4\text{He}_N$ nanodroplet as a rigid, grey sphere with constant density. \vec{R}_j ($j = 1, 2$) is the distance vector from each ion to the ${}^4\text{He}_N$ center of mass (COM) and \vec{R} the distance vector between the di-ion and the droplet centers of mass; \vec{r} is the distance vector between the ions; and R_N is the droplet sharp density radius.

V-4.2.2. Equations of Motion and Dynamics

Thanks to the symmetry of the initial configuration, the dynamics can be reduced to the following Jacobi coordinates : the inter-ion distance $\vec{r} = \vec{R}_2 - \vec{R}_1$ and the distance between the helium droplet and the di-ion centers of mass $R = \sqrt{R_2^2 - r^2/4}$. The droplet position is thus described as that of an atom of mass $M_{\text{HeN}} = N M_{\text{He}}$ located at its center of mass.

In these coordinates, Hamilton's equations of motion are

$$\dot{r} = P_r/\mu \quad (\text{V.5a})$$

$$\dot{R} = P_R/M \quad (\text{V.5b})$$

$$P_r = \frac{1}{r^2} - \frac{r}{2R_2} \left(\pi \frac{C_4}{R_2} \rho_0 \left[\frac{2R_N(R_2^2 + R_N^2)}{(R_2^2 - R_N^2)^2} + \frac{1}{R_2} \ln \left(\frac{R_2 - R_N}{R_2 + R_N} \right) \right] + 6 \frac{C_6 R_2 N}{(R_2^2 + R_N^2)^4} \right) \quad (\text{V.5c})$$

$$P_R = -2 \frac{R}{R_2} \left(\pi \frac{C_4}{R_2} \rho_0 \left[\frac{2R_N(R_2^2 + R_N^2)}{(R_2^2 - R_N^2)^2} + \frac{1}{R_2} \ln \left(\frac{R_2 - R_N}{R_2 + R_N} \right) \right] + 6 \frac{C_6 R_2 N}{(R_2^2 + R_N^2)^4} \right) \quad (\text{V.5d})$$

where the Ak⁺-Ak⁺ Coulomb repulsion potential was taken as $V_c(r) = 1/r$, the reduced masses are $\mu = M_{AK}/2$ for r and $M = 2M_{Ak}M_{\text{HeN}}/(2M_{Ak} + M_{\text{HeN}})$ for R . In order to derive Eqs. (V.5c-d), use was made of the chain rule and of the derivative

of Eq. (V.4) with respect to coordinate R_j :

$$\frac{dV_{He-Ak^+}(R_1)}{dR_1} = \frac{dV_{He-Ak^+}(R_2)}{dR_2} = \left(\pi \frac{C_4}{R_2} \rho_0 \left[\frac{2R_N(R_2^2 + R_N^2)}{(R_2^2 - R_N^2)^2} + \frac{1}{R_2} \ln \left(\frac{R_2 - R_N}{R_2 + R_N} \right) \right] + \frac{6C_6 R_2 N}{(R_2^2 + R_N^2)^4} \right) \quad (\text{V.6})$$

These equations can be solved numerically for any droplet size, and their propagation takes only a few seconds of CPU time. The initial conditions are taken as follows:

$$r(t = t_0) = r_0 \quad R(t = t_0) = R_N + r_2 \quad (\text{V.7})$$

$$P_r(t = t_0) = P_r^0 \quad P_R(t = t_0) = P_R^0 \quad (\text{V.8})$$

where r_2 is the distance between the center of mass of the diatomic and the droplet surface.

Since the dimple shape is not reproduced in this model, we have adjusted the initial position for the center of mass of the dialkali as follows. For the droplet sizes for which there was a ⁴He-TDDFT result, we have fitted $r_2 = R(t_0) - R_N$ in order to achieve the same deflection angle at the end of the simulations, starting at 4 different values of the propagation time: $t_0 = 0, 0.1, 0.2,$ and 0.3 ps. Hence the initial conditions were taken as $r(t_0), R(t_0) = R_N + r_2, P_r(t_0),$ and $P_R(t_0),$ where $r(t_0), P_r(t_0),$ and $P_R(t_0),$ were taken from their value in the corresponding ⁴He-TDDFT simulation, and r_2 was adjusted by trial and error. In particular, for $t_0 = 0, r(t_0) = r_e(\text{Ak}_2),$ the equilibrium distance of the neutral Ak₂ molecule, and $P_r(t_0) = P_R(t_0) = 0.$

We have tested the model on the Coulomb explosion of Na₂(³Σ_u⁺) for droplets made of $N = 1\,000$ to $50\,000$ He atoms. Figure V.11 displays the velocity components v_z ($z//R$) and v_y ($y//r$) of each ion as a function of N in the ⁴He-TDDFT simulations, at $t = t_0,$ the different values of t_0 for which the fit of r_2 will be made. Notice that v_y is quasi-constant with varying droplet size for all the values of t_0 tested. This is due to the fact that the Coulomb repulsion is much stronger than the attraction towards the droplet, and that the latter is almost parallel to the z axis during the first tenths of picoseconds. In contrast, the v_z component

increases in absolute value as N increases. In the case of $t = 0.1$ ps, it tends to a constant asymptotic value. This is probably also the case for $t = 0.2$ and 0.3 ps, but at $N = 50\,000$ it is still varying. In addition, as can be seen in Fig. V.11 (right panel), for $t_0 = 0.1$ ps, r_2 tends to a constant value when increasing N (note that the scale in N is logarithmic), as was the case for the ⁴He-TDDFT simulations, whereas it is still varying when $N = 50\,000$ for $t_0 = 0.2$ and 0.3 ps. We think that 0.1 ps is therefore a reasonable choice, being close to the time it takes for the ions to get away from the dimple region, beyond which the rigid sphere approximation is more reasonable. As shown in Fig. V.12, there is a compensation of errors in the time evolution of the angle between the ion velocity vectors: in the rigid sphere model it starts increasing faster than in the ⁴He-TDDFT simulations, but it tends earlier to the asymptotic value.

For droplet sizes $N > 50\,000$, we have used $t_0 = 0.1$ ps, with the values $r(t_0)$, $P_r(t_0)$, and $P_R(t_0)$ taken from the $N = 50\,000$ simulation, and $R(t_0) = R_N + r_2$ with r_2 fitted for $N = 50\,000$ ($r_2 = 3.0$ Å), see Fig V.13.

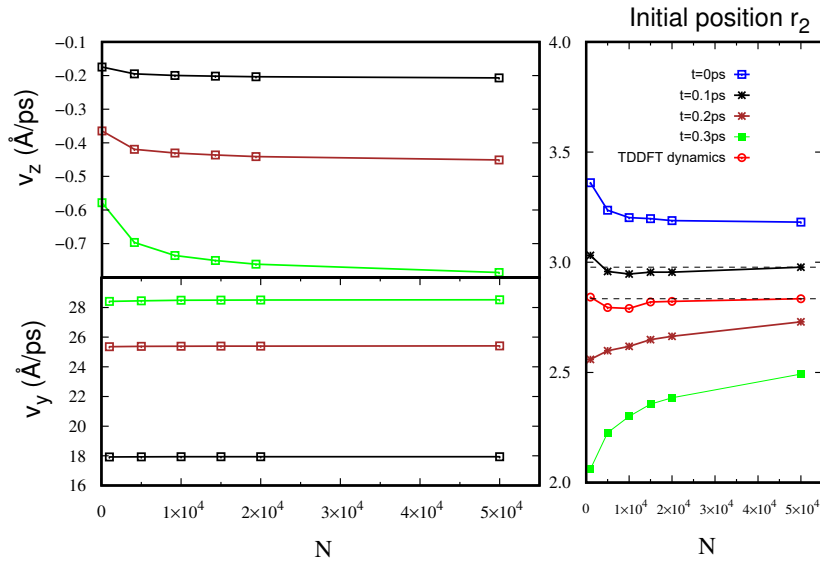


Figure V.11. Left panel: velocity components v_z ($z // R$) and v_y ($y // r$) of each Na^+ ion as a function of N in the ^4He -TDDFT simulations of $\text{Na}_2(^3\Sigma_u)$ Coulomb explosion on He_N , at $t = 0, 1$ (black), 0.2 (brown), and 0.3 (green) ps. Right panel: Fitted values of r_2 (see text) as a function of droplet size N for $t_0 = 0$ (blue curve, empty squares), 0.1 (black curve with asterisks), 0.2 (brown curve with asterisks), and 0.3 (green curve with full squares) ps, compared to the $R - R_N$ values obtained in the ^4He -TDDFT simulations (red curve with empty circles).

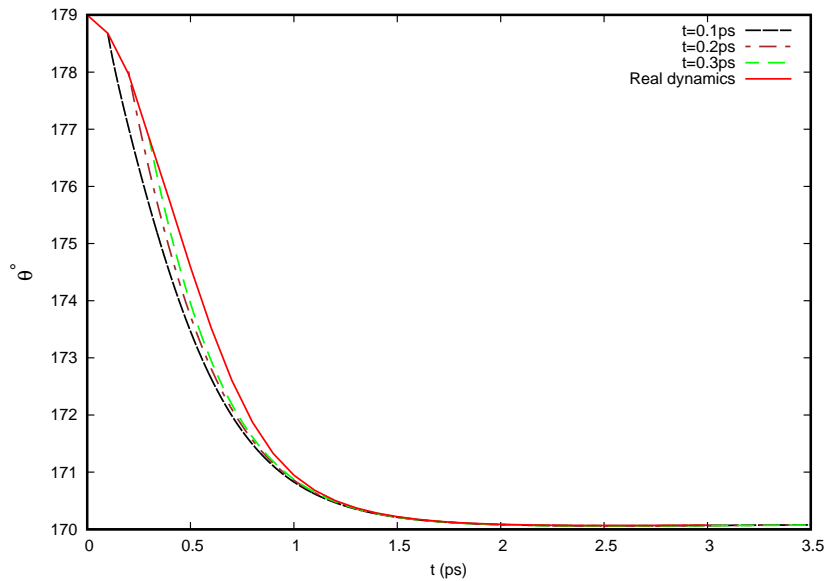


Figure V.12. Time evolution of the angle θ between the Na^+ ion velocity vectors for $\text{Na}_2^{++}@^4\text{He}_{50000}$ Coulomb explosion. Solid red line: from the ^4He -TDDFT simulations (with frozen helium density); Dashed lines: rigid sphere model, with $t_0 = 0.1$ (black), 0.2 (brown), or 0.3 (green) ps.

V-4.2.3. Results

Figure V.13 shows the final value of the angle between Na⁺ ion velocities as a function of droplet size N for Na₂⁺⁺@⁴He _{N} Coulomb explosion, obtained within the rigid sphere model for the three different values of t_0 tested. The most reliable one, $t_0 = 0,1$ ps, gives $N_{\max} \simeq 800\,000$, so that for $N \gtrsim N_{\max}$, the ions fall back on the droplet and cannot be detected. Note that the other two values give a different result, $N_{\max} \simeq 700\,000$, but it is the same order of magnitude. Given the level of approximation of the model, this is quite reassuring.

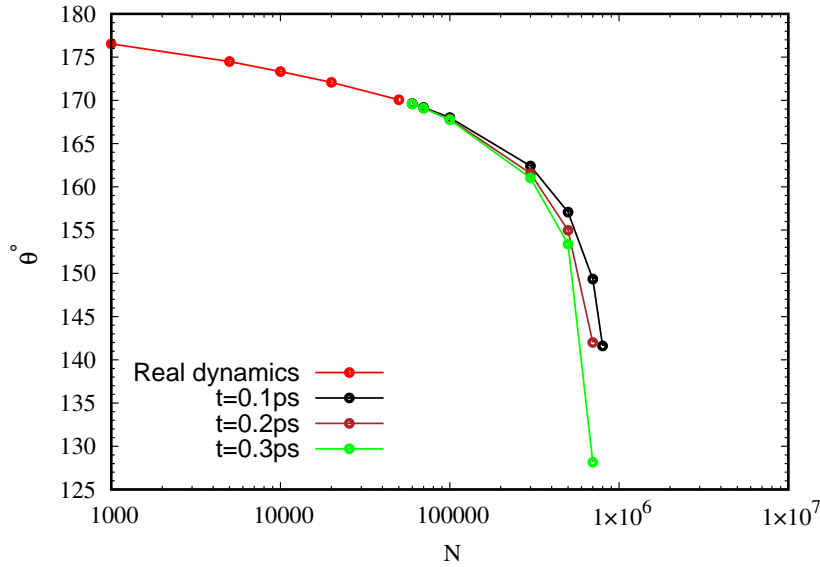


Figure V.13. Final value of the angle θ between the Na⁺ ion velocity vectors as a function of N for Na₂⁺⁺@⁴He _{N} Coulomb explosion. Red line: ⁴He-TDDFT simulations (with frozen helium density if $N > 15\,000$); Black, brown, and green lines: rigid sphere model, with $t_0 = 0.1$ (black), 0.2 (green), or 0.3 (blue) ps. The last point in each curve is the highest value of N for which the ions could escape de droplet. See text for more details.

V-4.2.4. Analytical fit

In order to facilitate the comparison with the experiments of Kristensen *et al.* [116], we have fitted the calculated points with an analytical function.

After several trials and errors, we have chosen the following function :

$$\theta = \frac{\theta_0}{\ln N_X} \ln \left\{ N_X \left[1 - \left(\frac{N_{\text{He}}}{N_X} \right)^a \right] \right\} \quad (\text{V.9})$$

with $\theta_0 = 180^\circ$. As can be seen in Fig. V.14, it seems to give a very acceptable fit for the whole range of calculated values. It also has the advantage of θ tending to 180° for N_{He} tends to zero.

Fig. V.14 shows 3 different fits: they only differ by the sets of points that were taken into account for the fit. The first one included all points, i.e. from the ^4He -TDDFT as well as rigid sphere model, and 3 additional “artificial” points to give more weight to the region near $N_{\text{He}} = 0$ ($N_{\text{He}} = 1, 2, 3$ with $\theta = 180^\circ$).

$$a=0.218 \pm 0.009, N_X = 1.05 \pm 0.03 \cdot 10^6.$$

The second one did not take into account these artificial points and the resulting fit is very similar. $a=0.216 \pm 0.009, N_X = 1.06 \pm 0.03 \cdot 10^6$.

The third one only takes into account the ^4He -TDDFT points.

$$a = 0.194 \pm 0.011, N_X = 1.17 \pm 0.21 \cdot 10^6.$$

It fits a little better those points, of course, but in addition, it gives a reasonable fit of the rigid sphere model points.

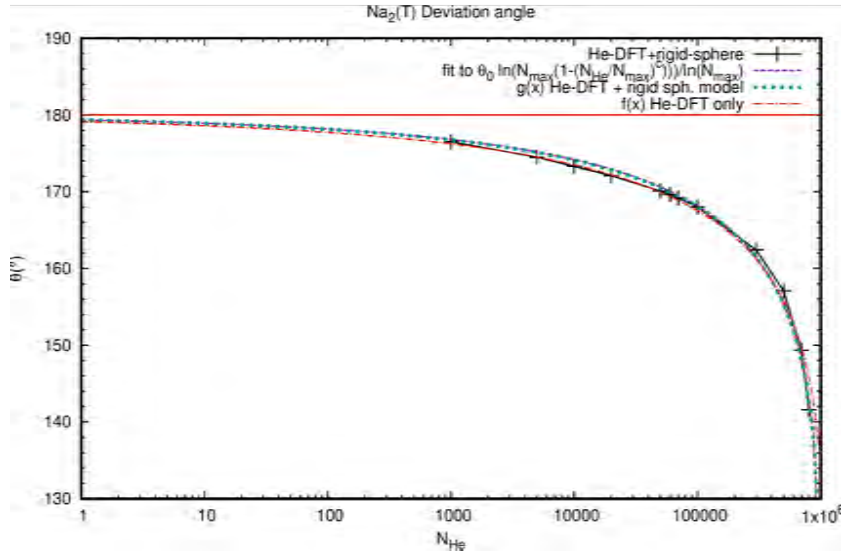


Figure V.14. Analytical fit of the final value of the angle θ between the Na^+ ion velocity vectors as a function of N for $\text{Na}_2^{++} @ ^4\text{He}_N$ Coulomb explosion. Black line with markers: all the calculated points (^4He -TDDFT and rigid sphere model). The other lines are the result of the fit described in Eq. (V.9). Purple, dashed line: including all points, plus 3 “artificial” ones ($N_{\text{He}} = 1, 2, 3$ with $\theta = 180^\circ$); green, dotted line: only the calculated points (^4He -TDDFT and rigid sphere model); red, dotted-dashed line: only the ^4He -TDDFT calculated points ($N_{\text{He}} \leq 50\,000$). The red, horizontal line marks the $\theta = 180^\circ$ asymptote for $\theta \rightarrow 0$. Note the logarithmic scale for N_{He} .

V-5. Conclusions

We have shown that the hypothesis of the weak influence of the helium nanodroplet on the trajectory of the ions resulting the Coulomb explosion of alkaline molecules on their surface is well verified.

The experimental maxima of ion kinetic energy distributions are fairly well reproduced, but the width is still too small.

An unexpected effect was detected in our theoretical work: the deviation of the ion trajectory from the horizontal, due to the attraction of helium, which should be measurable.

This work is not finished yet because we are collaborating with the experimentalists to verify our predictions about the angular deviation of the ion velocity vectors.

 CHAPTER VI

DROPLETS COALESCENCE AND QUANTUM VORTEX NUCLEATION

VI-1. Introduction

Very large superfluid ${}^4\text{He}_N$ drops (VLD) produced by Rayleigh breakup of a liquid jet into vacuum have been shown to host quantum vortices [70, Tanyag *et al* 33]. They are believed to acquire angular momentum when interacting with the walls of the nozzle [70], which is then stored as quantum vortices and/or capillary waves upon normal to superfluid transition.

We explore here another mechanism for quantum vortex nucleation : the droplet-droplet collisions. In a very large droplet (VLD) beam, Kolatzki *et al.*[36] have observed equidistant drops with almost uniform size which sometimes could coalesce downstream. The relative velocities explored here are somewhat higher than the ones in that experiment, but they are within the range of the ones in smaller droplets experiments produced by gaseous helium expansion.

In this study, the ${}^4\text{He}$ -TDDFT method is required because it can describe the dynamics of a quantum vortex, in addition to the other helium collective modes that can be excited during the collision process (in particular, capillary waves, which can also carry angular momentum).

VI-2. Method

In order to prepare the collision, the equilibrium structure of a ${}^4\text{He}_{500}$ droplet is firstly calculated, see Annex G for technical details. We have found it convenient to obtain the structure of each droplet inside the larger calculation box in which the dynamics will be carried out, placing their centers of mass so that their dividing surfaces (where the helium density equals half the liquid density value, $R = r_0 N^{1/3}$, with $r_0 = 2.22 \text{ \AA}$) are 8 \AA apart and the impact parameter equals the chosen value (see Fig VI.1). At this distance, droplets are far enough apart that their interaction energy is negligible: the energy of the two droplets constituting the starting configuration is -4947.0 K , to be compared to that of two droplets at infinite distance, -4943.8 K , giving an interaction energy of -3.2 K at $t = 0$. This is quite small, even compared to the kinetic energy (94.3 K for $v = 20 \text{ ms}^{-1}$). This yields two equal density profiles centered at different points of the calculation box, $\rho_1(r)$ and $\rho_2(r)$

We build an effective wave function giving the droplets opposite velocities in the z direction as follows:

$$\Psi(\mathbf{r}, t = 0) = \sqrt{\rho_1(\mathbf{r})} e^{-ikz} + \sqrt{\rho_2(\mathbf{r})} e^{ikz}$$

where the wave number k is related to the droplet velocity v as $v = \hbar k / m_4$.

Under Experimental conditions ($T_0 = 30\text{K}$, $P_0 = 5 - 80 \text{ bar}$) and at small droplets sizes, the velocity spread is about $\frac{\Delta v}{v_{\text{jet}}} \approx 2 - 6 \%$ [1, 119] and, hence the velocity range is $10 (0.1) < \Delta v < 34 (0.34) \text{ ms}^{-1} (\text{\AA ps}^{-1})$.

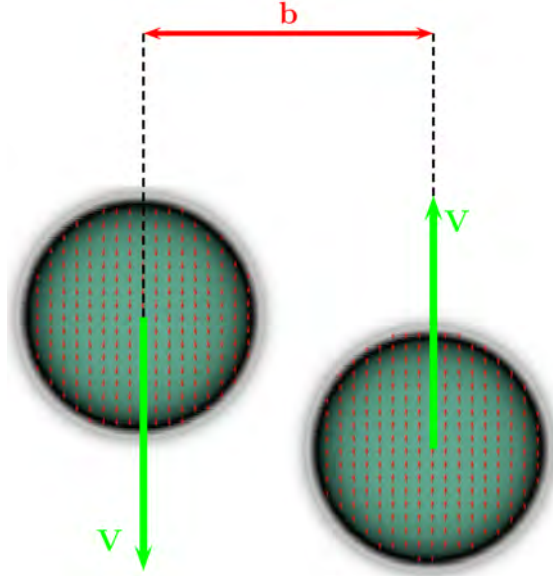


Figure VI.1. ${}^4\text{He}_N$ - ${}^4\text{He}_N$ collision with an impact parameter b and a relative velocity $\Delta v=2v$, where v is the velocity for each droplet. Collision plane (yz)

The angular momentum L created in the merged droplet is given by $L = bNm_4\Delta v\hbar$, where N is the number of helium atoms in each colliding droplet. For a vortex line along the diameter of the coalesced spherical droplet, one has $L = 1000\hbar$ (see section II-6.6), which yields the critical impact parameter for vortex nucleation

$$b_{\text{cr}} = 2 \frac{\hbar}{m_4} \frac{1}{\Delta v} \quad (\text{VI.1})$$

Different initial conditions (impact parameter b , relative velocity $\Delta v=2v$) were tested in the collision of two ${}^4\text{He}_{500}$ droplets of radius $R = 17.6 \text{ \AA}$. Given the computing cost of the simulations, it was not possible to explore a complete range of b and v values. We have selected a few representative initial conditions that could allow for a vortex nucleation, *i.e.* fulfilling Eq.(VI.1): $b = 3R/2$, $\Delta v = 12 \text{ ms}^{-1}$, and for a more central collision with $b = R$, $\Delta v = 18 \text{ ms}^{-1}$. Since part of the angular momentum will go into capillary waves or will be taken away by atom evaporation, we have also considered two larger values for Δv , namely 20 and 40 ms^{-1} . Specifically, we have chosen the following combinations of droplet velocity v and impact parameter b . Head-on collision ($b = 0$, $v = 40 \text{ ms}^{-1}$, $L=0$), $b = 3R/2$ for $v = 10, 20$, and 40 ms^{-1} ($L=825, 1650$ and $3300 \hbar$), grazing collision ($b = 2R$)

at $v = 20$ and 40 ms^{-1} ($L=2200, 4400 \hbar$) and distal collision ($b = 5R/2$, $v = 20 \text{ ms}^{-1}$, $L=2750 \hbar$). In addition, we have also studied a nonsymmetric case of two droplets, one of 300 atoms and the other of 700 atoms ($L=1650 \hbar$).

VI-3. Results

Figure VI.2 displays the two-dimensional cuts of the helium density in the (y, z) collision plane ${}^4\text{He}_N - {}^4\text{He}_N$ (and $\text{He}_{N_1} + \text{He}_{N_2}$ in the last case) at the end of each simulation (t_f).

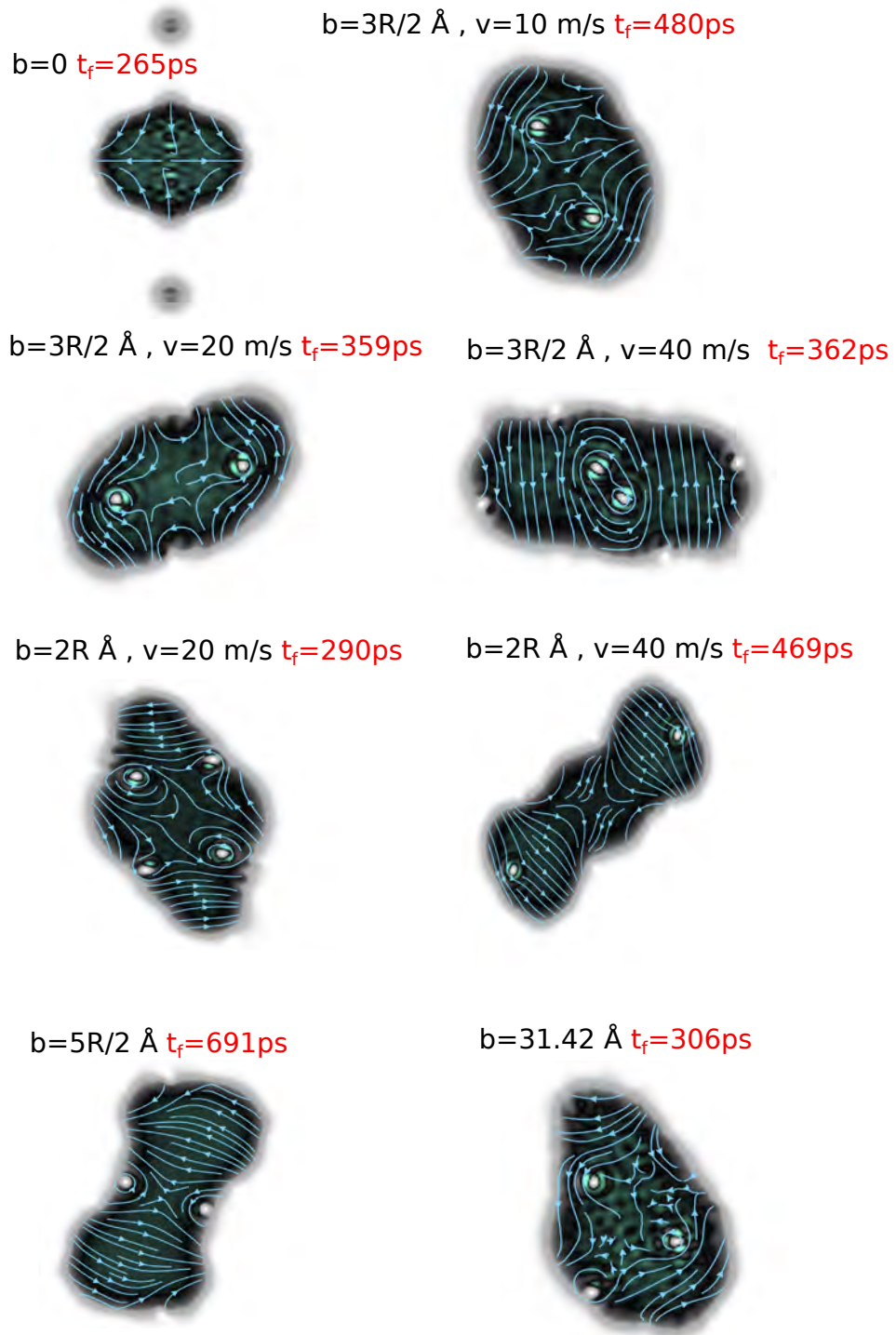


Figure VI.2. Snapshots of two-dimensional cuts in the (y, z) collision plane of ${}^4\text{He}_N$ - ${}^4\text{He}_N$ at the end of each simulation (t_f) and for different initial dynamics conditions. All cases corresponds to symmetric collision except that with impact parameter $b = 31.42 \text{ \AA}$ $N_1=300$ and $N_2=700$, and velocity equal to $v = 12.28 \text{ ms}^{-1}$ ($L=1650\hbar$). Superimposed arrows represent the superflow current. White spots within the droplet represent the intersection of (bent) vortex lines with the plane.

The evolving dynamics of two helium droplets made of 500 He atoms each, with impact parameter ($b=3R/2$) and $v = 20\text{ms}^{-1}$ ($L=1650 \hbar$) is shown in Figure VI.3 and VI.4. Notice that not only one, but two vortices are nucleated, the nucleation of the two vortex lines being simultaneous in this symmetric collision. This surprising result is possible because equation governing the minimum angular momentum $L = N\hbar$ to nucleate a vortex is only valid for a vortex line going through the center in cylindrical symmetry (see section II-6.6). The merged droplet is highly deformed and rotates in order to maintain the angular momentum involved in the collision.

In the collisions described here, the angular momentum is split between capillary waves and vortex nucleation.

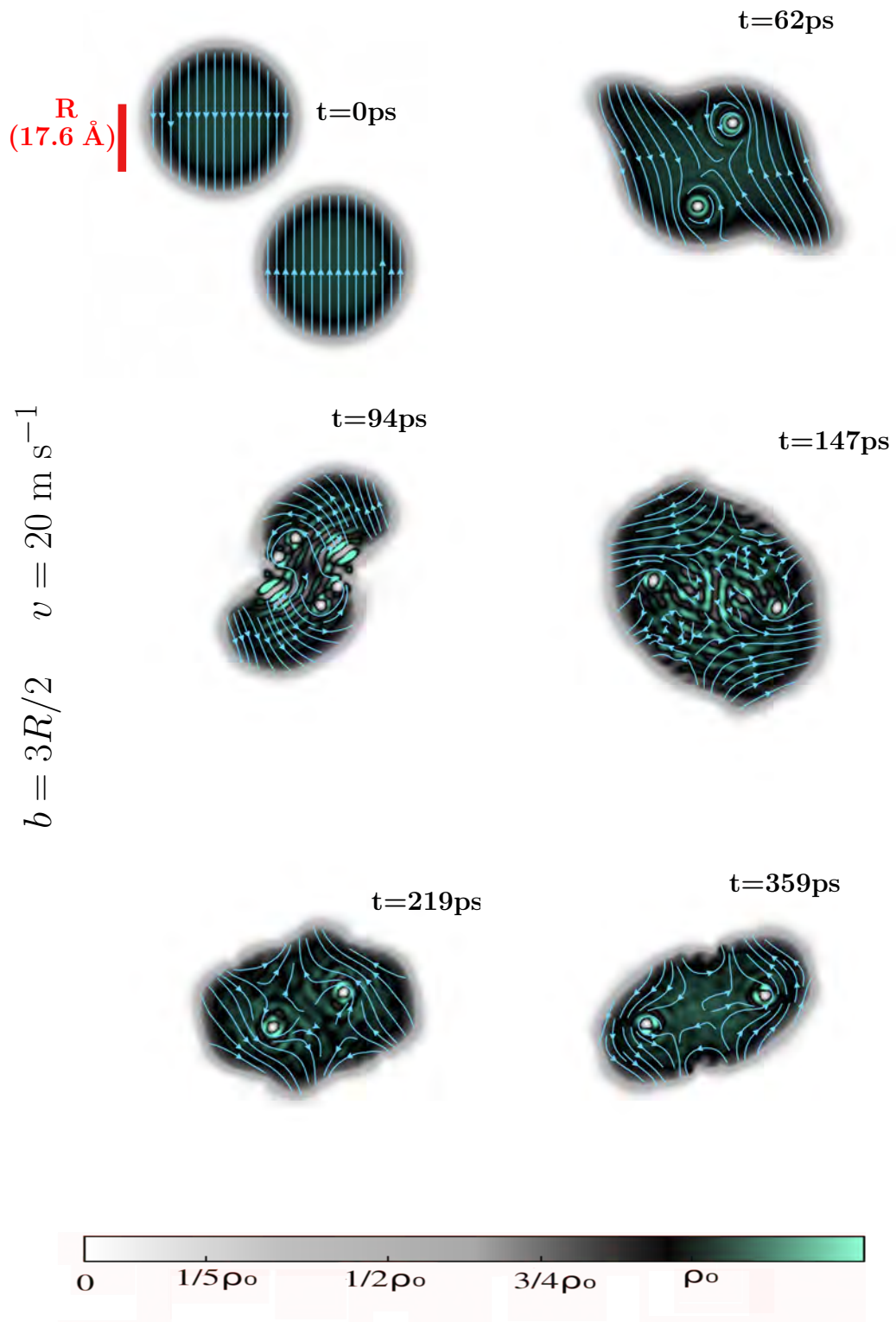


Figure VI.3. Snapshots of two-dimensional cuts in the (y, z) collision plane of ${}^4\text{He}_N$ - ${}^4\text{He}_N$ for $(b=3R/2)$ and $v = 20\text{ms}^{-1}$ ($L=1640 \hbar$) initial conditions. Superimposed arrows represent the superflow current. White spots within the droplet represent the intersection of (bent) vortex lines with the plane.

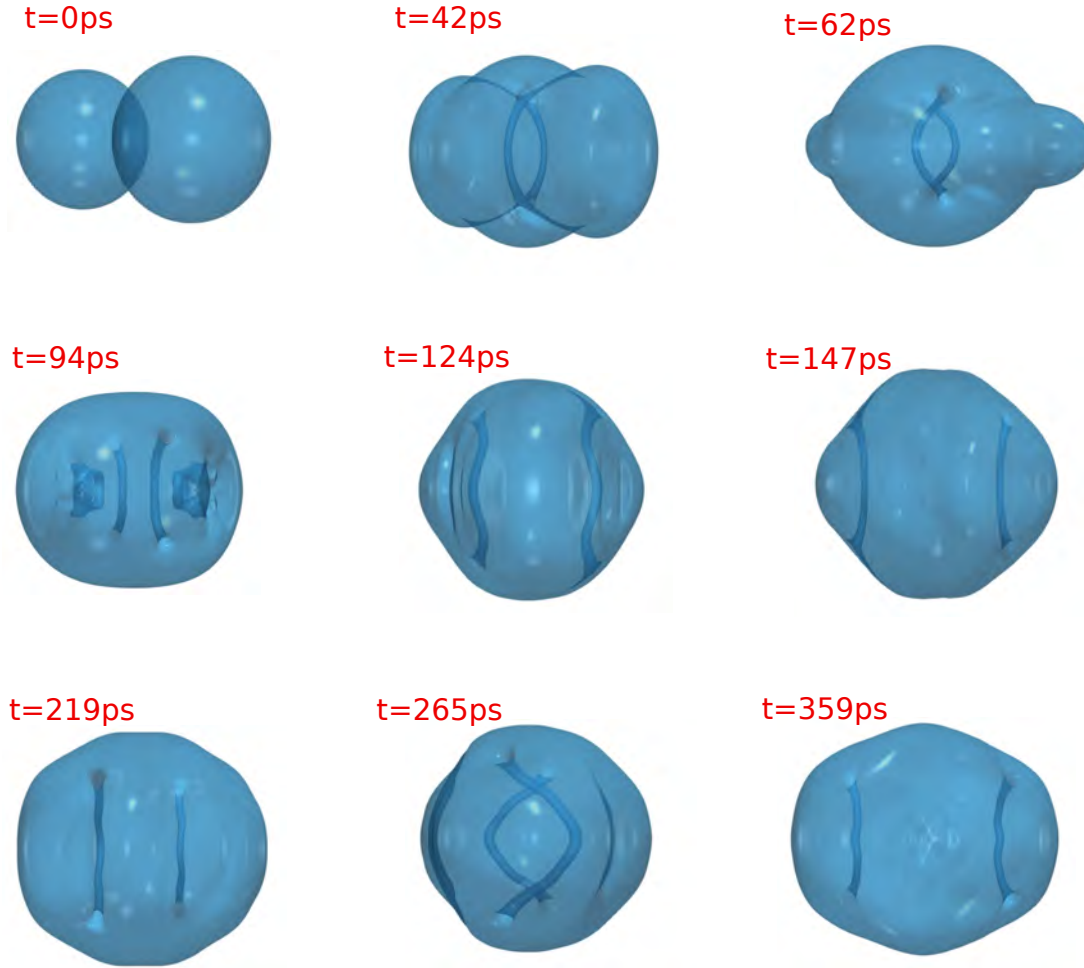


Figure VI.4. Three-dimensional plot of ${}^4\text{He}_N$ - ${}^4\text{He}_N$ collision in the plane xy ($N = 500$; $b = 3R/2$ Å; $v = 20\text{ms}^{-1}$, $L=1650$ \hbar). Two (bent) vortex lines are visible starting from the second snapshot, because they are empty (the helium density is zero at the core).

The time evolution of the total angular momentum and of the vortex contribution L_v for a ${}^4\text{He}_{500} + {}^4\text{He}_{500}$ merging collision with impact parameter $b = 3R/2$ and initial droplet velocity $v = 10, 20$ ms^{-1} are shown in Figure VI.5 and VI.6 respectively. The angular momentum contained in the vortices (L_v), is estimated by subtracting the angular momentum due to capillary waves $L_{\text{cap}} = \mathcal{I}_{\text{irr}}\omega$ [120] from the total angular momentum L , where

$$\mathcal{I}_{\text{irr}} = m_4 N \frac{[\langle y^2 \rangle - \langle z^2 \rangle]^2}{\langle y^2 \rangle + \langle z^2 \rangle} \quad (\text{VI.2})$$

and

$$\omega = \frac{\Delta\theta}{\Delta t} \quad (\text{VI.3})$$

In this equation, ω is the angular velocity and θ is defined as the rotation of the merged ${}^4\text{He}$ droplet around the x axis (axis perpendicular to the (y, z) collision plane).

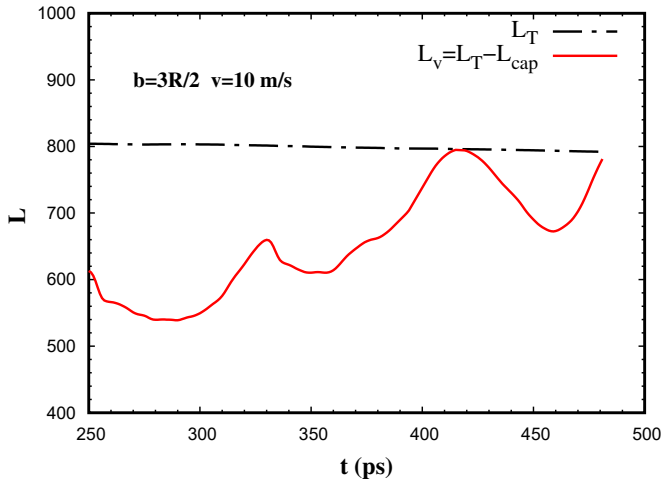


Figure VI.5. Time evolution of the total angular momentum and of the vortex contribution L_v for ${}^4\text{He}_{500} + {}^4\text{He}_{500}$ ($b = 3R/2$ and $v = 10 \text{ ms}^{-1}$)

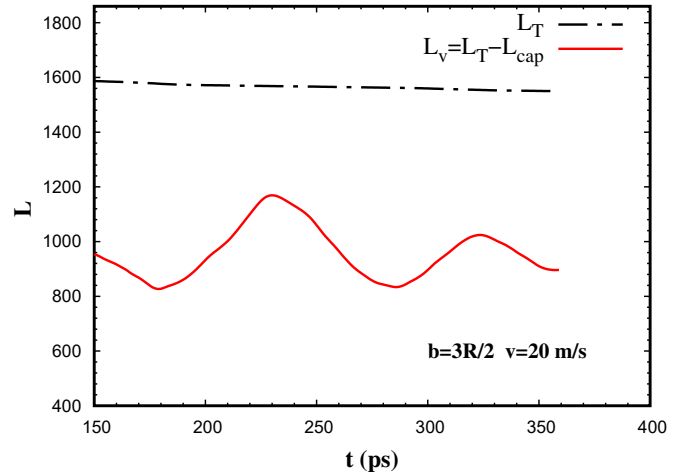


Figure VI.6. Time evolution of the total angular momentum and of the vortex contribution L_v for ${}^4\text{He}_{500} + {}^4\text{He}_{500}$ ($b = 3R/2$ and $v = 20 \text{ ms}^{-1}$)

VI-4. Conclusions

We evidence the nucleation of quantum vortices upon superfluid helium droplet collision. They are produced in pairs under symmetric conditions [120]. The collisions of superfluid ${}^4\text{He}$ droplets display similarities with classical droplet collisions. In both cases, the merged droplet is highly deformed and rotates in order to maintain the angular momentum involved in the collision. We have found that quantum vortices are readily nucleated by the surface indentations mechanism, yielding vortex rings less for head-on collisions, and off center linear vortices (which carry angular momentum, although smaller than centered vortices) for non-zero impact parameter collisions. The off axis nucleation makes it possible to nucleate vortices even if the total angular momentum is smaller than $N\hbar$. Since indentations appear

whenever droplets merge, the indentation mechanism is independent of the droplet size. It could therefore apply to a wide range of droplet sizes and velocities.

Quantized vortex nucleation in collisions of superfluid nanoscopic helium droplets at zero temperature

Cite as: J. Chem. Phys. 159, 074305 (2023); doi: 10.1063/5.0165820

Submitted: 30 June 2023 • Accepted: 3 August 2023 •

Published Online: 21 August 2023



View Online



Export Citation



CrossMark

Ernesto García-Alfonso,¹ Francesco Ancilotto,^{2,3} Manuel Barranco,^{4,5} Martí Pi,^{4,5} and Nadine Halberstadt^{1,a)}

AFFILIATIONS

¹Laboratoire Collisions, Agrégats, Réactivité (LCAR), Université de Toulouse, CNRS, 31062 Toulouse, France

²Dipartimento di Fisica e Astronomia “Galileo Galilei” and CNISM, Università di Padova, Via Marzolo 8, 35122 Padova, Italy

³CNR-IOM Democritos, Via Bonomea, 265 - 34136 Trieste, Italy

⁴Departament FQA, Facultat de Física, Universitat de Barcelona, Av. Diagonal 645, 08028 Barcelona, Spain

⁵Institute of Nanoscience and Nanotechnology (IN2UB), Universitat de Barcelona, Barcelona, Spain

^{a)}Author to whom correspondence should be addressed: Nadine.Halbertadt@irsamc.ups-tlse.fr

ABSTRACT

We address the collision of two superfluid ${}^4\text{He}$ droplets at non-zero initial relative velocities and impact parameters within the framework of liquid ${}^4\text{He}$ time-dependent density functional theory at zero temperature. Despite the small size of these droplets (1000 He atoms in the merged droplet) imposed by computational limitations, we have found that quantized vortices may be readily nucleated for reasonable collision parameters. At variance with head-on collisions, where only vortex rings are produced, collisions with a non-zero impact parameter produce linear vortices that are nucleated at indentations appearing on the surface of the deformed merged droplet. Whereas for equal-size droplets, vortices are produced in pairs, an odd number of vortices can appear when the colliding droplet sizes are different. In all cases, vortices coexist with surface capillary waves. The possibility for collisions to be at the origin of vortex nucleation in experiments involving very large droplets is discussed. An additional surprising result is the observation of the drops coalescence even for grazing and distal collisions at relative velocities as high as 80 and 40 m/s, respectively, induced by the long-range van der Waals attraction between the droplets.

Published under an exclusive license by AIP Publishing. <https://doi.org/10.1063/5.0165820>

I. INTRODUCTION

Superfluid helium droplets are routinely produced in beams obtained by expanding the high purity gas or liquid through a nozzle into a vacuum. The temperature T_0 and pressure P_0 values at the source chamber and the characteristics of the nozzle determine the appearance of the jet and the size and velocity of the droplets.¹ Once formed, drops cool down through evaporative cooling, eventually becoming superfluid. The activity in the field has been comprehensively presented in a recent monograph.²

The study of vortices in helium droplets has been a subject of continuous interest since they were first detected in droplets made of $\sim 10^{8-11}$ atoms,^{3,4} hereafter referred to as “very large droplets”

(VLDs). VLDs are believed to acquire angular momentum as they pass through the nozzle. As a result of the superfluid transition, most of the angular momentum deposited in the droplet is stored in nucleated quantized vortices, while some remains as surface capillary waves in the deformed droplets and some is taken away by evaporated He atoms. The morphology of these VLDs has been addressed in detail,⁵ and the coexistence of quantized vortices and capillary waves has been established.^{6,7}

The capture of impurities by droplets may also lead to vortex nucleation. Indeed, it has been shown that impurity capture by droplets made of $N = 1000$ atoms produces vortex rings and vortex loops.⁸⁻¹⁰ However, detecting vortices in these small droplets is a challenge. Methods based on studying the absorption spectrum of atomic impurities attached to the vortex cores have been

proposed,^{11–13} but, so far, vortices in small droplets have eluded detection.

In this work, we concentrate on the study of an alternative vortex formation mechanism, namely droplet–droplet collisions at a non-zero impact parameter. Experiments on He drops collisions, although feasible in principle, have not been carried out; they would be technically challenging and require rather expensive cryogenic cooling. At variance, molecular-beam scattering experiments where a beam of He droplets interacted with a secondary beam of Ar or Kr atoms have been performed to determine the appearance of ${}^4\text{He}$ and ${}^3\text{He}$ droplets made of $O(10^3\text{--}10^4)$ atoms.^{14,15} Let us mention that coalescence experiments of helium droplets magnetically levitated have been carried out. Using a static magnetic field, drops of less than 1 cm radius at a temperature of 0.7 K were confined and made to collide at velocities as small as a few cm/s.¹⁶

Recently, experimental activity has been conducted on the fragmentation of thin liquid helium jets into vacuum.^{17,18} It has been found that under suitable conditions, equidistant droplets of almost uniform size are produced from the breakup of the jet and that sometimes these drops coalesce downstream.^{17–19} These droplet collisions can occur because of the spread of droplet velocities inside the jet,²⁰ which, although small, can be the source of non-zero relative velocities and impact parameters.

Our goal is to describe binary collisions of zero temperature superfluid ${}^4\text{He}$ droplets within the ${}^4\text{He}$ density functional theory (He-DFT) approach.^{21–24} This approach is similar, in the superfluid ${}^4\text{He}$ phase, to the Gross–Pitaevskii (GP) approach, which has successfully been applied to the description of cold gases in the superfluid Bose–Einstein condensate phase, in particular in the study of quantized vortices.^{25–27}

In a recent study, some of us have addressed the coalescence of superfluid ${}^4\text{He}$ droplets,²⁸ initially at rest, which were drawn together by their mutual van der Waals (vdW) long-range attraction. The merging of vortex-free helium droplets has unveiled the appearance of vortex–antivortex ring pairs nucleated at the droplet surface that either wrap around the coalesced droplet or penetrate into it, eventually annihilating each other yielding an intense roton burst. This work has been later extended to the case of vortex-hosting droplets.²⁹ To our knowledge, no other description of superfluid (i.e., inviscid and irrotational) ${}^4\text{He}$ droplet collisions is available in the literature. We want to mention the existence of theoretical and experimental studies on head-on collisions of “quantum droplets” made of a very low temperature gas of ${}^{39}\text{K}$ atoms in two different hyperfine states constituting a superfluid Bose mixture,^{30,31} which bears some similarities with the problem of ${}^4\text{He}$ droplet collisions.

Binary collisions of droplets made of viscid fluids occur in, e.g., raindrop formation or spray processes. In addition to the dependence on the initial velocity and impact parameter, the collision outcome depends on the rheological properties of the droplets: droplet bouncing, droplet coalescence, and drop stretching separation have been found with increasing Weber numbers. It is worth mentioning that ${}^3\text{He}$ droplets collisions were described long ago in the Vlasov dynamics.³² These drops were found to bear collision properties that, on the one hand, are common to classical mesoscopic systems, such as, e.g., mercury drops,^{33,34} and, on the other hand, are common to heavy-ion reactions, such as fusion, fission and deep-inelastic processes.³⁵

Classically, binary collisions are addressed by solving the Navier–Stokes (NS) and continuity equations subject to appropriate boundary conditions, see e.g., Ref. 36 and references therein. It is naturally assumed that the solution of the NS equation for small enough viscosities should be nearly indistinguishable from the inviscid limit.^{37,38} However, as emphasized in Ref. 39, neither time-dependent GP nor He-DFT equations appropriate for superfluids reduce to the zero-viscosity limit of the NS equation (Euler equation) for a barotropic fluid in irrotational flow.²⁶ Indeed, in the superfluid case, an extra term appears involving the gradient of the so-called quantum pressure Q

$$Q = \frac{\hbar^2}{2m_4} \frac{\nabla^2 \rho^{1/2}}{\rho^{1/2}}, \quad (1)$$

where m_4 is the mass of the ${}^4\text{He}$ atom and ρ is the atom density. This term plays a crucial role when the density is highly inhomogeneous, as is the case near the core of a quantized vortex, for instance. Quantum pressure is a key ingredient naturally included in our time-dependent He-DFT approach.

Helium density functional and time-dependent density functional theory (He-TDDFT) methods have proven to be very powerful tools to study the properties and dynamics of superfluid ${}^4\text{He}$ droplets. Within the He-DFT approach, the finite range of the helium–helium van der Waals (vdW) interaction is explicitly incorporated in the simulations. As a consequence, the liquid–vacuum interface has a non-zero surface width, which is important in the description of nanoscopic ${}^4\text{He}$ droplets like those studied in the present work. The finite compressibility of the fluid is taken into account, and therefore possible density excitations (ripples, phonons, and rotons) are naturally reproduced. The possibility of atom evaporation from the ${}^4\text{He}$ sample during the real-time dynamics is also included.⁴⁰

This work is organized as follows: In Sec. II, we briefly present the He-DFT approach. In Sec. III, we discuss the results obtained for the collision dynamics. Due to the computational burden associated with fully three-dimensional He-DFT simulations, we only address a few illustrative cases corresponding to selected values of the initial droplets velocity and impact parameter. A summary with some concluding remarks is presented in Sec. IV. In complement to the main text, the supplementary material provides movies of the real-time dynamics of the ${}^4\text{He}$ droplet collisions addressed in this work. This multimedia material constitutes an important part of this work, since it helps capture physical details that would otherwise escape the written account.

II. METHOD

To describe the droplet–droplet collisions, we have applied the ${}^4\text{He}$ density functional (DFT) and time-dependent density functional (TDDFT) methods thoroughly described in Refs. 21 and 22. Let us briefly recall that within DFT, the energy of the droplet is written as a functional of the atom density $\rho(\mathbf{r})$ as

$$E[\rho] = T[\rho] + E_c[\rho] = \frac{\hbar^2}{2m_4} \int d\mathbf{r} |\nabla\Psi(\mathbf{r})|^2 + \int d\mathbf{r} \mathcal{E}_c[\rho], \quad (2)$$

where the first term is the kinetic energy with $\rho(\mathbf{r}) = |\Psi(\mathbf{r})|^2$ and the functional \mathcal{E}_c contains the interaction term (in the Hartree approx-

imation) and additional terms that describe non-local correlation effects.⁴¹

The droplet equilibrium configuration is obtained by solving the Euler–Lagrange equation resulting from the functional variation of Eq. (2)

$$\left\{ -\frac{\hbar^2}{2m_4} \nabla^2 + \frac{\delta \mathcal{E}_c}{\delta \rho} \right\} \Psi(\mathbf{r}) \equiv \mathcal{H}[\rho] \Psi(\mathbf{r}) = \mu \Psi(\mathbf{r}), \quad (3)$$

where μ is the ${}^4\text{He}$ chemical potential corresponding to the number of He atoms in the droplet, $N = \int d\mathbf{r} |\Psi(\mathbf{r})|^2$.

To prepare for the collision, we have first calculated the equilibrium structure of a ${}^4\text{He}_{500}$ droplet. We have found it convenient to obtain the structure of each single droplet inside the larger calculation box where the dynamics will be carried out, placing their centers of mass so that their dividing surfaces (loci where the helium density equals half the liquid density value, $R = r_0 N^{1/3}$, with $r_0 = 2.22 \text{ \AA}$) are 8 \AA apart and the impact parameter equals the chosen value. At this distance, the initial snapshots of the movies in the supplementary material show that the droplets are well apart. Only the surface helium densities closest to each other have their velocity starting to incurve toward each other after 2–4 ps as can be seen from the superimposed superflow current. In addition, the energy of the two droplets constituting the starting configuration is -4947.0 K , to be compared to that of two droplets at infinite distance, -4943.8 K , giving an interaction energy of -3.2 K at $t = 0$. This is quite small, even compared to the kinetic energy (94.3 K for $v = 20 \text{ m/s}$). This yields two equal density profiles centered at different points of the calculation box, $\rho_1(\mathbf{r})$ and $\rho_2(\mathbf{r})$.

Next, we build an effective wave function giving the droplets opposite velocities in the z direction as follows:

$$\Psi(\mathbf{r}, t = 0) = e^{-ikz} \sqrt{\rho_1(\mathbf{r})} + e^{ikz} \sqrt{\rho_2(\mathbf{r})}, \quad (4)$$

where the wave number k is related to the droplet velocity v as $v = \hbar k / m_4$. The TDDFT equation

$$i\hbar \frac{\partial}{\partial t} \Psi(\mathbf{r}, t) = \mathcal{H}[\rho] \Psi(\mathbf{r}, t) \quad (5)$$

is solved by taking Eq. (4) as the starting effective wave function.

We have set (y, z) as the reaction plane and the z axis as the direction of incidence. The angular momentum, written in units of \hbar thorough this paper, is calculated as

$$L(t) = -i \int d\mathbf{r} \Psi^*(\mathbf{r}, t) \left(y \frac{\partial}{\partial z} - z \frac{\partial}{\partial y} \right) \Psi(\mathbf{r}, t), \quad (6)$$

where $-i(y\partial/\partial z - z\partial/\partial y) = \hat{L}_x$ is the angular momentum operator in the x direction.

In practice, Eqs. (3) and (5) have been solved using the ${}^4\text{He}$ -DFT-BCN-TLS computing package,⁴² see Refs. 21 and 22 and references therein for details. We work in cartesian coordinates, with $\rho_i(\mathbf{r})$ and $\Psi(\mathbf{r})$ defined at the nodes of a 3D grid inside a calculation box large enough to accommodate the droplets in such a way that the He density is sensibly zero at the box surface. Periodic boundary conditions are imposed so that the convolutions involved in the DFT mean field $\mathcal{H}[\rho]$ can be carried out using the fast Fourier transform.⁴³ The differential operators in $\mathcal{H}[\rho]$ are approximated by

13-point formulas. All the simulation grids had 288 points equally spaced by 0.4 \AA in each direction, except for the head-on collision for which the grid had to be extended along the incidence axis (z) to 576 points.

The TDDFT equation is solved using Hamming's predictor–modifier–corrector method⁴⁴ initiated by a fourth-order Runge–Kutta–Gill method,⁴⁴ with a time step of 0.1 fs . During the time evolution some helium may evaporate from the droplets, eventually reaching the cell boundary. To prevent this material from reentering the cell due to the imposed periodic boundary conditions, we include an absorption buffer of 2 \AA inside the calculation box^{22,45} in each direction. This particle—and thus angular momentum and energy—leaking is obviously physical. Space and time steps have been chosen to keep energy and angular momentum well conserved in the absence of atom evaporation.

III. RESULTS

Our main goal is to investigate whether vortices could be nucleated during a droplet–droplet collision for reasonable values of their initial velocity and impact parameter. Let us first obtain a crude estimate of the critical impact parameter b_{cr} leading to vortex nucleation. As stated in the Introduction, we assume that the droplet collision may result from the finite velocity dispersion in the droplet beam.

If Δv is the velocity spreading in the jet system of reference, which moves with a velocity v_j with respect to the laboratory system, the maximum relative velocity is $2\Delta v$. The angular momentum L created in the merged droplet is given by $L\hbar = bNm_4\Delta v$, where N is the number of helium atoms in each colliding droplet. For a vortex line along the diameter of the coalesced spherical droplet, one has $L = 2N$, which yields the critical impact parameter

$$b_{cr} = 2 \frac{\hbar}{m_4} \frac{1}{\Delta v}. \quad (7)$$

Let us take as an example the velocity range $29 \leq v_j \leq 310 \text{ m/s}$ explored in the experiments of Kolatzki *et al.*,¹⁸ in which droplet beams are obtained by fragmentation of thin liquid helium jets into vacuum.^{17,18} Under these experimental conditions, $\Delta v/v \sim 0.01$,²⁰ i.e., $0.3 \leq \Delta v \leq 3 \text{ m/s}$; hence, $106.7 \leq b_{cr} \leq 1067 \text{ \AA}$. For a grazing collision, $b_{cr} = 2R$; hence, $53.4 \leq R \leq 534 \text{ \AA}$, thus giving $1.4 \times 10^4 \leq N \leq 1.4 \times 10^7$.

As indicated above, this is only a crude estimate. Even if enough angular momentum is available from the start, a vortex will not necessarily be nucleated since part of the angular momentum will be stored in capillary waves.⁷ This is all the more true since the merged droplet will be deformed for quite some time. In addition, it is not obvious *a priori* if a grazing collision can lead to droplet coalescence. On the other hand, less angular momentum is required to nucleate a non-centered vortex line.^{46,47}

The previous estimate makes it clear that a realistic simulation of the collision process between droplets arising from jet breaking in usual experimental conditions is beyond the TDDFT capabilities due to the large size of the involved droplets. On the other hand, the whole collision process can be simulated in detail for smaller droplets. Experimentally, they are obtained in a different expansion regime, called regime 1 or supercritical in the recent review by Toennies,⁴⁸ in which droplets are formed by gas condensation.

Depending on experimental conditions, their size can vary from several atoms up to about 10 000 atoms. For instance, in a $5\ \mu\text{m}$ diameter nozzle at $P_0 = 80$ bars and $T_0 = 24$ K, the maximum of the log-normal size distribution has been measured to be 1930.⁴⁹ In these conditions, the beam velocity is 480 m/s,⁴⁹ and the velocity spread is $\Delta v/v \approx 2\%$.¹⁴ These conditions would give $\Delta v \approx 10$ m/s and $b_{cr} = 31.8$ Å. For a grazing collision, this would correspond to a droplet radius of about 16 Å, slightly smaller than the radius of a 500-atom droplet (17.6 Å) investigated in our work. Higher nozzle temperatures lead to log-normal size distributions peaking at lower sizes.

We address here the collision, at non-zero relative velocity and impact parameter, of two ${}^4\text{He}_{500}$ droplets of radius $R = r_0 N^{1/3}$ with $r_0 = 2.22$ Å, i.e., $R = 17.6$ Å. From Eq. (7), for a not so grazing collision with $b = 3R/2$, $\Delta v = 12$ m/s, whereas for a more central collision with $b = R$, $\Delta v = 18$ m/s. Since part of the angular momentum will go into capillary waves or will be taken away by atom evaporation, in our study we have also considered two larger values for Δv , namely 20 and 40 m/s. Specifically, we have chosen as cases of study the following combinations of droplet velocity v and impact parameter b :

- $b = 0$, $v = 40$ m/s (head-on collision).
- $b = 3R/2$, $v = 10, 20$, and 40 m/s.
- $b = 2R$, $v = 20$ and 40 m/s (grazing collision).
- $b = 5R/2$, $v = 20$ m/s (distal collision, $b > 2R$).

These selected values allow for comparing the results at a given impact parameter as a function of the initial velocity and the other way around. Since the two droplets are of equal size, the relative velocity in the collisions is $v_{rel} = 2v$. We have also studied a non-symmetric case of two droplets, one of 300 atoms and the other of 700 atoms.

A. Head-on collision at $v = 40$ m/s

This is a zero-angular momentum collision. Figure 1 shows snapshots of 2D density cuts in the (y, z) collision plane during the real-time dynamics. Superimposed to the density, we have plotted the superflow current. This format is common to all 2D density figures in this paper. Upon droplet contact, due to the fairly large relative velocity, a density bulge develops at the collision region (frame at 7 ps), which expands laterally because of the large incompressibility of helium. This bulge is absent in the simulation of two droplets drawn against each other²⁸ only by the vdW attraction because of the smaller velocity involved in that process.

One may see the nucleation of vortex rings at surface indentations (frame at 40 ps). Due to the symmetry of the process, vortices appear in pairs of rings–antirings. As in Ref. 28, vortex rings/antirings are also nucleated at the density protrusions symmetrically placed along the collision direction (frame at 59 ps). These ring pairs eventually collide and annihilate, producing a roton burst (frame at $t = 83$ ps). As discussed in the following, the density waves produced by the rings annihilation induce He atom evaporation as they reach the droplet surface. After the fusion, the merged droplet in the figure undergoes wide amplitude oscillations. Interestingly, two satellite droplets appear (frame at 226 ps), which eventually detach from the fused droplet (frame at 250 ps). Any residual friction/viscosity remaining in the system might hinder this process.

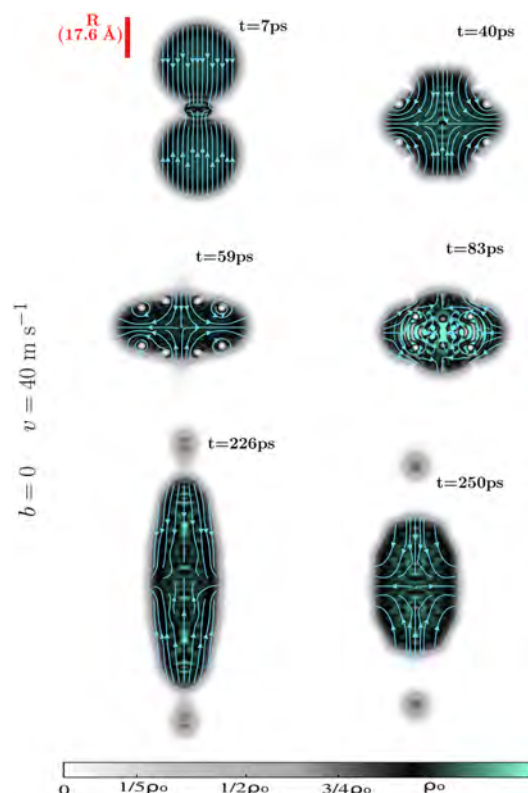


FIG. 1. Snapshots of two-dimension cuts in the (y, z) collision plane for impact parameter $b = 0$ (“head-on collision”) and initial droplet velocity $v = 40$ m/s. ρ_0 in the density scale is the bulk superfluid helium density, $\rho_0 = 0.0218\ \text{Å}^{-3}$. Superimposed arrows represent the superflow current.

Density oscillations are also expected to be damped for the same reason.

Notice that atom evaporation, which also contributes to the damping, is naturally occurring in our simulations. Figure 2 shows the time evolution of the energy and number of atoms in the system. The roton burst observed in the $t = 83$ ps snapshot induces strong helium atom evaporation: ~ 8 atoms in ~ 20 ps, dissipating ~ 110 K (about 14 K/atom). This is followed by slower atom evaporation and energy dissipation. During the time elapsed by the simulation (265 ps), 13 He atoms are emitted, taking away an average energy of about 11 K/atom.

B. Collisions with impact parameter $b = 3R/2$

1. $v = 10$ m/s collision

The angular momentum involved in this collision is $L = 825$. Figure 3 shows snapshots of the 2D density during the collision process, which displays several interesting features. A low-density bridge appears between the droplets before touching due to the long range attractive vdW mutual interaction, here exemplified by the frame at 10 ps. Interestingly, despite the small velocity, quantized vortices are nucleated at surface indentations appearing at the

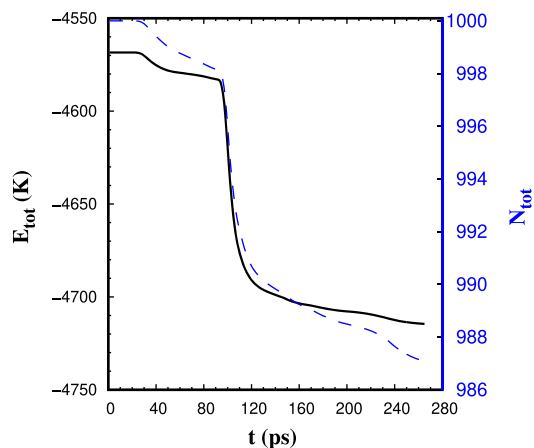


FIG. 2. Time evolution of the total energy E_{tot} (black line, left vertical axis) and number of helium atoms N_{tot} (dashed blue line, right vertical axis) for $\text{He}_{500} + \text{He}_{500}$ collision with impact parameter $b = 0$ (“head-on collision”) and initial droplet velocity $v = 40$ m/s.

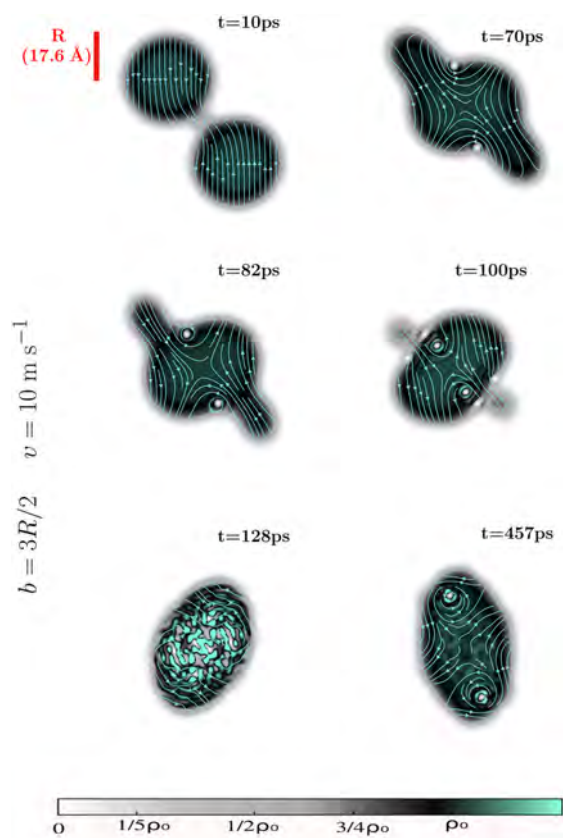


FIG. 3. Snapshots of two-dimension cuts in the (y, z) collision plane for impact parameter $b = 3R/2$ and initial droplet velocity $v = 10$ m/s.

droplets contacting region (frame at 70 ps). It is worth noting that a linear vortex can be nucleated even though $L = 825$ is smaller than the number of atoms in the merged droplet, $N_{\text{He}} = 1000$: The formula $Lh = N_{\text{He}}\hbar$ is strictly valid only for a linear vortex along the symmetry axis of an axisymmetric droplet, with L being smaller for vortex lines displaced off the symmetry axis.^{46,47}

Here, these vortices appear in pairs because of the symmetry of the system; they are vortex lines (not rings) of equal circulation, constituting a vortex dimer.²⁹ Surface protrusions appear as in the head-on collision case (frame at 82 ps), and their collapse nucleates a pair of vortex–antivortex rings (frame at 100 ps). The interaction of the vortex dimer with the pair of vortex rings inside the small volume of the fused droplet causes the annihilation of the ring pair and the appearance of a roton burst, leaving the droplet in a turbulent state (frame at 128 ps). Eventually, the fused droplet pacifies yielding a droplet in apparent rotation alongside the vortex dimer inside it, as shown in the $t = 457$ ps frame.

We, thus, see that vortices are readily nucleated in the course of the collision, even for moderate values of the relative velocity and impact parameter. At long times, the merged droplet “rotates” adopting an ellipsoidal-like shape, inside which the vortex dimer moves. We shall estimate later (Sec. III F) how angular momentum is shared between capillary waves, responsible for the apparent rotation of the droplet, and the vortex dimer.

Figure 4 shows the time evolution of the energy and number of atoms in the system. Atomic evaporation starts around 130 ps, when turbulence sets in; then, it gradually slows down. During the first 480 ps, about 15 He atoms are evaporated, taking away an average energy of 8 K per atom and an angular momentum of about 2.3 units per atom. Note that the initial excess energy with respect to a vortex free 1000-He atom droplet is 476 K in this case, so that the merged droplet still contains a significant amount of internal energy at the end of the simulation, even taking into account the additional energy contained in a vortex-hosting droplet. Unfortunately, it is not possible to continue the simulation for much longer times.

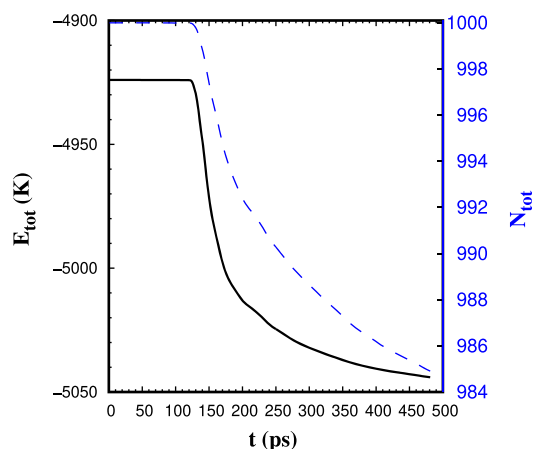


FIG. 4. Time evolution of the total energy (black line, left vertical axis) and number of helium atoms N_{tot} (dashed blue line, right vertical axis) for $\text{He}_{500} + \text{He}_{500}$ collision with impact parameter $b = 3R/2$ and initial droplet velocity $v = 10$ m/s.

TABLE I. Summary of the results for $\text{He}_{500} + \text{He}_{500}$ collisions, except for the last line, labeled *Asym.* which refers to the $\text{He}_{300} + \text{He}_{700}$ collision. The first three columns correspond to initial conditions: impact parameter b ($R = 17.6 \text{ \AA}$, the 500-droplet radius); initial droplet velocity v in m/s (in the case of the asymmetric collision, the He_{300} velocity is $v_1 = 28 \text{ m/s}$ and the He_{700} velocity is $v_2 = 12 \text{ m/s}$); resulting initial angular momentum L_0 . t_f is the total duration of the simulation; L_f is the angular momentum at the end of the simulation; n is the number of evaporated helium atoms; $\Delta E/n$ is the average energy loss per evaporated atom.

b	v (m/s)	L_0	t_f (ps)	L_f	n	$\Delta E/n$ (K)
0	40	0	265	0	12.9	11.3
$3R/2$	10	825	480	791	15.0	8.0
	20	1650	359	1549	10.0	9.2
	40	3300	362	3062	15.7	6.2
$2R$	20	2200	290	2098	5.0	7.0
	40	4400	469	4280	5.5	5.1
$5R/2$	20	2750	691	2683	3.0	3.6
Asym. (25/21)(3R/2)	$v_1 = 28$ $v_2 = 12$	1650	306	1533	7.3	8.6

The results for all the collisions studied in this work are collected in Table I.

2. $v = 20$ and 40 m/s collisions

The angular momentum involved in these collisions is $L = 1650$ and 3300 , respectively. The collision dynamics is similar to the case with $v = 10 \text{ m/s}$, see the corresponding movies in the supplementary material. Vortices are nucleated by the same mechanism at indentations appearing on the fused droplet surface. We have found that the number of vortices of equal circulation increases from two at 10 m/s to four at 20 and 40 m/s . During the real time evolution of the fused droplet, some of these vortices are evaporated. This does not mean that L changes, angular momentum simply goes into capillary waves. The interplay between vortices and capillary waves is readily seen in these movies, which also show the tendency of increasing the number of stable nucleated vortices with increasing droplet velocity.

The time evolution of the total angular momentum for $v = 20 \text{ m/s}$ is shown in Fig. 5, in addition to that of the total energy and number of atoms in the merged droplet. As expected, the decrease in angular momentum follows that in energy, and it is due to helium atoms evaporating from the droplet, which are removed from the simulation box by the action of the absorbing buffer. During the 360 ps covered by the simulations, about 10 He atoms are evaporated for the collision at $v = 20 \text{ m/s}$ taking away an energy of 9.2 K/atom and an angular momentum of 10 units per atom. At $v = 40 \text{ m/s}$, we have found that 15 He atoms are evaporated, taking away an average energy of 6.3 K/atom and an angular momentum of 16 units per atom.

C. Collisions with $b = 2R$ and $v = 20$ and 40 m/s

Grazing collisions are especially relevant since it is not obvious that the vdW attraction between the colliding droplets may compensate for the kinetic energy in the colliding droplets and lead to droplet coalescence.

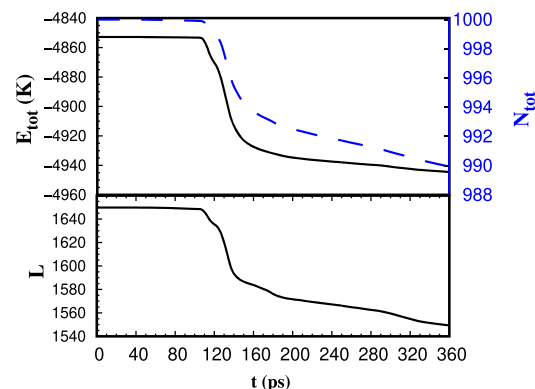


FIG. 5. Bottom plot: time evolution of the total angular momentum for $\text{He}_{500} + \text{He}_{500}$ collision with impact parameter $b = 3R/2$ and initial droplet velocity $v = 20 \text{ m/s}$. Top plot: Time evolution of the total energy E_{tot} (black line, left vertical axis) and number of helium atoms N_{tot} (dashed blue line, right vertical axis) for the same collision.

The angular momentum involved in these distal collisions is $L = 2200$ and 4400 , respectively. Figure 6 shows snapshots of the 2D density for the $v = 40 \text{ m/s}$ case. A density bridge perpendicular to the collision direction appears, connecting both droplets (frame at 10 ps). A vortex dimer is nucleated at $t = 20 \text{ ps}$, and another dimer appears at 50 ps. The interplay between capillary waves and vortices leads to the evaporation of one of the vortex dimers (frame at 100 ps), which is nucleated again later on (frame at 240 ps) and re-evaporated at $t = 365 \text{ ps}$. The coalesced droplet is very stretched due to the angular momentum deposited in the system.

During the 475 ps elapsed by the real time simulations, about 5 He atoms are evaporated, taking away an energy of 13.6 K/atom and an angular momentum of 23 units per atom. As shown in the movies, the evolutions at $v = 20$ and 40 m/s are qualitatively similar.

D. Distal collision at $b = 5R/2$ and $v = 20 \text{ m/s}$

The angular momentum involved in this distal collision is $L = 2750$. This collision highlights the relevance of the finite range of the vdW interaction in the outcome of the process. Indeed, if the collision were modeled by a surface tension plus kinetic energy model, inherent to any classical model based on the NS approach, it would lead to the non-interaction of the approaching droplets. At variance, we have found that the colliding droplets merge.

Figure 7 shows snapshots of the 2D density. A tiny, low-density bridge is clearly visible at 52 ps. Eventually, droplets merge, yielding a vortex-free droplet for a relatively long amount of time, as illustrated by the frame at $t = 190 \text{ ps}$, where the merged droplet undergoes a complete rotation with all the angular momentum stored in the form of capillary waves. Eventually, a vortex dimer starts being nucleated at $t = 245 \text{ ps}$ by the familiar surface indentations mechanism; it is clearly visible, e.g., at $t = 412 \text{ ps}$. The vortex dimer later evaporates (frame at $t = 483 \text{ ps}$), but it is nucleated again at $t = 555 \text{ ps}$. This evaporation-nucleation process continues until the end of the real time simulation (691 ps). During the time elapsed by the simulation, about 3 He atoms are evaporated, taking away

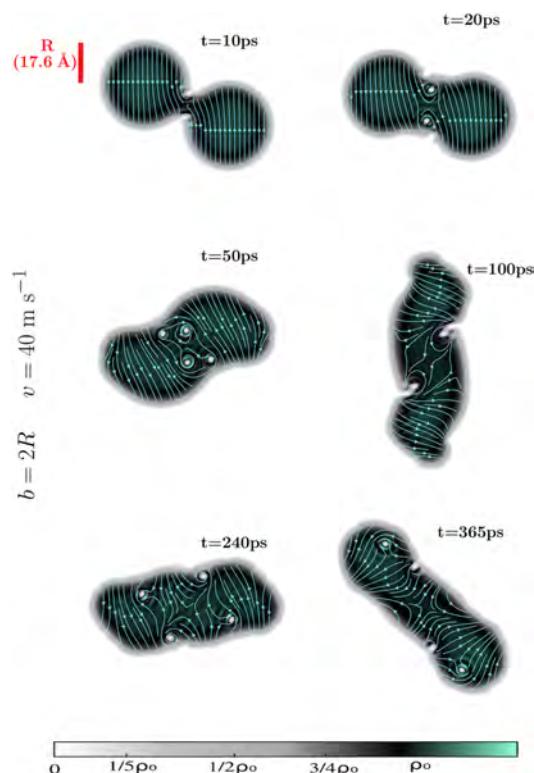


FIG. 6. Snapshots of two-dimension cuts in the (y, z) collision plane for impact parameter $b = 2R$ ("grazing collision") and initial droplet velocity $v = 40$ m/s.

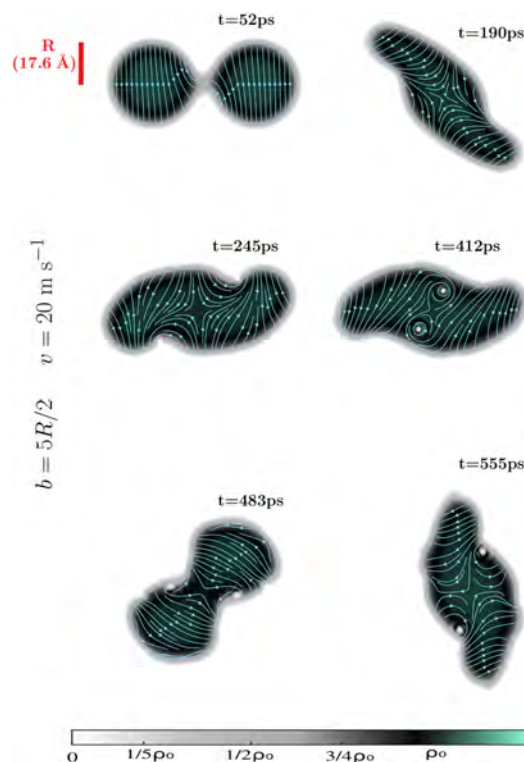


FIG. 7. Snapshots of two-dimension cuts in the (y, z) collision plane for impact parameter $b = 5R/2$ ("distal collision") and initial droplet velocity $v = 20$ m/s.

an energy of 3.7 K/atom and an angular momentum of 22 units per atom.

In addition to the difference between the initial L_0 and final L_f value of the angular momentum as a function of v for given b , which steadily increases with v , Table I does not reflect a clear trend in the number of evaporated atoms or in the average energy taken away per atom. On the one hand, this likely reflects the complexity of the coalescence process, which is far from trivial and eludes any simple systematics. On the other hand it is also a consequence of the different times t_{sim} elapsed by the different simulations (see Table I). However, even choosing the same value of t_{sim} for all would not give a satisfactory comparison since helium atom evaporation starts at different times depending on initial conditions. Only if all simulations could be conducted up to the final relaxed state of the merged droplet would the result be significant. Unfortunately, this is not feasible from a computational point of view.

E. Asymmetric collisions

We have seen that, due to the symmetry of the binary collision between two identical droplets, vortices are nucleated in pairs by the surface indentation mechanism. A less symmetric collision might lead to the nucleation of an odd number of vortices. To check

this possibility, and see the influence of the asymmetry on the collision outcome, we have conducted one simulation with droplets of different sizes, namely $N_1 = 300$ and $N_2 = 700$. The initial conditions $v_1 = 28$ m/s, $v_2 = 12$ m/s, and $b = (25/21)(3R/2)$ were chosen so as to be as close as possible to the case of identical droplets with $v = 20$ m/s and $b = 3R/2$ in order to compare the collision processes for the same relative velocity and total angular momentum.

Figure 8 shows snapshots of the 2D density. The usual density bridge can be seen at 15 ps, and one single vortex is nucleated at 30 ps. Yet, another vortex is later nucleated at 60 ps, and a third one appears at 80 ps. The latter panel also shows a surface protrusion whose collapse yields a vortex ring and a series of density waves propagating inside the droplet. One of the vortices gets ejected at $t = 215$ ps, but then it gets nucleated again as can be seen in the final snapshot at $t = 306$ ps. During the whole simulation, about 7 He atoms are evaporated, taking away an energy of 8.6 K/atom and an angular momentum of 16.1 units per atom.

F. Sharing angular momentum between capillary waves and vortex lines

It is well known that angular momentum in superfluid ${}^4\text{He}$ droplets can be stored in the form of capillary waves and/or quantized vortices, see e.g., Refs. 6, 7, and 50. As discussed in the previous

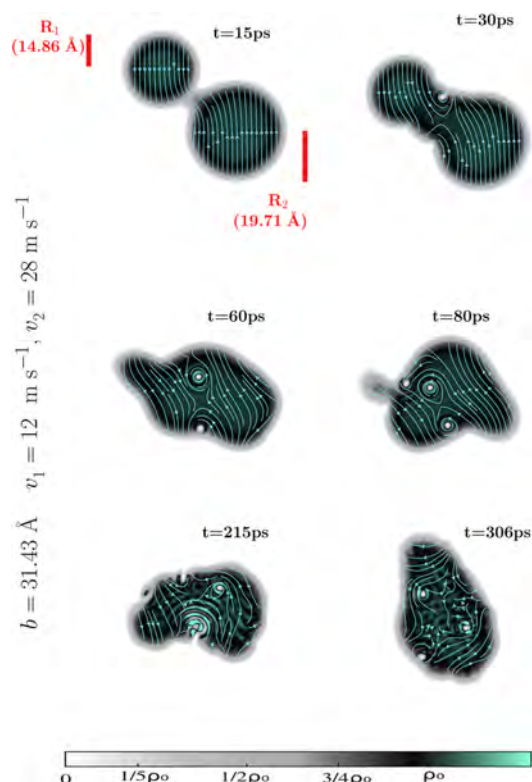


FIG. 8. Snapshots of two-dimensional cuts in the (y, z) collision plane for $\text{He}_{300} + \text{He}_{700}$ asymmetric collision with impact parameter $b = 31.4 \text{ \AA}$ and velocities $v_1 = 28 \text{ m/s}$ (upper left droplet, $N_1 = 300$) and $v_2 = 12 \text{ m/s}$ (lower right droplet, $N_2 = 700$), chosen to be as close as possible to the $b = 3R/2$, $v = 20 \text{ m/s}$ case for two identical, $N = 500$ droplets (same relative velocity and total angular momentum).

sections, and as it is clearly apparent from the figures, both vortices and capillary waves appear in the merged droplets. It is quite natural to ask oneself how much angular momentum is stored in vortices and how much is in capillary waves. This question has not a rigorous answer, as one cannot split the effective wave function of the superfluid $\Psi(\mathbf{r}, t)$ into a component arising from vortex contributions and another one from capillary waves, both being intimately entangled.

A simple estimate of vortex (L_v) and capillary wave (L_{cap}) contributions to the total angular momentum can be obtained as done in Refs. 6 and 7, when the shape of the rotating droplet is approximately ellipsoidal. It consists of determining L_{cap} from the angular velocity ω of the apparent rotation of the merged droplet and using an ellipsoid approximation for the droplet shape, since the angular momentum of an ellipsoid made of an irrotational fluid rotating around a principal axis at angular velocity ω is known.⁵¹ L_v is obtained as $L - L_{cap}$. These are only estimates that could be more meaningful near the end of the simulations when the droplet reaches a quasi-steady rotational state.

We have proceeded as follows: We first determine the classical axes of inertia by diagonalizing the classical matrix of inertia in the lab frame,

$$I_{jk} = m_4 \int d\mathbf{r} (r^2 \delta_{jk} - r_j r_k) \rho(\mathbf{r}). \quad (8)$$

Since the x axis is maintained constant by symmetry, the instantaneous inertia axes were determined by rotation by a single angle θ about x . The angular velocity ω is then calculated as

$$\omega = \frac{\Delta\theta}{\Delta t}. \quad (9)$$

The angular momentum due to capillary waves is finally expressed as $L_{cap} = \mathcal{I}_{irr} \omega$, where⁵¹

$$\mathcal{I}_{irr} = m_4 N_{tot} \frac{[\langle y^2 \rangle - \langle z^2 \rangle]^2}{\langle y^2 \rangle + \langle z^2 \rangle} \quad (10)$$

is the irrotational moment of inertia calculated in the rotating frame, with

$$\langle y^2 \rangle = \frac{1}{N_{tot}} \int d\mathbf{r} y^2 \rho(\mathbf{r}) \quad \text{and} \quad \langle z^2 \rangle = \frac{1}{N_{tot}} \int d\mathbf{r} z^2 \rho(\mathbf{r}), \quad (11)$$

N_{tot} being the total number of atoms in the merged droplet. For vortex-free droplets, the above-mentioned expressions have been found to reproduce the DFT results within 5%.⁷

As illustrative examples, we show in Fig. 9 the total angular momentum L (which changes with time due to atom evaporation) and vortex contribution L_v for the collision corresponding to $b = 3R/2$ and $v = 10 \text{ m/s}$, for times $t > 250 \text{ ps}$. Figure 10 shows the same quantities for the collision corresponding to $b = 3R/2$ and $v = 20 \text{ m/s}$, and times $t > 150 \text{ ps}$. We want to stress here that these qualitative results should be taken with caution, as some of the considered droplet configurations are not as ellipsoidal as they should be to justify the application of the above-mentioned expressions.

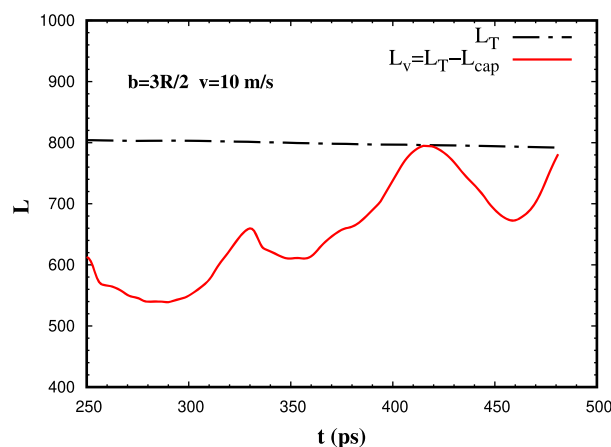


FIG. 9. Time evolution of the total angular momentum and of the vortex contribution L_v , estimated by subtracting the angular momentum due to capillary waves L_{cap} from the total angular momentum L (see the text) for $\text{He}_{500} + \text{He}_{500}$ merging collision with impact parameter $b = 3R/2$ and initial droplet velocity $v = 10 \text{ m/s}$.

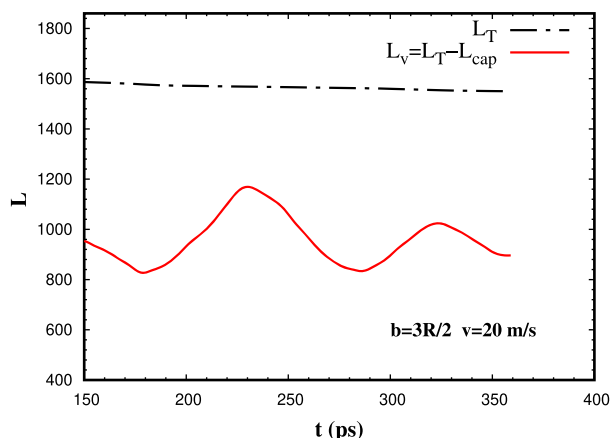


FIG. 10. Time evolution of the total angular momentum and of the vortex contribution L_v , estimated by subtracting the angular momentum due to capillary waves L_{cap} from the total angular momentum L (see the text) for $\text{He}_{500} + \text{He}_{500}$ merging collision with impact parameter $b = 3R/2$ and initial droplet velocity $v = 20$ m/s.

IV. SUMMARY AND CONCLUDING REMARKS

We have addressed binary collisions of superfluid helium drops within the He-DFT approach. The simulations have been carried out for ${}^4\text{He}_{500}$ droplets and several values of the impact parameter and relative velocity. To see the influence of droplet asymmetry, we have also addressed the collision of two droplets with different numbers of atoms. Asymmetric collisions seem to favor the appearance of an odd number of vortices, whereas this number can only be even in binary collisions of equal sized droplets.

Not surprisingly, collisions of superfluid ${}^4\text{He}$ droplets display similarities with classical droplet collisions. In both cases, the merged droplet is highly deformed and rotates in order to maintain the angular momentum involved in the collision: compare, e.g., the morphology of the droplets shown in Ref. 36 with those displayed in this work. The substantial difference between both situations is the ubiquitous appearance of quantized vortices in the case of helium, made possible within the He-TDDFT framework. In addition to this important point, the He-TDDFT approach differs from classical ones based on the solution of the Navier–Stokes or Euler equations, in which the former takes into account the finite range of the van der Waals interaction, which facilitates droplet merging for grazing and distal collisions, whereas it is not possible for the latter approaches, where droplet interaction is mediated by the surface tension and kinetic energy of the colliding droplets.

Computational limitations make it impossible to implement the He-TDDFT method in the experimental conditions under which very large droplets are made, which involve a much larger number of atoms at smaller relative velocities.^{17–19} Yet, an interesting conclusion is readily transferable to that experimental situation. Using a nozzle shape specifically devised to reduce angular momentum acquisition when droplets travel through the source chamber, a recent experiment¹⁹ still identified a few vortex-hosting droplets from the appearance of Xe filament-shaped structures in x-ray diffraction images. These observations suggest that droplet collisions

produced during the expansion from the source chamber might be the cause of angular momentum acquisition and subsequent vortex nucleation. Our calculations make this scenario plausible. On the one hand, we have found that quantum vortices are readily nucleated by the surface indentations mechanism, yielding vortex rings (which carry no angular momentum) for head-on collisions, and off center vortices (which carry angular momentum, although smaller than centered vortices) for non-zero impact parameter collisions. Since indentations appear whenever droplets merge, the indentation mechanism is independent of the droplet size.

In addition, we have unexpectedly found that, even for grazing and distal collisions, droplets coalesce at relative velocities as large as 40 m/s instead of stretching and separating again; these velocities are much larger than those found in the experiments.^{17–19} Thus, droplet collisions over a broad interval of impact parameters and relative velocities would lead to vortex nucleation.

Our simulations also show that droplet–droplet collisions could also nucleate vortices in smaller droplets, in the range of a thousand atoms. Unfortunately, a systematic study allowing for a prediction of the fraction of droplets susceptible to host a vortex in experimental conditions is out of reach due to the computational cost of the simulations. Vortex appearance would be favored in conditions where velocity spread is larger. So far, no convincing way of detecting them in small droplets has been demonstrated.

He-TDDFT simulations have other unavoidable limitations. On the one hand, the method is strictly a zero temperature approach, and there is no dissipation; energy can only be lost by atom evaporation, whereas any residual viscosity remaining in the system would contribute to stabilize the merged droplet and damp density oscillations. On the other hand, due to the limited time elapsed by the simulations, droplets do not reach the stationary state of apparent rotation and stabilized vortex array structures found in the experiments.^{3,6}

SUPPLEMENTARY MATERIAL

See the supplementary material for the video files showing the real time evolution of the processes discussed in the present work.

ACKNOWLEDGMENTS

We are very indebted to Rico Tanyag and Thomas Möller for their useful exchanges. A computer grant from CALMIP high performance computer center (Grant No. P1039) is gratefully acknowledged. This work has been performed under Grant No. PID2020-114626GB-I00 from the MICIN/AEI/10.13039/501100011033 and benefited from COST, Action CA21101 “Confined molecular systems: form a new generation of materials to the stars” (COSY), supported by COST (European Cooperation in Science and Technology).

AUTHOR DECLARATIONS

Conflict of Interest

The authors have no conflicts to disclose.

Author Contributions

Ernesto García-Alfonso: Data curation (lead); Investigation (equal); Visualization (lead). **Francesco Ancilotto:** Conceptualization (equal); Data curation (equal); Formal analysis (equal); Investigation (equal); Methodology (equal); Supervision (equal); Validation (equal); Visualization (equal); Writing – original draft (equal); Writing – review & editing (equal). **Manuel Barranco:** Conceptualization (equal); Data curation (equal); Formal analysis (equal); Investigation (equal); Methodology (equal); Supervision (equal); Validation (equal); Visualization (equal); Writing – original draft (equal); Writing – review & editing (equal). **Martí Pi:** Conceptualization (equal); Data curation (equal); Formal analysis (equal); Investigation (equal); Methodology (equal); Supervision (equal); Validation (equal); Visualization (equal); Writing – original draft (equal); Writing – review & editing (equal). **Nadine Halberstadt:** Conceptualization (equal); Data curation (equal); Formal analysis (equal); Investigation (equal); Methodology (equal); Supervision (equal); Validation (equal); Visualization (equal); Writing – original draft (equal); Writing – review & editing (equal).

DATA AVAILABILITY

The data that support the findings of this study are available from the corresponding author upon reasonable request.

REFERENCES

- J. P. Toennies and A. F. Vilesov, *Angew. Chem., Int. Ed.* **43**, 2622 (2004).
- Molecules in Superfluid Helium Nanodroplets, Topics in Applied Physics*, edited by A. Slenczka and J. P. Toennies (Springer, 2022), Vol. 145.
- L. F. Gomez, K. R. Ferguson, J. P. Cryan, C. Bacellar, R. M. P. Tanyag, C. Jones, S. Schorb, D. Anielski, A. Belkacem, C. Bernardo, R. Boll, J. Bozek, S. Carron, G. Chen, T. Delmas, L. Englert, S. W. Epp, B. Erk, L. Foucar, R. Hartmann, A. Hexemer, M. Huth, J. Kwok, S. R. Leone, J. H. S. Ma, F. R. N. C. Maia, E. Malmerberg, S. Marchesini, D. M. Neumark, B. Poon, J. Prell, D. Rolles, B. Rudek, A. Rudenkov, M. Seifrid, K. R. Siefertmann, F. P. Sturm, M. Swiggers, J. Ullrich, F. Weise, P. Zwart, C. Bostedt, O. Gessner, and A. F. Vilesov, *Science* **345**, 906 (2014).
- O. Gessner and A. F. Vilesov, *Annu. Rev. Phys. Chem.* **70**, 173 (2019).
- B. Langbehn, K. Sander, Y. Ovcharenko, C. Peltz, A. Clark, M. Coreno, R. Cucini, M. Drabbels, P. Finetti, M. Di Fraia, L. Giannessi, C. Grazioli, D. Iablonskyi, A. C. LaForge, T. Nishiyama, V. Oliver Álvarez de Lara, P. Piseri, O. Plekan, K. Ueda, J. Zimmermann, K. C. Prince, F. Stienkemeier, C. Callegari, T. Fennel, D. Rupp, and T. Möller, *Phys. Rev. Lett.* **121**, 255301 (2018).
- S. M. O. O'Connell, R. M. P. Tanyag, D. Verma, Ch. Bernardo, W. Pang, C. Bacellar, C. A. Saladrigas, J. Mahl, B. W. Toulson, Y. Kumagai, P. Walter, F. Ancilotto, M. Barranco, M. Pi, Ch. Bostedt, O. Gessner, and A. F. Vilesov, *Phys. Rev. Lett.* **124**, 215301 (2020).
- M. Pi, J. M. Escartín, F. Ancilotto, and M. Barranco, *Phys. Rev. B* **104**, 094509 (2021).
- D. Mateo, A. Leal, A. Hernando, M. Barranco, M. Pi, F. Cargnoni, M. Mella, X. Zhang, and M. Drabbels, *J. Chem. Phys.* **140**, 131101 (2014).
- A. Leal, D. Mateo, A. Hernando, M. Pi, M. Barranco, A. Ponti, F. Cargnoni, and M. Drabbels, *Phys. Rev. B* **90**, 224518 (2014).
- F. Coppens, A. Leal, M. Barranco, N. Halberstadt, and M. Pi, *J. Low Temp. Phys.* **187**, 439 (2017).
- J. D. Close, F. Federmann, K. Hoffmann, and N. Quaa, *J. Low Temp. Phys.* **111**, 661 (1998).
- A. Hernando, M. Barranco, R. Mayol, M. Pi, and M. Krosnicki, *Phys. Rev. B* **77**, 024513 (2008).
- E. García-Alfonso, F. Coppens, M. Barranco, M. Pi, F. Stienkemeier, and N. Halberstadt, *J. Chem. Phys.* **152**, 194109 (2020).
- J. Harms, J. P. Toennies, and F. Dalfovo, *Phys. Rev. B* **58**, 3341 (1998).
- J. Harms, J. P. Toennies, M. Barranco, and M. Pi, *Phys. Rev. B* **63**, 184513 (2001).
- C. L. Vicente, C. Kim, H. J. Maris, and G. M. Seidel, *J. Low Temp. Phys.* **121**, 627 (2000).
- R. M. P. Tanyag, A. J. Feinberg, S. M. O. O'Connell, and A. F. Vilesov, *J. Chem. Phys.* **152**, 234306 (2020).
- K. Kolatzki, M. L. Schubert, A. Ulmer, T. Möller, D. Rupp, and R. M. P. Tanyag, *Phys. Fluids* **34**, 012002 (2022).
- A. Ulmer, A. Heilrath, B. Senfftleben, S. M. O. O'Connell-Lopez, B. Kruse, L. Seiffert, K. Kolatzki, B. Langbehn, A. Hoffmann, T. M. Baumann, R. Boll, A. S. Chatterley, A. De Fanis, B. Erk, S. Erukala, A. J. Feinberg, T. Fennel, P. Grychtol, R. Hartmann, M. Ilchen, M. Izquierdo, B. Krebs, M. Kuster, T. Mazza, J. Montaña, G. Noffz, D. E. Rivas, D. Schlosser, F. Seel, H. Stapelfeldt, L. Strüder, J. Tiggesbäumker, H. Yousef, M. Zabel, P. Ziolkowski, M. Meyer, Y. Ovcharenko, A. F. Vilesov, T. Möller, D. Rupp, and R. M. P. Tanyag, "Generation of large vortex-free superfluid helium nanodroplets," *Phys. Rev. Lett.* (to be published) (2023); [arXiv:2302.07355v3](https://arxiv.org/abs/2302.07355v3).
- R. E. Grisenti and J. P. Toennies, *Phys. Rev. Lett.* **90**, 234501 (2003).
- F. Ancilotto, M. Barranco, F. Coppens, J. Eloranta, N. Halberstadt, A. Hernando, D. Mateo, and M. Pi, *Int. Rev. Phys. Chem.* **36**, 621 (2017).
- M. Barranco, F. Coppens, N. Halberstadt, A. Hernando, A. Leal, D. Mateo, R. Mayol, and M. Pi, Zero temperature DFT and TDDFT for ${}^4\text{He}$: A short guide for practitioners, <https://github.com/bcntls2016/DFT-Guide/blob/master/dft-guide.pdf>.
- M. Barranco, R. Guardiola, S. Hernández, R. Mayol, J. Navarro, and M. Pi, *J. Low Temp. Phys.* **142**, 1 (2006).
- F. Dalfovo, A. Lastrì, L. Pricapenko, S. Stringari, and J. Treiner, *Phys. Rev. B* **52**, 1193 (1995).
- L. Pitaevskii and S. Stringari, *Bose-Einstein Condensation and Superfluidity, International Series of Monographs on Physics* (Oxford University Press, 2016), Vol. 164.
- C. F. Barenghi and N. G. Parker, *A Primer on Quantum Fluids* (Springer Briefs in Physics, 2016).
- Progress in Low Temperature Physics*, edited by M. Tsubota and W. P. Halperin (Elsevier, Amsterdam; London, 2009), Vol. XVI.
- J. M. Escartín, F. Ancilotto, M. Barranco, and M. Pi, *Phys. Rev. B* **99**(14), 140505 (2019).
- J. M. Escartín, F. Ancilotto, M. Barranco, and M. Pi, *Phys. Rev. B* **105**, 024511 (2022).
- G. Ferioli, G. Semeghini, L. Masi, G. Giusti, G. Modugno, M. Inguscio, A. Gallemí, A. Recati, and M. Fattori, *Phys. Rev. Lett.* **122**, 090401 (2019).
- V. Cikojević, L. V. Markić, M. Pi, M. Barranco, F. Ancilotto, and J. Boronat, *Phys. Rev. Res.* **3**, 043139 (2021).
- M. Guilleumas, M. Pi, M. Barranco, and E. Suraud, *Z. Phys. D: At., Mol. Clusters* **34**, 35 (1995).
- A. Menchaca-Rocha, A. Cuevas, M. Chapa, and M. Silva, *Phys. Rev. E* **47**, 1433 (1993).
- A. Menchaca-Rocha, F. Huidobro, A. Martínez-Davalos, K. Michaelian, A. Perez, V. Rodriguez, and N. Cárjan, *J. Fluid Mech.* **346**, 291 (1997).
- C. Ngô, *Prog. Part. Nucl. Phys.* **16**, 139 (1986).
- N. Nikolopoulos, A. Theodorakakos, and G. Bergeles, *Int. J. Heat Mass Transfer* **52**, 4160 (2009).
- C. R. Anthony, P. M. Kamat, M. T. Harris, and O. A. Basaran, *Phys. Rev. Fluids* **4**, 093601 (2019).
- J. Hoepffner and G. Paré, *J. Fluid Mech.* **734**, 183 (2013).
- F. Ancilotto, M. Barranco, and M. Pi, *J. Chem. Phys.* **158**, 144306 (2023).
- E. García-Alfonso, M. Barranco, D. A. Bonhommeau, N. Halberstadt, M. Pi, and F. Calvo, *J. Chem. Phys.* **157**, 014106 (2022).
- F. Ancilotto, M. Barranco, F. Caupin, R. Mayol, and M. Pi, *Phys. Rev. B* **72**, 214522 (2005).
- M. Pi, F. Ancilotto, F. Coppens, N. Halberstadt, A. Hernando, A. Leal, D. Mateo, R. Mayol, and M. Barranco, ${}^4\text{He}$ -DFT BCN-TLS: A Computer Package for Simulating Structural Properties and Dynamics of Doped Liquid Helium-4 Systems, <https://github.com/bcntls2016/>.
- M. Frigo and S. G. Johnson, *Proc. IEEE* **93**, 216 (2005).

⁴⁴A. Ralston and H. S. Wilf, *Mathematical Methods for Digital Computers* (John Wiley and Sons, New York, 1960).

⁴⁵D. Mateo, D. Jin, M. Barranco, and M. Pi, *J. Chem. Phys.* **134**, 044507 (2011).

⁴⁶G. H. Bauer, R. J. Donnelly, and W. F. Vinen, *J. Low Temp. Phys.* **98**, 47 (1995).

⁴⁷K. K. Lehmann and R. Schmied, *Phys. Rev. B* **68**, 224520 (2003).

⁴⁸J. P. Toennies, *Molecules in Superfluid Helium Nanodroplets*, *Topics in Applied Physics*, edited by A. Slenczka and J. P. Toennies (Springer, 2022), Vol. 145, p. 1.

⁴⁹M. Lewerenz, B. Schilling, and J. P. Toennies, *Chem. Phys. Lett.* **206**, 381 (1993).

⁵⁰F. Ancilotto, M. Barranco, and M. Pi, *Phys. Rev. B* **97**, 184515 (2018).

⁵¹F. Coppens, F. Ancilotto, M. Barranco, N. Halberstadt, and M. Pi, *Phys. Chem. Chem. Phys.* **19**, 24805 (2017).

 CHAPTER VIIALKALI SPECTROSCOPY FOR
VORTEX DETECTION IN
NANODROPLETS

VII-1. Ak@⁴He₁₀₀₀

Quantum vortices have been detected in droplets made of 10^8 - 10^{10} ⁴He atoms by Gomez *et al* [121,122] using X-ray diffraction of individual droplets. When these droplets go through the nozzle (see any experimental setup involving helium droplets Ref [121] for instance) they can acquire enough angular momentum to nucleate vortices which become quantum vortices upon the normal to superfluid transition. Such big droplets could be analyzed as single objects by X-ray and extreme ultraviolet (XUV) light using intense high harmonics sources [122]. This has made it possible to determine their shapes and, doping them with Xe atoms [123], the presence of vortices, confirming their superfluid nature. However, this technique is not applicable to smaller droplets, and no experimental signature of the presence of a vortex has been found in droplets made of several thousand helium atoms so far. One possible reason could be that there are no vortices in these smaller droplet, or that there is no method for their detection.

We study here a simple method as a good possibility for detecting quantum vortices in droplets of small sizes. It is based on the light absorption or fluorescence excitation spectroscopy of alkali atoms attached to superfluid ⁴He₁₀₀₀ droplets. Since a linear vortex has an empty core of about 1 Å radius, an alkali (Ak) atom at the droplet surface would sit deeper at the “mouth” of the vortex, and this should affect its electronic spectroscopy

Since light absorption spectroscopy is very sensitive to the impurity environment, it is a good candidate as a tool for detecting impurities attached to vortices. We have calculated the absorption spectrum of alkali (Ak) atoms from Li to Cs when attached to a vortex line in a superfluid droplet and compared to the same spectrum with no vortex. The goal is to provide a quantitative answer to the size of the shift that can be expected and therefore to the possibility for photon absorption experiments to detect the presence of vortices. The absorption spectrum of alkali atoms attached to He droplets has been thoroughly studied experimentally in the past (see Refs [124-129]), and earlier works have simulated photon absorption spectra of alkali atoms attached to vortex-free helium nanodroplets using different functionals and/or He-alkali pair potentials [22,124-125,130-132]. We have repeated them in order to ensure comparison with vortex-hosting droplets with exactly the same parameters. To the best of our knowledge, the spectrum of alkali atoms attached to vortex-hosting droplets has not been previously addressed theoretically

VII-2. Method

We make use of the ⁴He-Density Functional Theory (⁴He-DFT) [22] to calculate the equilibrium configuration and energetics of alkali atoms attached to a droplet without or with a vortex, since it can correctly describes the influence of a quantum vortex on the helium density.

Once the equilibrium state has been reached for both conditions we proceed to perform the dipole absorption spectrum of the alkali.

Absorption spectra were computed by generating a large number ($nc \approx 10^6$) of helium-impurity configurations. Each configuration consisted of N ⁴He atoms positions and that of the impurity (Ak). If the impurity is treated quantum mechanically we additionally sample its position using the zero-point distribution $|\phi^{gs}(\mathbf{r})|^2$ and V_m^{ex} is the m^{th} eigenvalue of the excited potential. The absorption spectrum is finally obtained as a histogram of the absorption line positions, calculated as the energy difference between the excited and ground state, corresponding to each configuration. See Annex C for further details.

VII-3. Results

When the droplet hosts a vortex line, the Ak atom sits deeper (and the dimple is deeper too) into the helium droplet.

Figure VII.2 displays the absorption spectrum of Li from the 2s state to the 2p excited electronic state, denoted as ($2p \leftarrow 2s$), Na ($3p \leftarrow 3s$), K ($4p \leftarrow 4s$), Rb ($5p \leftarrow 5s$) and Cs ($6p \leftarrow 6s$). In the case of Li, Na and K a quantum treatment was applied. We also used a classical treatment for Na, K in order to ascertain the importance of quantum effects. For the heavier alkalis like Rb and Cs, only a classical treatment was implemented.

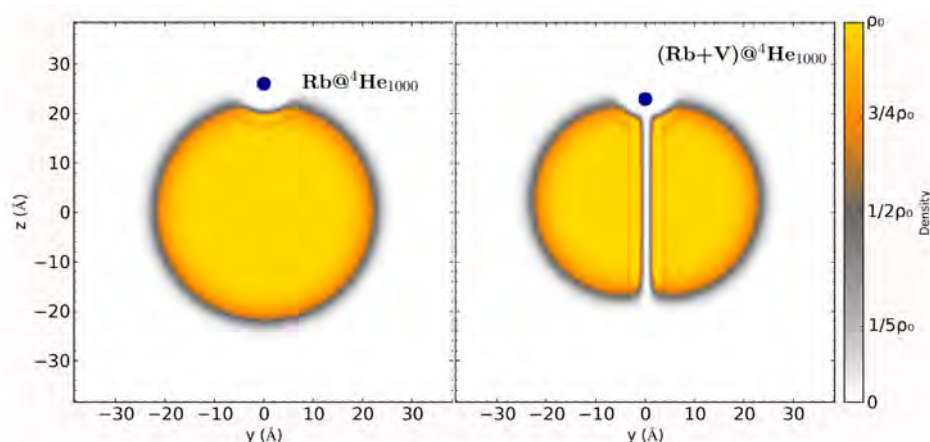


Figure VII.1. 2D density in a plane of symmetry of a ⁴He₁₀₀₀ droplet doped with a Rb atom (blue dot). The color bar shows the ⁴He atom density in units of Å⁻³. Left: vortex-free droplet; right: vortex-hosting droplet

Next, we explored the idea of higher excited ($n' > n$) electronic states since the electronic orbital is then more diffuse and more extended. Therefore its sensitivity to changes in the surrounding helium density is increased (the helium-electron interaction is repulsive). Absorption spectra to ($n' > n$) excited states could thus reveal more differences between vortex-hosting and vortex-free droplets than $np \leftarrow ns$ ones. Figure VII.3 shows the only three cases studied K: $5s \leftarrow 4s$, Rb: $6p \leftarrow 5s$ and Cs $7s \leftarrow 6s$.

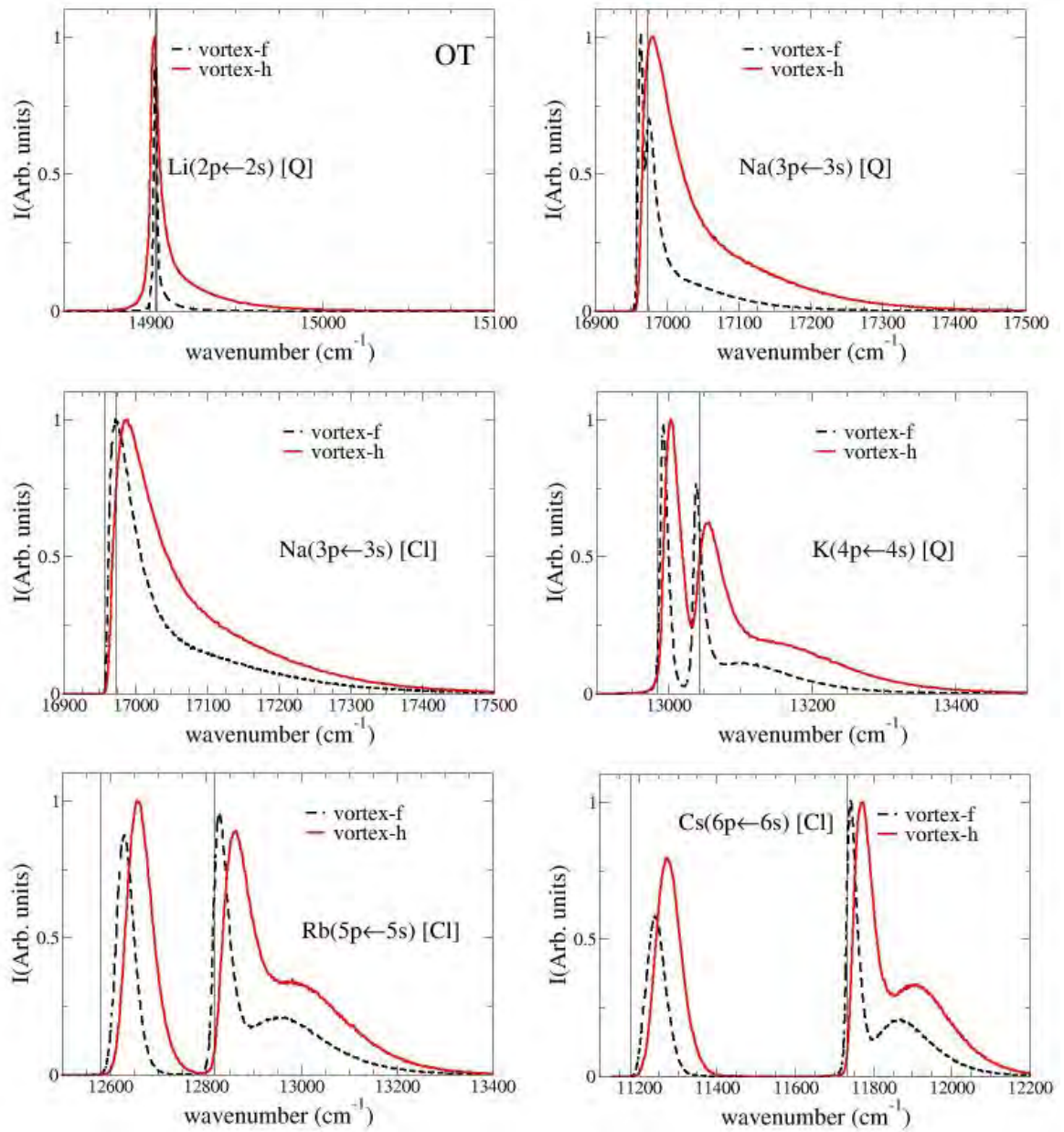


Figure VII.2. Absorption spectrum $np \leftarrow ns$: Li ($2p \leftarrow 2s$) (quantum), Na ($3p \leftarrow 3s$) (classical and quantum treatment), K ($4p \leftarrow 4s$), Rb ($5p \leftarrow 5s$) and Cs ($6p \leftarrow 6s$). For all spectra graphs the black line corresponds to a vortex free droplet and the red one to a droplet hosting a vortex line.

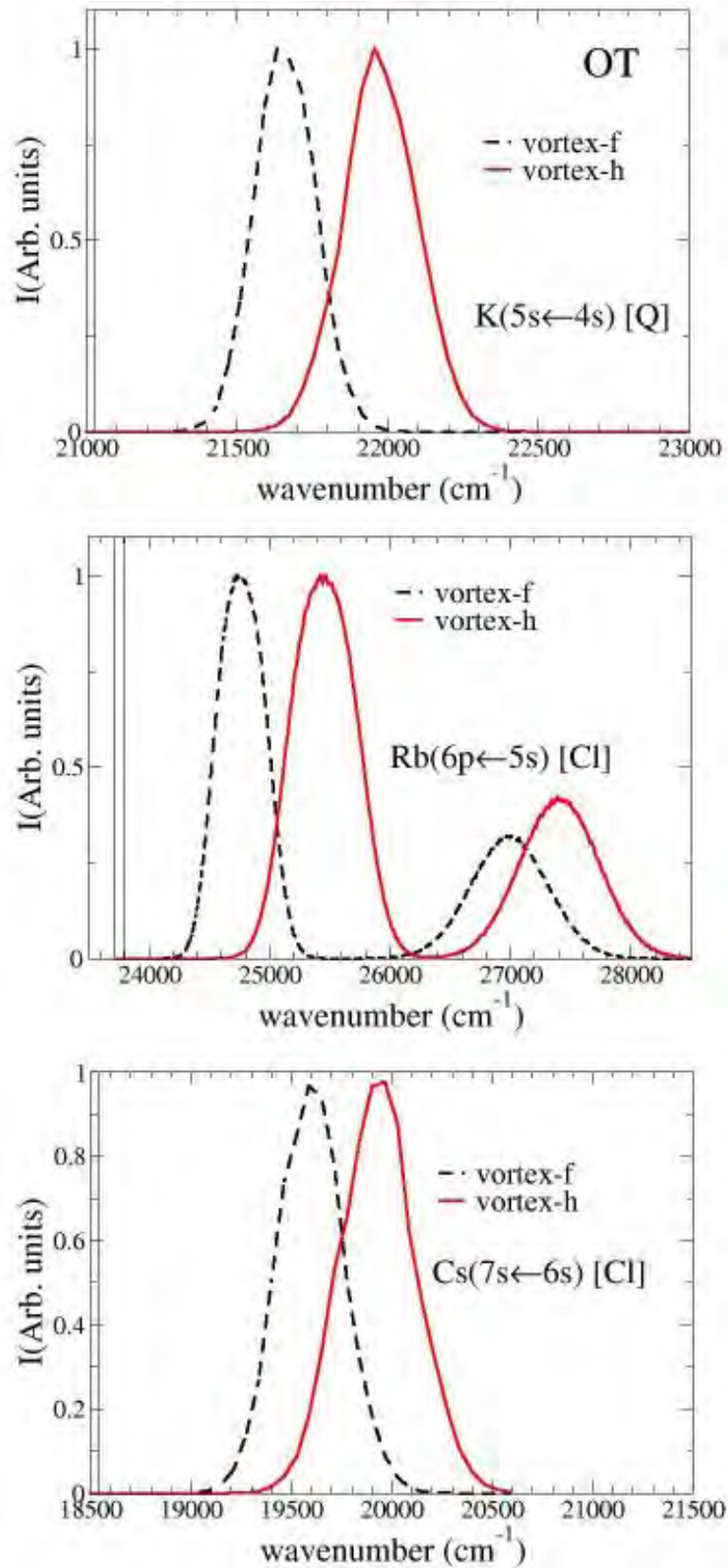


Figure VII.3. Absorption spectrum K: $5s \leftarrow 4s$, Rb: $6p \leftarrow 5s$ and Cs $7s \leftarrow 6s$. For all spectra graphs the black line corresponds to a vortex free droplet and the red one to a droplet hosting a vortex line.

VII-4. Conclusion

Our simulation results predict a blue-shifted (higher frequencies) and broadened spectrum in vortex hosting droplets compared to vortex-free droplets, both for $np \leftarrow ns$ and ($n's \leftarrow ns$, $n'p \leftarrow ns$) transitions respectively. This shift comes from the fact that an alkali atom sits deeper into the droplet when a vortex is present, which is visible in its dimple depth. These spectral modifications are insufficient for vortex detection in the case of $np \leftarrow ns$ excitation but for higher $n'p \leftarrow ns$ or $n's \leftarrow ns$ ($n' > n$) excitations, where the excited state orbital is more extended and therefore more sensitive to changes in the surrounding helium density, the spectral modifications are more important and could lead to vortex detection.

Alkali atoms attached to vortex-hosting helium nanodroplets

Cite as: J. Chem. Phys. 152, 194109 (2020); doi: 10.1063/5.0008923

Submitted: 26 March 2020 • Accepted: 3 May 2020 •

Published Online: 20 May 2020



View Online



Export Citation



CrossMark

Ernesto García-Alfonso,^{1,2} Francois Coppens,² Manuel Barranco,^{2,3,4} Martí Pi,^{3,4,a)} Frank Stienkemeier,^{5,b)} and Nadine Halberstadt^{2,c)}

AFFILIATIONS

¹Facultad de Física, Universidad de La Habana, 10400 La Habana, Cuba

²Université Toulouse 3 and CNRS, Laboratoire des Collisions, Agrégats et Réactivité, IRSAMC, 118 route de Narbonne, F-31062 Toulouse Cedex 09, France

³Departament FQA, Facultat de Física, Universitat de Barcelona, Diagonal 645, 08028 Barcelona, Spain

⁴Institute of Nanoscience and Nanotechnology (IN2UB), Universitat de Barcelona, Barcelona, Spain

⁵Physikalisches Institut, Universität Freiburg, 79104 Freiburg, Germany

^{a)} Author to whom correspondence should be addressed: marti@fqa.ub.edu

^{b)} Electronic mail: stienkemeier@uni-freiburg.de

^{c)} Electronic mail: Nadine.Halberstadt@irsamc.ups-tlse.fr

ABSTRACT

Light absorption or fluorescence excitation spectroscopy of alkali atoms attached to ⁴He droplets is investigated as a possible way for detecting the presence of vortices. To this end, we have calculated the equilibrium configuration and energetics of alkali atoms attached to a ⁴He₁₀₀₀ droplet hosting a vortex line using ⁴He density functional theory. We use them to study how the dipole absorption spectrum of the alkali atom is modified when the impurity is attached to a vortex line. Spectra are found to be blue-shifted (higher frequencies) and broadened compared to vortex-free droplets because the dimple in which the alkali atom sits at the intersection of the vortex line and the droplet surface is deeper. This effect is smaller for lighter alkali atoms and all the more so when using a quantum description since, in this case, they sit further away from the droplet surface on average due to their zero-point motion. Spectral modifications due to the presence of a vortex line are minor for $np \leftarrow ns$ excitation and therefore insufficient for vortex detection. In the case of higher $n'p \leftarrow ns$ or $n's \leftarrow ns$ ($n' > n$) excitations, the shifts are larger as the excited state orbital is more extended and therefore more sensitive to changes in the surrounding helium density.

Published under license by AIP Publishing. <https://doi.org/10.1063/5.0008923>

I. INTRODUCTION

⁴He droplets nucleated in supersonic beam experiments at a temperature of about 0.37 K.¹ At this temperature, they become superfluid, which makes them ideal ultra-cold matrices for spectroscopy studies of captured dopants. They are also ideal laboratories for addressing superfluidity at the nanoscale.^{2–6} In particular, they may host quantized vortices, a dramatic fingerprint of the superfluid state.^{7–9} Since their existence was proposed by Onsager and Feynman, the study and detection of quantized vortices in superfluid and superconducting systems has not ceased, which attracts the interest of physicists and chemists working in low temperature processes, semiconductors, quantum optics, and atomic and molecular

physics and chemistry. It is hard to find a more widespread subject of study.

Quantized vortices are ubiquitous in quantum systems under rotation, e.g., liquid helium samples at temperatures below 2.17 K (the superfluid transition temperature),⁷ cold-gas Bose–Einstein condensates,¹⁰ and electron droplets in low-dimensional quantum dots in a magnetic field.¹¹ However, the only small self-bound system where vortices are likely to occur is a ⁴He droplet.^{12,13}

So far, no clear experimental signature of vortex formation in small ⁴He droplets has been found, although this has been the subject of several experimental and theoretical proposals and studies. Many of them involve light absorption or laser-induced fluorescence excitation spectroscopy, which usually gives similar spectra, the

former being easier to simulate theoretically and the latter being easier to measure experimentally: we will refer to them as light absorption spectroscopy, or simply absorption spectroscopy, throughout this article. Close *et al.*¹⁴ suggested the light absorption spectrum of Ag atoms in the bulk of superfluid droplets as a possible candidate: if Ag atoms are attached to the vortex line, their environment changes, and this could be reflected in the absorption spectrum. To our knowledge, this possibility has never been explored. Along the same line, a theoretical study has been carried out for electron bubbles attached to vortex lines in superfluid liquid helium as a function of pressure. It was shown that the electron absorption spectrum is shifted by the presence of a vortex line, but the shift is too small to be experimentally detectable.¹⁵

Another theoretical proposal,¹⁶ which has not been tested experimentally either, suggested that microwave absorption spectroscopy of a Ca dopant could show a difference when a vortex was present. More recently, absorption spectroscopy was also suggested¹⁷ for the same dopant. The rationale is basically the same as for Ag atoms: the change induced in the dopant environment due to its binding to a vortex line would translate as a change in the absorption spectrum. Ca impurities are known to reside in a deep dimple at the surface of the helium droplet.¹⁷ Their binding to a vortex line would result in their further sinking inside the droplet. As a result, their absorption spectrum would evolve from that of an impurity on the droplet surface to that of an impurity in its bulk. Hence, a satellite peak should appear, which would be blue-shifted from the main peak, with an intensity depending on the number of vortex-hosting droplets. Inspection of existing experimental results¹⁸ showed no such signature.

It is worth stressing that these proposals and experiments involve droplets made of several thousand He atoms created by the adiabatic expansion of a helium gas into vacuum.¹ All attempts to detect the presence of vortices in droplets of this size have failed so far. Very recently, large ⁴He droplets made of 10⁸–10¹¹ atoms have been created using the hydrodynamic instability of a cryogenic liquid helium jet passing through the nozzle of a molecular beam apparatus, as reviewed in Refs. 9 and 19. Helium drops, which are initially produced in the normal, non-superfluid phase, can acquire angular momentum during the passage of the fluid through the nozzle. Such droplets could be analyzed as single objects by x-ray and extreme ultraviolet (XUV) light using intense high harmonics sources.^{20,21} This has made it possible to determine their shapes and, doping them with Xe atoms,^{20,22} the presence of vortices, confirming their superfluid nature.

The following questions therefore arise: why have vortices not been detected in smaller droplets (10³–10⁴ atoms)? Is it because no clear signature of their presence has been found yet? Or is it because vortices are too scarce due to the droplet formation and doping mechanisms? Let us recall that droplets containing a few thousand He atoms are produced in subcritical conditions by atom condensation and evaporative cooling,¹ which does not favor deposition of large amounts of angular momentum in the droplet. Some angular momentum is transferred to the droplet during the impurity pickup, which does nucleate vortex rings and loops.^{23–26} However, they are dynamically unstable. At variance, large droplets such as those detected as single objects using x-ray or XUV light are created using hydrodynamic instabilities of a very cold but non-superfluid He jet. They can acquire a large amount of angular momentum

during their passage through the nozzle of the experimental apparatus. When the droplets become superfluid, this angular momentum helps to nucleate vortex arrays stable enough to be experimentally detected.^{20,22}

Since light absorption spectroscopy is very sensitive to the impurity environment, it is a good candidate as a tool for detecting impurities attached to vortices. We have therefore calculated the absorption spectrum of alkali (Ak) atoms from Li to Cs when attached to a vortex line in a superfluid droplet and compared to the same spectrum with no vortex. The goal is to provide a quantitative answer to the size of the shift that can be expected and therefore to the possibility for photon absorption experiments to detect the presence of vortices. The absorption spectrum of alkali atoms attached to He droplets has been thoroughly studied experimentally in the past (see, e.g., Refs. 27–32), and earlier works have simulated photon absorption spectra of alkali atoms attached to vortex-free helium nanodroplets using different functionals and/or He-alkali pair potentials.^{27,28,33–37} We have repeated them in order to ensure comparison with vortex-hosting droplets with exactly the same parameters. To the best of our knowledge, the spectrum of alkali atoms attached to vortex-hosting droplets has not been previously addressed theoretically.

This article is organized as follows: In Sec. II, we outline the ⁴He Density Functional Theory (⁴He-DFT) approach used to simulate doped ⁴He droplets and their photon absorption spectrum. The results are presented and discussed in Sec. III, and a summary and outlook are given in Sec. IV.

II. THE ⁴He-DFT APPROACH

We have used the ⁴He-DFT method to describe superfluid helium droplets. We refer the interested reader to Ref. 35, where one may find all the details for its application to pure and doped ⁴He drops hosting or not vortex lines. We only give here the main features and some details to help following the discussion of the results.

Within ⁴He-DFT, the total energy of a ⁴He_N droplet at zero temperature is written as a function of the ⁴He atomic density $\rho(\mathbf{r})$,

$$E[\rho] = T[\rho] + E_c[\rho] = \frac{\hbar^2}{2m} \int d\mathbf{r} |\nabla\Psi(\mathbf{r})|^2 + \int d\mathbf{r} \mathcal{E}_c[\rho], \quad (1)$$

where $T[\rho]$ is the kinetic energy, $\Psi(\mathbf{r})$ is an effective wave function defined by $\rho(\mathbf{r}) = |\Psi(\mathbf{r})|^2$, and the functional \mathcal{E}_c contains the He-He interaction term (within Hartree approximation) as well as additional terms describing non-local correlation effects. *Stricto sensu*, for vortex-free droplets, $\Psi(\mathbf{r})$ is a real function, and hence, $\Psi(\mathbf{r}) = \sqrt{\rho(\mathbf{r})}$.

The results presented in this work have been obtained using the most accurate He functional to date, namely, the Orsay-Trento functional (OT).³⁸ It includes a non-local correction to the kinetic energy and a backflow contribution. The backflow term only plays a role in the presence of density currents, which is the case in vortex-hosting droplets. Both contributions (especially the backflow term) make the OT functional computationally quite expensive. In addition to the computational cost, numerical problems arise in the case of helium samples doped with very attractive impurities.³⁵ Several

variants of the OT functional have been designed and used to circumvent this problem. The so-called “solid functional”³⁹ has become very popular in static and time-dependent applications because it contains a “penalty term” to prevent the He density to become unphysically large when the helium sample is doped with very attractive impurities. The results obtained with this simplified functional are presented in the [supplementary material](#). Because the backflow term should be the main difference between both functionals (the alkali–helium interaction is only weakly attractive), comparing the results in the [supplementary material](#) with those presented here will give an idea of the importance of this term for absorption spectra in the presence of a vortex.

For alkali-doped droplets, Eq. (1) has to be modified to include the interaction of the droplet with the dopant. For the heavier alkalis, Ak ≡ K, Rb, or Cs, which can be described as point-like, classical particles, this is simply done by adding the impurity–liquid interaction energy to the energy functional $E[\rho]$. This term, which acts as an external field for the helium density, is constructed within the pairwise sum approximation by integrating the impurity–He atom interaction, V_{Ak} , over the liquid density,

$$E[\rho] \rightarrow E[\rho] + \int d\mathbf{r} \rho(\mathbf{r}) V_{Ak}(|\mathbf{r} - \mathbf{r}_{Ak}|), \quad (2)$$

where \mathbf{r}_{Ak} is the location of the impurity.

The droplet equilibrium configuration is obtained by solving the Euler–Lagrange equation deduced from the functional minimization of Eq. (2) with respect to $\Psi(\mathbf{r})$,

$$\left\{ -\frac{\hbar^2}{2m} \nabla^2 + \frac{\delta \mathcal{E}_c}{\delta \rho} + V_{Ak}(|\mathbf{r} - \mathbf{r}_{Ak}|) \right\} \Psi(\mathbf{r}) = \mu \Psi(\mathbf{r}), \quad (3)$$

where μ is the ⁴He chemical potential for the number of He atoms in the droplet, $N \equiv \int d\mathbf{r} |\Psi(\mathbf{r})|^2$. In this work, this number is fixed to $N = 1000$. The Ak–He potentials [V_{Ak} in Eqs. (2) and (3)] have been taken from Ref. 40, except for Li–He which is from Ref. 34. The lighter Ak atoms (Na and especially Li) require a quantum mechanical treatment. This implies solving an additional Schrödinger equation for the alkali, coupled to the ⁴He–DFT equation for helium (see Ref. 35 for more details).

The results presented in this work have been obtained using the 4He–DFT BCN-TLS computing package.⁴¹ Details on how Eq. (2) is solved can be found in Refs. 35 and 42 and references therein. In short, $\Psi(\mathbf{r})$ is written on a Cartesian grid, and extensive use is made of the fast-Fourier transform to compute the convolutions entering the definition of \mathcal{E}_c . The droplet equilibrium configuration is obtained by imaginary-time relaxation for $\Psi(\mathbf{r})$.

Including vortices does not require further developments in the formalism. A vortex line along the z axis, for instance, is obtained by the imprinting procedure in which imaginary-time relaxation starts from the effective wave function³⁵

$$\Psi(\mathbf{r}) = \frac{\rho_0^{1/2}(\mathbf{r})}{\sqrt{x^2 + y^2}} (x + iy), \quad (4)$$

where $\rho_0(\mathbf{r})$ is the density corresponding to a vortex-free droplet [note that in the presence of a vortex, $\Psi(\mathbf{r})$ must be complex]. Imaginary-time relaxation eventually converges to a configuration, which is an eigenstate of the angular momentum operator \hat{L}_z with eigenvalue $N\hbar$.

We have defined the following energies to characterize the alkali–droplet equilibrium configurations:³⁵

Solvation energy of the alkali:

$$S_{Ak} = E(\text{Ak}@^4\text{He}_N) - E(^4\text{He}_N). \quad (5)$$

Vortex (V) energy:

$$E_V = E(V@^4\text{He}_N) - E(^4\text{He}_N). \quad (6)$$

Binding energy of the alkali to the vortex line:

$$B_{Ak} = E[(\text{Ak} + V)@^4\text{He}_N] - E[(\text{Ak}@V)@^4\text{He}_N] \\ = S_{Ak} + E_V - \{E[(\text{Ak}@V)@^4\text{He}_N] - E(^4\text{He}_N)\}. \quad (7)$$

A negative solvation energy implies that the impurity is attached to the droplet, and a positive binding energy of the Ak atom to the vortex implies that it is attached to the vortex line. This binding energy is the result of a delicate balance between the contributing terms, and the resulting values are rather small. Intuitively, it corresponds to the kinetic energy of the superfluid flow in the volume excluded by the impurity.⁷

III. RESULTS

A. Statics

Figure 1 shows as an example a two-dimensional (2D) cut of the He density in a symmetry plane for a Cs-doped ⁴He₁₀₀₀ droplet, without or with a vortex. The appearance is qualitatively the same for all the alkali atoms. The vortex is visible as an empty line along the vertical axis. Its presence makes the dopant distance d to the droplet center of mass shorter, which is the results of two effects: the presence of a vortex flattens the droplet, and it makes the dimple deeper in which the alkali atom sits. This is general for all alkalis, as can be checked in Table I.

Table I shows the most relevant characteristics of the calculated equilibrium configurations. As can be seen there, the binding energy to the vortex line is positive for all the alkalis, indicating that all alkali-doped vortex-hosting droplets are more stable if the alkali atom sits at the intersection of the vortex core with the surface. The binding energy increases with the atomic number, except for the heaviest one studied here, Cs, which is slightly less bound to the vortex than Rb.

Lighter alkalis require a quantum treatment, as performed earlier in vortex-free droplets.^{33,34,36} This was performed here for Li, Na, and K. Because of zero-point delocalization, they sit further away from the droplet surface when described quantum mechanically. This is quite a sizable effect, especially for Li, as can be seen in Table I. As a consequence, the Ak solvation energy in the vortex-free droplet (S_{Ak}) is reduced (in absolute value), as already observed.³⁶ The effect becomes smaller with an increase in the atomic number, as expected. The binding energy to the vortex line (B_{Ak}) increases in the quantum treatment, likely because the excluded volume already mentioned⁷ increases due to zero point delocalization of the impurity.

As indicated before, we have also used the solid functional for this study. The resulting impurity distances to the droplet center of mass, solvation, and vortex-binding energies differ only very slightly

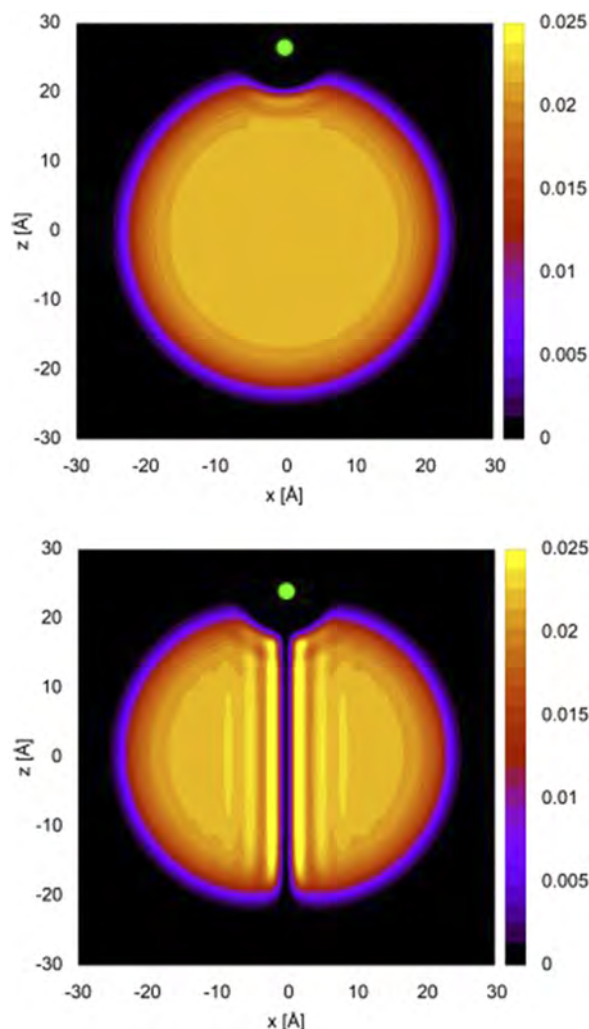


FIG. 1. 2D density in a plane of symmetry of a ⁴He₁₀₀₀ droplet doped with a Cs atom (green dot). The color bar shows the He atom density in units of Å⁻³. Top: vortex-free droplet; bottom: vortex-hosting droplet.

from the OT ones, as can be checked in Table I in the [supplementary material](#), and the qualitative conclusions are not affected.

B. Absorption spectra

We now turn to the influence of a vortex on the absorption spectrum of an alkali-doped helium droplet. Once the equilibrium configuration of the system has been determined, the absorption spectrum is calculated as explained in Ref. 17. The required excited Π and Σ Ak-He pair potentials were taken from Pascale,⁴³ except in the case of Li for which we have used those from Ref. 34. The method, semiclassical in nature, essentially yields the peak energies of the absorption spectrum and their relative intensity.

TABLE I. Influence of the presence of a vortex line V on the characteristics of an alkali doped ⁴He₁₀₀₀ droplet: total energy E and distance d of the impurity to the center of mass of the droplet. Ak@⁴He₁₀₀₀ stands for the vortex-free droplet, and (Ak@V)@⁴He₁₀₀₀ stands for the droplet hosting a linear vortex. S_{Ak} is the (vortex-free) impurity solvation energy defined in Eq. (5), and B_{Ak} is the binding energy of the impurity to the vortex line defined in Eq. (7). The results presented in this table are for the OT functional. The energy of the pure ⁴He₁₀₀₀ droplet is -5440.79 K when it is vortex-free and -5318.08 K when it hosts a linear vortex, giving $E_V = 122.71$ K for the energy for creating a vortex, Eq. (6). The asterisk in the first 3 lines of this table denotes a quantum treatment of the dopant.

Ak	Ak@ ⁴ He ₁₀₀₀		S_{Ak}	(Ak@V)@ ⁴ He ₁₀₀₀		B_{Ak}
	E (K)	d (Å)	(K)	E (K)	d (Å)	(K)
Li*	-5443.32	27.70	-2.53	-5325.24	23.66	4.63
Na*	-5446.07	26.55	-5.28	-5327.30	23.28	3.94
K*	-5447.95	26.83	-7.16	-5328.93	23.51	3.69
Li	-5450.62	25.06	-9.83	-5330.66	21.55	2.75
Na	-5450.47	25.37	-9.68	-5330.57	21.99	2.81
K	-5451.08	26.07	-10.29	-5331.11	22.96	2.74
Rb	-5451.99	26.06	-11.20	-5332.19	22.97	2.91
Cs	-5451.29	26.60	-10.50	-5331.30	23.55	2.72

The width of the spectrum comes from fluctuations in the helium density and/or, to a lesser extent, from the probability distribution given by the square of the Ak wave function when it is treated quantum mechanically. To incorporate the helium density fluctuations, we use the DF sampling method described in detail in Refs. 42 and 44. The additional spectral width originating from the dopant zero-point delocalization was negligible in comparison and was not calculated.

1. $np \leftarrow ns$ absorption spectra

Figure 2 shows the effect of a vortex on the $np \leftarrow ns$ absorption spectrum of the alkali atoms attached to a ⁴He₁₀₀₀ droplet. It can be seen that the absorption peaks are further blue-shifted and broadened in the presence of a vortex line. In addition, treating the dopant quantum mechanically decreases the shift and the width as expected since the impurity is on average further away from the droplet due to its zero point motion. This is illustrated in Fig. 2 for the case of Na and also happens for Li and K. The quantitative analysis of the corresponding spectral characteristics is presented in Table II.

Let us mention that the semiclassical approach is less justified in the case of Li for which the absorption spectrum is dominated by bound-bound transitions.^{27,34} Including them properly would require, e.g., to carry out a Fourier analysis of the time-correlation function of the Li atom moving in the full 3D ² $\Pi_{1/2}$, ² $\Pi_{3/2}$, and ² $\Sigma_{1/2}$ potentials.³⁴ Hence, the corresponding spectral characteristics are omitted in Table II. The spectrum obtained semiclassically is still presented in Fig. 2 for the sake of completeness.

It is tempting to make a direct comparison with experimental spectra that have been measured for all the calculated transitions. However, quantitative agreement of peak positions and line shapes from the DFT as well as the quality of available interaction potentials is very limited, and deviations from the measured absorption lines are beyond the vortex-induced differences calculated in this

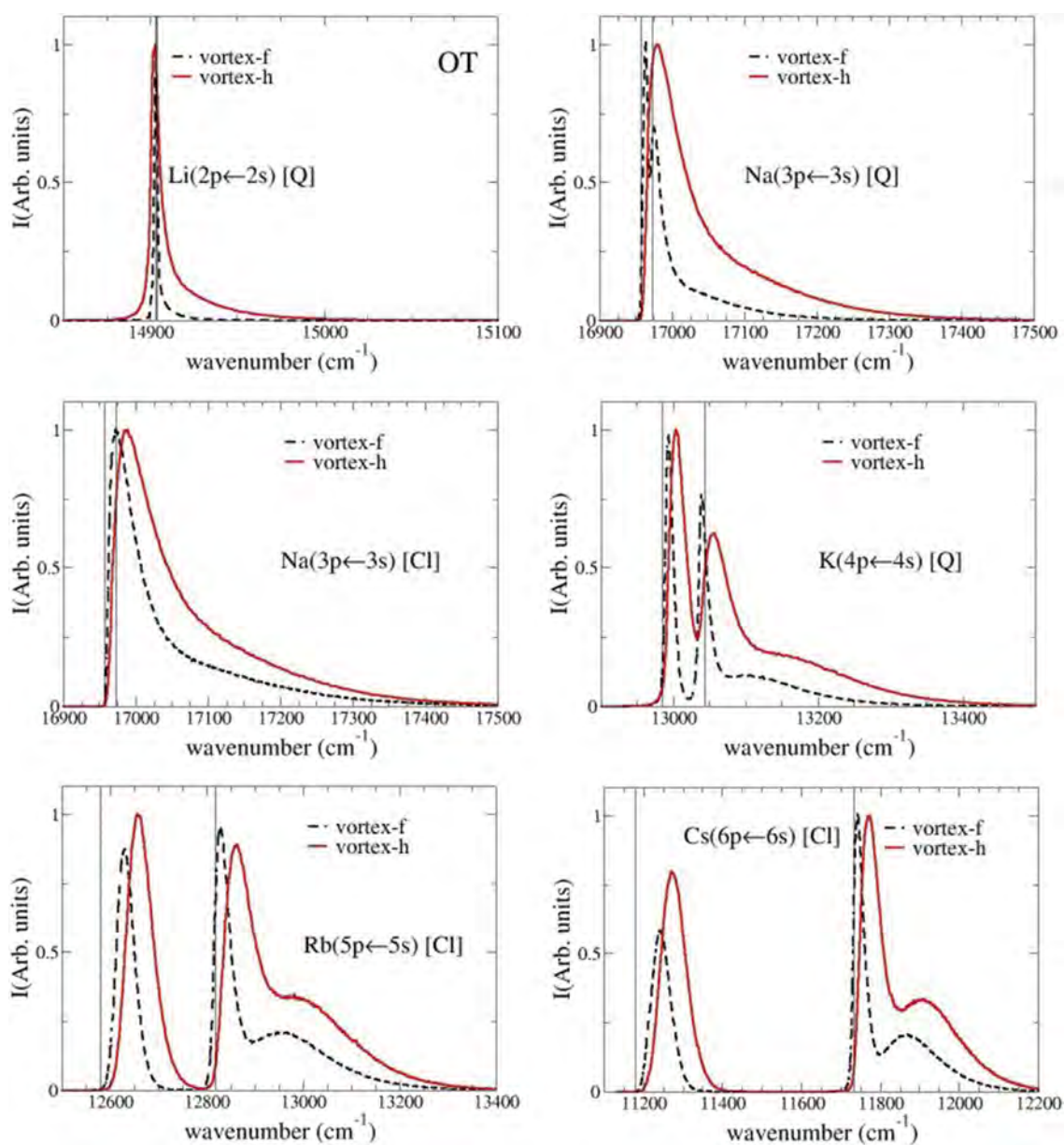


FIG. 2. $np \leftarrow ns$ absorption spectrum for the alkali-doped ${}^4\text{He}_{1000}$ droplet obtained with the OT functional. Li, Na, and K atoms are treated quantum mechanically ([Q]), whereas Rb and Cs are treated classically ([CI]). For the sake of comparison, the results for Na obtained with the classical description are also shown. Black dashed line: vortex-free (vortex-f) droplet; red solid line: vortex-hosting (vortex-h) droplet. Gas-phase atomic transitions are represented by thin vertical lines. Units are arbitrary for absorption intensity and cm^{-1} for excitation energy.

work. In particular, shifts due to the presence of a vortex are significantly smaller than the widths of the peaks. This is all the more clear when examining Table III, where the difference Δ between the shift with and without vortex is compared to the average full width at half maximum (FWHM). For all cases studied here, the average

width is of the order of twice the difference in shifts. Having said this, comparing line positions and shapes is not suited to experimentally assess the presence of vortices for these transitions. Moreover, for very large droplets, coherent diffraction imaging results suggest that the proportion of droplets hosting a vortex is only on the

TABLE II. Comparison of the spectral characteristics of an alkali atom sitting on a vortex-free (vortex-f) and vortex-hosting (vortex-h) ⁴He₁₀₀₀ nanodroplet. Second to fourth columns: energy shifts $(\Delta E)_{\text{vortex-f}}$ for the vortex-free droplet with respect to the gas-phase atomic lines, calculated from the absorption maxima for the ²Π_{1/2}, ²Π_{3/2}, and ²Σ_{1/2} final states; fifth to seventh columns: energy shifts $(\Delta E)_{\text{vortex-h}}$ for the vortex-hosting droplet; last six columns: full width at half maximum (FWHM) for each peak for the vortex-free or vortex-hosting droplet. The first six entries of this table is for $np \leftarrow ns$ absorption spectra, and the last four entries are for $(n+1)s \leftarrow ns$ or $(n+1)p \leftarrow ns$ absorption spectra. The asterisk denotes a quantum treatment of the dopant.

Ak	$(\Delta E)_{\text{vortex-f}} (\text{cm}^{-1})$						$(\Delta E)_{\text{vortex-h}} (\text{cm}^{-1})$						FWHM (cm^{-1})					
	² Π _{1/2}		² Π _{3/2}		² Σ _{1/2}		² Π _{1/2}		² Π _{3/2}		² Σ _{1/2}		² Π _{1/2}		² Π _{3/2}		² Σ _{1/2}	
	Vortex-f	Vortex-h	Vortex-f	Vortex-h	Vortex-f	Vortex-h	Vortex-f	Vortex-h	Vortex-f	Vortex-h	Vortex-f	Vortex-h	Vortex-f	Vortex-h	Vortex-f	Vortex-h	Vortex-f	Vortex-h
Na* ($3p \leftarrow 3s$)	6.4	3.1	58.3	12.9	18.5	76.5	10	21	18	43	111	132						
K* ($4p \leftarrow 4s$)	7.6	-4.5	66.4	14.8	7.0	97.8	13	22	14	34	120	135						
Na ($3p \leftarrow 3s$)	17.4	29.9	140.0	33.0	65.9	171.1	28	51	63	99	204	212						
K ($4p \leftarrow 4s$)	13.4	3.9	116.8	25.1	26.7	151.2	21	36	34	62	178	185						
Rb ($5p \leftarrow 5s$)	51.2	11.0	138.6	74.0	37.1	169.7	43	59	37	63	176	185						
Cs ($6p \leftarrow 6s$)	62.6	9.5	131.3	88.9	34.0	168.5d	57	71	31	53	158	167						
K* ($5s \leftarrow 4s$)	618.9	880.6	242	270						
K ($5s \leftarrow 4s$)	839.4	1079.3	282	307						
Rb ($6p \leftarrow 5s$)	942.6	1101.3	3205.7	1518.0	1766.8	3535.6	314	421	326	428	743	761						
Cs ($7s \leftarrow 6s$)	1070.3	1402.1	384	434						

order of a few percent,²⁰⁻²² implying that changes in the overall peak shape are at most on the same level. Although experimental spectra can readily be obtained on that level of signal-to-noise ratios, only methods being able to detect differences between vortex-free and vortex-hosting droplets would contain valuable information. As long as there are no methods at hand to specifically control the content of vortices of produced droplets in spectroscopic measurements, spectral changes will remain concealed.

2. $(n+1)s \leftarrow ns$ or $(n+1)p \leftarrow ns$ absorption spectra

The spectral characteristics of alkali-doped helium droplets are mostly governed by the usually repulsive interaction of their

TABLE III. Comparison of the energy shift difference Δ between the vortex-hosting and vortex-free droplet and Γ , the half sum of the FWHM of the spectra with or without vortex, calculated from the data in Table II.

Ak	² Π _{1/2}		² Π _{3/2}		² Σ _{1/2}	
	Δ	Γ	Δ	Γ	Δ	Γ
	(cm^{-1})	(cm^{-1})	(cm^{-1})	(cm^{-1})	(cm^{-1})	(cm^{-1})
Na* ($3p \leftarrow 3s$)	6.4	15.5	15.5	30.5	18.2	121.5
K* ($4p \leftarrow 4s$)	7.2	17.5	11.5	24	31.4	127.5
Na ($3p \leftarrow 3s$)	15.7	39.5	36.0	81	31.1	208
K ($4p \leftarrow 4s$)	11.7	28.5	22.8	48	34.4	181.5
Rb ($5p \leftarrow 5s$)	22.8	51	26.0	50	31.1	180.5
Cs ($6p \leftarrow 6s$)	26.3	74	24.5	42	37.2	162.5
K* ($5s \leftarrow 4s$)	262	256
K ($5s \leftarrow 4s$)	240.0	294.5
Rb ($6p \leftarrow 5s$)	575.3	367.5	665.5	377	329.9	752
Cs ($7s \leftarrow 6s$)	331.8	409

excited state orbital with the surrounding helium at the equilibrium configuration of the ground state. Since this orbital is more diffuse and more extended in higher ($n' > n$) electronic states, its sensitivity to changes in the surrounding helium density is increased. Hence, absorption spectra to $n' > n$ excited states could reveal more differences between vortex-hosting and vortex-free droplets than $np \leftarrow ns$ ones.

We have tested this idea on three cases, which have already been studied before in vortex-free droplets, namely, K($5s \leftarrow 4s$), Rb($6p \leftarrow 5s$), and Cs($7s \leftarrow 6s$) absorption spectra.^{32,36,45,46} Figure 3 shows the corresponding absorption spectra, and the shifts and FWHM are shown in the lower part of Table II. As expected, the difference in shifts between spectra originating from vortex-hosting and vortex-free droplets is much larger than in the $np \leftarrow ns$ spectra. They are now of the same order of magnitude as the spectral widths, as can be seen more clearly in Table III. This could make them distinguishable in the most favorable cases. Yet, several groups have examined $(n+1) \leftarrow n$ and higher transitions and did not report any unassigned shoulder or separated peak.²⁹⁻³² This is not surprising, providing, as discussed above, an expected contribution of vortices only on the percent level. Since the peak shapes and consequently also the far-out wings cannot be reproduced by the simulations on that level of accuracy, without the ability of measuring difference spectra, it will be very difficult to confirm vortices in spectroscopic measurements also at these transitions.

Checking which case would be the most favorable one for vortex-line detection would require a systematic search for all the alkalis and their $(n+1) \leftarrow n$ or even $(n+2) \leftarrow n$ transitions, which, in turn, would call for systematic improvement of the commonly used Pascale's helium-alkali interactions in the excited electronic states; for instance, the He-Rb* ($6p$) interactions are notoriously too repulsive, resulting in too large spectral shifts. This systematic study is beyond the scope of the present work.

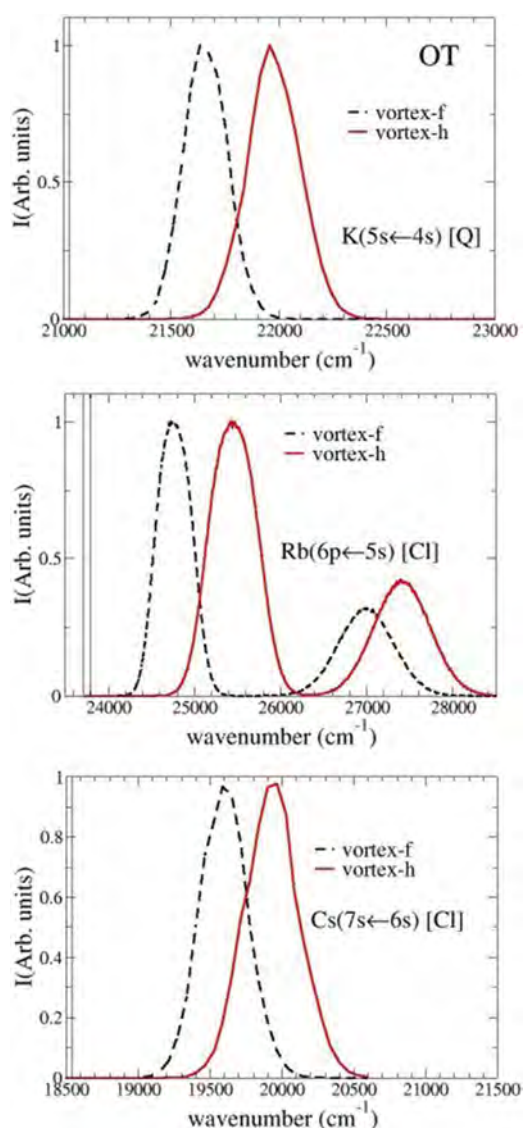


FIG. 3. Dipole absorption spectrum for $K(5s \leftarrow 4s)$ (top), $Rb(6p \leftarrow 5s)$ (middle), and $Cs(7s \leftarrow 6s)$ (bottom) transitions in a vortex-free (black dashed line) or vortex-hosting (red solid line) ${}^4\text{He}_{1000}$ droplet obtained with the OT functional. The K atom is treated quantum mechanically, and the Rb and Cs atoms are treated classically. The thin vertical lines represent gas-phase atomic transitions. Units are arbitrary for absorption intensity and cm^{-1} for excitation energy.

IV. SUMMARY AND OUTLOOK

We have investigated the possibility of using alkali absorption spectroscopy as a means of detecting the presence of vortices in a superfluid helium droplet. To this end, we have conducted ${}^4\text{He}$ -DFT simulations using the most accurate functional to date, namely, the OT functional. For the sake of completeness, the absorption spectra

of Figs. 2 and 3 obtained using the solid functional of Ref. 39, which lacks the backflow and non-local kinetic energy terms, are presented in the [supplementary material](#), together with the corresponding table of their spectral characteristics.

The results show a blue shift and broadening of the absorption peaks in a vortex-hosting compared to a vortex-free droplet. However, these spectral modifications are very modest for $np \leftarrow ns$ excitation: the shifts are significantly smaller than the peak widths. Since the proportion of droplets hosting a vortex is expected to be small, these modifications will be difficult to extract from experimental observations. In addition, the experimental droplet size distribution also affects the spectrum, which would make the identification of vortex presence even more difficult.

The situation is more favorable when turning to higher $n'p \leftarrow ns$ or $n's \leftarrow ns$ ($n' > n$) excitations. In this case, the excited state orbital of the alkali atom is more diffuse and more extended, which makes it more sensitive to changes in its local environment. As a consequence, the corresponding $n'p$ or $n's \leftarrow ns$ absorption spectra are more clearly affected, with larger blue shifts and broadening of the peaks, the shifts being then of the same order of magnitude as the widths. This could make experimental detection of vortex-hosting droplets feasible, at least if one finds ways to increase their proportion.

Note that in previous works simulating the capture of dopants by vortex-hosting droplets, dopants were found to spin around vortex lines rather than being attached to them.^{26,47,48} Spectral modifications in the alkali absorption spectrum would be smaller in that case. However, these simulations were describing the first several hundred picoseconds of the capture dynamics. The alkali location used in the current work corresponds to its equilibrium location, i.e., at the vortex line-droplet surface intersection. The flight time of the droplet between the pickup cell and the detection is of the order of millisecond, which gives plenty of time for the system to relax after the capture process and to reach its equilibrium configuration.

In droplets formed by the supersonic expansion of helium gas into vacuum, vortex nucleation is expected to be scarce. When occurring, it is due to collisions with impurities, as observed in studies of impurity capture by helium nanodroplets.^{23,24} The faster the impurity, the more probable the vortex creation. On the other hand, if the impurity is too fast, it can escape the droplet even if the He-impurity interaction is attractive. Combining these arguments, one could imagine a two-step experiment where the amount of vortices could be changed: collision with fast heliophilic impurities to create vortices and then usual pickup of alkalis for detection through $n's \leftarrow ns$ or $n'p \leftarrow ns$ ($n' \geq n$) absorption spectroscopy. Additional doping from the first step could be discriminated by spectroscopy. Certainly, the first step also induces changes in the droplet size distribution. However, corresponding effects are reasonably understood and can be modeled.⁴⁹ Moreover, cluster size dependencies of electronic spectra of alkalis appear to be weak beyond a few thousand helium atoms per droplet and can be accurately characterized.⁵⁰

Direct diffractive imaging of small droplets being impossible at present, the ultimate detection of vortices in helium droplets made of a few thousand atoms will likely be based on finding an observable

sensitive to the changes caused by vortices in the impurity environment, which might be simultaneously studied experimentally and theoretically. Let us point out that femtosecond pump–probe photoionization of alkali atoms attached to helium droplets provides observables such as desorption/fall-back times and final velocities of desorbed atoms and ions.⁴⁵ However, it does not seem that these observables will be more sensitive to the presence of vortices than the alkali absorption spectrum.

SUPPLEMENTARY MATERIAL

See the [supplementary material](#) for the results obtained with the solid density functional of Ref. 39.

ACKNOWLEDGMENTS

This work has been performed under Grant No. FIS2017-87801-P (AEI/FEDER, UE). M.B. and E.G.-A. thank the Université Fédérale Toulouse Midi-Pyrénées for financial support throughout the “Chaires d’Attractivité 2014” Programme IMDYNHE. A computer grant from the CALMIP high performance computer center (Grant No. P1039) is gratefully acknowledged.

DATA AVAILABILITY

The data that support the findings of this study are available from the corresponding author upon reasonable request.

REFERENCES

- J. P. Toennies and A. F. Vilesov, *Angew. Chem. Phys.* **43**, 2622 (2004).
- K. K. Lehmann and G. Scoles, *Science* **279**, 2065 (1998).
- F. Stienkemeier and K. K. Lehmann, *J. Phys. B: At., Mol. Opt. Phys.* **39**, R127 (2006).
- M. Y. Choi, G. E. Douberly, T. M. Falconer, W. K. Lewis, C. M. Lindsay, J. M. Merritt, P. L. Stiles, and R. E. Miller, *Int. Rev. Phys. Chem.* **25**, 15 (2006).
- J. Tiggesbäumker and F. Stienkemeier, *Phys. Chem. Chem. Phys.* **9**, 4748 (2007).
- C. Callegari and W. E. Ernst, in *Handbook of High Resolution Spectroscopy* (Wiley, New York, 2011), Vol. 3, p. 1551.
- R. J. Donnelly, *Quantized Vortices in Helium II*, Cambridge Studies in Low Temperature Physics Vol. 3 (Cambridge University Press, Cambridge, UK, 1991).
- F. Ancilotto, M. Pi, and M. Barranco, *Phys. Rev. B* **97**, 184515 (2018).
- O. Gessner and A. F. Vilesov, *Annu. Rev. Phys. Chem.* **70**, 173 (2019).
- A. L. Fetter, *Rev. Mod. Phys.* **81**, 647 (2009).
- H. Saarikoski, S. M. Reimann, A. Harju, and M. Manninen, *Rev. Mod. Phys.* **82**, 2785 (2010).
- M. Barranco, R. Guardiola, S. Hernández, R. Mayol, J. Navarro, and M. Pi, *J. Low Temp. Phys.* **142**, 1 (2006).
- E. Sola, J. Casulleras, and J. Boronat, *Phys. Rev. B* **76**, 052507 (2007).
- J. D. Close, F. Federmann, K. Hoffmann, and N. Quaaas, *J. Low Temp. Phys.* **111**, 661 (1998).
- D. Mateo, A. Hernando, M. Barranco, and M. Pi, *J. Low Temp. Phys.* **158**, 397 (2010).
- F. Ancilotto, M. Barranco, and M. Pi, *Phys. Rev. Lett.* **91**, 105302 (2003).
- A. Hernando, M. Barranco, R. Mayol, M. Pi, and M. Krošnicki, *Phys. Rev. B* **77**, 024513 (2008).
- F. Stienkemeier, F. Meier, and H. O. Lutz, *J. Chem. Phys.* **107**, 10816 (1997).
- R. M. Tanyag, C. F. Jones, C. Bernardo, S. M. O’Connell, D. Verma, and A. F. Vilesov, in *Theoretical and Computational Chemistry*, edited by O. Dulieu and A. Osterwalder Royal Society of Chemistry, Cambridge, 2018), Vol. 11, p. 389.
- L. F. Gomez, K. R. Ferguson, J. P. Cryan, C. Bacellar, R. M. P. Tanyag, C. Jones, S. Schorb, D. Anielski, A. Belkacem, C. Bernardo, R. Boll, J. Bozek, S. Carron, G. Chen, T. Delmas, L. Englert, S. W. Epp, B. Erk, L. Foucar, R. Hartmann, A. Hexemer, M. Huth, J. Kwok, S. R. Leone, J. H. S. Ma, F. R. N. C. Maia, E. Malmerberg, S. Marchesini, D. M. Neumark, B. Poon, J. Prell, D. Rolles, B. Rudek, A. Rudenko, M. Seifrid, K. R. Siefertmann, F. P. Sturm, M. Swiggers, J. Ullrich, F. Weise, P. Zwart, C. Bostedt, O. Gessner, and A. F. Vilesov, *Science* **345**, 906 (2014).
- B. Langbehn, K. Sander, Y. Ovcharenko, C. Peltz, A. Clark, M. Coreno, R. Cucini, M. Drabbels, P. Finetti, M. Di Fraia, L. Giannessi, C. Grazioli, D. Iablonskyi, A. C. LaForge, T. Nishiyama, V. Oliver Álvarez de Lara, P. Piseri, O. Plekan, K. Ueda, J. Zimmermann, K. C. Prince, F. Stienkemeier, C. Callegari, T. Fennel, D. Rupp, and T. Möller, *Phys. Rev. Lett.* **121**, 255301 (2018).
- S. M. O’Connell, R. M. P. Tanyag, D. Verma, Ch. Bernardo, W. Pang, C. Bacellar, C. A. Saladrigas, J. Mahl, B. W. Toulson, Y. Kumagai, P. Walter, F. Ancilotto, M. Barranco, M. Pi, Ch. Bostedt, O. Gessner, and A. F. Vilesov, *Phys. Rev. Lett.* “Angular momentum in rotating superfluid droplets,” (to be published) (2020); [arXiv:1910.12926](#).
- A. Leal, D. Mateo, A. Hernando, M. Pi, and M. Barranco, *Phys. Chem. Chem. Phys.* **16**, 23206 (2014).
- D. Mateo, A. Leal, A. Hernando, M. Barranco, M. Pi, F. Cargnoni, M. Mella, X. Zhang, and M. Drabbels, *J. Chem. Phys.* **140**, 131101 (2014).
- A. Leal, D. Mateo, A. Hernando, M. Pi, M. Barranco, A. Ponti, F. Cargnoni, and M. Drabbels, *Phys. Rev. B* **90**, 224518 (2014).
- F. Coppens, F. Ancilotto, M. Barranco, N. Halberstadt, and M. Pi, *Phys. Chem. Chem. Phys.* **19**, 24805 (2017).
- F. Stienkemeier, J. Higgins, C. Callegari, S. I. Kanorsky, W. E. Ernst, and G. Scoles, *Z. Phys. D: At., Mol. Clusters* **38**, 253 (1996).
- O. Bünermann, G. Droppelmann, A. Hernando, R. Mayol, and F. Stienkemeier, *J. Phys. Chem. A* **111**, 12684 (2007).
- A. Pifradier, O. Allard, G. Auböck, C. Callegari, W. E. Ernst, R. Huber, and F. Ancilotto, *J. Chem. Phys.* **133**, 164502 (2010).
- F. Lackner, G. Krois, M. Theisen, M. Koch, and W. E. Ernst, *Phys. Chem. Chem. Phys.* **13**, 18781 (2011).
- E. Loginov, C. Callegari, F. Ancilotto, and M. Drabbels, *J. Phys. Chem. A* **115**, 6779 (2011).
- L. Fechner, B. Grüner, A. Sieg, C. Callegari, F. Ancilotto, F. Stienkemeier, and M. Mudrich, *Phys. Chem. Chem. Phys.* **14**, 3843 (2012).
- A. Hernando, M. Barranco, R. Mayol, M. Pi, F. Ancilotto, O. Bünermann, and F. Stienkemeier, *J. Low Temp. Phys.* **158**, 105 (2010).
- A. Hernando, R. Mayol, M. Pi, M. Barranco, I. S. K. Kerkin, and A. Mavridis, *Int. J. Quantum Chem.* **111**, 400 (2011).
- F. Ancilotto, M. Barranco, F. Coppens, J. Eloranta, N. Halberstadt, A. Hernando, D. Mateo, and M. Pi, *Int. Rev. Phys. Chem.* **36**, 621 (2017).
- M. Martínez, F. Coppens, M. Barranco, N. Halberstadt, and M. Pi, *Phys. Chem. Chem. Phys.* **21**, 3626 (2019).
- F. Coppens, J. von Vangerow, A. Leal, M. Barranco, N. Halberstadt, M. Mudrich, M. Pi, and F. Stienkemeier, *Eur. Phys. J. D* **73**, 94 (2019).
- F. Dalfovo, A. Lastrì, L. Pricapenko, S. Stringari, and J. Treiner, *Phys. Rev. B* **52**, 1193 (1995).
- F. Ancilotto, M. Barranco, F. Caupin, R. Mayol, and M. Pi, *Phys. Rev. B* **72**, 214522 (2005).
- S. H. Patil, *J. Chem. Phys.* **94**, 8089 (1991).
- M. Pi, F. Ancilotto, F. Coppens, N. Halberstadt, A. Hernando, A. Leal, D. Mateo, R. Mayol, and M. Barranco, 4He-DFT BCN-TLS: A Computer Package for Simulating Structural Properties and Dynamics of Doped Liquid Helium-4 Systems, <https://github.com/bcncnls2016/>.
- M. Barranco, F. Coppens, N. Halberstadt, A. Hernando, A. Leal, D. Mateo, R. Mayol, and M. Pi, Zero temperature DFT and TDDFT for 4He: A short guide for practitioners, <https://github.com/bcncnls2016/>.
- J. Pascale, *Phys. Rev. A* **28**, 632 (1983).

⁴⁴D. Mateo, A. Hernando, M. Barranco, R. Mayol, and M. Pi, *Phys. Rev. B* **83**, 174505 (2011).

⁴⁵J. von Vangerow, F. Coppens, A. Leal, M. Pi, M. Barranco, N. Halberstadt, F. Stienkemeier, and M. Mudrich, *J. Phys. Chem. Lett.* **8**, 307 (2017).

⁴⁶J. von Vangerow, A. Sieg, F. Stienkemeier, M. Mudrich, A. Leal, D. Mateo, A. Hernando, M. Barranco, and M. Pi, *J. Phys. Chem. A* **118**, 6604 (2014).

⁴⁷F. Coppens, F. Ancilotto, M. Barranco, N. Halberstadt, and M. Pi, *Phys. Chem. Chem. Phys.* **21**, 17423 (2019).

⁴⁸I. A. Pshenichnyuk and N. G. Berloff, *Phys. Rev. B* **94**, 184505 (2016).

⁴⁹O. Bünermann and F. Stienkemeier, *Eur. Phys. J. D* **61**, 645 (2011).

⁵⁰F. Stienkemeier, J. Higgins, W. E. Ernst, and G. Scoles, *Z. Phys. B: Condens. Matter* **98**, 413 (1995).

**Supplementary Material for the manuscript
“Alkali atoms attached to vortex-hosting Helium nanodroplets”**

Ernesto García-Alfonso,^{1,2} Francois Coppens,² Manuel Barranco,^{2,3,4}

Martí Pi,^{3,4} Frank Stienkemeier,⁵ and Nadine Halberstadt²

¹*Facultad de Física, Universidad de La Habana, 10400 La Habana, Cuba*

²*Université Toulouse 3 and CNRS, Laboratoire des Collisions,*

Agrégats et Réactivité, IRSAMC, 118 route de Narbonne,

F-31062 Toulouse Cedex 09, France

³*Departament FQA, Facultat de Física,*

Universitat de Barcelona. Diagonal 645, 08028 Barcelona, Spain

⁴*Institute of Nanoscience and Nanotechnology (IN2UB),*

Universitat de Barcelona, Barcelona, Spain.

⁵*Physikalisches Institut, Universität Freiburg, 79104 Freiburg, Germany.*

(Dated: March 24, 2020)

This Supplementary Material document provides the results for the equilibrium configurations of alkali-doped vortex-free and vortex-hosting ⁴He₁₀₀₀ droplets, as well as the corresponding characteristics of the absorption spectra, obtained using the so-called “solid functional” referenced in the main article. As mentioned there, the results differ only slightly from those obtained with the OT functional and the qualitative conclusions are not affected. We recall that the solid functional is often used due to its lower computational cost, and hence comparing their results with the more accurate ones obtained using the OT functional is a valuable information.

The most relevant characteristics of the calculated equilibrium configurations for an alkali atom doped ⁴He₁₀₀₀ droplet are given in Table I.

Ak	Ak@ ⁴ He ₁₀₀₀		S_{Ak} (K)	(Ak+V)@ ⁴ He ₁₀₀₀		B_{Ak} (K)
	E (K)	d (Å)		E	d (Å)	
Li*	-5398.12	28.07	-2.20	-5277.51	24.42	1.47
Na*	-5400.68	26.87	-4.76	-5281.00	23.41	2.40
K*	-5402.52	27.09	-6.60	-5283.26	23.80	2.82
Li	-5404.91	25.38	-8.99	-5286.37	20.94	3.53
Na	-5404.83	25.68	-8.91	-5286.22	22.34	3.45
K	-5405.49	26.28	-9.57	-5286.95	23.12	3.54
Rb	-5406.36	26.34	-10.44	-5288.08	23.13	3.79
Cs	-5405.75	26.79	-9.83	-5287.21	23.68	3.54

TABLE I: Influence of the presence of a vortex line V on the characteristics of an alkali doped ⁴He₁₀₀₀ droplet: total energy E , and distance d of the impurity to the center-of-mass of the droplet. Ak@⁴He₁₀₀₀ stands for the vortex-free droplet and (Ak+V)@⁴He₁₀₀₀ for the droplet hosting a linear vortex. S_{Ak} is the (vortex-free) impurity solvation energy defined in Eq. (5) of the main text, and B_{Ak} is the binding energy of the impurity to the vortex line defined in Eq. (7) of the main text. The energy of the pure, vortex-free ⁴He₁₀₀₀ droplet is -5395.92 K, and that of the pure ⁴He₁₀₀₀ droplet hosting a vortex line is -5273.84 K. Hence, $E_V = 122.08$ K. The asterisk in the first 3 lines of the table denotes a quantum treatment of the dopant.

Figure 1 shows the effect of a vortex line on the $np \leftarrow ns$ absorption spectrum of the alkali atoms attached to a ⁴He₁₀₀₀ droplet. The shifts and FWHM are collected in Table II.

Figure 2 shows the K($5s \leftarrow 4s$), Rb($6p \leftarrow 5s$), and Cs($7s \leftarrow 6s$) absorption spectra. The shifts and FWHM are collected in the lower part of Table II.

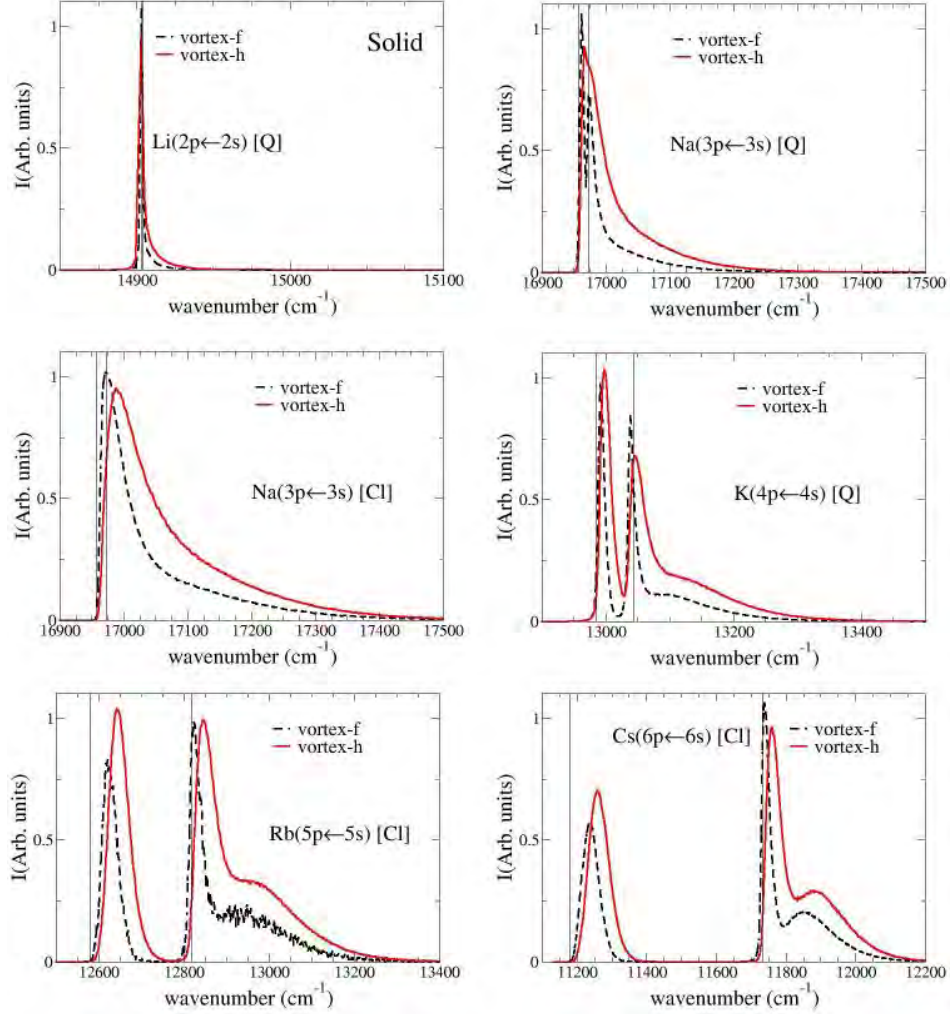


FIG. 1: $np \leftarrow ns$ absorption spectrum for the alkali-doped ⁴He₁₀₀₀ droplet. Li, Na, and K atoms are treated quantum-mechanically ([Q]), whereas Rb, and Cs are treated classically ([Cl]). For the sake of comparison, the results for Na obtained with the classical description are also shown. Black dashed line: vortex-free (vortex-f) droplet; red solid line: vortex-hosting (vortex-h) droplet. Gas-phase atomic transitions are represented by thin vertical lines. Units are arbitrary for absorption intensity, and cm^{-1} for excitation energy.

Ak	$(\Delta E)_{\text{vortex-f}}$ (cm ⁻¹)			$(\Delta E)_{\text{vortex-h}}$ (cm ⁻¹)			FWHM (cm ⁻¹)					
	² Π _{1/2}		² Σ _{1/2}	² Π _{1/2}		² Σ _{1/2}	² Π _{1/2}		² Π _{3/2}		² Σ _{1/2}	
	vortex-f	vortex-h	vortex-f	vortex-h	vortex-f	vortex-h	vortex-f	vortex-h	vortex-f	vortex-h	vortex-f	vortex-h
Na* (3p ← 3s)	5.4	0.9	35.4	10.3	12.1	70.4	8.2	17.3	13.1	36.4	97.8	124.5
K* (4p ← 4s)	6.4	-5.1	5.4	12.3	7.9	2.8	17.2	19.5	11.7	29.1	110.0	128.8
Na (3p ← 3s)	13.6	21.0	119.2	26.6	46.2	151.1	22.8	41.3	54.1	87.2	194.6	206.8
K (4p ← 4s)	11.5	1.4	105.9	21.1	19.6	132.8	18.5	31.7	28.9	55.9	170.8	180.6
Rb (5p ← 5s)	43.5	6.4	125.6	61.3	28.3	146.4	40.8	54.0	33.0	53.3	171.9	178.2
Cs (6p ← 6s)	57.7	5.5	117.6	79.7	26.6	146.7	57.1	68.5	27.9	48.1	159.3	166.1
K* (5s ← 4s)	—	—	574.5	—	—	832.0	—	—	—	—	226.4	283.9
K (5s ← 4s)	—	—	737.0	—	—	1008.9	—	—	—	—	260.1	310.6
Rb(6p ← 5s)	848.1	998.6	3074.7	1376.6	1586.9	3409.0	296.9	395.5	310.4	406.6	731.9	735.5
Cs(7s ← 6s)	—	—	953.7	—	—	1333.1	—	—	—	—	376.5	448.2

TABLE II: Comparison of the spectral characteristics for an alkali atom sitting on a vortex-free (vortex-f) or a vortex-hosting (vortex-h) ⁴He₁₀₀₀ nanodroplet. 2nd to 4th columns: energy shifts $(\Delta E)_{\text{vortex-f}}$ with respect to the atomic lines calculated from the absorption maxima for the ²Π_{1/2}, ²Π_{3/2}, and ²Σ_{1/2} final states; 5th to 7th columns: energy shifts $(\Delta E)_{\text{vortex-h}}$ for a vortex-hosting droplet; last 6 columns: full width at half maximum (FWHM) for each peak for a vortex-free or vortex-hosting droplet. The first part of the table is for $np \leftarrow ns$ absorption spectra and the second part, separated by a horizontal line, is for $(n+1)s \leftarrow ns$ or $(n+1)p \leftarrow ns$ absorption spectra. The asterisk denotes a quantum treatment of the dopant.

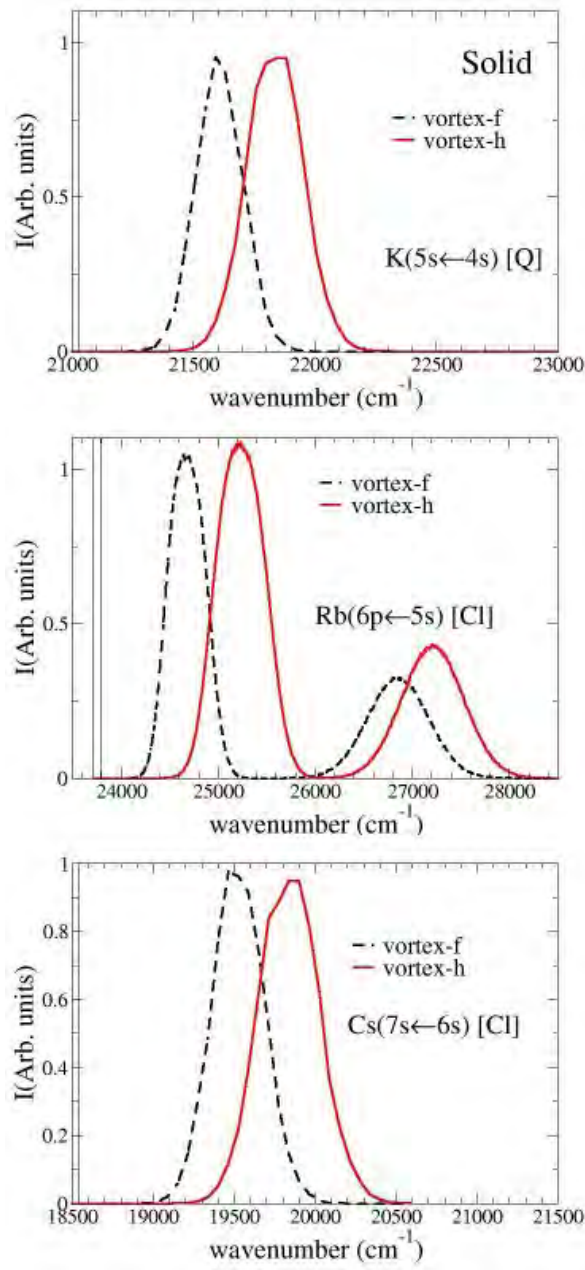


FIG. 2: Photon absorption spectrum for K($5s \leftarrow 4s$) (top), Rb($6p \leftarrow 5s$) (middle), and Cs($7s \leftarrow 6s$) (bottom) transitions in a vortex-free (black dashed line) or vortex-hosting (red solid line) ⁴He₁₀₀₀ droplet. The K atom is treated quantum mechanically and the Rb and Cs atoms classically. Gas-phase atomic transitions are represented by thin vertical lines. Units are arbitrary for absorption intensity, and cm⁻¹ for excitation energy.

 CHAPTER VIIITO CONCLUDE

VIII-1. Summary of the work

Throughout this thesis we have studied a number of dynamical processes involving superfluid ^4He nanodroplets within the ^4He -DFT approach at $T = 0$ K, in its statics and dynamics version. Thanks to this theoretical tool, we have been able to address and study cluster formation of Ar atoms within a $^4\text{He}_{1000}$ droplet and ion solvation of alkali atoms ($\text{Ak}^+ = \text{Li}^+, \text{Na}^+, \text{K}^+, \text{Rb}^+$ and Cs^+) into a $^4\text{He}_{1000}$ droplet. We also made an extensive study of Coulomb explosion of Ak_2 diatomics at the surface of droplets of different sizes, for both the singlet and triplet state. We have investigated the effect of the zero point motion of the Ak_2 vibration and of the zero point orientation distribution of Ak_2 (φ) on the droplet surface. We have also explored the possibility of another mechanism for quantum vortex nucleation, $^4\text{He}_N + ^4\text{He}_N$ collisions under symmetric and non-symmetric conditions and we proposed a mechanism to detect vortex signatures in smallest droplets, $N = 1000$ for instance.

A small introduction about bulk superfluid properties of He bulk liquid and their detection in droplets was addressed in Chapter I, whereas in Chapter II we introduced the main concepts of the ^4He -Density Functional Theory. In the following chapters, we presented our research previously published in peer-review journal,

with an extended introduction and further figures that could not be included in those articles.

In the clustering study presented in chapter III, the ^4He -DFT simulation results were compared to those of approximate atomistic approaches. Although quantum and superfluidity effects are better described with ^4He -TDDFT, several common features are demonstrated. The most stable gas phase configuration is usually not produced, but an isomer with fewer bonds instead, and/or more dilute structures because of the rigidity of the helium solvation shell around the Rg atoms.

In the study on alkali ion sinking inside helium droplets presented in chapter IV, our simulations show the progressive build up of the first solvation shell around the ions. The number of helium atoms in this shell is found to linearly increase with time during the first stages of the dynamics. For the lighter alkalis, the solvation shell is incomplete at the end of the dynamics, suggesting a kinetic rather than thermodynamical control of its formation.

In the study of the Coulomb explosion of a dialkali molecule on the surface of a helium droplet presented in chapter V, our simulations reveal an interesting consequence of the presence of HND: ions trajectories are bent because of the attractive interaction with helium. The latter could be used to measure droplet sizes individually, something that has only been possible up to now for very large sizes (by X-ray diffraction). This angular deviation is measurable and depends on several factors such as the $\text{Ak}^+-^4\text{He}_N$ interaction strength and the time of flight of the dopants, which is related to the initial bond length of the diatomic and to the Ak^+ mass.

In our study of droplet-droplet collision as an alternative mechanism to nucleate quantum vortices, presented in chapter VI, we have evidenced the nucleation of quantum vortices at indentations of the merged droplet, which are produced in pairs under symmetric conditions. This makes the proposed mechanism quite general.

In chapter VII we have proposed to use the electronic absorption or excitation spectroscopy of alkali atoms as a way to detect the presence of vortices in smaller droplets. Our results show that: a vortex shifts and broadens the alkali spectrum. The effect could be measurable above the first excited states. The blue-shift (towards higher frequencies) and the broadening occur because the alkali sits deeper into the droplet, a feature that can also be appreciated by the depth of its dimple.

VIII-2. Future prospects

In the near future, we plan to follow up on the alkali ion sinking dynamics into helium droplets by addressing the complete pump-probe process. It consists in adding a neutral Xe atom at the center of the helium droplet during the pump process (ionization of the alkali at the droplet surface followed by its solvation) and in a second step (probe) in suddenly ionizing the Xe atom, the same way as we did for the ionization of Ak. The probe step will trigger a Coulomb explosion between Ak^+ and Xe^+ . This description of the whole process will be much more demanding in computational effort.

We would also like to study the photodissociation of Ak_2 , including possible electronic transitions induced by the helium environment. This could be done using the DIM (Diatomics in Molecules) model [133] to describe the interactions between the dialkali and the 4He_N nanodroplet and the couplings between the electronic states of the dialkali molecule induced by helium. The DIM model is now well underway.

In a more distant future, since the field of spectroscopic and dynamics studies in superfluid helium nanodroplets is rapidly expanding, it would be interesting to continue developing the 4He -DFT and 4He -TDDFT methods in order to apply them to molecules, and to make the codes more user-friendly for novice researchers.

REFERENCES

- [1] A. SLENCZKA and J. P. TOENNIES, *Molecules in Superfluid Helium Nanodroplets*, Springer (Open Access), 2022.
- [2] J. F. ALLEN and H. JONES, *Nature* **141**, 243 (1938).
- [3] L. TISZA, *Nature* **141**, 913 (1938).
- [4] L. D. LANDAU and E. M. LIFSHITZ, *Fluid Mechanics*, volume 6 of Course of Theoretical Physics Second English Edition, Pergamon Press, 1987.
- [5] D. R. TILLEY and J. TILLEY, *Superfluidity and Superconductivity*, Graduate Student Series in Physics, 1990.
- [6] L. PITAEVSKII and S. STRINGARI, *Bose-Einstein Condensation and Superfluidity*, Oxford Science Publications, 2016.
- [7] A. BORGHESANI, *Ions and Electrons in Liquid Helium*, Oxford Science Publications, 2007.
- [8] R. J. DONNELLY and C. F. BARENGHI, *Journal of Physical and Chemical Reference Data* **27**, 1217 (1998).
- [9] J. NAVARRO and M. BARRANCO, “Density Functional Theory of Superfluid Helium and Droplets”, Unpublished, 2017.
- [10] D. G. HENSHAW and A. D. B. WOODS, *Physical Review Journals Archive* **121**, 1266 (1961).
- [11] D.F.GOBLE, *Canadian Journal of Physics* **48**, 11 (1969).

-
- [12] H. GODFRIN, K. BEAUVOIS, A. SULTAN, E. KROTSCHECK, J. DAWIDOWSKI, B. FAK, and J. OLLIVIER, *Physical Review B* **103**, 104516 (2021).
- [13] J. F. ANNETT, *Superconductivity, Superfluids and Condensates*, OXFORD MASTER SERIES IN PHYSICS, 2004.
- [14] E. W. BECKER, R. KLINGELHÖFER, and P. LOHSE, *Zeitschrift für Naturforschung A* **146**, 333 (1956).
- [15] S. GREBENEV, J. P. TOENNIES, and A. F. VILESOV, *Science* **279**, 2083 (1998).
- [16] J. P. TOENNIES, A. F. VILESOV, and K. B. WHALEY, *Phys. Today* **54(2)**, 31 (2001).
- [17] A. SCHEIDEMANN, J. P. TOENNIES, and J. A. NORTHBY, *Physical Review Letters* **64**, 1899 (1990).
- [18] M. HARTMANN, R. E. MILLER, J. P. TOENNIES, and A. F. VILESOV, *SCIENCE* **272** (1996).
- [19] K. NAUTA and R. E. MILLER, *Science* **283**, 5409 (1999).
- [20] K. W. JUCKS and R. E. MILLER, *The Journal of Chemical Physics* **88**, 2196 (1988).
- [21] J. P. TOENNIES and A. F. VILESOV, *Angew. Chem. Int. Ed* **43**, 2622 (2004).
- [22] F. ANCILOTTO, M. BARRANCO, F. COPPENS, J. ELORANTE, N. HALBERSTADT, A. HERNANDO, D. MATEO, and M. PI, *International Reviews in Physical Chemistry* **36**, 4.621 (2017).
- [23] F. ANCILOTTO, M. BARRANCO, M. PI, F. COPPENS, and N. HALBERSTADT, Lecture: DFT study of vortices in superfluid ^4He nanodroplets, 2017.
- [24] K. K. LEHMANN and R. SCHMIED, *Physical Review B* **224520** (2003).

-
- [25] D. MATEO, J. ELORANTA, and G. A. WILLIAMS, *The Journal of Chemical Physics* **142**, 064510 (2015).
- [26] M. PI, R. MAYOL, A. HERNANDO, M. BARRANCO, and F. ANCILOTTO, *The Journal of Chemical Physics* **126**, 244502 (2007).
- [27] F. ANCILOTTO, M. PI, and M. BARRANCO, *Physical review B* **91**, 100503 (2015).
- [28] F. DALFOVO, R. MAYOL, and M. B. M PI, *Physical Review Letter* **85(5)**, 1028 (2000).
- [29] L. F. GOMEZ, E. LOGINOV, R. SLITER, and A. F. VILESOV, *The Journal of Chemical Physics* **135**, 154201 (2011).
- [30] O. DULIEU and A. OSTERWALDER, editors, *Cold Chemistry Molecular Scattering and Reactivity Near Absolute Zero*, Royal Society of Chemistry, 2013.
- [31] D. M. LUBMAN, C. RETINER, and R. N. ZARE, *J. Phys. Chem* **86**, 1129 (1982).
- [32] H. PAULY, *Atom, Molecule and Cluster Beams I. Basic Theory, Production and Detection of Thermal Energy Beams*, Atomic, Optical and Plasma Physics. Springer, 2000.
- [33] O. DULIEU and A. OSTERWALDER, editors, *Cold Chemistry Molecular Scattering and Reactivity Near Absolute Zero*, The Royal Society of Chemistry, 2017.
- [34] H. BUCHENAU, E. L. KNUTH, J. NORTHBY, J. P. TOENNIES, and C. WINKLER, *The Journal of Chemical Physics* **92**, 6875 (1990).
- [35] J. HARMS, J. P. TOENNIES, and F. DALFOVO, *Physical Review B* **58** (1998).
- [36] K. KOLATZKI, M. L. SCHUBERT, A. ULMER, T. MÖLLER, D. RUPP, and R. M. P. TANYAG, *Physics of Fluids* **34**, 012002 (2022).

-
- [37] R. E. GRISENTI and J. P. TOENNIES, *Physical Review Letters* **90**, 234501 (2003).
- [38] E. KROTSCHECK and J. NAVARRO, *World Scientific, Singapore* **4** (2002).
- [39] M. BARRANCO, R. GUARDIOLA, S. HERNÁNDEZ, R. MAYOL, J. NAVARRO, and M. PI, *Journal of Low Temperature Physics* **142**, 1 (2012).
- [40] F. DALFOVO, *Journal of Low Temperature Physics* **89**, 314 (1992).
- [41] F. DALFOVO, A. LASTRI, L. PRICAUPENKO, S. STRINGARI, and J. TREINER, *Physical Review B* **52**, 1193 (1995).
- [42] F. DALFOVO, *Z.Phys. D* **29**, 61 (1994).
- [43] M. BARRANCO and E. HERNÁNDEZ, *Physical Review B* **49**, 7 (1994).
- [44] F. STIENKEMEIER, O. BÜNERMANN, R. MAYOL, F. ANCILOTTO, M. BARRANCO, and M. PI, *Physical Review B* **70**, 214509 (2004).
- [45] S. STRINGARI and J. TREINER, *Physical Review B* **36**, 8369 (1987).
- [46] S. STRINGARI and J. TREINER, *The Journal of Chemical Physics* **87**, 5021 (1987).
- [47] R. FEYNMAN and M. COHEN, *Physical Review* **102**, 1189 (1956).
- [48] F. ANCILOTTO, M. BARRANCO, F. CAUPIN, R. MAYOL, and M. PI, *Physical Review B* **72**, 214522 (2005).
- [49] F. CAUPIN, F. ANCILOTTO, M. BARRANCO, R. MAYOL, and M. PI, *Journal of Low Temperature Physics* **148**, 731 (2007).
- [50] L. LEHTOVAARA, J. TOIVANEN, and J. ELORANTA, *Journal of Computational Physics* **221**, 148 (2006).
- [51] E. RUNGE and E. K. U. GROSS, *Physical Review Letters* **52**, 997 (1984).
- [52] L. LEHTOVAARA, T. KILJUNEN, and J. ELORANTA, *Journal of Computational Physics* **194**, 78 (2004).

-
- [53] M. FRIGO and S. JOHNSON, *Proc. IEEE* **93**, 216 (2005).
- [54] DAVID J. TANNOR, *Introduction to Quantum Mechanics*, UNIVERSITY SCIENCE BOOKS, 2007.
- [55] A. RALSTON and H. S. WILF, *Mathematical methods for digital computers*, John Wiley and Sons, New York, 1960.
- [56] E. G. ALFONSO, F. COPPENS, M. BARRANCO, M. PI, and N. HALBERSTADT, <https://github.com/4He-DFT-BCN-TLS>.
- [57] E. LOGINOV, L. F. GOMEZ, N. CHIANG, A. HALDER, N. GUGGEMOS, V. V. KRESIN, and A. F. VILESOV, *Physical Review Letters* **106**, 233401 (2011).
- [58] K. NAUTA and R. E. MILLER, *Science* **287**, 293 (2000).
- [59] J. D. PICKERING, B. SHEPPERSON, L. CHRISTIANSEN, and H. STAPELFELDT, *The Journal of Chemical Physics* **149**, 154306 (2018).
- [60] A. M. ELLIS, J. A. DAVIES, and E. Y. F. CALVO, *The Journal of Chemical Physics* **156**, 174304 (2022).
- [61] E. LOTTNER and A. SLENCZKA, *The Journal of Physical Chemistry* **124**, 2 (2020).
- [62] V. MOZHAYSKIY, M. N. SLIPCHENKO, V. K. ADAMCHUK, and A. F. VILESOV, *The Journal of Chemical Physics* **127**, 094701 (2007).
- [63] G. HABERFEHLNER, P. THALER, D. KNEZ, A. VOLK, F. HOFER, W. E. ERNST, and G. KOTHLEITNER, *Nature Communications* **6**, 8779 (2015).
- [64] A. VOLK, P. THALER, D. KNEZ, A. W. HAUSER, J. STEURER, W. GROGGER, F. HOFER, and W. E. ERNST, *Physical Chemistry Chemical Physics* **18**, 1451 (2016).
- [65] J. TOENNIES, *The Chemical Physics of Atomic and Molecular Clusters*, in *Proceedings of the International School of Physics "Enrico Fermi" Course CVII*, North Holland, Amsterdam, 1990.

-
- [66] J. GSPANN and H. VOLLMAR, *The Journal of Chemical Physics* **73**, 1657 (1980).
- [67] M. LEWERENZ, B. SCHILLING, and J. P. TOENNIES, *The Journal of Chemical Physics* **102**, 8191 (1998).
- [68] J. ELORANTA, *Physical Review B* **77**, 134301 (2008).
- [69] A. HERNANDO, M. BARRANCO, R. MAYOL, M. PI, and M. KROŚNICKI, *Physical Review B* **77**, 024513 (2008).
- [70] L. F. GOMEZ, E. LOGINOV, and A. F. VILESOV, *Physical Review letters* **108**, 155302 (2012).
- [71] E. LATIMER, D. SPENCE, C. FENG, A. BOATWRIGHT, A. M. ELLIS, and S. YANG, *Nano Letters* **14**, 2902 (2014).
- [72] P. THALER, A. VOLK, F. LACKNER, J. STEURER, D. KNEZ, W. GROGGER, F. HOFER, and W. E. ERNST, *Physical Review B* **90**, 155442 (2014).
- [73] F. COPPENS, J. VON VANGEROW, M. BARRANCO, N. HALBERSTADT, F. STIENKEMEIER, M. PI, and M. MUDRICH, *Physical Chemistry Chemical Physics* **20**, 9309 (2018).
- [74] K.T.TANG and J. TOENNIES, *The Journal of Chemical Physics* **118**, 4976 (2003).
- [75] A. WADA, T. TAKAYANAGI, and M. SHIGA, *The Journal of Chemical Physics* **119**, 5478 (2003).
- [76] T. TAKAYANAGI and M. SHIGA, *Phys.Chem.Chem.Phys* **6**, 3241 (2004).
- [77] I. R. CRAIG and D. E. MANOLOPOULOS, *The Journal of Chemical Physics* **121**, 3368 (2004).
- [78] E. J. HELLER, *The Journal of Chemical Physics* **75**, 2923 (1981).
- [79] N. HALBERSTADT and D. A. BONHOMMEAU, *The Journal of Chemical Physics* **152**, 234305 (2020).

-
- [80] D. BONHOMMEAU, M. LEWERENZ, and N. HALBERSTADT, *The Journal of Chemical Physics* **128**, 054302 (2008).
- [81] A. CASTILLO-GARCÍA, A. W. HAUSER, M. P. DE LARA-CASTELLS, and A. W. HAUSER, *Molecules* **26(19)**, 5783 (2021).
- [82] F. CALVO, E. YURTSEVER, and O. BIRER, *The Journal of Physical Chemistry* **120,10**, 1727 (2016).
- [83] M. STERLING, Z. LI, and V. A. APKARIAN, *The Journal of Chemical Physics* **103**, 5679 (1995).
- [84] E. G. ALFONSO, M. BARRANCO, D. A. BONHOMMEAU, N. HALBERSTADT, M. PI, and F. CALVO, *The Journal of Chemical Physics* **157**, 014106 (2022).
- [85] D. J. WALES, J. P. K. DOYE, A. DULLWEBER, M. P. HODGES, F. Y. NAUMKIN, F. CALVO, J. HERNÁNDEZ-ROJAS, and T. F. MIDDLETON, <https://www-wales.ch.cam.ac.uk/wales/CCD/AzizAr.html>.
- [86] T. GONZÁLEZ-LEZANA, O. ECHT, M. GATCHELL, M. BARTOLOMEI, J. CAMPOS-MARTÍNEZ, and P. SCHEIER, *International Reviews in Physical Chemistry* **39:4**, 465 (2020).
- [87] E. G. ALFONSO, F. COPPENS, M. BARRANCO, M. PI, F. STIENKEMEIER, and N. HALBERSTADT, *Journal Chemical Physics* **152**, 194109 (2020).
- [88] A. LEAL, D. MATEO, A. HERNANDO, M. PI, M. BARRANCO, A. PONTI, F. CARGNONI, and M. DRABELLS, *Physical Review B* **90**, 224518 (2014).
- [89] S. H. ALBRECHTSEN, C. A. SCHOUDER, A. V. MUNOZ, J. K. CHRISTENSEN, C. E. PETERSEN, M. PI, M. BARRANCO, and H. STAPELFELDT, *Nature* **623**, 319 (2023).
- [90] Y. MARCUS, *Ions in solution and their solvation*, John Wiley & Sons, 2015.
- [91] E. GARCIA-ALFONSO, M. BARRANCO, N. HALBERSTADT, and M. PI, *The Journal of Chemical Physics* **160**, 164308 (2024).

-
- [92] F. STIENKEMEIER, J. HIGGINS, W. E. ERNST, and G. SCOLES, *Physical Review Letters* **74**, 3592 (1995).
- [93] W. E. ERNST, R. HUBER, S. JIANG, R. BEUC, M. MOVRE, and G. PICHLER, *The Journal of Chemical Physics* **124**, 024313 (2006).
- [94] G. AUBÖCK, J. NAGL, C. CALLEGARI, and W. E. ERNST, *The Journal of Physical Chemistry* **111**, 31 (2007).
- [95] O. ALLARD, J. NAGL, G. AUBÖCK, C. CALLEGARI, and W. E. ERNST, *Journal of Physics B* **39**, 1169 (2006).
- [96] J. NAGL, G. AUBÖCK, A. W. HAUSER, O. ALLARD, C. CALLEGARI, and W. E. ERNST, *Physical Review Letters* **100**, 063001 (2008).
- [97] J. NAGL, G. AUBÖCK, A. W. HAUSER, O. ALLARD, C. CALLEGARI, and W. E. ERNST, *The Journal of Chemical Physics* **128**, 154320 (2008).
- [98] O. BUNERMANN and F. STIENKEMEIER, *The European Physical Journal D* **61**, 645 (2011).
- [99] H. H. KRISTENSEN, L. KRANABETTER, C. A. SHOUDER, C. STAPPER, J. ARLT, M. MUDRICH, and H. STAPELFELDT, *Physical Review Letters* **128**, 093201 (2022).
- [100] C. SHOUDER, A. S. CHATTERLEY, F. CALVO, L. CHRISTIANSEN, and H. STAPELFELDT, *Structural Dynamics* **6**, 044301 (2019).
- [101] J. D. PICKERING, B. SHEPPERSON, L. CHRISTIANSEN, and H. STAPELFELDT, *Physical Review A* **99**, 043403 (2019).
- [102] H. H. KRISTENSEN, L. KRANABETTER, C. A. SHOUDER, J. ARLT, F. JENSEN, and H. STAPELFELDT, *Physical Review B* **107**, 023104 (2023).
- [103] P. JASIK and J. SIENKIEWICZ, *Chemical Physics* **323**, 563 (2006).
- [104] O. DULIEU and R. VEXIAU, private communication, 2021.
- [105] A. A. ZAVITSAS, *Journal of Chemical Physics* **124**, 144318 (2006).

-
- [106] L. LI, A. M. LYYRA, W. T. LUH, and W. C. STWALLEY, *Journal of Chemical Physics* **93**, 8542 (1990).
- [107] C. AMIOT, *Journal of Molecular Spectroscopy* **146**, 370 (1991).
- [108] G. GUILLON, private communication, 2021.
- [109] A. KOUTSELOS, E.A.MASON, and L.A.VIEHLAND, *J.Chem.Phys* **93**, 7125 (1990).
- [110] F. ANCILOTTO, G. DETOFFOL, and F. TOIGO, *Phys. Rev. B* **52**, 16125 (1995).
- [111] F. ANCILOTTO, M. W. COLE, G. DETOFFOL, P. B. LERNER, and F. TOIGO, *J. Low T. Phys.* **101**, 325 (1995).
- [112] G. GUILLON, A. ZANCHET, M. LEINO, A. VIEL, and R. E. ZILLICH, *Journal of Physical Chemistry* **115**, 6918 (2011).
- [113] N. HALBERSTADT, J. A. BESWICK, and K. C. JANDA, *The Journal of Chemical Physics* **87(7)**, 3966 (1987).
- [114] B. P. REID, K. C. JANDA, and N. HALBERSTADT, *The Journal of Physical Chemistry* **92**, 587 (1988).
- [115] E. G. ALFONSO, F. COPPENS, M. BARRANCO, M. PI, and N. HALBERSTADT, https://github.com/4He-DFT-BCN-TLS/He_DFT_2024.
- [116] H. KRISTENSEN, private communication.
- [117] G. GUILLON, A. VIEL, and J.-M. LAUNAY, *The Journal of Chemical Physics* **126**, 174307 (2012).
- [118] S.H.PATIL, *The Journal of Chemical Physics* **94**, 8089 (1991).
- [119] L. W. BRUCH, W. SCHÖLLKOPF, and J. P. TOENNIES, *The Journal of Chemical Physics* **117**, 1544 (2002).
- [120] E. GARCÍA-ALFONSO, F. ANCILOTTO, M. BARRANCO, M. PI, and N. HALBERSTADT, *The Journal of Chemical Physics* **159**, 074305 (2023).

-
- [121] L. F. GOMEZ, K. R. FERGUSON, and A. E. A. CRYAN, JAMES P, *Science* **345**, 6199 (2014).
- [122] L. F. GOMEZ, K. R. FERGUSON, J. P. CRYAN, C. BACELLAR, R. M. P. TANYAG, C. JONES, S. SCHORB, D. ANIELSKI, A. BELKACEM, C. BERNANDO, R. BOLL, J. BOZEK, S. CARRON, G. CHEN, T. DELMAS, L. ENGLERT, S. W. EPP, B. ERK, L. FOUCAR, R. HARTMANN, A. HEXEMER, M. HUTH, J. KWOK, S. R. LEONE, J. H. S. MA, F. R. N. C. MAIA, E. MALMERBERG, S. MARCHESINI, D. M. NEUMARK, B. POON, J. PRELL, D. ROLLES, B. RUDEK, A. RUDENKO, M. SEIFRID, K. R. SIEFERMANN, F. P. STURM, M. SWIGGERS, J. ULLRICH, F. WEISE, P. ZWART, C. BOSTEDT, O. GESSNER, and A. F. VILESOV, *Science* **345**, 906 (2014).
- [123] B. LANGBEHN, K. SANDER, Y. OVCHARENKO, C. PELTZ, A. CLARK, M. CORENO, R. CUCINI, M. DRABBELS, P. FINETTI, M. D. FRAIA, L. GIANNESI, C. GRAZIOLI, D. IABLONSKYI, A. C. LAFORGE, T. NISHIYAMA, V. O. A. DE LARA, P. PISERI, O. PLEKAN, K. UEDA, J. ZIMMERMANN, K. C. PRINCE, F. STIENKEMEIER, C. CALLEGARI, T. FENNEL, D. RUPP, and T. MÖLLER, *Physical Review Letter* **121**, 255301 (2018).
- [124] F. STIENKEMEIER, J. HIGGINS, C. CALLEGARI, S. I. KANORSKY, W. E. ERNST, and G. SCOLES, *Zeitschrift für Physik D Atoms, Molecules and Clusters* **38**, 253 (1996).
- [125] O. BÜNERMANN, G. DROPPELMANN, A. HERNANDO, R. MAYOL, and F. STIENKEMEIER, *Journal Physical Chemistry* **111**, 12684 (2007).
- [126] A. PIFRADER, O. ALLARD, G. AUBÖCK, C. CALLEGARI, W. E. ERNST, R. HUBER, and F. ANCILOTTO, *The Journal of Chemical Physics* **133**, 164502 (2010).
- [127] F. LACKNER, G. KROIS, M. THEISEN, M. KOCHA, and W. E. ERNST, *Physical Chemistry Chemical Physics* **13**, 18781 (2011).

-
- [128] E. LOGINOV, C. CALLEGARI, F. ANCILOTTO, and M. DRABBELS, *The Journal of Physical Chemistry* **115**, **25**, 6779 (2011).
- [129] L. FECHNER, B. GRÜNER, A. C. C. A. SIEG, F. ANCILOTTO, F. STIENKEMEIER, and M. MUDRICHA, *Physical Chemistry Chemical Physics* **14**, 3843 (2012).
- [130] A.HERNANDO, M.BARRANCO, R. MAYOL, M.PI, F.ANCILOTTO, O. BÜNERMANN, and F.STIENKEMEIER, *Journal of Low Temperature Physics* **158**, 105 (2010).
- [131] M. MARTINEZ, F. COPPENS, M. BARRANCO, N. HALBERSTADT, and M. PI, *Physical Chemistry Chemical Physics* **21**, 3626 (2019).
- [132] F. COPPENS, J. VON VANGEROW, A. LEAL, M. BARRANCO, N. HALBERSTADT, M. MUDRICH, M. PI, and F. STIENKEMEIER, *The European Physical Journal* **73**, 94 (2019).
- [133] F. O. ELLISON, N. T. HUFF, and J. C. PATEL, *Journal of the American Chemical Society* **85**, 3540 (1963).
- [134] D.TANNOR, *Introduction to Quantum Mechanics: A Time-dependent Perspective*, Science Books, 2007.
- [135] K. K. REBANE, *Impurity Spectra of Solids. Elementary Theory of vibrational Structure*, Plenum Press. New York-London, 1970.
- [136] R. SCHINKE, *Photodissociation dynamics*, Cambridge University Press, Cambridge, UK, 1995.
- [137] D. MATEO, A. HERNANDO, M. BARRANCO, R. MAYOL, and M. PI, *Physical Review B* **83**, 174505 (2011).
- [138] J. W. COOLEY, *Math. Comp.* **15**, 363 (1961).
- [139] D. G. TRUHLAR, *J. Comput. Phys.* **10**, 123 (1972).
- [140] C. AMIOT, *Journal of Chemical Physics* **93**, 8591 (1990).

-
- [141] S.MAGNIER, P. MILLIÉ, O.DULIEU, and F. MASNOU-SEEUWS, *The Journal Chemical Physics* **98**, 9 (1993).
- [142] G.-H. JEUNG, *Journal of Molecular Spectroscopy* **182**, 113 (1996).
- [143] M.FOUCRAULT, P. MILLIE, and J.P.DAUDEY, *The Journal of Chemical Physics* **96**, 1257 (1992).
- [144] FRANÇOIS COPPENS, F. ANCILOTTO, M. BARRANCO, N. HALBERSTADT, and M. PI, *Physics Chemical-Chemical Physics* **21**, 17423 (2019).
- [145] FRANÇOIS COPPENS, F. ANCILOTTO, M. BARRANCO, N. HALBERSTADT, and M. PI, *Physical Chemisty-Chemical Physics* **19**, 24805 (2017).

ANNEXES

A. ^4He and ^3He physical properties

Table A.1. ^4He and ^3He physical properties. First row a constant value definition for each isotope. Second row display the bulk superfluid helium density at zero temperature (ρ_0), third one the surface tension (σ), the volumen per atom is characterized by $V_{\text{atom}} = 4\pi R^3/3$ being $R \sim 1.3\text{\AA}$ whereas $V_{\text{atom}} \cdot \rho_0$ is a measure of how compact the system is (dimensionless parameter), last row show the ratio between effective mass (m_0^*) and atomic mass (m). Last row correspond to the temperature which the phase transition (λ -line) to superfluid occur, for ^4He (at saturated vapor pressure) and ^3He (at about 33 atm). Data extracted from Ref [9]

	^4He	^3He
$\hbar/2m$ (K \AA)	6.0597	8.0418
ρ_0 (\AA^{-3})	0.021836	0.0163457
σ (K \AA^{-2})	0.274	0.113
$V_{\text{atom}} \cdot \rho_0$	0.2	0.15
m_0^*/m	1	2.81
Temperature	2.17 K	2.7 mK

B. OT-DFT parameters

Table B.2. Model parameters for the OT-DFT and solid functionals (see Ref [22])

$\epsilon_{LJ}(\text{k})$	$\sigma(\text{\AA})$	$h(\text{\AA})$	$c_2 (\text{K } \text{\AA}^6)$	$c_3 (\text{K } \text{\AA}^9)$	$\alpha_s(\text{\AA}^3)$
10.22	2.556	2.190323	$-2.41186 \cdot 10^4$	$1.8585 \cdot 10^6$	54.31
$\rho_{0s}(\text{\AA}^{-3})$	$l(\text{\AA})$	C(Hartree)	$\beta(\text{\AA}^3)$	$\rho_m(\text{\AA}^{-3})$	γ_{11}
0.04	1	0.1	40	0.37	-19.7544
$\gamma_{12}(\text{\AA}^{-2})$	$\alpha_1(\text{\AA}^{-2})$	γ_{21}	$\gamma_{22}(\text{\AA}^{-2})$	$\alpha_2(\text{\AA}^{-2})$	
12.5616	1.023	-0.2395	0.0312	0.14912	

C. Simulation of absorption and emission spectra using the density fluctuation method

Considering a Born-Oppenheimer framework, the electronic and nuclear wave functions can be split. Within the time-dependent formulation [134], the line shape for an electronic transition from the initial (ground) “i” to the final (excited) “f” electronic state is obtained as the Fourier transform of the time-correlation function.

$$I(\omega) \propto \sum_m \int dt e^{i(\omega+\omega^i)t} \int d^3\mathbf{r}_I \Phi^{i*} e^{(-it/\hbar)H_m^f} \Phi^i \quad (\text{C.1})$$

where, $\Phi^i(\mathbf{r}_I) = \mu_{f \leftarrow i} \phi^i(\mathbf{r}_I)$, $\phi^i(\mathbf{r}_I)$ is the eigenfunction of the impurity in the initial state with energy $\hbar\omega^i$; $\mu_{f \leftarrow i}$ the electronic transition dipole moment from i to f; and H_m^f is the dopant Hamiltonian in the final state. It is written as $H_m^f = T_{\text{kin}} + V_m^f(\mathbf{r}_I)$, where T_{kin} is the kinetic energy operator and $V_m^f(\mathbf{r}_I)$ is the potential energy surface in the final state. For a single excited electronic state (e.g. S excited state for an atom) index m can be omitted. In the case of multiple electronic states, $V_m^f(\mathbf{r}_I)$ is the m^{th} eigenvalue of the excited potential matrix.

The dependence of $\mu_{f \leftarrow i}$ on \mathbf{r}_I is weak and it can be taken as a good first approximation to be independent of \mathbf{r}_I (Condon approximation, [135]). In this case the initial state on the excited-state potential is an exact replica of the initial vibrational state $\phi(\mathbf{r}_I)$. One speaks of the initial vibrational state $\phi(\mathbf{r}_I)$ as making a vertical, or Franck-Condon, transition to the excited-electronic state, and the region of the excited state potential where the initial state is born is called the Franck-Condon region. Therefore, $\phi^i(\mathbf{r}_I)$ is expanded in the basis set of the eigenfunctions $\varphi_\nu^m(\mathbf{r})$ of H_m^f with energies $\hbar\omega_\nu^m$

$$\phi^i(\mathbf{r}) = \sum_\nu a_\nu^m \varphi_\nu^m(\mathbf{r}_I), \quad a_\nu^m = \int d^3\mathbf{r} \varphi_\nu^{m*}(\mathbf{r}_I) \phi^i(\mathbf{r}_I) \quad (\text{C.2})$$

Introducing this expression in Eq. (C.1), we obtain

$$\begin{aligned}
I(\omega) &\propto \sum_m \int dt e^{-i(\omega+\omega^i)t} \sum_\nu |a_\nu^m|^2 e^{i\omega_\nu^m t} \\
&= \sum_m \sum_\nu |a_\nu^m|^2 \delta [\omega - (\omega_\nu^m - \omega^i)]
\end{aligned} \tag{C.3}$$

The spectrum is a series of lines at energies $\hbar(\omega_\nu^m - \omega^i)$ with relative intensities $|a_\nu^m|^2 \cdot |a_\nu^m|^2$ are called the Franck-Condon factors. In the case where the final states correspond to the continuous or quasi-continuous spectrum of H_m^f , it can be assumed that $\langle T_{\text{kin}} \rangle \ll \langle V_m^f \rangle$, and the Hamiltonian is approximated as $H_m^f \approx V_m^f(\mathbf{r})$. Inserting this approximation in Eq. (C.1) and integrating over time we get the semiclassical expression for $I(\omega)$, also called “reflection principle”[136], that we use to simulate absorption or emission spectra

$$I(\omega) \propto \sum_m \int d^3\mathbf{r}_I |\phi^i(\mathbf{r}_I)|^2 \delta [\omega - (V_m^f(\mathbf{r}_I)/\hbar - \omega^i)] \tag{C.4}$$

The density fluctuation (DF) sampling method constructs this expression stochastically by generating a large number of helium-impurity configurations n_c , of the order of 10^6 . Each configuration consists of a set of N positions for the He atoms in the simulation box. If the impurity is treated quantum mechanically, its position is also randomly generated using $|\phi^i(\mathbf{r}_I)|^2$ as its probability density distribution. Otherwise only its equilibrium position in the i electronic state is used.

The helium positions are randomly generated by using the helium density $\rho(\mathbf{r})/N$ as the probability density distribution. A hard-sphere repulsion between He atoms to approximately take into account He-He correlations is added. The diameter of the exclusion sphere has to be of the order of $h = 2,18\text{\AA}$ in order to be consistent with the DF description of the liquid, since h is the length used in the functional to screen the Lennard-Jones interaction between particles and to compute the coarse grained density (see annex B). So, if the next helium position falls within the exclusion volume around any of the already selected heliums, it is rejected and a new sample is done. Hence, we have chosen a density-dependent sphere radius of the form

$$R_j = R(\mathbf{r}_j) = \frac{h}{2} \left(\frac{\rho_0}{\bar{\rho}(\mathbf{r}_j)} \right)^{1/3} \quad (\text{C.5})$$

around helium atom j at \mathbf{r}_j , where ρ_0 is the saturation density value and $\bar{\rho}$ is the coarsegrained density, defined as the averaged density over a sphere of radius h . Although this scaling has no effect in the bulk, it is essential to correctly reproduce the density in the droplet surface region. The rationale for choosing this form for R_j is sketched in the Appendix of Ref [137]

Finally, by collecting the transition energies of all the sampled configurations in a histogram is possible to get the line shape of the spectrum. Specifically, for a given sampled configuration $\{k\}$ the transition energy is

$$E\{k\} = V_m^f\{k\} - V^i\{k\} \quad (\text{C.6})$$

where $V^i\{k\} = \sum_j V_{He-I}^i(|\mathbf{r}_j^{\{k\}} - \mathbf{r}_I^{\{k\}}|)$ is the sum of helium-dopant pairwise interactions in the initial state and $V_m^f\{k\}$ are the eigenvalues of the excited state interaction energy matrix $\sum_j U(|\mathbf{r}_j^{\{k\}} - \mathbf{r}_I^{\{k\}}|) + H^{SO}$. The histogram of the collected stochastic energies is identified with the absorption spectrum

$$I(\omega) \propto \sum_m \frac{1}{n_c} \sum_{\{k\}}^{n_c} \delta[\omega - (V_m^f\{k\} - V^i\{k\})/\hbar] \quad (\text{C.7})$$

In this way, we obtain the absorption spectrum of impurities in liquid helium including shape fluctuations [22].

D. Details of the Coulomb explosion simulation

D.4.1. Ak_2 ($v = 0$) wave function

The Ak_2 $v = 0$ vibrational wave functions were obtained by fitting the Ak_2 potential energy curves to a Morse function around the minimum

$$V(R) = D_e [e^{-\alpha(R-R_e)} - 2e^{-\alpha(R-R_e)}] \quad (\text{D.1})$$

The one-dimension Schrödinger equation was then solved using finite difference followed by Numerov-Cooley integration [138, 139]. The resulting Morse parameters and the points R_- and R_+ at which the probability distribution (i.e. the square of the $v = 0$ vibrational function) is equal to half its maximum value are displayed in Table D.3. ^4He -TDDFT simulations at R_- and R_+ are used to determine the width of the observables, see section II.C in the main text.

Table D.3. Ak_2 Morse parameters and R_- and R_+ distances used to determine the FWHM of the $v = 0$ bond length distribution (see text). The reference for the potential energy curves fitted to obtain the Morse parameters are given in the Ref. row.

	Li_2		Na_2		K_2		Rb_2		Cs_2	
	$^1\Sigma_g^+$	$^3\Sigma_u^+$	$^1\Sigma_g^+$	$^3\Sigma_u^+$	$^1\Sigma_g^+$	$^3\Sigma_u^+$	$^1\Sigma_g^+$	$^3\Sigma_u^+$	$^1\Sigma_g^+$	$^3\Sigma_u^+$
D_e (cm^{-1})	8613.2	344.4	5901.5	161.3	4450.7	254.2	6653.9	224.0	3644.8	285.0
α (\AA^{-1})	0.848	0.794	0.829	0.768	0.745	0.730	0.56	0.69	0.694	0.654
R_e (\AA)	2.659	4.134	3.07	5.20	3.92	5.79	4.22	6.11	4.61	6.35
Ref.	[103]	[103]	[104]	[104]	[107,105]	[106]	[140]	[117]	[104]	[104]
R_- (\AA)	2.532	3.891	2.96	4.96	3.82	5.59	4.13	5.93	4.53	6.19
R_+ (\AA)	2.809	4.541	3.19	5.56	4.05	6.06	4.32	6.34	4.71	6.55

D.4.2. $Ak^+ - Ak^+$ interaction

We use the charge-charge Coulomb interaction,

$$g(R) = \frac{q^2}{4\pi\epsilon_0 R} \quad (\text{D.2})$$

where q is the absolute value of the electron charge, to which a volume effect term is added to take into account the overlap of the singly charged ion cores. The volume effect is important at small distances [141–143]. The data from Jeung [142] were fitted to an exponential form

$$f(R) = B \cdot e^{-R \cdot A} \quad (\text{D.3})$$

and added to the Coulombic $Ak^+ - Ak^+$ charge-charge interaction of Eq. (D.2). The values of the parameters of the exponential fit are collected in Table D.4. Note that the volume effect contribution was not found to be very important at the distances considered in this work. In addition, no volume effect was reported for Li_2^{2+} in Jeung’s paper [142] so it is not included. It is expected to be even less important than for the other alkalis at the Li_2^{2+} distances considered in this work.

Table D.4. Parameters for the one-exponential fit, Eq.(D.3), of the volume effect repulsion. We fitted $\log f(x)$ instead of $f(x)$ to get the A and B parameters, in order to counterbalance the excessive weight of the highly repulsive energies at very short distances.

Ak_2^{2+}	Parameters	
	A (\AA^{-1})	B (K)
Na_2^{2+}	5.055	$42.748 \cdot 10^6$
K_2^{2+}	4.228	$218.738 \cdot 10^6$
Rb_2^{2+}	3.753	$228.740 \cdot 10^6$
Cs_2^{2+}	3.231	$216.217 \cdot 10^6$

E. Details about the Coulomb explosion results

E.5.1. $Ak_2@^4He_N$ equilibrium configuration

Table E.5. Equilibrium configurations for $Ak_2@^4He_{1000}$ ground singlet ($^1\Sigma_g^+$) and triplet ($^3\Sigma_u^+$) states. $r_e(Ak-Ak)$ is the Ak_2 equilibrium bond length; d_{Ak-COM} is the distance of each Ak atom to the helium center of mass; d_{COM} is the distance of Ak_2 center of mass to the droplet center of mass; V_{D-He} is the dopant (Ak_2 or Ak) interaction energy with the droplet; S_D is the solvation energy (see text). The results for $Ak@He_N$, $N=1000$ (Ref. [87] or 5000 (this work) are given for comparison. The sharp density radius of the droplet is 22.2 Å for $N=1000$ and 38.0 Å for $N=5000$. The total energy of the $^4He_{1000}$ droplet is -5395.9 K, and that of $^4He_{5000}$ droplet is -30632.9 K.

		Li ₂		Li	Na ₂		Na	K ₂		K	Rb ₂		Rb	Cs ₂		Cs
		$^1\Sigma_g^+$	$^3\Sigma_u^+$		$^1\Sigma_g^+$	$^3\Sigma_u^+$		$^1\Sigma_g^+$	$^3\Sigma_u^+$		$^1\Sigma_g^+$	$^3\Sigma_u^+$		$^1\Sigma_g^+$	$^3\Sigma_u^+$	
	$r_e(Ak-Ak)$ (Å)	2.658	4.134	—	3.072	5.2	—	3.924	5.773	—	4.23	6.11	—	4.647	6.50	—
$N=1000$	d_{Ak-COM} (Å)	23.9	24.5	25.4	24.5	25.2	25.7	25.2	25.5	26.3	25.4	25.9	26.3	26.0	26.4	26.8
	d_{COM} (Å)	23.9	24.4	—	24.5	25.0	—	25.2	25.6	—	25.4	25.7	—	25.9	26.2	—
	V_{D-He} (K)	-36.8	-31.8	-14.0	-32.4	-27.8	-13.5	-31.8	-28.7	-13.9	-34.0	-30.9	-15.1	-30.5	-28.1	-13.9
	S_D (K)	-22.5	-20.1	-9.0	-20.9	-18.4	-8.9	-21.0	-19.4	-9.6	-22.6	-20.9	-10.4	-21.0	-19.7	-9.8
$N=5000$	d_{Ak-COM} (Å)	39.5	40.2	41.0	40.2	40.8	41.4	41.0	41.3	41.8	41.0	41.5	42.0	42.0	42.0	42.3
	d_{COM} (Å)	39.5	40.2	—	40.1	40.8	—	40.9	41.2	—	40.9	41.4	—	41.6	41.9	—
	V_{D-He} (K)	-41.3	-35.9	-16.6	-36.8	-31.8	-15.4	-36.8	-33.6	-16.6	-39.6	-36.0	-17.6	-35.9	-33.2	-16.8
	S_D (K)	-26.1	-23.4	-13.2	-24.0	-21.3	-10.4	-25.1	-23.2	-13.7	-27.1	-25.3	-12.4	-25.4	-23.9	-14.1

The equilibrium configuration of $Ak_2@^4He_N$ taken as initial conditions for the dynamics are characterized by the equilibrium distance of the Ak_2 center of mass to the droplet center of mass, d_{COM} , and the solvation energy of Ak_2 , S_D , collected in Table E.5, together with the corresponding values for $Ak@^4He_N$ for the sake of comparison. The solvation energy S_D is defined as the difference between the total energy of the dopant (Ak_2 or Ak) on the $^4He_{1000}$ droplet and that of the pure droplet (see Ref. [87] for further details)

E.5.2. Effect of Ak_2 bond length distribution on the final angle between the ions velocity vectors

Table E.6. Width of the final angle between the ions velocity vectors $\Delta\theta$ due to Ak_2 $v = 0$ zero-point bond length distribution. It was calculated as the difference of the θ values obtained at R_+ and R_- , the two points defining the FWHM of the bond length distribution.

Ak	state	$\Delta\theta$	$\Delta\theta$
		${}^4\text{He}_{1000}$	@ ${}^4\text{He}_{5000}$
Li	${}^1\Sigma_g^+$	0.2°	0.4°
	${}^3\Sigma_u^+$	0.4°	1.2°
Na	${}^1\Sigma_g^+$	0.1°	0.2°
	${}^3\Sigma_u^+$	0.3°	0.3°
K	${}^1\Sigma_g^+$	0.1°	0.2°
	${}^3\Sigma_u^+$	0.2°	0.3°
Rb	${}^1\Sigma_g^+$	0.1°	0.2°
	${}^3\Sigma_u^+$	0.2°	0.3°
Cs	${}^1\Sigma_g^+$	0.1°	0.1°
	${}^3\Sigma_u^+$	0.2°	0.2°

Table E.7. Ion kinetic energy upon double ionization of $\text{Na}_2 \ ^3\Sigma_u^+ @^4\text{He}_{1000}$ as a function of the angle φ between the diatomic axis and the normal to the droplet surface. K_{droplet} or K_{free} stands for the ion going towards or away from the droplet, respectively (except in the case of $\varphi=90^\circ$ where both ions are equivalent). Note that angle values $\varphi < 60^\circ$ are not populated for $\text{Na}_2 \ ^3\Sigma_u^+$, but they show how the evolution for other states or alkalis for which smaller angles could be populated.

φ	K_{droplet}	K_{free}	θ
($^\circ$)	(eV)	(eV)	($^\circ$)
90	1.369	1.369	176.5
75	1.355	1.370	175.4
70	1.339	1.370	175.1
60	1.268	1.372	174.6
45	1.043	1.377	172.8
30	0.937	1.378	178.4
15	0.868	1.379	175.1
0	0.903	1.377	180.0

E.5.3. Check on the effect of the three-body potential for $\text{Rb}_2 \ ^3\Sigma_u^+$

Table E.8. Comparison between $\text{Rb}_2 \ ^3\Sigma_u^+ @^4\text{He}_{1000}$ using the 3-Body $\text{Rb}_2\text{-He}$ interaction from Guillon *et al.*[117] and the sum of 2-Body Rb-He interactions from Patil[118] (static properties).

	2-Body	3-Body
$d_{\text{Ak-COM}}$ (\AA)	25.9	26.0
d_{COM} (\AA)	25.7	25.8
$V_{\text{Rb}_2\text{-He}}$ (K)	-30.9	-29.9
S_{Rb_2} (K)	-20.9	-20.4

Table E.9. Comparison between 2-body and 3-body interactions on the results of Coulomb explosion of $\text{Rb}_2@^4\text{He}_{1000}$ ($^3\Sigma_u^+$, R_e).

	2-Body	3-Body
K (eV)	1.164	1.167
θ ($^\circ$)	177.0	177.1

F. Main characteristics of the interaction potentials

Table F.10. Main characteristics of the interaction potentials for Ak-He, Ak⁺-He, Ar-He and Ar-Ar involved in this thesis. Second column and third column correspond the equilibrium configuration at distance (R_{eq}) and dissociation energy (De), given in Å and K respectively. References are shown in the fourth column.

Interaction	R_{eq} (Å)	De (K)	Ref
Li-He	6.19	-1.93	[118]
Li ⁺ -He	1.93	-852.59	[109]
Na-He	6.42	-1.73	[118]
Na ⁺ -He	2.41	-410.51	[109]
K-He	7.18	-1.40	[118]
K ⁺ -He	2.91	-236.51	[109]
Rb-He	7.33	-1.41	[118]
Rb ⁺ -He	3.09	-203.99	[109]
Cs-He	7.73	-1.21	[118]
Cs ⁺ -He	3.38	-168.94	[109]
Ar-He	3.49	-29.59	[74]
Ar-Ar	3.76	-143.36	[74]

G. Technical details for the ^4He -TDDFT calculations

Table G.11. Technical details for the ^4He -TDDFT calculations. The “ * ” mark means that several grid sizes were taken in order to address small (few thousands ^4He atoms) and big droplets. On the other hand, “ \star ” correspond to those dynamics where a frozen helium droplet was considered.

Parameters	Chapter III	Chapter IV	Chapter V	Chapter VI
Integration time (fs)	0.1	0.05	0.01-0.05*	0.1
Grid step [x,y,z] (\AA)	[0.4, 0.4, 0.4]	[0.3, 0.3, 0.3]	[0.4, 0.4, 0.4]	[0.4, 0.4, 0.4]
Simulation box [x,y,z](\AA)	[44.8, 44.8, 56]	[48, 48, 54]	*	[57.6, 57.6, 57.6]

RÉSUMÉ ÉTENDU EN FRANÇAIS

1. Introduction

L'hélium-4 liquide devient superfluide quand la température est inférieure à celle de la transition dite lambda, à 2,17 K. Il manifeste alors un certain nombre de propriétés remarquables, comme une viscosité négligeable et un transport de la chaleur extrêmement efficace. Dans les années 50, Becker *et al.* [14] ont posé la question de savoir si et comment ces propriétés de superfluidité pouvaient se manifester dans des systèmes de taille finie. Depuis, tout un domaine de recherche s'est développé autour de la production de nanogouttes d'hélium (HND) et de leurs propriétés. Ces nanogouttes sont formées par détente dans le vide d'hélium-4 (gaz ou liquide) refroidi, et comportent de $\sim 10^3$ à 10^{12} atomes d' ^4He . Plusieurs propriétés de superfluidité ont été démontrées par spectroscopie de molécules-hôtes. D'un autre côté, la recherche s'est intéressée au potentiel de ces nanogouttes en tant que matrice pour étudier la spectroscopie et la dynamique de molécules ou d'agrégats. En effet, ces nanogouttes présentent des qualités exceptionnelles de ce point de vue, au point que Scoles et Lehmann les ont qualifiées de "The ultimate spectroscopic matrix": elles peuvent recueillir n'importe quel dopant, elles sont fluides et même superfluides à une température très basse (0.4 K), leur interaction avec les atomes ou molécules-hôtes est très faible, elles sont transparentes à la lumière jusqu'aux UV...

Dans cette thèse on s'intéresse à la description théorique de plusieurs processus dynamiques impliquant des HND. Les processus étudiés se rangent selon deux axes: caractérisation de propriétés superfluides dans un système de taille finie

(nucléation et détection de vortex quantiques), et utilisation de HND comme environnement idéal pour étudier la spectroscopie et la dynamique de dopants (formation d'agrégats, solvatation d'ions et explosion coulombienne). L'outil principal de ces simulations est l'approche de la fonctionnelle de la densité d'hélium.

2. Les méthodes $^4\text{He-DFT}$ et $^4\text{He-TDDFT}$

La théorie de la fonctionnelle de la densité d'hélium ($^4\text{He-DFT}$) est semblable à celle de la DFT électronique: elle cherche à résoudre l'équation de Schrödinger d'un système à N atomes d' ^4He par la détermination de la densité d'hélium à un corps au lieu de celle de la fonction d'onde à N -corps. Elle constitue un compromis entre la précision de méthodes *ab initio* (comme celles de Monte Carlo quantique (QMC) [38]) et la faisabilité numérique [39]. Elle peut s'appliquer à des systèmes beaucoup plus grands que ces méthodes, et permet également la description de la dynamique, grâce à sa version dépendante du temps ($^4\text{He-TDDFT}$). Elle est à ce jour la seule méthode capable de reproduire avec succès les résultats d'une large gamme d'expériences résolues en temps sur des nanogouttes de taille réaliste, tout en incluant les effets d'échange et de corrélation *via* la fonctionnelle choisie: par exemple, l'interface liquide-vapeur [40-41], les nanogouttes pures ou dopées [41-43], l'adsorption d'atomes d'alcalins en surface de nanogouttes [44,73, 144], la stabilité et l'influence de vortex en nanogouttes [28,145].

2.1. $^4\text{He-DFT}$ pour des nanogouttes pures

L'approche $^4\text{He-DFT}$ est basée sur le théorème de Hohenberg et Kohn, qui permet d'exprimer l'énergie totale E d'un système quantique à N atomes ^4He à $T = 0$ et $P = 0$ comme fonctionnelle de la densité à une particule $\rho(\mathbf{r}) = \langle \Phi | \sum_i \delta(\mathbf{r} - \mathbf{r}_i) | \Phi \rangle$, Φ étant la fonction d'onde à N corps

$$E[\rho] = \mathcal{T}[\rho] + \int d\mathbf{r} \mathcal{E}[\rho] \quad (\text{F.1})$$

Dans cette équation, le terme $\mathcal{T}[\rho]$ représente l'énergie cinétique d'un système fictif de particules sans interactions, de même densité que celle d'origine, décrit par des orbitales à un corps $\phi_i(\mathbf{r})$.

$$\mathcal{T} = \sum_i \mathcal{T}_i = -\frac{\hbar^2}{2m_4} \sum_i \langle \phi_i | \nabla^2 | \phi_i \rangle = -\frac{\hbar^2}{2m_4} \sum_i \int d\mathbf{r} \phi_i^*(\mathbf{r}) \nabla^2 \phi_i(\mathbf{r}) \quad (\text{F.2})$$

où m_4 est la masse d'un atome ^4He . Notez que la différence avec l'énergie cinétique correcte est incluse dans la fonctionnelle $\mathcal{E}[\rho]$, ainsi que l'échange et les corrélations.

Dans le régime superfluide à $T = 0$, tous les atomes ^4He occupent la même orbitale à une particule ϕ_0 , comme dans un condensat de Bose-Einstein (BEC). La fonction d'onde à N corps et la densité deviennent alors

$$\Phi(\mathbf{r}_1, \mathbf{r}_2, \dots, \mathbf{r}_N) = \prod_i \phi_0(\mathbf{r}_i) \quad \text{et} \quad \rho(\mathbf{r}) = \sum_i |\phi_i(\mathbf{r})|^2 = N |\phi_0(\mathbf{r})|^2 \quad (\text{F.3})$$

et l'énergie cinétique s'écrit alors

$$\mathcal{T} = -\frac{\hbar^2}{2m_4} N \langle \phi_0 | \nabla^2 | \phi_0 \rangle = -\frac{\hbar^2}{2m_4} \int d\mathbf{r} \left| \nabla \sqrt{\rho(\mathbf{r})} \right|^2 = -\frac{\hbar^2}{2m_4} \int d\mathbf{r} |\nabla \Psi(\mathbf{r})|^2 \quad (\text{F.4})$$

où $\Psi(r)$ est la *pseudo-fonction d'onde* ou le *paramètre d'ordre* (qui représente la transition de phase entre le liquide normal et le superfluide), reliée à $\rho(r)$ par

$$\rho(\mathbf{r}) = \Psi^*(\mathbf{r})\Psi(\mathbf{r}) \quad \text{et} \quad \Psi(\mathbf{r}) = \sqrt{N}\phi_0(\mathbf{r}) \quad (\text{F.5})$$

Dans toutes les simulations effectuées au cours de cette thèse, nous avons utilisé la fonctionnelle d'Orsay-Trento (OT)

$$\begin{aligned} \mathcal{E}[\rho] = & \frac{1}{2} \int d\mathbf{r}' \rho(\mathbf{r}) V_{LJ}(|\mathbf{r} - \mathbf{r}'|) \rho(\mathbf{r}') \\ & + \frac{1}{2} c_2 \rho(\mathbf{r}) [\bar{\rho}(\mathbf{r})]^2 + \frac{1}{3} c_3 \rho(\mathbf{r}) [\bar{\rho}(\mathbf{r})]^3 \\ & - \frac{\hbar^2}{4m_4} \alpha_s \int d\mathbf{r}' F(|\mathbf{r} - \mathbf{r}'|) [1 - \tilde{\rho}(\mathbf{r})/\rho_{0s}] \nabla \rho(\mathbf{r}) \cdot \nabla' \rho(\mathbf{r}') [1 - \tilde{\rho}(\mathbf{r}')/\rho_{0s}] \\ & - \frac{m_4}{4} \int d\mathbf{r}' V_J(|\mathbf{r} - \mathbf{r}'|) \rho(\mathbf{r}) \rho(\mathbf{r}') [\mathbf{v}(\mathbf{r}) - \mathbf{v}(\mathbf{r}')]^2 \end{aligned} \quad (\text{F.6})$$

Elle a été calibrée pour reproduire le comportement de l'hélium liquide macroscopique à température nulle $T = 0$ [22]. Le premier terme de l'équation Eq.(F.6) correspond à une interaction classique de Lennard-Jones entre atomes d'hélium, qui est tronquée à courtes distances où les effets de corrélation deviennent importants. La deuxième ligne tient compte des effets de corrélation à court terme. La troisième ligne (terme en α_s) est une correction d'énergie cinétique non locale (KC) et le dernier terme est une contribution de reflux (BF pour "backflow" en anglais) qui affecte la réponse dynamique de la fonction. Ce terme BF ne contribue que si le paramètre d'ordre est une fonction complexe (par ex. pour une problème dépendant du temps ou une nanogoutte comprenant un ou plusieurs vortex).

2.2. ${}^4\text{He}$ -(TD)DFT pour des nanogouttes dopées

Les impuretés ou dopants (les deux termes sont utilisés indifféremment pour désigner des atomes ou des molécules à l'intérieur des gouttelettes d'hélium) beaucoup plus lourds que l'hélium peuvent être décrits comme des particules classiques, alors que les autres nécessitent un traitement quantique. Dans cette thèse, nous avons étudié des nanogouttes d'hélium (HND) dopées avec des atomes d'alcalins ($\text{Ak} \equiv \text{Li, Na, K, Rb, Cs}$) et des atomes de gaz rares tels que Ar et Xe. La plupart des dopants étudiés sont plus lourds que les atomes d'hélium, sauf Li et Na (dont les masses sont similaires), et sont donc traités comme des particules classiques. L'interaction ${}^4\text{He}_N$ -dopant représente alors simplement un champ externe pour l'hélium.

$$E[\rho] \rightarrow E[\rho] + \int d\mathbf{r} \rho(\mathbf{r}) V_X(|\mathbf{r} - \mathbf{r}_I|) \quad (\text{F.7})$$

où l'interaction hélium-dopant est approximée comme somme d'interactions de paires V_X et \mathbf{r}_I est le vecteur position de l'impureté.

Les équations d'Euler-Lagrange qui déterminent la densité d'hélium à l'état fondamental [Eq.(F.8)] sont obtenues en minimisant $E[\rho]$ par rapport à $\rho(\mathbf{r})$ ou $\Psi(\mathbf{r})$, sous contrainte d'un nombre d'atomes d'hélium $N = \int d\mathbf{r} \rho(\mathbf{r})$ constant

$$\left\{ -\frac{\hbar^2}{2m_4} \nabla^2 + \frac{\delta \mathcal{E}_c}{\delta \rho} + V_X(|\mathbf{r} - \mathbf{r}_I|) \right\} \Psi(\mathbf{r}) = \mu \Psi(\mathbf{r}) \quad (\text{F.8})$$

où μ est le potentiel chimique (multiplicateur de Lagrange pour la contrainte).

Les dopants légers comme Li, et dans une moindre mesure Na, nécessitent un traitement quantique. Dans ce cas, $E[\rho]$ doit également prendre en compte leur mouvement au point zéro

$$E[\rho] \rightarrow E[\rho] + \frac{\hbar^2}{2m_I} \int d\mathbf{r}_I |\nabla_I \phi(\mathbf{r}_I)|^2 + \iint d\mathbf{r} d\mathbf{r}_I \rho(\mathbf{r}) V_X(|\mathbf{r} - \mathbf{r}_I|) |\phi(\mathbf{r}_I)|^2 \quad (\text{F.9})$$

où $\phi(\mathbf{r}_I)$ est la fonction d'onde de l'impureté et m_I sa masse. Il en résulte deux équations couplées, l'une pour le liquide et l'autre pour l'impureté

$$\begin{aligned} \left\{ -\frac{\hbar^2}{2m_4} \nabla^2 + \frac{\delta \mathcal{E}_c}{\delta \rho} + \int d\mathbf{r}_I V_X(|\mathbf{r} - \mathbf{r}_I|) |\phi(\mathbf{r}_I)|^2 \right\} \Psi(\mathbf{r}) &= \mu \Psi(\mathbf{r}) \\ \left\{ -\frac{\hbar^2}{2m_I} \nabla_I^2 + \int d\mathbf{r} V_X(|\mathbf{r} - \mathbf{r}_I|) \rho(\mathbf{r}) \right\} \phi(\mathbf{r}_I) &= \epsilon \phi(\mathbf{r}_I) \end{aligned} \quad (\text{F.10})$$

Les équations (F.8) ou (F.10) sont ensuite résolues par la méthode de propagation en temps imaginaire [50] (ITM, pour “Imaginary Time Propagation Method” en anglais) en coordonnées cartésiennes. Les calculs sont effectués en trois dimensions, sans imposer de symétries. Toutes les quantités sont discrétisées sur une grille cartésienne régulièrement espacée, avec une maille typiquement de l’ordre de 0,4 Å. Les opérateurs différentiels sont évalués à l’aide d’une méthode de différences finies à k points où, dans la plupart des applications, $k = 13$ est suffisamment précis. Tous les termes de la fonctionnelle OT dans l’équation (F.6) qui représentent des convolutions [41, 48, 52] peuvent être évalués dans l’espace des moments en exploitant le théorème de convolution, à l’aide d’algorithmes de transformée de Fourier rapide (FFT) parallèles hautement optimisés [53].

Dans le cas de la dynamique de nanogouttes dopées par n impuretés classiques (seul cas étudié dans cette thèse), les équations gouvernant la dynamique sont obtenues en minimisant l’action par rapport à la pseudo-fonction d’onde, après avoir rajouté le terme d’énergie cinétique (classique) du ou des impuretés. On obtient alors les équations couplées suivantes

$$i\hbar \frac{\partial}{\partial t} \Psi(\mathbf{r}) = \left[-\frac{\hbar^2}{2m_{He}} \nabla^2 + \frac{\partial \mathcal{E}_c}{\partial \rho(\mathbf{r})} + \sum_{i=1}^n V_{He-I}(|\mathbf{r} - \mathbf{r}_i|) \right] \Psi(\mathbf{r}) \quad (\text{F.11})$$

$$m_I \ddot{\mathbf{r}}_i = - \left\{ \int d\mathbf{r} V_{He-I}(|\mathbf{r} - \mathbf{r}_i|) \nabla \rho(\mathbf{r}) + \sum_{i \neq j} \left[\frac{\mathbf{r}_i - \mathbf{r}_j}{R_{ij}} \frac{dV_{I-I}(R)}{dR} \Big|_{R=R_{ij}} \right] \right\} \quad (\text{F.12})$$

où \mathbf{r}_i est le vecteur position de l’impureté numéro i et $R_{ij} = |\mathbf{r}_j - \mathbf{r}_i|$, le dernier terme de l’équation (F.12) n’étant présent que si $n > 1$.

2.3. Vortex linéaire

L’existence de vortex (ou tourbillons) quantiques est une propriété typique de superfluidité. Ces vortex peuvent en effet se maintenir indéfiniment (absence de friction). Leur champ de vitesse est dit *irrotationnel*: $\nabla \times \mathbf{v} = \mathbf{0}$, et la circulation autour d’une ligne de vortex est quantifiée. On peut également montrer que leur cœur (la ligne du vortex) est vide, sur un rayon de l’ordre de 1 Å.

Dans le cadre de la méthode ^4He -(TD)DFT, un vortex linéaire le long de l'axe z peut être produit en initialisant la simulation statique (ITM) avec la pseudo-fonction d'onde suivante

$$\Psi(r, \theta) = \frac{\rho^{1/2}(r)}{\sqrt{x^2 + y^2}}(x + iy) \quad (\text{F.13})$$

où $\rho_0(r)$ est la densité correspondant à une gouttelette pure ou dopée sans vortex.

2.4. Bilan énergétique

Dans ce travail, il sera fait référence à différentes énergies caractéristiques. Nous les définissons ici

- Énergie de solvatation de l'impureté X:

$$S_X = E(X@^4\text{He}_N) - E(^4\text{He}_N)$$

- L'énergie du vortex (V) :

$$E_V = E(V@^4\text{He}_N) - E(^4\text{He}_N)$$

- Énergie de liaison de l'impureté au vortex, également appelée "énergie de substitution"

$$B_X = \{E(X@^4\text{He}_N) - E(^4\text{He}_N)\} - \{E((X + V)@^4\text{He}_N) - E(V@^4\text{He}_N)\}$$

3. Formation d'agrégats en nanogouttelettes d'hélium

La formation d'agrégats en nanogouttes d'hélium comporte deux étapes: le dopage et la formation de liaisons entre atomes ou molécules-hôtes.

Les études expérimentales sur le dopage de nanogouttes d'hélium ont été abordées par Toennies et ses collaborateurs [65, 66] dans les années 80. Des résultats importants ont été obtenus, parmi lesquels on peut souligner qu'en fonction des différents paramètres de collision comme le paramètre d'impact, la vitesse relative et la force de l'interaction dopant-hélium, le dopant pouvait être capturé, s'échapper ou passer au travers de la nanogoutte. Lors de la capture, une proportion importante de l'énergie cinétique de l'impureté est dissipée dans la gouttelette. Elle est relaxée par évaporation multiple d'atomes d'hélium [67].

Lorsque plusieurs dopants sont captés, ils finissent par se rencontrer et former une liaison. L'environnement d'hélium superfluide peut interférer dans ce processus, donnant lieu à des formations inhabituelles telles que des structures peu liées qui ont été appelées "mousse à bulles" ou "gel quantique" pour des impuretés légères et à faible interaction entre elles, telles que Ne [68] ou Mg [69]. Ceci a été attribué à la formation d'une coquille d'hélium autour des atomes, empêchant la formation d'une liaison directe entre eux. En outre, la présence de tourbillons quantiques peut influencer sur la morphologie de l'agrégat de dopants en formation, car les cœurs des vortex agissent comme des sites de nucléation, avec pour résultat la constitution de filaments le long de ceux-ci [70 - 72].

Comme les nanogouttelettes peuvent être considérées comme superfluides à la température expérimentale habituelle ($T \approx 0.4$ K), la formation de systèmes liés devrait présenter les mêmes caractéristiques en nanogouttes qu'en phase gazeuse en raison de la viscosité négligeable. Cependant, les structures résultantes peuvent être différentes, en raison de la conductivité thermique très élevée du superfluide. Des structures métastables peuvent alors être obtenues, leur formation résultant d'un contrôle cinétique plutôt que thermodynamique [21, 19- 57].

Dans les travaux pionniers, Nauta et Miller [19] ont observé que l'auto-assemblage de molécules de HCN (cyanure d'hydrogène) formait des chaînes linéaires au lieu des structures compactes attendues. Ce résultat surprenant a été attribué à la forte conductivité thermique de l'hélium superfluide, combinée au moment dipolaire élevé de HCN. À longue distance, l'interaction dipôle-dipôle domine et tend à orienter les molécules en colinéaire à leur entrée dans la nanogoutte. A cause de la forte conductivité thermique de l'hélium, leur énergie cinétique est très rapidement dissipée et lorsqu'elles arrivent à proximité des autres molécules déjà solvatées, elles n'ont plus assez d'énergie cinétique pour se réorienter et former la structure thermodynamique la plus stable (compacte). La structure résultante est alors une longue chaîne (jusqu'à 7 molécules).

Plus généralement, la cinétique joue un rôle important dans le processus de formation de liaison en nanogoutte d'hélium, en particulier dans le cas habituel de dopage séquentiel. En effet, les complexes formés précocement peuvent être gelés dans des conformations métastables, le réarrangement et l'isomérisation dans des conditions aussi froides étant pratiquement impossible [58, 59- 61].

Lorsque plusieurs chambres de dopage sont utilisées, cela peut conduire à des structures originales, telles que des agrégats cœur-coquille [62- 63], et des nanofils [64] évoqués plus haut.

3.1. Méthode

Coppens *et al.* [73] ont étudié la formation d'agrégats d'argon dans une goutte de ${}^4\text{He}_{5000}$ en utilisant la théorie fonctionnelle de densité dépendante du temps (${}^4\text{He}$ -TDDFT). Leurs résultats ont montré la production de configurations faiblement liées en raison de la formation d'une coquille d'hélium de haute densité autour de chaque atome d'argon. Cependant, le choix particulier de conditions initiales hautement symétriques pourrait avoir affecté cette observation. Ici, nous revisitons le processus de formation d'agrégats en considérant le cas plus réaliste de dopage successif, dans lequel les atomes d'argon entrent en collision avec des gouttelettes

d'hélium dopées avec des monomères d'argon ou de petits agrégats. Les potentiels d'interaction sont tirés de la littérature [74]. En plus de ^4He -TDDFT, deux approches atomistiques approximatives sont également testées : les méthodes de dynamique moléculaire “Ring Polymer Molecular Dynamics” (RPMD) [75-77] et la dynamique moyennée sur le point zéro (ZPAD pour “Zero-Point Averaged Dynamics” en anglais) [78-80].

La méthode RPMD utilise une description intégrale du mouvement nucléaire et fournit une description au niveau atomistique à des températures basses mais finies. Elle a déjà été utilisée pour traiter les réactions chimiques dans les gouttelettes d'hélium [81], y compris un cas de dimérisation métastable [82]. La méthode ZPAD est basée sur l'approche de paquets d'ondes gaussiens gelés de Heller [78] et les potentiels effectifs équivalents de Sterling *et al* [83] pour décrire le mouvement nucléaire des atomes d'hélium. La délocalisation de point zéro est décrite par une fonction d'onde gelée attachée à chaque atome He, ce qui revient à effectuer une dynamique classique dans des potentiels d'interaction effectifs. Dans ces deux méthodes, les effets d'échange bosoniques ne sont pas pris en compte.

La méthode ZPAD fournit un moyen très efficace de simuler les gouttelettes d'hélium dopées à la température de 0.4 K, une fois les potentiels effectifs obtenus. Il est également possible d'étendre les trajectoires à l'échelle de temps des nanosecondes ou même au-delà. L'approche RPMD est intermédiaire entre les méthodes de ^4He -TDDFT et ZPAD en termes de coût de calcul. Alors que la ^4He -TDDFT est, en principe, plus réaliste pour décrire des gouttelettes superfluides, puisqu'elle prend en compte les effets quantiques et d'échange-corrélation, elle est significativement plus coûteuses en temps de calcul que les deux méthodes atomistiques approchées. Elle est également généralement limitée aux simulations de température nulle.

Les potentiels d'interaction Ar-Ar et Ar-He utilisés étaient ceux de Tang et Toennies [74] (pour les trois méthodes). Leurs références et caractéristiques sont rassemblées dans le tableau F.10 (annexe F).

3.2. Formation de dimères d'argon

Les cas *A* et *B* présentés dans la Fig. F.1 correspondent à un atome d'argon entrant en collision avec une goutte d'hélium hébergeant un atome Ar, pour former un dimère. La collision est testée pour un paramètre d'impact de ($b = 0$) et $b=10 \text{ \AA}$ (selon x), respectivement. Dans les deux cas, la vitesse initiale $v_z=5 \text{ \AA/ps}$ est définie le long de la direction z pour le dopant externe. Les résultats montrent un dimère lié pour *A* et un état indirectement lié pour *B*. Ce dernier correspond à la présence de densité d'hélium entre les atomes d'argon qui empêche la formation directe de liaison Ar-Ar.

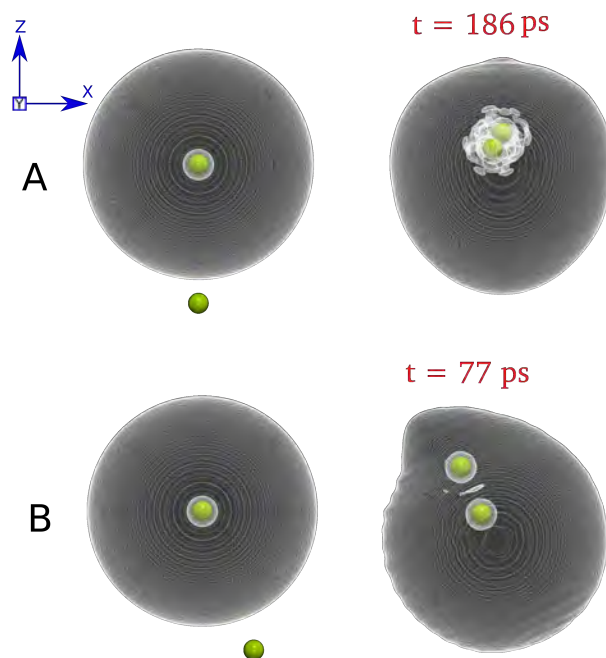


Figure F.1. Ar+Ar@4He₁₀₀₀ collision. La configuration initiale est indiquée dans la colonne de gauche à un moment donné (t). Deux paramètres d'impact ont été explorés : $b = 0$ (cas A) et $b = 10 \text{ \AA}$ (cas B).

3.3. Formation d'un trimère d'argon

Dans le cas *C* présenté dans la Fig. III.2, deux atomes d'argon entrent en collision avec une nanogoutte d'hélium dopée d'un argon en son centre. Les deux atomes-projectiles sont initialement situés sur l'axe z de part et d'autre de la nanogoutte.

Le paramètre d'impact est $b = 0$, et la vitesse des atomes est $v_z = 5 \text{ \AA}/\text{ps}$ et $v_z = -5 \text{ \AA}/\text{ps}$, respectivement. La configuration obtenue est linéaire et symétrique. C'est une configuration métastable puisque le trimère thermodynamiquement le plus stable en phase gazeuse correspond à un triangle équilatéral [85].



Figure F.2. Ar+Ar+Ar@4He₁₀₀₀ collision. La configuration initiale est affichée dans la colonne de gauche et la configuration finale t dans la colonne de droite.

3.4. Formation de pentamères d'argon (Ar_5)

Nous avons étudié la formation de pentamères en partant de plusieurs configurations initiales différentes, le coût des calculs ne permettant malheureusement pas une étude systématique.

Les deux premiers cas, D et E, présentés dans la Fig. F.3, correspondent à un atome d'argon entrant en collision avec la base d'un tétramère Ar_4 (pyramique à base triangulaire) dopant une nanogoutte $^4He_{1000}$. Les valeurs du paramètre d'impact sont $b = 0$ et $b = 10 \text{ \AA}$, respectivement, et la vitesse est $v_z = 5 \text{ \AA}/\text{ps}$ dans les deux cas. La configuration la plus stable du pentamère est une bipyramide à base triangulaire [85]. Dans le cas D on obtient un complexe faiblement lié ("loosely bound"), où l'argon incident reste séparé du centre de gravité de la base triangulaire par une couche de densité d'hélium. Dans le cas E, dont les conditions initiales étaient moins symétriques, on n'obtient pas non plus la configuration thermodynamiquement la plus stable, mais un isomère métastable dans lequel l'atome incident a formé deux liaisons (avec deux atomes d'une arête de la pyramide Ar_4).

Les deux autres cas, F et G, présentés dans la Fig. F.4, correspondent au même système, mais l'atome incident provient de l'autre côté du tétramère dopant, visant le sommet sur l'axe z (vertical sur la figure). Le paramètre d'impact est $b = 0$ dans le cas F et $b = 10 \text{ \AA}$ dans le cas G, et la vitesse est $v_z = -5 \text{ \AA/ps}$ dans les deux cas. Dans le cas F une configuration métastable est obtenue, dans laquelle l'atome incident n'a formé qu'une liaison avec l'argon du sommet du tétraèdre. Dans le cas G, un complexe faiblement lié est formé, dans lequel une couche de densité d'hélium sépare l'argon incident d'une des faces du tétraèdre.

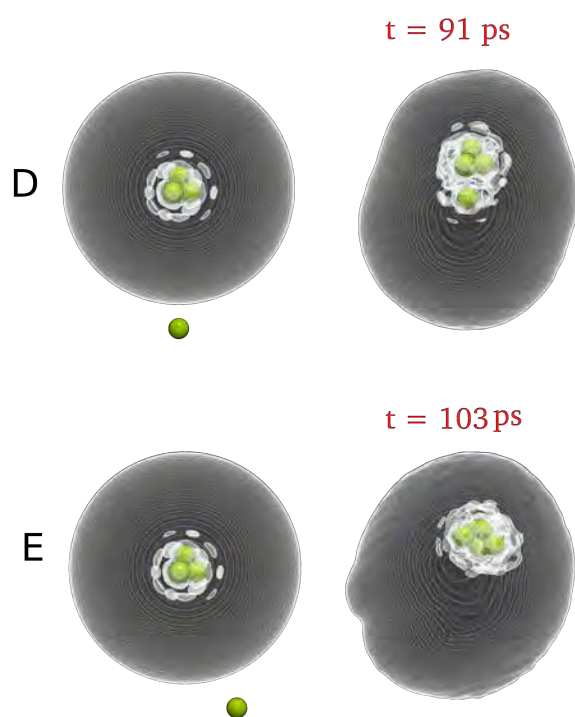


Figure F.3. Collision $\text{Ar} + \text{Ar}_4 @ ^4\text{He}_{1000}$ pour former le pentamère Ar_5 . La configuration initiale est affichée dans la colonne de gauche et la configuration finale à t dans la colonne de droite.

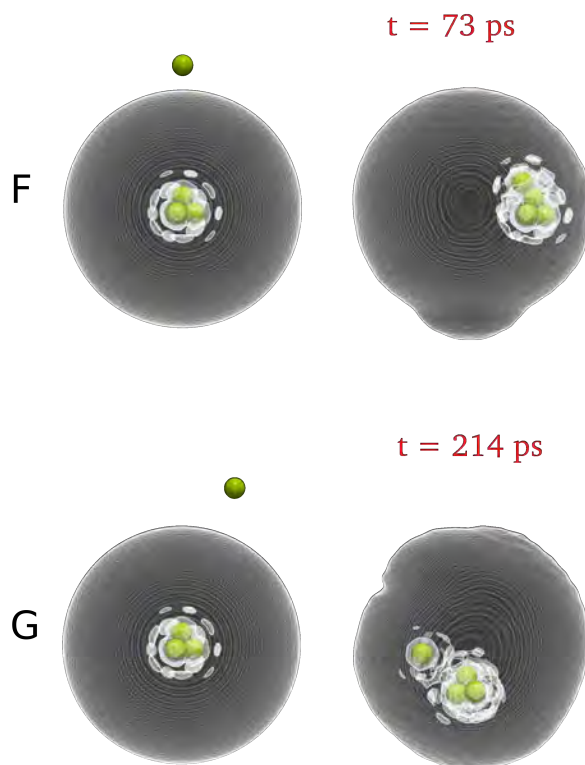


Figure F.4. Collision $\text{Ar} + \text{Ar}_4 @ ^4\text{He}_{1000}$ pour former le pentamère Ar_5 . La configuration initiale est affichée dans la colonne de gauche et la configuration finale à t dans la colonne de droite.

3.5. Conclusions

Les résultats présentés dans ce chapitre ne sont que ceux obtenus par la méthode ⁴He-TDDFT puisqu'ils faisaient partie de mon travail de thèse. Dans les travaux publiés, ils ont été comparés à ceux des deux autres méthodes atomistiques. Les trois méthodes prédisent que la gouttelette d'hélium joue un rôle dans la formation de l'agrégat Ar_n . Il entrave la liaison directe entre les dopants en constituant une structure en coquille autour d'eux. De plus, les effets cinématiques gèlent l'agrégat en formation dans des configurations métastables. Les seules conditions dynamiques qui conduisent à une configuration d'agrégat lié comme dans la phase gazeuse sont celles de la formation du dimère Ar_2 par collision $\text{Ar} + \text{Ar} @ ^4\text{He}_{1000}$ avec paramètre d'impact zéro.

4. Solvatation d'ions alcalins Ak⁺ en nanogoutte d'hélium ⁴He₂₀₀₀

4.1. Introduction

L'interaction d'un atome He avec un cation est très forte par rapport à celle d'un atome neutre. Cela conduit à l'apparition d'une couche de solvatation de haute densité, parfois solide, autour du cation, à l'intérieur d'une gouttelette d'hélium ou du liquide macroscopique, appelée "boule de neige" [22]. Souvent, plusieurs couches de solvation supplémentaires peuvent être distinguées. Pour les interactions très fortes, la première couche est presque isolée, ce qui entrave les échanges bosoniques avec le reste du superfluide. Notez que le terme "boule de neige" peut avoir des significations différentes dans la littérature, de sorte qu'il est quelque peu mal défini [86]. Ici, il fera référence à la première couche d'hélium de haute densité apparaissant autour du cation.

Les atomes alcalins neutres (Ak) ont la propriété particulière de rester à l'extérieur, dans une dépression ou "cuvette", à la surface des nanogouttes [87]. Lors de l'ionisation, le cation Ak⁺ résultant s'enfonce dans la gouttelette [88]. Contrairement à la situation dans le liquide macroscopique, ce mouvement ne nécessite pas l'application d'un champ électrique externe.

Dans une expérience récente, Albrechtsen *et al* [89] ont utilisé ce processus comme modèle pour dévoiler les principales étapes de la solvatation ionique dans les nanogouttes d'hélium. Il s'agit d'une réalisation remarquable, surtout si l'on considère la citation récente de Markus [90] "*Il est impossible de suivre par des mesures un processus expérimental réel de transfert d'un seul ion de son état isolé dans la phase gazeuse à son état entièrement solvato dans une solution. Un tel processus, cependant, peut être traité comme un processus de pensée et des considérations théoriques peuvent y être appliquées*". Pour atteindre cet objectif, une nanogoutte d'hélium dopée avec un Xe à l'intérieur et un Na à la surface a été interrogée dans une expérience laser pompe-sonde.

L'impulsion pompe ionise l'atome de sodium, initiant ainsi le processus de solvation ionique. Après un délai de temps variable, l'impulsion sonde ionise l'atome de xénon, déclenchant la répulsion de Coulomb entre les ions Xe⁺ et Na⁺. Cela conduit à l'éjection de Na⁺ avec un nombre n d'atomes He attachés. Les complexes Na⁺@⁴He _{n} résultants sont détectés et caractérisés par imagerie de vecteur vitesse. En analysant en détail les rendements des ions Na⁺-⁴He _{n} en fonction du délai, les auteurs ont conclu que le processus était Poissonnien jusqu'à $n = 5$: les premiers atomes d'hélium s'attachent à l'ion Na⁺ indépendamment les uns des autres avec un taux constant, comme le montre la dépendance linéaire en temps du pic de la distribution de probabilité $n(t) = At$. Ceci a été confirmé par une simulation théorique basée sur l'approche ⁴He-TDDFT [89].

4.2. Méthode

Nous avons étudié la solvation des cations alcalins Ak⁺ (Li⁺, Na⁺, K⁺, Rb⁺ et Cs⁺) dans une nanogoutte superfluide ⁴He₂₀₀₀ en utilisant la ⁴He-TDDFT. La configuration d'équilibre de Ak neutre sur une goutte de ⁴He₂₀₀₀ est déterminée à l'aide de simulations statiques comme décrit dans le chapitre II. La dynamique est déclenchée en substituant l'atome d'Ak par son cation Ak⁺, ce qui équivaut à une ionisation soudaine. Le cation Ak⁺ entre alors dans la nanogoutte et se dirige vers sa position d'équilibre au centre. Tous les ions alcalins ont été traités comme des particules classiques.

Afin de comparer avec l'expérience, il a été supposé dans le cas de Na⁺ que les n premiers atomes d'hélium attachés à l'ion pendant le processus de pénétration dans la nanogoutte resteraient étroitement liés à lui pendant le processus de répulsion de Coulomb à l'étape sonde et conduiraient à la détection de Ak⁺ ⁴He _{n} . Cela était justifié par la force de l'interaction Ak⁺-He. Ici, nous avons utilisé la même hypothèse, et pour chaque cation alcalin, $n(t)$ est ajusté à une forme linéaire $n(t) = At$ pour n jusqu'à 5; le paramètre A peut être identifié avec le taux de liaison.

4.3. Résultats

La figure F.5 montre le processus de solvatation de l'ion Rb⁺ dans une nanogoutte ⁴He₂₀₀₀ sous forme d'instantanés à différents moments de la simulation ($t=0, 2, 6, 10, 30, 60, 80$ et 100.8 ps). Comme on peut le voir sur cette figure, une couche de haute densité se forme rapidement autour de l'ion, presque aussitôt qu'il pénètre dans la nanogoutte. De plus, le mouvement de l'ion et de son complexe de solvatation vers le centre de la gouttelette crée beaucoup d'excitations à l'intérieur de l'hélium.

Afin de quantifier le processus de solvatation, nous avons déterminé la moyenne sphérique de la densité d'hélium en fonction de la distance à l'ion. Il est présenté dans la Fig F.6 pour la solvatation de Rb⁺ aux mêmes temps que les instantanés de la Fig F.5. Le nombre d'atomes d'hélium dans la première (n_1) ou la seconde (n_2) couche de solvatation est également indiqué (lignes horizontales bleues). Ils ont été obtenus en déterminant d'abord le rayon des couches de solvatation r_1 et r_2 (pointillés bleus verticaux dans la figure IV.2) dans un calcul statique séparé de Rb⁺@He₂₀₀₀, puis en intégrant la densité d'hélium autour de Rb⁺ de 0 à r_1 et r_2 , respectivement. On peut voir que la structure de solvation est stable à environ 30 ps, bien qu'elle continue de gagner un peu plus d'hélium.

La Fig F.7 montre la coupe bidimensionnelle de la densité d'hélium en parallèle avec la moyenne sphérique de la densité autour de la position du cation à la fin de la simulation pour chaque ion alcalin étudié. Dans chaque cas, la structure de solvation est stabilisée. Notez que pour les ions les plus attractifs, Li⁺ et Na⁺ (les caractéristiques des potentiels d'interaction sont collectées dans le tableau F.10 de l'annexe F), la première couche de solvation est bien séparée de la seconde, empêchant l'échange entre les deux.

Afin de relier nos résultats à l'expérience d'Albrechtsen *et al.* [89], nous avons déterminé le nombre d'atomes de He (n) dans la première couche de solvation en fonction du temps comme la partie entière de n_1 décrit plus haut. Nous avons ensuite ajusté $n(t)$ à une forme linéaire, $n(t) = At$. Chaque ajustement a été

effectué deux fois, une fois pour chacune des définitions suivantes de $n(t)$. La première définition correspond à la première fois que la densité intégrée dans la sphère de solvation atteint n ; la seconde définition correspond à la première fois qu'elle atteint n sans plus de fluctuations de retour à $n - 1$. La première définition donne une valeur plus élevée de A que la seconde. Les régions ombrées entre les deux lignes dans les panneaux de la Fig F.8 donnent une idée de l'incertitude sur les taux obtenus dans l'approche ⁴He-TDDFT.

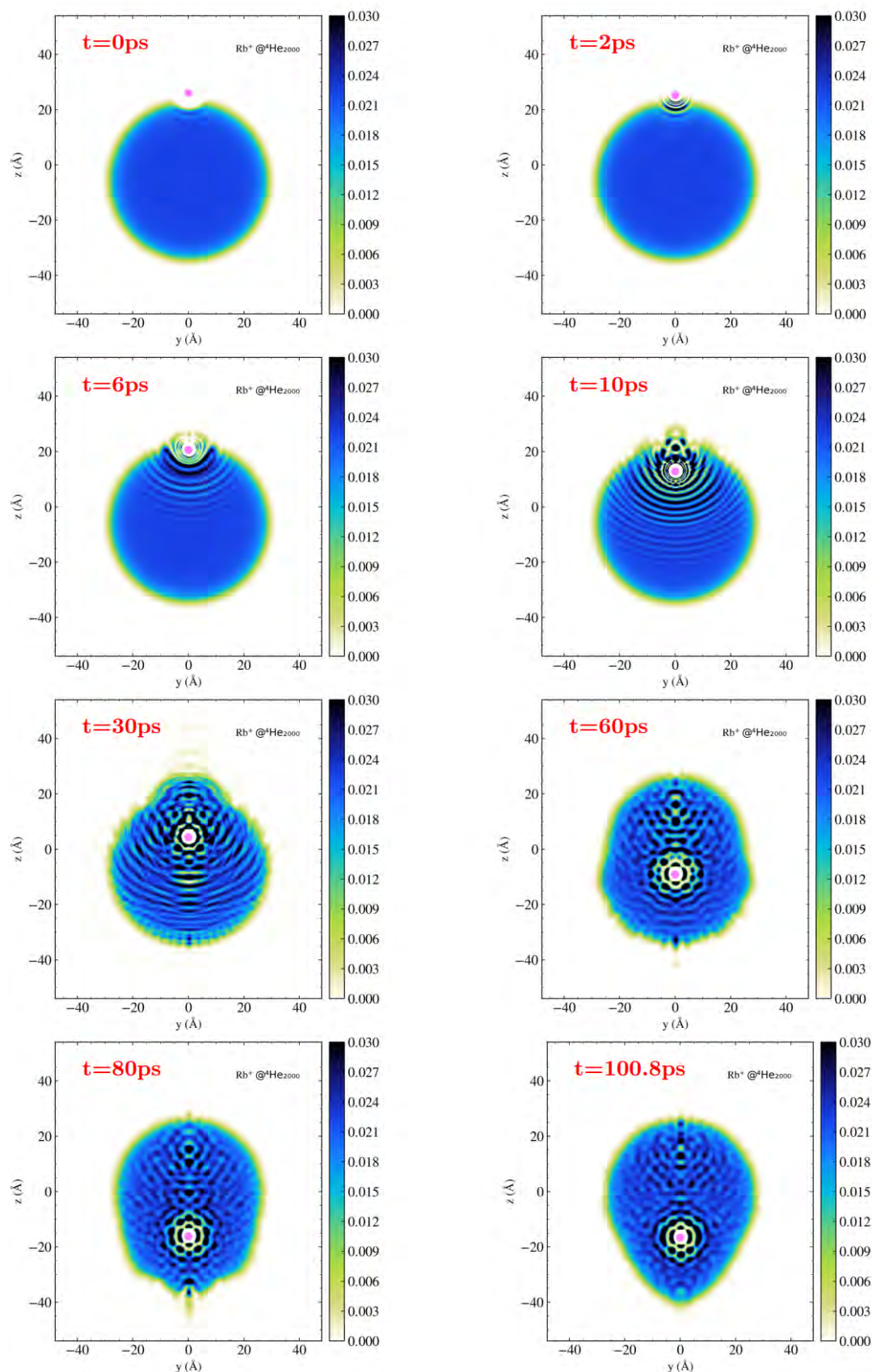


Figure F.5. Coupe bidimensionnelle de la densité d'hélium dans un plan de symétrie et position des ions pour la solvation de Rb^+ à $t=0, 2, 6, 10, 30, 60, 80$ et 100.8 ps. L'échelle de couleur à droite de chaque panneau correspond à la densité d'hélium superfluide donnée en \AA^{-3} (densité d'hélium superfluide 0.0218\AA^{-3} à $T = P = 0$); densité du solide 0.026\AA^{-3}).

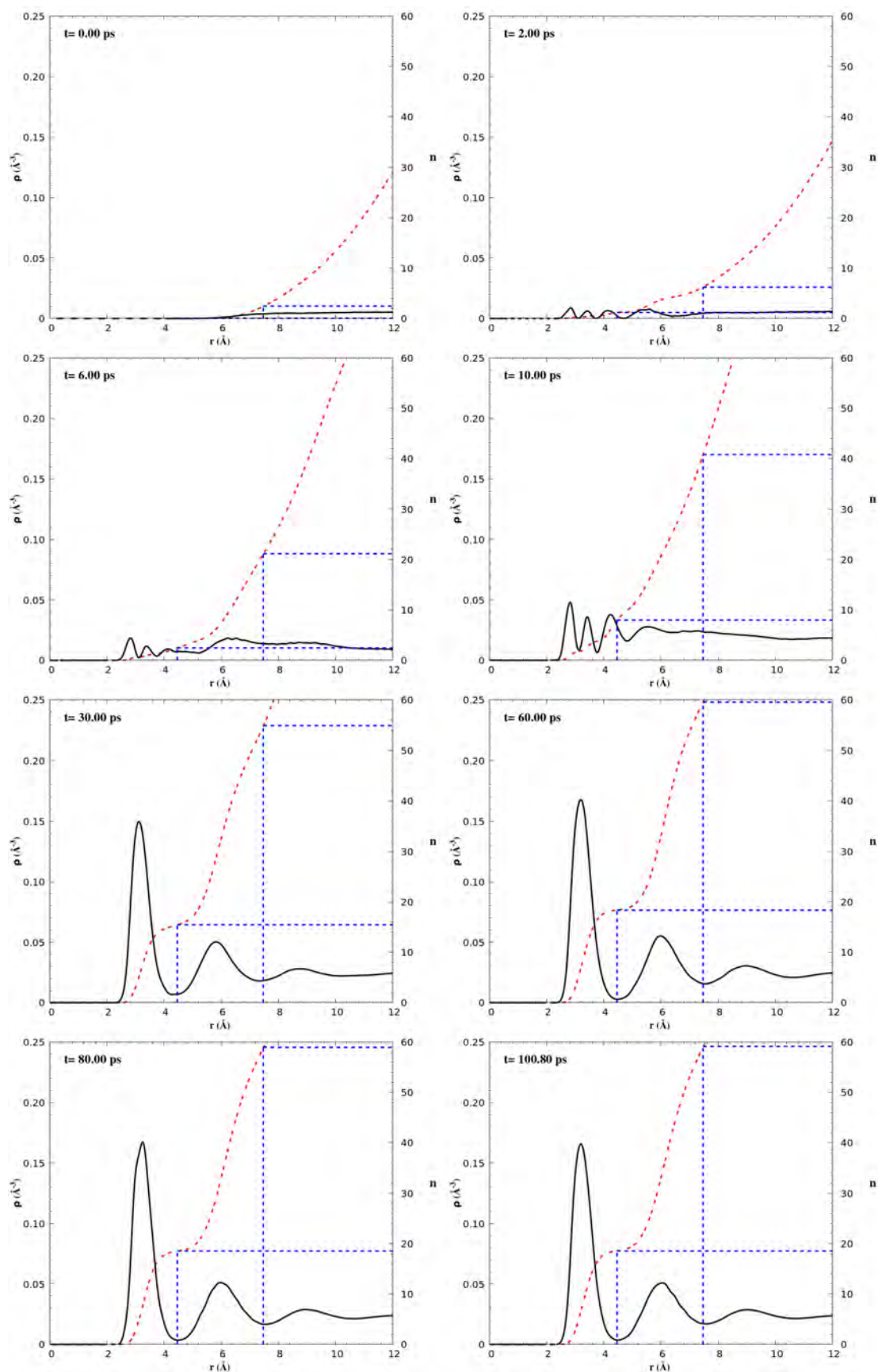


Figure F.6. Moyenne sphérique (courbe noire solide) (à $t=0, 2, 6, 10, 30, 60, 80$ et $100,8$ ps) de la densité d'hélium en fonction de la distance à l'ion Rb^+ , nombre d'atomes He n (ligne pointillée rouge). Les lignes verticales en pointillés bleus montrent le rayon de la première et de la seconde couche de solvation, et les lignes horizontales en pointillés bleus la densité intégrée dans la couche correspondante.

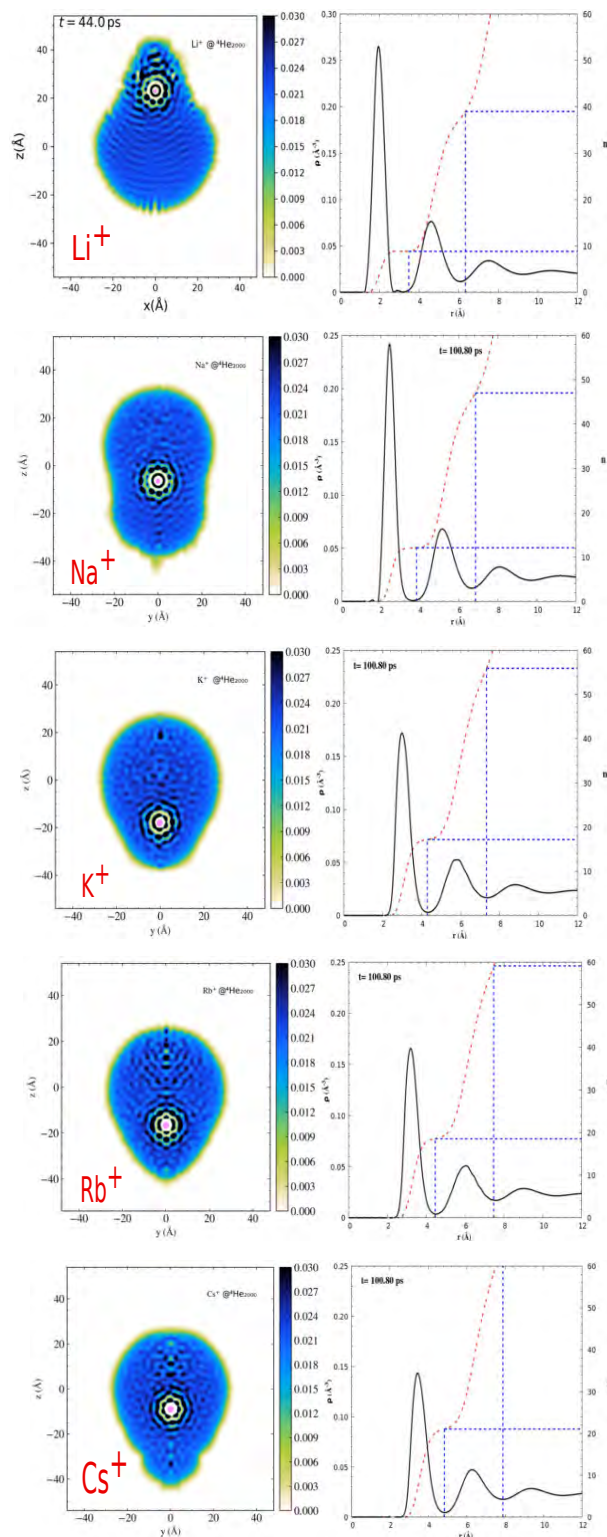


Figure F.7. Solvation de Ak^+ dans une nanogoutte ${}^4\text{He}_{2000}$ à $t=44, 100.8, 100.8, 100.8, 100, 100.8$ ps pour $\text{Li}^+, \text{Na}^+, \text{K}^+, \text{Rb}^+$ et Cs^+ respectivement. Chaque illustration est composée de deux panneaux. Panneau de gauche : coupe bidimensionnelle de la densité d'hélium dans un plan de symétrie et position des ions; panneau de droite : moyenne sphérique de la densité d'hélium en fonction de la distance à Ak^+ .

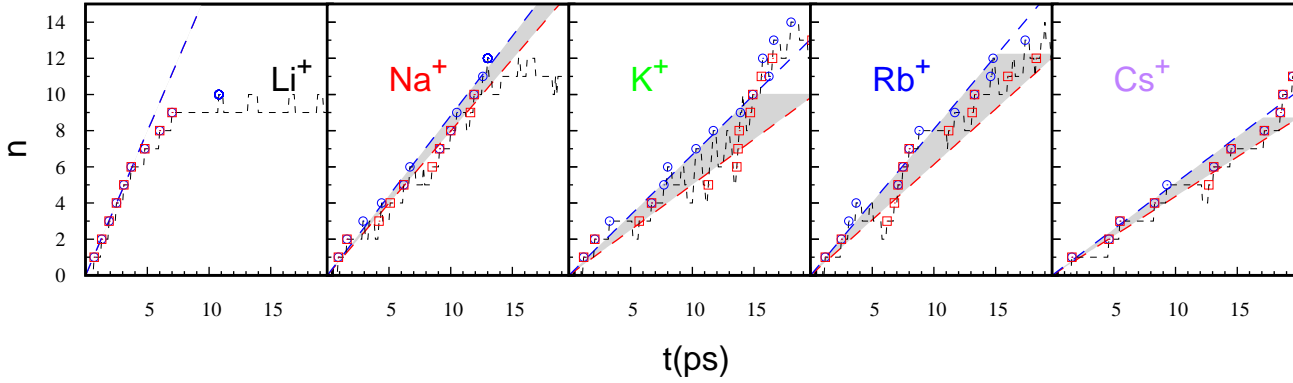


Figure F.8. Nombre d’atomes d’hélium n autour des ions Ak^+ en fonction de t pour $Ak^+@^4\text{He}_{2000}$. Les cercles bleus ou les carrés vides rouges correspondent respectivement à la première ou à la deuxième définition de $n(t)$ expliquée dans le texte. Les lignes en pointillés correspondent au fit $n(t) = At$ pour les complexes $Ak^+@^4\text{He}_n$ jusqu’à $n = 5$, voir le texte pour explication.

4.4. Conclusions

Comme on peut le voir sur la Fig. F.7, les nanogouttes sont encore excitées à la fin des simulations. Elles sont loin de leur configuration d’équilibre final, qui correspond à un ion Ak^+ au repos au centre de la goutte sphérique restante $^4\text{He}_M$ (avec $M < 2000$). Une partie importante de l’énergie d’excitation reste dans la nanogoutte sous forme d’ondes de densité et de modes de surface de grande amplitude, plus une certaine énergie cinétique dans l’ion et dans la nanogoutte elle-même.

Les simulations montrent la formation progressive de la première couche de solvation autour des cations [91]. Le nombre d’atomes d’hélium dans cette couche augmente linéairement avec le temps au cours des premières étapes de la dynamique. Cela indique un processus de capture Poissonnienne, comme le concluent les travaux d’Albrechtsen *et al* [89].

Une simulation plus exigeante est en cours, celle du procédé pompe-sonde complet. Il consiste à ajouter un atome Xe neutre au centre de la nanogoutte d’hélium pendant le processus de pompe (ionisation de l’alcalin à la surface de la gouttelette suivie de sa solvation) et dans une deuxième étape (sonde) à ioniser soudainement l’atome Xe. L’étape de la sonde déclenchera une explosion de Coulomb entre

Ak⁺ et Xe⁺. Les simulations devraient fournir une mesure directe de la cinétique de l'éjection de Ak⁺ et du nombre d'atomes He qui lui sont attachés, et aussi si le complexe éjecté He_nAk⁺ est stable ou s'il peut encore perdre des atomes He au cours de son trajet vers la zone de détection.

5. Ak₂ Coulomb Explosion

5.1. Introduction

Des études antérieures ont montré que les atomes d'alcalins Ak restent à la surface des nanogouttes d'hélium [87], provoquant une petite dépression dans le profil de densité lisse de la surface d'hélium connue sous le nom de "dimple" (ou cuvette), comme mentionné également dans la section précédente (4). Les dimères [92-95] et trimères [92, 96, 97] en surface de nanogouttes d'hélium ont également fait l'objet de nombreuses études depuis 1995 où elles ont été rapportées pour la première fois par Stienkemeier *et al.* [92]. Après avoir impacté la nanogoutte, les atomes d'Ak finissent par se rencontrer à leur surface et par former une molécule diatomique Ak₂. Selon l'orientation relative initiale des spins électroniques des atomes, l'état électronique formé est le singulet (antiparallèle) ou le triplet (parallèle). Statistiquement, le rapport du triplet au singulet devrait être 3 : 1 (d'après les statistiques de spin). Cependant, un ratio de 90 : 1 a été détecté dans la Ref [98] pour une taille moyenne de gouttelettes entre 5000 et 20000, et un ratio de 50 : 1 pour des gouttelettes plus grandes. La différence avec le rapport statistique a été attribuée au mécanisme de dissipation d'énergie dans les HND. La dissipation de l'énergie de liaison du dimère induit l'évaporation d'atomes d'hélium, jusqu'à ce que la température des nanogouttelettes dopées se soit rééquilibrée à 0,4 K. L'énergie de liaison beaucoup plus importante de l'état singulet (8490.94 K pour le singulet et 232.07 K pour le triplet de Na₂ par exemple) peut provoquer la désorption de la molécule alcaline ou la déviation de la gouttelette hors de l'axe du faisceau, ou même l'évaporation complète des gouttelettes les plus petites. Par conséquent, les gouttelettes dopées avec Ak₂ dans l'état triplet seraient plus susceptibles d'être détectées que celles où elle est dans l'état singulet.

5.2. Méthode

Le groupe de Stapelfeldt a estimé le rapport d'abondance des états triplet et singulet de Ak₂ [99] formée à la surface d'une nanogouttelette d'hélium pour Ak≡Li, Na, Rb et Cs en utilisant l'explosion de Coulomb. C'est une technique idéale pour étudier la structure des petites molécules [100, 101]. On peut ainsi mesurer la distribution de la longueur de liaison des diatomiques, et donc différencier les états triplet et singulet de Ak₂ grâce à la différence de distance d'équilibre ($r_{\text{eq}} = 5.2$ et 3.072 Å pour Na₂ triplet et singulet respectivement, voir Annexe D, Tableau D.3).

L'explosion coulombienne est déclenchée par double ionisation de Ak₂@⁴He_N à l'aide d'une impulsion laser femtoseconde intense [102]. Les ions Ak⁺ se séparent brutalement, leur énergie potentielle initiale de Coulomb se transformant en énergie cinétique. La distance interatomique initiale de Ak₂ peut être déduite de leur énergie cinétique finale enregistrée lors de la détection. Comme la distance d'équilibre Ak₂ est plus courte dans le singulet que dans le triplet, l'énergie cinétique finale devrait être plus élevée pour le premier que pour le second. Une distribution d'énergie cinétique $P(E_{\text{kin}})$ a été mesurée pour chaque ion fragment Ak⁺ [100, 101].

Dans une publication plus récente [102] le groupe de Stapelfeldt a comparé la distribution des distances entre les noyaux $P(r)$, déterminée par inversion des distributions d'énergie cinétique $P(E_{\text{kin}})$ *via* le potentiel de Coulomb, avec la densité $|\Psi(r)|^2$ du dimère isolé dans son état électronique fondamental (singulet ou triplet). La fonction d'onde $\Psi(r)$ a été calculée théoriquement en résolvant l'équation de Schrödinger. Pour les états singulet et triplet de Li₂, K₂ et Rb₂, le centre de la distribution $P(r)$ s'est avéré déplacé du centre $|\Psi(r)|^2$, alors que dans le cas de Na₂ et Cs₂, seul un petit décalage a été observé. Dans tous les cas, la distribution $P(r)$ était significativement plus large que $|\Psi(r)|^2$.

Nous avons utilisé ⁴He-TDDFT pour effectuer des simulations d'explosion coulombienne afin de comprendre l'effet de la HND sur la dynamique de fragmentation Ak₂⁺⁺ (Li, Na, K, Rb, Cs). Les conditions initiales (à l'état singulet ou triplet) ont

été déduites de la surface d'énergie potentielle (PES) expérimentale suivante : Li₂ [103], Na₂ [104], K₂ [105, 106], Rb₂ [107, 108] et Cs₂ [104].

Plusieurs paramètres ont été examinés tels que : l'effet de taille des gouttelettes (HND de quelques milliers (N=1000, 5000) ⁴He atomes), le mouvement du point zéro de l'Ak₂ isolé en phase gazeuse et la distribution d'orientation du point zéro de Ak₂ (φ) sur la surface des gouttelettes.

5.3. Résultats

5.3.1. Influence de la taille des gouttelettes

Les énergies cinétiques asymptotiques des ions Ak⁺ sont affichées dans le tableau [F.12](#) pour toutes les valeurs de taille des gouttelettes considérées dans ce travail. Elles montrent que l'énergie cinétique des ions Ak⁺ diminue quand la taille des gouttelettes augmente, comme on pouvait s'y attendre puisque le temps d'interaction des ions avec la gouttelette augmente. Par exemple, pour l'état triplet Na₂, le décalage par rapport à l'absence de nanogoutte passe de -16 meV à -22 meV pour une augmentation de la taille des gouttelettes de 1000 à 5000 atomes : leur énergie cinétique finale est 1.369 eV pour $N = 1000$, contre 1.363 eV pour $N = 5000$.

		X ¹ Σ _g ⁺	a ³ Σ _u ⁺	corr*
Li ₂	gas phase	2.709	1.742	—
	N=1000	2.690	1.725	—
	N=5000	2.683	1.719	—
	experiment	—	1.69	—
Na ₂	gas phase	2.344	1.385	—
	N=1000	2.327	1.369	—
	N=5000	2.321	1.363	—
	N*=10 000	—	1.367	1.361
	N*=20 000	—	1.366	1.359
	N*=50 000	—	1.365	1.356
experiment	2.15	1.39	—	
K ₂	gas phase	1.841	1.247	—
	N=1000	1.822	1.235	—
	N=5000	1.816	1.230	—
	experiment	1.80	1.25	—
Rb ₂	gas phase	1.703	1.178	—
	N=1000	1.689	1.164	—
	N=5000	1.681	1.157	—
	experiment	1.65	1.16	—
Cs ₂	gas phase	1.549	1.133	—
	N=1000	1.539	1.121	—
	N=5000	1.531	1.113	—
	experiment	1.41	1.03	—

Table F.12. Énergie cinétique finale (asymptotique) des ions (en eV) suite à la double ionisation de l'état singulet ou triplet dans nos simulations ⁴He-TDDFT pour une gouttelette de 1000 ou 5000 atomes, par rapport à l'expérience et aux valeurs en phase gazeuse. Dans le cas de Na₂ ³Σ_u⁺, les valeurs de N* correspondent aux simulations à densité gelée, et la colonne supplémentaire (corr*) à la valeur incluant une correction pour tenir compte de l'énergie supplémentaire transférée à l'hélium (voir texte). Les valeurs en phase gazeuse sont obtenues à partir de la valeur de l'interaction Ak⁺-Ak⁺ à t=0; Les valeurs expérimentales proviennent de Kristensen *et al.*, [99, 102] pour des gouttelettes moyennes d'environ 15 000 ⁴He atomes.

5.3.2. Largeurs de la distribution d'énergie cinétique des ions due aux vibrations

Nous avons déterminé la contribution de la distribution de longueur de liaison des molécules de dialcalin dans leur niveau vibrationnel ($v=0$) à la largeur des pics d'énergie cinétique. Le tableau F.13 affiche les largeurs à mi-hauteur (FWHM) correspondantes par rapport aux valeurs expérimentales de Kristensen *et al.* [99, 102], trouvées par ajustements aux données publiées [116]. Pour tous les dimères alcalins, cette largeur est essentiellement la même que celle de Ak₂($v = 0$) dans la phase gazeuse. Bien que la position des pics d'énergie cinétique des ions dépende de la taille des gouttelettes, comme indiqué dans la section précédente, leur largeur ne varie pas dans la plage testée. En fonction des alcalins et de l'état électronique initial, la largeur d'origine vibrationnelle représente entre un tiers et la moitié de la largeur expérimentale.

La prise en compte de la largeur supplémentaire d'environ 20 meV due à la distribution en taille des gouttelettes (voir section V-3.2) donne un accord légèrement meilleur mais pas assez pour retrouver les valeurs expérimentales.

Table F.13. FWHM des distributions d'énergie cinétique des ions suite à la double ionisation de Ak₂ sur ⁴He_N dans l'état électronique singulet ou triplet, résultant de la distribution de longueur de liaison de Ak₂(*v* = 0) (voir texte). Les valeurs expérimentales sont de Kristensen *et al.* [99, 102].

Ak ₂		X ¹ Σ _g ⁺		a ³ Σ _u ⁺	
		Δ <i>K</i> _{vib} (eV)	expt. (eV)	Δ <i>K</i> _{vib} (eV)	expt. (eV)
Li ₂	gas phase	0.281		0.264	
	<i>N</i> =1000	0.280	--	0.264	0.53
	<i>N</i> =5000	0.280		0.266	
Na ₂	gas phase	0.176		0.156	
	<i>N</i> =1000	0.176	0.42	0.155	0.33
	<i>N</i> =5000	0.176		0.155	
K ₂	gas phase	0.110		0.101	
	<i>N</i> =1000	0.106	0.25	0.101	0.18
	<i>N</i> =5000	0.107		0.101	
Rb ₂	gas phase	0,080		0.079	
	<i>N</i> =1000	0.080	0.21	0.079	0.16
	<i>N</i> =5000	0.080		0.079	
Cs ₂	gas phase	0.062		0.063	
	<i>N</i> =1000	0.064	0.20	0.063	0.18
	<i>N</i> =5000	0.063		0.066	

Il est intéressant de noter que les FWHM en phase gazeuse sont très similaires pour les états singulet et triplet. Cela résulte de la compensation de deux effets opposés. La largeur de la fonction d'onde vibrationnelle est plus grande pour l'état triplet mais la pente de la courbe répulsive de Coulomb à la distance d'équilibre est plus petite.

Comme mentionné ci-dessus, Kristensen *et al.* [102] ont déterminé la distribution initiale des distances internucléaires $P(R)$ pour les dimères alcalins à partir de la distribution d'énergie cinétique $P(E_{kin})$ des fragments Ak^+ , en inversant le potentiel de Coulomb régissant la libération d'énergie cinétique en fonction de la distance interatomique. En comparant la distribution de distance internucléaire obtenue à partir de cette inversion à celle obtenue comme le carré de la fonction d'onde de Ak_2 , ils ont conclu que l'expérience donnait des pics plus larges que prévu, et pour certains des alcalins, les pics étaient décalés.

Ceci est en accord avec notre conclusion que les pics expérimentaux de distribution d'énergie cinétique sont plus larges que prévu par la distribution de longueur de liaison $v = 0$, et que certains pics sont décalés, en particulier pour Na_2 : le déplacement de l'énergie cinétique est plus petit que celui expérimental pour l'état singulet, et légèrement trop grand pour l'état triplet

5.3.3. Effet de l'angle de la molécule diatomique avec la surface de la nanogoutte

La configuration d'équilibre de la molécule de dialcalin est parallèle à la surface de la nanogoutte, mais d'autres orientations sont permises par le mouvement angulaire de point zéro. Dans ce cas, l'un des deux ions est initialement plus proche de la surface et peut interagir plus fortement avec l'hélium, ce qui pourrait conduire à une largeur supplémentaire des pics de la distribution d'énergie cinétique des ions.

Nous avons effectué des simulations pour $Na_2(a, {}^3\Sigma_u^+)@{}^4He_{1000}$ comme test, en utilisant la méthode décrite dans la section V-2.3. Les énergies totales de $Na_2(a, {}^3\Sigma_u^+)@{}^4He_{1000}$ obtenues à partir de simulations statiques de 4He -DFT pour un certain nombre de valeurs de \mathcal{R} et de φ sont représentées dans le panneau supérieur de la Fig. F.9 (\mathcal{R} étant la distance entre le centre de masse de Na_2 et celui de la nanogoutte, et φ l'angle entre l'axe de la diatomique et la normale à la surface passant par son centre de masse). L'énergie minimum est de $-5414,0$ K à $\mathcal{R} = 25,0$ Å pour

$\varphi = 90^\circ$. La fonction d'onde de l'état fondamental est représentée dans le panneau central de Fig. F.9. Son énergie est de $-5412,7$ K, c.-à-d. $1,3$ K au-dessus de l'énergie minimale. Les fréquences d'élongation et de pliage sont de $1,0$ K et $1,6$ K respectivement, de sorte qu'aucun état excité ne peut être peuplé à la température de la nanogoutte de $0,37$ K.

Kranabetter *et al.* [102] ont également calculé la distribution angulaire du dimère $\text{Na}_2(a, {}^3\Sigma_u^+)$ dans le potentiel effectif de la gouttelette, modélisée comme un film d'hélium. Leur distribution présente un maximum pour $\varphi=90^\circ$, et s'étend jusqu'à $\sim 45^\circ$. Notre distribution est plus étroite, ce qui pourrait être dû à la courbure de la surface de la nanogoutte.

Le panneau inférieur de la Fig. V.4 représente l'énergie cinétique des deux ions en fonction de l'angle d'orientation initial φ de Na_2 . La courbe est assez plate autour de $\varphi = 90^\circ$ (configuration parallèle à la surface) En observant les films réalisés pour ces dynamiques, nous avons vu qu'à partir de $\varphi \leq 60^\circ$, un des deux ions pénètre dans la nanogoutte : sa trajectoire est donc fortement ralentie. De façon surprenante, bien qu'une partie de sa trajectoire se déroule dans la nanogoutte, l'ion ressort sans hélium attaché. Cela doit être dû à sa très grande vitesse, puisque son énergie cinétique est encore de $0,9$ eV dans le cas de plus grande interaction avec la nanogoutte ($\varphi = 0$). L'autre ion s'échappe librement et son énergie cinétique n'est pas affectée (elle est seulement légèrement augmentée pour $\varphi \leq 60^\circ$, parce que l'ion pénétrant dans la nanogoutte est ralenti, et la distance inter-ions n'augmente pas aussi vite: en conséquence, la répulsion coulombienne agit un peu plus longtemps).

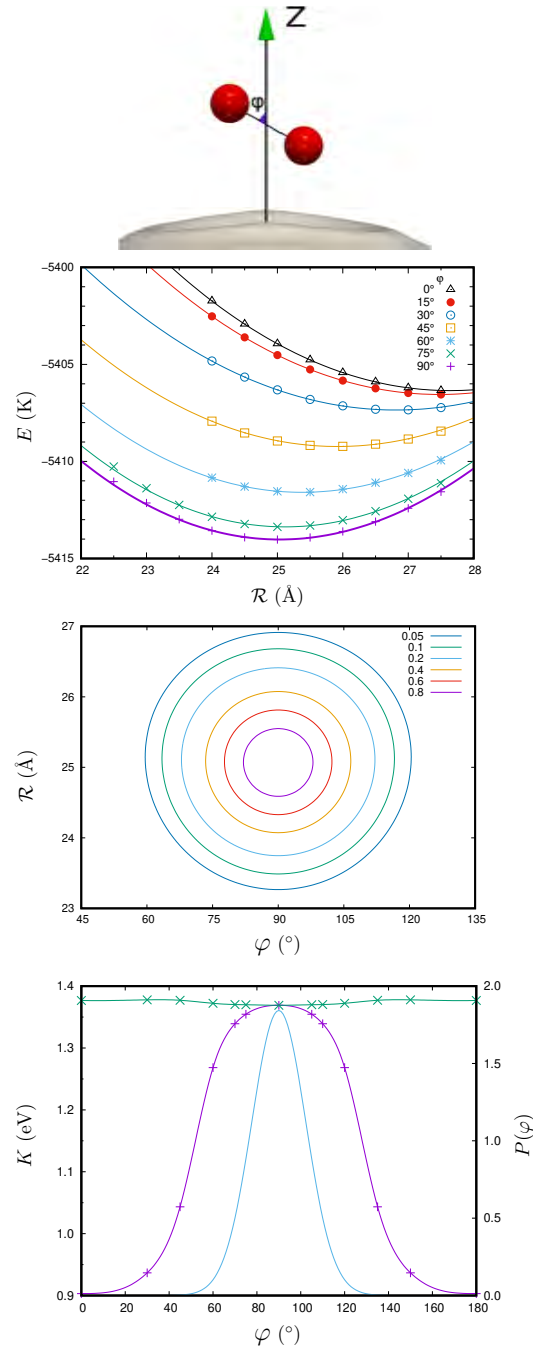


Figure F.9. De haut en bas : Schéma : Définition de l'angle φ (entre l'axe interatomique Na₂ et la ligne reliant les centres de masse de la gouttelette et du dialkali). Panneau supérieur : Énergie totale de Na₂ $^1\Sigma_g^+$ @⁴He₁₀₀₀ en fonction de la distance \mathcal{R} entre le centre de masse de Na₂ et celui de la gouttelette, pour plusieurs valeurs de l'angle φ . Panneau du milieu : distribution de probabilité à deux dimensions (carré de la fonction d'onde à deux dimensions multiplié par $\sin \varphi$) en fonction de φ et de \mathcal{R} ; Panneau inférieur : énergie cinétique asymptotique de l'ion Na⁺ allant vers (ligne violette, marqueurs +) ou s'éloignant de (ligne verte, marqueurs x) la nanogoutte d'hélium, et distribution de probabilité $P(\varphi)$ intégrée sur \mathcal{R} (ligne cyan, pas de marqueur, axe vertical de droite).

5.3.4. Déviation de la trajectoire des ions par la nanogoutte d'hélium

Nos simulations révèlent une conséquence intéressante de la présence de HND : les trajectoires des ions sont déviées par l'interaction avec l'hélium, comme on peut le voir sur la Fig F.10). Cette déviation angulaire est mesurable et dépend de plusieurs facteurs tels que la force de l'interaction $Ak^+ - {}^4\text{He}_N$ et le temps de vol des dopants, lui-même gouverné par la distance interatomique initiale et la masse des ions.

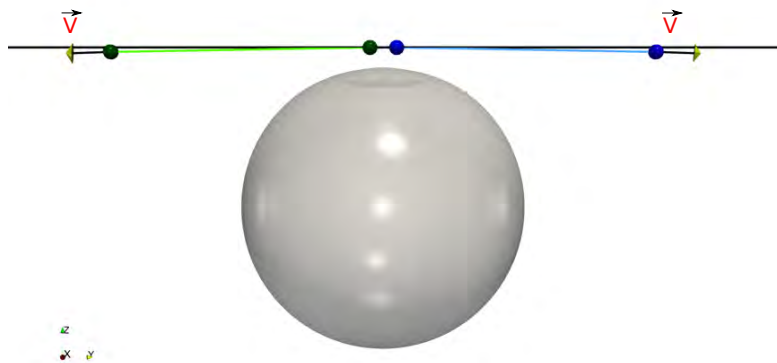


Figure F.10. Trajectoire des ions Rb^+ (lignes bleues et vertes) lors de l'explosion coulombienne de $\text{Rb}_2 (X, {}^1\Sigma_g) @ {}^4\text{He}_{1000}$ dans le plan (y, z) . Les vecteurs vitesse \vec{v} forment un angle θ différent de 180° , la valeur attendue en l'absence de la nanogoutte d'hélium.

L'écart par rapport à 180° est plus important pour une goutte de 5 000 atomes que pour une de 1 000, comme on pouvait s'y attendre. Pour $\text{Na}_2(a, {}^3\Sigma_u^+)$ sur de plus grandes gouttelettes (la dynamique était alors effectuée en gelant la densité d'hélium, une fois la structure d'équilibre obtenue), l'écart peut atteindre 10° pour la plus grande taille étudiée ($N = 50\,000$). Pour la taille moyenne expérimentale de $\langle N \rangle = 15\,000$, l'angle θ entre les vecteurs de vitesse est de $172,6^\circ$. La déviation est plus importante pour l'état triplet que pour le singulet. C'est parce que la longueur de liaison de la diatomique est plus longue à l'état triplet, ce qui rend la répulsion coulombienne plus faible. Cela a deux conséquences qui vont dans le même sens. Dès le départ l'effet relatif de l'attraction de l'hélium par rapport à la force coulombienne est plus grand et la force résultante sur l'ion dévie plus de

l'horizontale pour le triplet que pour le singulet (en supposant que l'attraction Na⁺-hélium n'est que peu modifiée, ce qui est le cas puisque la position de Na₂ n'est que très peu modifiée entre les deux états). En outre, les ions ressentent l'attraction des gouttelettes pendant un temps plus long en raison de l'explosion de Coulomb qui est plus lente.

5.4. Conclusion

Nous avons montré que l'hypothèse de la faible influence de la nanogoutte sur la trajectoire des ions résultant de l'explosion coulombienne de molécules d'alcalins à leur surface est bien vérifiée. Les maxima expérimentaux des distributions d'énergie cinétique des ions sont assez bien reproduits, mais la largeur est encore trop faible.

Nous avons également montré un effet inattendu: la déviation de la trajectoire des ions par rapport à l'horizontale, due à l'attraction de l'hélium, et qui devrait être mesurable.

Ce travail n'est pas encore terminé car nous collaborons avec les expérimentateurs afin de pouvoir vérifier nos prédictions sur la déviation angulaire des vecteurs vitesse.

6. Coalescence de nanogouttes et nucléation de vortex quantiques

6.1. Introduction

Il a été démontré que de très grandes gouttes superfluides de ${}^4\text{He}_N$ (VLD pour “Very Large Droplets” en anglais) produites par la rupture Rayleigh d’un jet liquide dans le vide hébergeaient des vortex quantiques [70, citenumOlivierDulieubook]. On pense que les gouttes acquièrent un moment angulaire par interaction avec les parois de la buse [70], qui est ensuite stocké sous forme de vortex quantique et/ou d’ondes capillaires lors de la transition du liquide normal au superfluide.

Nous explorons ici un autre mécanisme de nucléation de vortex quantique : les collisions entre gouttelettes pour en former de plus grosses par coalescence. Dans un faisceau de VLD, Kolatzki *et al.* [36] ont observé des gouttes équidistantes de taille pratiquement uniforme qui pouvaient parfois coalescer en aval. Les vitesses relatives explorées ici sont un peu plus élevées que celles de cette expérience, mais elles sont dans la gamme de celles des expériences de gouttelettes plus petites produites par détente supersonique de l’hélium gazeux.

6.2. Méthode

Afin de préparer la collision entre deux nanogouttes de 500 atomes, on détermine d’abord la structure d’équilibre d’une goutte de ${}^4\text{He}_{500}$. Nous avons trouvé plus pratique d’obtenir la structure de chaque gouttelette à l’intérieur de la plus grande boîte de calcul dans laquelle la dynamique sera effectuée, en plaçant leurs centres de masse de sorte que leurs surfaces de division (lorsque la densité d’hélium est égale à la moitié de la valeur de la densité du liquide, $\rho_0 = 0.0218 \text{ \AA}^{-3}$) soient à 8 \AA pour le paramètre d’impact choisi (voir Fig F.11). A cette distance, les gouttelettes sont suffisamment espacées pour que leur énergie d’interaction soit négligeable : l’énergie des deux gouttelettes constituant la configuration de départ

est de -4947.0 K, à comparer à celle de deux gouttelettes à distance infinie, -4943.8 K, donnant une énergie d'interaction de -3.2 K à $t = 0$. C'est assez faible, même comparé à l'énergie cinétique (94.3 K pour $v = 20$ ms^{-1}). Cela donne deux profils de densité égaux centrés à différents points de la grille de calcul, $\rho_1(\mathbf{r})$ et $\rho_2(\mathbf{r})$.

La fonction d'onde initiale donnant aux gouttelettes des vitesses opposées dans la direction z est alors construite comme

$$\Psi(\mathbf{r}, t = 0) = \sqrt{\rho_1(\mathbf{r})} e^{-ikz} + \sqrt{\rho_2(\mathbf{r})} e^{ikz}$$

où le nombre d'onde k est lié à la vitesse de la gouttelette v par $v = \hbar k / m_4$.

Dans des conditions expérimentales ($T_0 = 30\text{K}$, $P_0 = 5 - 80$ bar) produisant de petites gouttelettes, la dispersion en vitesse dans le jet est d'environ $\Delta v / v_{\text{jet}} \approx 2 - 6\%$ [1, 119] et, par conséquent, la plage de vitesses est $10 < \Delta v < 34$ ms^{-1} ($0,1 < \Delta v < 0,34$ \AA ps^{-1}).

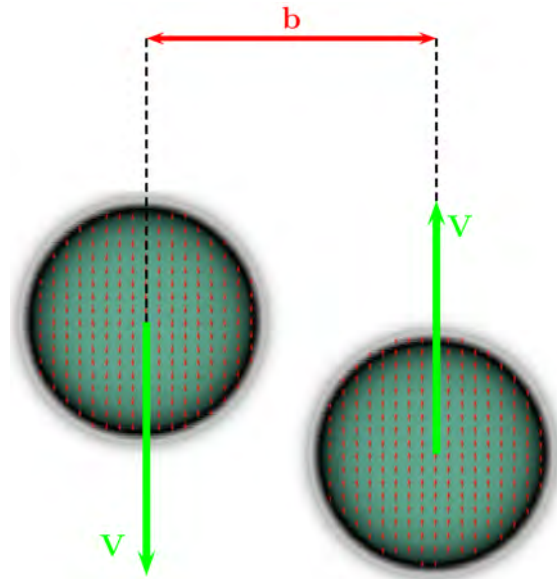


Figure F.11. ${}^4\text{He}_N$ - ${}^4\text{He}_N$ collision avec un paramètre d'impact b et une vitesse relative $\Delta v = 2v$, où v est la vitesse de chaque gouttelette. Plan de collision (yz)

Le momentum angulaire L créé dans la gouttelette fusionnée est donné par $L\hbar = bNm_4\Delta v$, où N est le nombre d'atomes d'hélium de chaque gouttelette. Pour une ligne de vortex le long du diamètre de la gouttelette sphérique fusionnée, on a

$L = 1000\hbar$ (voir la section II-6.6), qui donne le paramètre d'impact critique pour la nucléation de vortex

$$b_{\text{cr}} = 2 \frac{\hbar}{m_4} \frac{1}{\Delta v} \quad (\text{F.14})$$

Différentes conditions initiales (paramètre d'impact b , vitesse relative $\Delta v=2v$) ont été testées dans la collision de deux gouttelettes de rayon $R({}^4\text{He}_{500}) = 17,6 \text{ \AA}$. Compte-tenu du coût de calcul des simulations, il n'a pas été possible d'explorer une gamme complète de valeurs de b et de v . Nous avons sélectionné quelques conditions initiales représentatives qui pourraient permettre une nucléation de vortex, *i.e.* qui vérifient l'Eq.(F.14) : $b = 3R/2$, $\Delta v = 12 \text{ ms}^{-1}$, et pour une collision plus centrale avec $b = R$, $\Delta v = 18 \text{ ms}^{-1}$. Puisqu'une partie du moment angulaire ira dans les ondes capillaires ou sera emportée par l'évaporation d'atomes, nous avons également considéré deux valeurs plus importantes pour Δv , à savoir 20 et 40 ms^{-1} . Plus précisément, nous avons choisi les combinaisons suivantes de vitesse de gouttelettes v et de paramètre d'impact b :

- Collision frontale ($b = 0$, $v = 40 \text{ ms}^{-1}$, $L=0$),
- $b = 3R/2$ pour $v = 10, 20$ et 40 ms^{-1} ($L=825, 1650$ et $3300 \hbar$),
- collision rasante ($b = 2R$) à $v = 20$ et 40 ms^{-1} ($L=2200, 4400\hbar$),
- et collision distante ($b = 5R/2$, $v = 20 \text{ ms}^{-1}$, $L=2750\hbar$).

De plus, nous avons également étudié un cas de collision non symétrique avec une nanogoutte de 300 et l'autre de 700 atomes ($L=1650 \hbar$).

6.3. Résultats

La dynamique d'évolution de deux gouttelettes d'hélium de 500 He chacune, avec paramètre d'impact ($b=3R/2$) et $v = 40\text{ms}^{-1}$ ($L=3300 \hbar$) est illustrée par la Fig. F.12. On remarque l'apparition non pas d'un, mais deux vortex (vus en transparence par leur cœur qui est vide), la nucléation des deux lignes de vortex étant

simultanée dans cette collision symétrique. Ce résultat surprenant est possible parce que l'équation qui détermine le moment angulaire minimum $L = N\hbar$ pour nucléer un vortex n'est valide que pour une ligne de vortex passant par le centre en symétrie cylindrique (voir la section II-6.6). La gouttelette fusionnée est fortement déformée et les lignes de vortex tournent afin de maintenir le moment angulaire impliqué dans la collision.

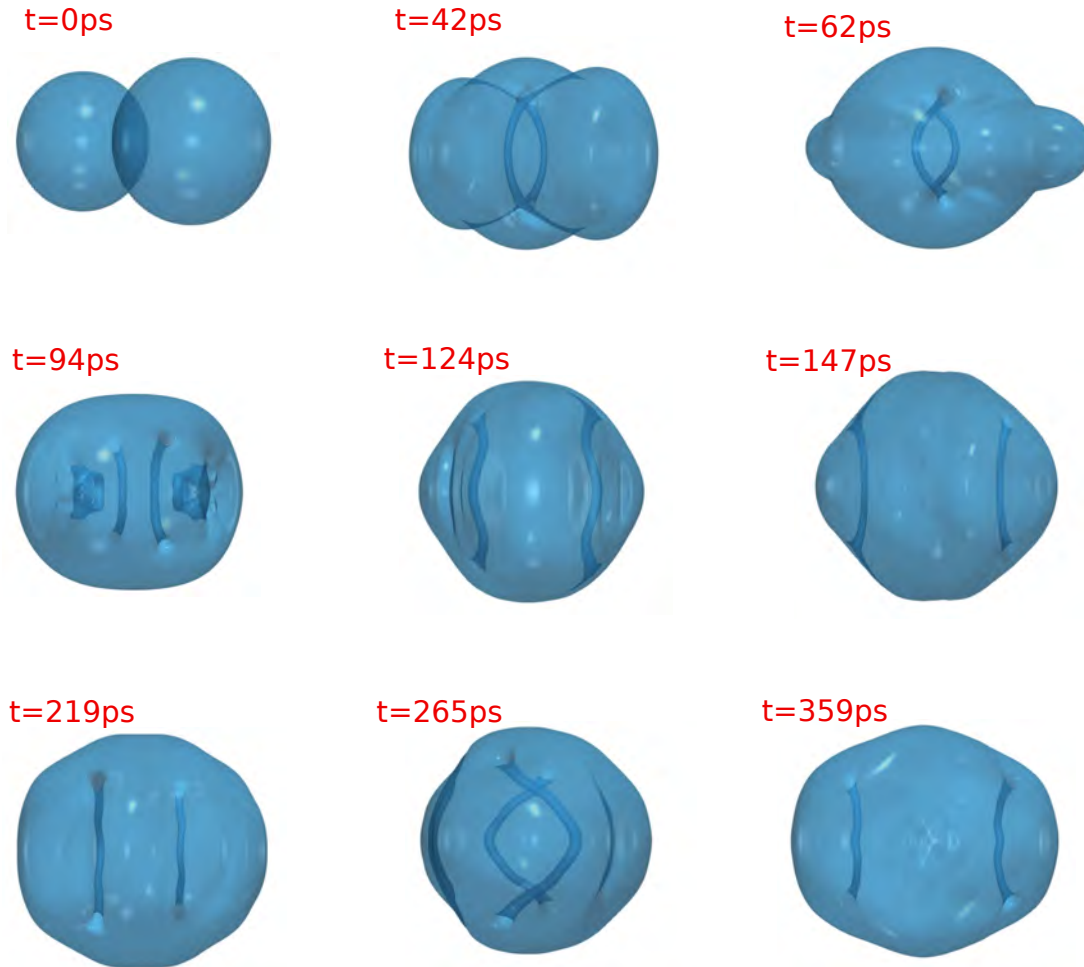


Figure F.12. Représentation tridimensionnel de la collision ${}^4\text{He}_N + {}^4\text{He}_N$ ($N = 500$; $b = 3R/2 \text{ \AA}$; $v = 20\text{ms}^{-1}$, $L = 1640 \hbar$). Deux lignes de vortex (courbées) sont visibles à partir du second cliché, car elles sont vides (la densité d'hélium est nulle au cœur).

La Fig. F.13 affiche les coupes en deux dimensions de la densité d'hélium dans le plan de collision (y, z) pour les collisions ${}^4\text{He}_N + {}^4\text{He}_N$ (et ${}^4\text{He}_{N_1} + {}^4\text{He}_{N_2}$ dans le dernier cas) à la fin de chaque simulation (t_f).

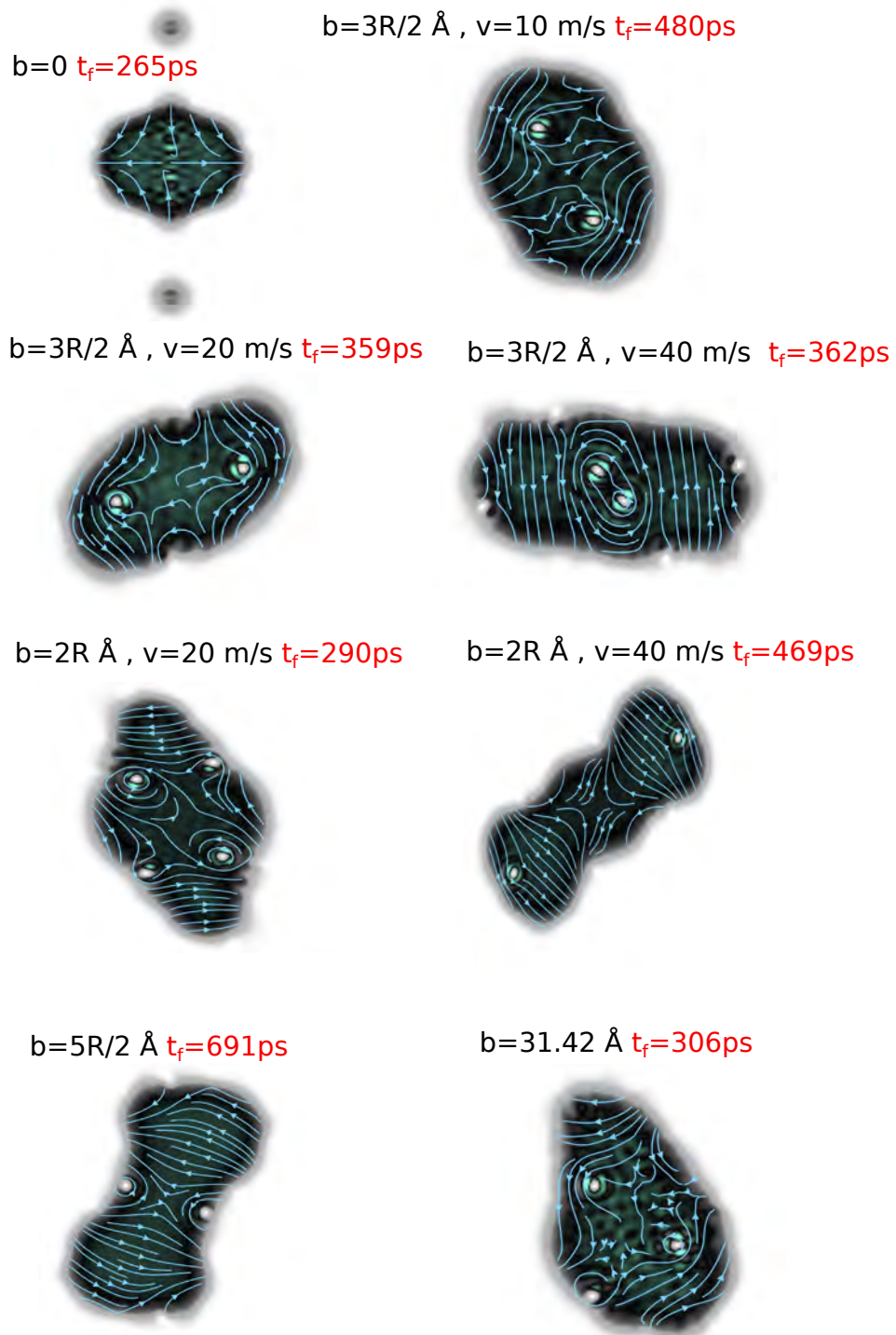


Figure F.13. Instantanés de coupes bidimensionnelles dans le plan (y, z) pour la collision ${}^4\text{He}_N + {}^4\text{He}_N$ à la fin de chaque simulation (t_f) et pour différentes conditions initiales. Tous les cas correspondent à une collision symétrique $N = 500$ sauf celui avec le paramètre d'impact $b = 31,42 \text{ \AA}$ qui correspond à $N_1=300$ et $N_2=700$ et $v = 12.28 \text{ ms}^{-1}$ ($L = 1650 \hbar$). Les flèches superposées à la densité représentent le courant du superfluide. Les régions blanches à l'intérieur de la gouttelette représentent l'intersection des lignes de vortex (courbées) avec le plan.

Dans les collisions décrites ici, le moment angulaire est réparti entre les ondes capillaires et les vortex.

L'évolution temporelle du moment angulaire total et de la contribution vortex L_v pour la collision ${}^4\text{He}_{500} + {}^4\text{He}_{500}$ avec paramètre d'impact $b = 3R/2$ et vitesse initiale des nanogouttes $v = 10$ et 20 ms^{-1} est présentée dans les Figs. F.14 et F.15 respectivement. Le moment angulaire contenu dans les vortex, (L_v), est estimé en soustrayant le moment angulaire dû aux ondes capillaires $L_{\text{cap}} = \mathcal{I}_{\text{irr}}\omega$ [120] du moment angulaire total L , où

$$\mathcal{I}_{\text{irr}} = m_4 N \frac{[\langle y^2 \rangle - \langle z^2 \rangle]^2}{\langle y^2 \rangle + \langle z^2 \rangle} \quad (\text{F.15})$$

et

$$\omega = \frac{\Delta\theta}{\Delta t} \quad (\text{F.16})$$

Dans cette équation, ω est la vitesse angulaire et θ est défini comme l'angle de rotation de la goutte fusionnée autour de l'axe x (axe perpendiculaire au plan de collision (y, z)).

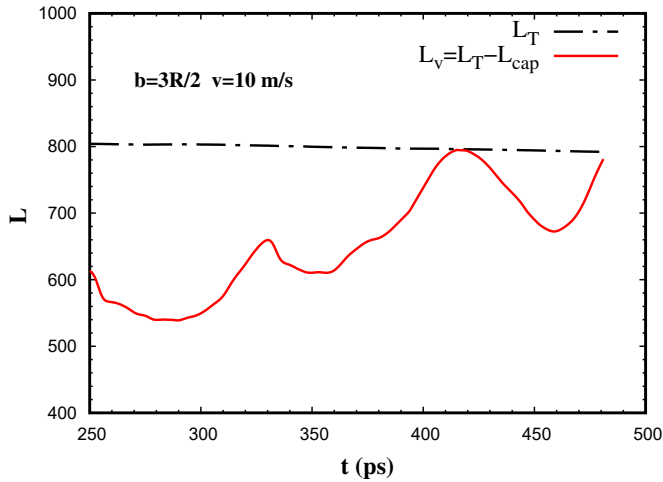


Figure F.14. Evolution temporelle du moment angulaire total et de la contribution des vortex L_v pour la collision ${}^4\text{He}_{500} + {}^4\text{He}_{500}$ ($b = 3R/2$ et $v = 10 \text{ ms}^{-1}$).

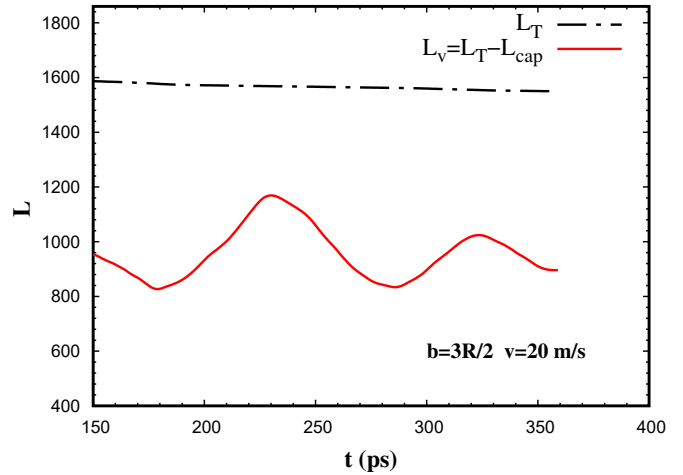


Figure F.15. Evolution temporelle du moment angulaire total et de la contribution des vortex L_v pour la collision ${}^4\text{He}_{500} + {}^4\text{He}_{500}$ ($b = 3R/2$ et $v = 20 \text{ ms}^{-1}$).

6.4. Conclusions

Nous avons mis en évidence la nucléation de vortex quantiques lors d'une collision de nanogouttes d'hélium superfluide. Ces vortex sont produits par paires dans des

conditions symétriques [120]. Les collisions de nanogouttes d'hélium-4 superfluide présentent des similitudes avec les collisions de nanogouttes classiques. Dans les deux cas, la gouttelette fusionnée est fortement déformée et tourne afin de maintenir le moment angulaire impliqué dans la collision. Nous avons constaté que les tourbillons quantiques sont facilement nucléés par le mécanisme d'indentations de surface, ce qui donne des tourbillons linéaires décentrés (qui portent un moment angulaire plus petit que les tourbillons centrés) pour les collisions avec des paramètres d'impact non nul. La nucléation hors axe permet de nucléer des vortex même si le moment angulaire total est inférieur à $N\hbar$. Puisque les indentations apparaissent chaque fois que des gouttelettes fusionnent, ce mécanisme de nucléation de vortex est indépendant de la taille des gouttelettes. Il pourrait donc s'appliquer à une large gamme de tailles et de vitesses de gouttelettes, et notamment aux nanogouttes les plus petites, dans lesquelles la présence de vortex n'a pas pu être mise en évidence jusqu'à présent. Une raison pourrait en être qu'il n'y a pas de procédé connu pour les mettre en évidence, la diffraction d'objets uniques par rayons X ou UV n'étant applicable qu'aux VLD. L'objectif de la section suivante est justement de proposer un moyen de détecter la présence de vortex linéaires dans des nanogouttes de petite taille (quelques milliers d'atomes).

7. Spectroscopie d'alcalins pour la détection de vortex en nanogouttes

7.1. Détection de vortex quantiques dans les nanogouttes

Des vortex quantiques ont été détectés dans des gouttelettes faites de 10^8 - 10^{12} atomes ^4He par Gomez *et al.* [121, 122] en utilisant la diffraction de rayons X par des gouttelettes individuelles. Cela a permis de déterminer leurs formes et, en les dopant avec des atomes de Xe [123], la présence de vortex, confirmant leur nature superfluide. Cependant, cette technique ne s'applique pas aux gouttelettes plus petites, et aucune signature expérimentale de la présence d'un vortex n'a été trouvée jusqu'à présent dans les gouttelettes faites de plusieurs milliers d'atomes d'hélium. Une raison possible pourrait être qu'il n'y a aucun vortex dans ces gouttelettes plus petites, ou qu'on ne connaît pas encore de méthode pour leur détection.

Nous étudions ici une méthode simple qui pourrait permettre détecter des vortex quantiques dans des gouttelettes de petite taille. Elle est basée sur la spectroscopie d'absorption ou d'excitation de la fluorescence d'atomes alcalins attachés à des nanogouttes superfluides $^4\text{He}_{1000}$. Étant donné qu'un vortex linéaire a un noyau vide d'un rayon d'environ 1 \AA , un atome alcalin (Ak) à la surface de la gouttelette se localiserait plus profondément dans la "bouche" du vortex, ce qui devrait affecter son spectre d'absorption électronique. En effet, la spectroscopie d'absorption de la lumière est très sensible à l'environnement de l'impureté, et c'est donc un bon candidat comme outil pour détecter des impuretés attachées aux vortex.

Nous avons calculé les spectres d'absorption des atomes d'alcalins (Ak) de Li à Cs lorsqu'ils sont attachés à un vortex linéaire dans une nanogoutte superfluide, et nous les avons comparés aux mêmes spectres sans vortex. L'objectif est de fournir une réponse quantitative à la taille du déplacement spectral attendu et donc à la possibilité pour les expériences d'absorption de photons de détecter la présence de vortex. Le spectre d'absorption des atomes alcalins attachés aux gouttelettes

d'hélium a été étudié expérimentalement dans le passé (voir Réfs. [124- 129]), et des travaux antérieurs ont simulé des spectres d'absorption d'atomes d'alcalins attachés à des vortex-nanogouttelettes d'hélium libres utilisant différentes fonctions et/ou des potentiels de paires d'alcalins [22, 124- 125, 130- 132]. Nous les avons répétés afin d'assurer la comparaison avec des gouttelettes hébergeant un vortex avec exactement les mêmes paramètres. Le spectre d'atomes d'alcalins attachés à des nanogouttes hébergeant un vortex n'a pas été abordé théoriquement auparavant à notre connaissance.

7.2. Méthode

Nous utilisons la méthode ⁴He-DFT [22] pour calculer la configuration d'équilibre et l'énergie des atomes d'alcalins attachés à une nanogoutte sans ou avec un vortex.

Une fois la configuration d'équilibre obtenue pour chacune des deux conditions, nous procédons à la détermination du spectre d'absorption dipolaire de l'alcalin en surface de la nanogoutte. Le spectre d'absorption a été calculé en générant un grand nombre ($N_c \approx 10^6$) de configurations hélium-impureté qui reproduisent la même densité que celle obtenue dans la 1ère étape. Chaque configuration est composée de N ⁴He et de l'atome d'alcalin. Si l'alcalin est traité quantiquement, sa position est également échantillonnée en suivant sa distribution de point zéro donnée par $|\phi^{gs}(\mathbf{r})|^2$. Pour chaque configuration, on calcule la différence d'énergie entre l'état fondamental et le ou les états excités. Le spectre d'absorption est finalement obtenu sous forme d'histogramme de ces énergies. Voir l'annexe C pour plus de détails.

7.3. Résultats

Lorsque la nanogoutte héberge une ligne de vortex, l'atome Ak est localisé plus profondément (la cuvette est plus profonde) dans la bouche du vortex d'hélium. La Fig. F.17 présente le spectre d'absorption de Li de son état électronique fondamental 2s à son premier état excité 2 (transition dénotée par (2p ← 2s)), de Na

(3p ← 3s), de K (4p ← 4s), de Rb (5p ← 5s) et de Cs (6p ← 6s). Dans le cas de Li, Na et K, un traitement quantique a été appliqué, et dans le cas de Na, K, Rb et Cs, un traitement classique. Nous avons utilisé les deux pour Na et pour K afin de connaître l'importance des effets quantiques.

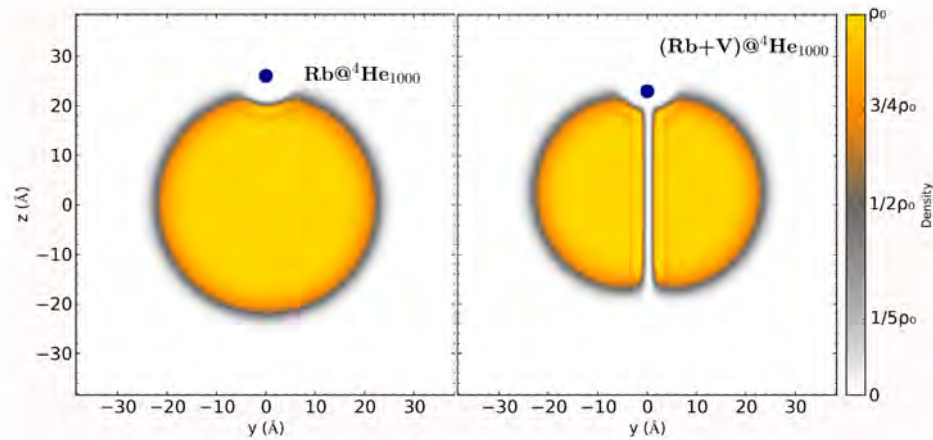


Figure F.16. Coupe en 2D de la densité d'hélium dans un plan de symétrie d'une nanogoutte de ${}^4\text{He}_{1000}$ dopée avec un atome Rb (point bleu). La barre de couleur montre la densité d'hélium en unités de $\rho_0 = 0,0218 \text{ \AA}^{-3}$, la densité de l'hélium superfluide à $T = 0$. À Gauche : nanogoutte sans vortex; à droite : nanogoutte avec vortex. Remarquer l'aplatissement de la nanogoutte contenant un vortex, ainsi que l'approfondissement de la cuvette dans laquelle est localisée l'alcalin.

Les spectres obtenus sont présentés dans la Fig. F.17. Ils montrent un déplacement spectral vers le bleu (hautes fréquences) et un élargissement des raies. Toutefois, le déplacement spectral n'est pas suffisant pour permettre la détection de vortex, puisqu'il est inférieur à la largeur des raies.

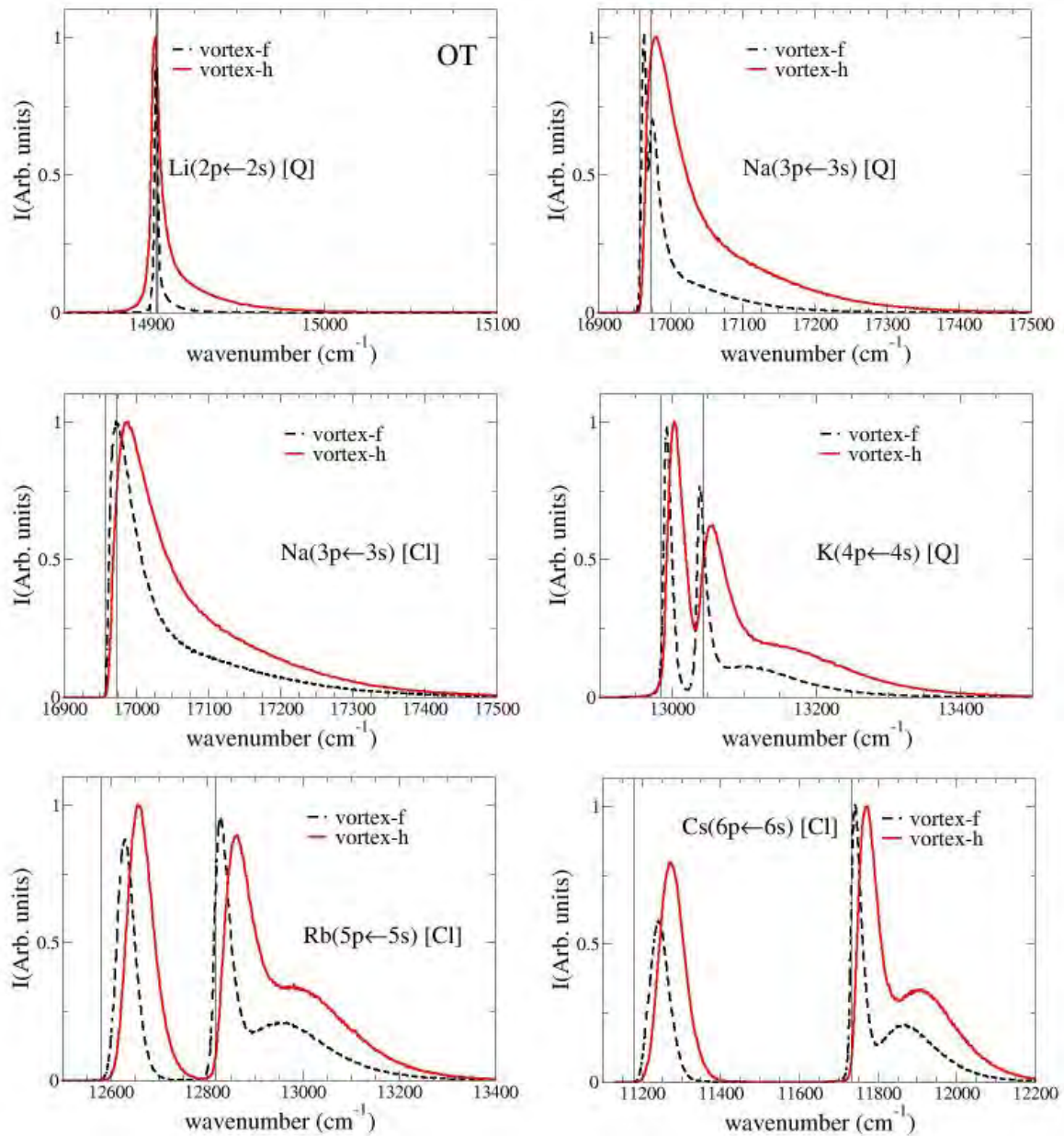


Figure F.17. Spectre d'absorption $np \leftarrow ns$: Li ($2p \leftarrow 2s$) (quantum), Na ($3p \leftarrow 3s$) (traitement classique et quantique), K ($4p \leftarrow 4s$), Rb ($5p \leftarrow 5s$) et Cs ($6p \leftarrow 6s$). Pour tous les spectres, la ligne noire correspond à une gouttelette libre de vortex et la ligne rouge à une gouttelette hébergeant une ligne vortex.

Nous avons ensuite exploré l'idée d'états électroniques plus élevés ($n's$ ou $n'p$ avec $n' > n$) puisque l'orbitale de l'électron de valence est alors plus diffuse et plus étendue. Par conséquent, sa sensibilité aux changements de la densité d'hélium environnante est augmentée (l'interaction hélium-électron est répulsive). Les spectres d'absorption vers ces états excités ($n' > n$) pourraient ainsi révéler plus de

différences entre les gouttelettes hébergeant ou non un vortex que ceux vers les premiers états excités np . La Fig. F.18 montre les trois cas étudiés K : ($5s \leftarrow 4s$), Rb : ($6p \leftarrow 5s$) et Cs ($7s \leftarrow 6s$). Comme on peut le voir, le déplacement spectral est plus important que pour les transitions ($np \leftarrow ns$), et pourrait être détecté car il est juste supérieur à la largeur des raies.

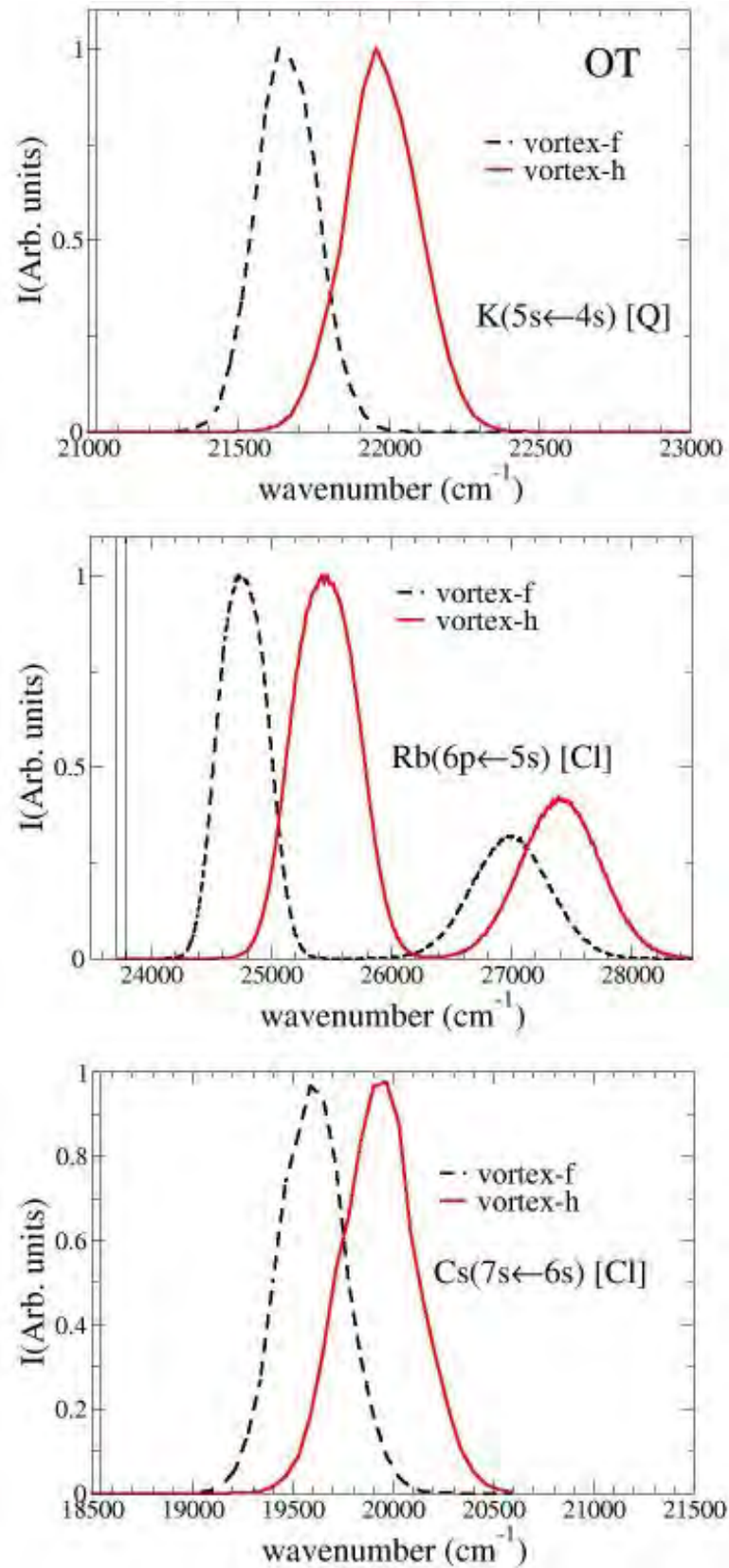


Figure F.18. Spectres d'absorption K : ($5s \leftarrow 4s$), Rb : ($6p \leftarrow 5s$) et Cs : ($7s \leftarrow 6s$). Pour tous les spectres, la ligne noire correspond à une gouttelette libre de vortex et la rouge à une gouttelette hébergeant un vortex linéaire.

7.4. *Conclusion*

Nos résultats de simulation prédisent des spectres d'absorption décalés vers le bleu (fréquences plus élevées) et élargi dans les nanogouttes hébergeant un vortex par rapport à celles sans vortex, à la fois pour les transitions ($np \leftarrow ns$), ($n's \leftarrow ns$) et ($n'p \leftarrow ns$) avec $n' > n$. Ce déplacement spectral vient du fait que l'alcalin se trouve plus profondément dans la nanogoutte quand un vortex est présent, ce qui est visible dans la profondeur de la cuvette où il réside. Ces modifications spectrales sont insuffisantes pour la détection de vortex dans le cas des transitions vers les premiers états excités ($np \leftarrow ns$), mais pour les états plus excités $n'p$ ou $n's$, $n' > n$, dans lesquels l'orbitale de l'électron de valence est plus étendue et donc plus sensible aux changements de la densité d'hélium environnante, les modifications spectrales sont plus importantes et pourraient conduire à la détection de vortex.

LIST OF FIGURES

I.1.	Pressure-temperature phase diagram of ^4He	2
I.2.	A helium II fountain	3
I.3.	Film flow of He II over the walls of a beaker	3
I.4.	Excitations in liquid He II	8
I.5.	Physical interpretation of the phonon and roton parts of the quasiparticle spectrum. The phonon motion corresponds to de Broglie wavelengths, $p = h/\lambda$. greater than a single atomic size, and leads to coupled motion of groups of atoms moving together, rather like a phonon in a solid. The roton corresponds to de Broglie wavelengths of order the interparticle separation. It corresponds to a central particle moving forward, while the close packed neighbors must move out of the way in a circular motion. Feynman notes that this combination of linear and circular motion has some nice similarity to a moving smoke-ring. Figure taken from Ref [13]	9
I.6.	OCS IR spectra	10
I.7.	Schematic representation of the mechanism leading to the formation of chains of polar molecules in ^4He droplets. a) A fourth molecule approaches a droplet containing a chain with three molecules. b) On entering the droplet some ^4He atoms are displaced and the molecule is aligned and attracted by the electric field of the trimer chain. Figure taken from Ref [21]	12
I.8.	Rigid body rotation , quantum vortex and a bathtub, “ordinary” vortex	13
I.9.	Typical Experimental Setup	14
I.10.	Calculated time evolution of the mean number sizes and temperatures of ^3He and ^4He droplets after they have grown to 10^3 atoms. It is assumed that the ^4He droplets have initially a temperature of 4.0 K and the ^3He droplets 0.8 K. Concomitant with the large evaporative loss the temperatures decrease by about an order of magnitude to below 0.3 K (^4He) and 0.1 K (^3He). Figure taken from [1]	16
I.11.	Helium droplet cooling in an absolute vacuum for droplets with initial diameters of 100 nm ($N_{\text{He},0}=10^7$), 1 μm ($N_{\text{He},0}=10^{10}$), and 10 μm ($N_{\text{He},0}=10^{13}$). The dashed curve shows the fraction of helium atoms remaining in a droplet with initial size of $N_{\text{He},0}=10^{10}$, corresponding to the vertical axis on the right. Figure taken from Ref [33]	17
I.12.	Expansion Regimes	18

I.13. Droplet size distribution	19
III.1. Ar+Ar@ ⁴ He ₁₀₀₀ collision	41
III.2. Ar+Ar+Ar@ ⁴ He ₁₀₀₀	42
III.3. Ar+Ar ₄ @ ⁴ He ₁₀₀₀ collision from the bottom	43
III.4. Ar+Ar ₄ @ ⁴ He ₁₀₀₀ collision from the top	44
IV.1. Rb ⁺ sinking dynamics	71
IV.2. Rb ⁺ spherical average	72
IV.3. Solvation of Ak cation at the end of each simulation	73
IV.4. Number of He atoms n around the Ak ⁺ ions as a function of t for Ak ⁺ @ ⁴ He ₂₀₀₀ . The blue empty circles or the red empty squares correspond to the first or second definition, respectively, of $n(t)$ explained in the text. The lines are the best fit to the law $n(t) = At$ for the Ak ⁺ @ ⁴ He _{n} complexes up to $n = 5$, see text for explanation.	74
V.1. Energy diagram of the Rb dimer showing the potential curves for the X ¹ Σ _{g} ⁺ and a ³ Σ _{u} ⁺ states [27] and for Rb ₂ ²⁺ [28]. The dashed curve depicts the Coulomb potential. The red shapes show the square of the wavefunction of the vibrational ground state in the X and a potentials. The blue vertical arrows represent the laser photons (not to scale) to illustrate the double ionization process that leads to Coulomb explosion into a pair of Rb ⁺ ions. Figure taken from Ref [99].	90
V.2. (ai)-(ei) Two-dimensional velocity images of Ak ⁺ ions. The white arrows in the bottom right corners indicate the polarization axis of the laser pulses. The annotated white rings designate the regions of the 1 ³ Σ _{u} ⁺ and 1 1 ¹ Σ _{g} ⁺ channels. (aii)-(eii) Kinetic energy spectra of the respective Ak ⁺ ions. Angular covariance maps are shown for the (biii)-(eiii) 1 1 ¹ Σ _{g} ⁺ and (aiv)-(eiv) 3Σ _{u} ⁺ channels. The T _{nozzle} was 11 K for the data in (a) and (b) and 12 K for the data in (c)-(e). Figure taken from Ref. [102]	91
V.3. Schematic of the key elements in the experiment (left). (a) 2D-velocity image of ⁸⁵ Rb ⁺ ions for T _{nozzle} = 12 K (right). The annotated white circles mark the regions of the inner and outer channel, see text. The polarization direction of the laser pulse is displayed in the bottom left corner. (c), (d) Angular covariance maps for the inner and the outer channels respectively. (e) Radial covariance map. The region after the red dashed line (1.72-2.02 kms ⁻¹) has been saturated to highlight the presence of the outer channel. The color bar to the right applies to (c), (d) and (e). Courtesy of Henrik Høj Kristensen [99]	92
V.4. Schematic view: Definition of the angle φ (between the Na ₂ interatomic axis and the line connecting the centers of mass of the droplet and of the dialkali	96
V.5. Snapshots every 0.2 ps following double ionization of Na ₂ on a ⁴ He ₁₀₀₀ nanodroplet	99

V.6. Details of the dynamics following the double ionization of $\text{Na}_2 X^1\Sigma_g^+$ @He ₁₀₀₀	100
V.7. Na^+ kinetic energy shift	105
V.8. Trajectory of the Rb^+ ions	110
V.9. He- Na^+ Koutselos interaction potential	114
V.10.3D representation of the rigid sphere model	115
V.11.Left panel: velocity components v_z ($z // R$) and v_y ($y // r$) of each Na^+ ion as a function of N in the ^4He -TDDFT simulations of $\text{Na}_2(^3\Sigma_u)$ Coulomb explosion on He _{N} , at $t = 0,1$ (black), 0.2 (brown), and 0.3 (green) ps. Right panel: Fitted values of r_2 (see text) as a function of droplet size N for $t_0 = 0$ (blue curve, empty squares), 0.1 (black curve with asterisks), 0.2 (brown curve with asterisks), and 0.3 (green curve with full squares) ps, compared to the $R - R_N$ values obtained in the ^4He -TDDFT simulations (red curve with empty circles).	118
V.12.Time evolution of the angle θ between the Na^+ ion velocity vectors	118
V.13.Final value of the angle θ between the Na^+ ion velocity vectors as a function of N for $\text{Na}_2^{++}@^4\text{He}_N$ Coulomb explosion. Red line: ^4He -TDDFT simulations (with frozen helium density if $N > 15\,000$); Black, brown, and green lines: rigid sphere model, with $t_0 = 0.1$ (black), 0.2 (green), or 0.3 (blue) ps. The last point in each curve is the highest value of N for which the ions could escape de droplet. See text for more details.	119
V.14.Analytical fit of the final value of the angle θ between the Na^+ ion velocity vectors as a function of N for $\text{Na}_2^{++}@^4\text{He}_N$ Coulomb explosion	120
VI.1. $^4\text{He}_N$ - $^4\text{He}_N$ symmetric collision	125
VI.2. Snapshots of two-dimensional cuts in the (y, z) collision at the end of each simulation	127
VI.3. Snapshots of two-dimensional cuts in the (y, z) collision at the end of each simulation for $(b=3R/2)$ and $v = 20\text{ms}^{-1}$ ($L=1650 \hbar$)	129
VI.4. 3D-He ₁₀₀₀ +Vortices	130
VI.5. Time evolution of the total angular momentum and of the vortex contribution L_v for $^4\text{He}_{500} + ^4\text{He}_{500}$ ($b = 3R/2$ and $v = 10 \text{ms}^{-1}$)	131
VI.6. Time evolution of the total angular momentum and of the vortex contribution L_v for $^4\text{He}_{500} + ^4\text{He}_{500}$ ($b = 3R/2$ and $v = 20 \text{ms}^{-1}$)	131
VII.12D density Rb@He ₁₀₀₀	147
VII.2Absorption spectra np \leftarrow ns	149
VII.3Absorption spectra \leftarrow ns	150
F.1. Ar+Ar@ $^4\text{He}_{1000}$ collision	208
F.2. Ar+Ar+Ar@ $^4\text{He}_{1000}$	209
F.3. Ar+Ar ₄ @ $^4\text{He}_{1000}$ collision par le bas	210
F.4. Ar+Ar ₄ @ $^4\text{He}_{1000}$ collision par le haut	211
F.5. Dynamique de solvataion de Rb^+	217
F.6. Rb^+ moyenne sphérique	218
F.7. Solvatation de Ak^+ à la fin de chaque simulation	219

F.8. Nombre d'atomes d'hélium n autour des ions Ak^+ en fonction de t pour $\text{Ak}^+@^4\text{He}_{2000}$. Les cercles bleus ou les carrés vides rouges correspondent respectivement à la première ou à la deuxième définition de $n(t)$ expliquée dans le texte. Les lignes en pointillés correspondent au fit $n(t) = At$ pour les complexes $\text{Ak}^+@^4\text{He}_n$ jusqu'à $n = 5$, voir le texte pour explication.	220
F.9. Influence de l'orientation de $\text{Na}_2(a, ^3\Sigma_u^+)$ φ par rapport à la surface de la nanogoutte sur la distribution d'énergie cinétique des ions Na^+	231
F.10. Déviation des ions Rb^+ par la nanogoutte	232
F.11. $^4\text{He}_N$ - $^4\text{He}_N$ symmetric collision	236
F.12. 3D- He_{1000} +Vortex	238
F.13. Instantanés de coupes bidimensionnelles dans la collision $^4\text{He}_N$ - $^4\text{He}_N$ à la fin de chaque simulation	239
F.14. Evolution temporelle du moment angulaire total et de la contribution des vortex L_v pour la collision $^4\text{He}_{500} + ^4\text{He}_{500}$ ($b = 3R/2$ et $v = 10 \text{ ms}^{-1}$).	240
F.15. Evolution temporelle du moment angulaire total et de la contribution des vortex L_v pour la collision $^4\text{He}_{500} + ^4\text{He}_{500}$ ($b = 3R/2$ et $v = 20 \text{ ms}^{-1}$).	240
F.16. 2D density $\text{Rb}@^4\text{He}_{1000}$	245
F.17. Spectres d'absorption $n\text{p} \leftarrow n\text{s}$	246
F.18. Spectres d'absorption $n's$ or $n'p \leftarrow n\text{s}$	248

LIST OF TABLAS

V.1. Final (asymptotic) kinetic energy of the ions (in eV) following double ionization of the singlet or triplet state in our ${}^4\text{He}$ -TDDFT simulations for a 1000 or 5000-atom droplet, compared to experiment and to gas phase values. In the case of $\text{Na}_2 \ ^3\Sigma_u^+$, N^* values correspond to frozen density simulations, and the extra column (corr*) to the value including a correction to take into account additional energy transferred to helium (see text). Gas phase values are obtained from the value of the Ak^+-Ak^+ interaction at $t=0$; Experimental values are from Kristensen <i>et al.</i> , [99, 102] for mean droplet sizes around 15 000 He atoms.	104
V.2. FWHM of the ions kinetic energy distributions following Ak_2 double ionization on ${}^4\text{He}_N$ from the singlet or triplet electronic state resulting from $\text{Ak}_2(v=0)$ bond length distribution (see text). Experimental values from Kristensen <i>et al.</i> [99, 102].	106
V.3. Angle θ between the ion velocity vectors at the end of the $\text{Ak}_2 \ ^1\Sigma_g^+$ or ${}^3\Sigma_u^+$ Coulomb explosion on a He_N droplet for $N = 1000$ and 5000 for all alkalis. The last row gives the result for $\text{Na}_2 \ ^3\Sigma_u^+$ on additional, larger droplets $N^* = 10000$ to 50000 , where the asterisk indicates that the helium density was maintained frozen during the dynamics. We have checked in the case of $N = 5000$ that the difference between frozen and non-frozen dynamics is less than 0.1°	112
A.1. ${}^4\text{He}$ and ${}^3\text{He}$ physical properties	184
B.2. OT-DFT parameters	185
D.3. Ak_2 Morse parameters and R_- and R_+ distances used to determine the FWHM of the $v = 0$ bond length distribution (see text). The reference for the potential energy curves fitted to obtain the Morse parameters are given in the Ref. row.	189
D.4. Parameters for the one-exponential fit, Eq.(D.3), of the volume effect repulsion. We fitted $\log f(x)$ instead of $f(x)$ to get the A and B parameters, in order to counterbalance the excessive weight of the highly repulsive energies at very short distances.	190

E.5.	Equilibrium configurations for $\text{Ak}_2@^4\text{He}_{1000}$ ground singlet ($^1\Sigma_g^+$) and triplet ($^3\Sigma_u^+$) states. $r_e(\text{Ak-Ak})$ is the Ak_2 equilibrium bond length; $d_{\text{Ak-COM}}$ is the distance of each Ak atom to the helium center of mass; d_{COM} is the distance of Ak_2 center of mass to the droplet center of mass; $V_{\text{D-He}}$ is the dopant (Ak_2 or Ak) interaction energy with the droplet; S_{D} is the solvation energy (see text). The results for $\text{Ak}@He_N$, $N=1000$ (Ref. [87] or 5000 (this work) are given for comparison. The sharp density radius of the droplet is 22.2 Å for $N=1000$ and 38.0 Å for $N=5000$. The total energy of the $^4\text{He}_{1000}$ droplet is -5395.9 K, and that of $^4\text{He}_{5000}$ droplet is -30632.9 K.	191
E.6.	Width of the final angle between the ions velocity vectors $\Delta\theta$ due to Ak_2 $v = 0$ zero-point bond length distribution. It was calculated as the difference of the θ values obtained at R_+ and R_- , the two points defining the FWHM of the bond length distribution.	192
E.7.	Ion kinetic energy upon double ionization of Na_2 $^3\Sigma_u^+$ $@^4\text{He}_{1000}$ as a function of the angle φ between the diatomic axis and the normal to the droplet surface. K_{droplet} or K_{free} stands for the ion going towards or away from the droplet, respectively (except in the case of $\varphi=90^\circ$ where both ions are equivalent). Note that angle values $\varphi < 60^\circ$ are not populated for Na_2 $^3\Sigma_u^+$, but they show how the evolution for other states or alkalis for which smaller angles could be populated.	193
E.8.	Comparison between Rb_2 $^3\Sigma_u^+$ $@^4\text{He}_{1000}$ using the 3-Body $\text{Rb}_2\text{-He}$ interaction from Guillon <i>et al.</i> [117] and the sum of 2-Body Rb-He interactions from Patil[118] (static properties).	193
E.9.	Comparison between 2-body and 3-body interactions on the results of Coulomb explosion of $\text{Rb}_2@^4\text{He}_{1000}$ ($^3\Sigma_u^+$, R_e).	194
F.10.	Main characteristics of the interaction potentials for Ak-He, $\text{Ak}^+\text{-He}$, Ar-He and Ar-Ar involved in this thesis. Second column and third column correspond the equilibrium configuration at distance (R_{eq}) and dissociation energy (De), given in Å and K respectively. References are shown in the fourth column.	195
G.11.	Technical details for the ^4He -TDDFT calculations. The “ * ” mark means that several grid sizes were taken in order to address small (few thousands ^4He atoms) and big droplets. On the other hand, “ * ” correspond to those dynamics where a frozen helium droplet was considered.	196

F.12. Énergie cinétique finale (asymptotique) des ions (en eV) suite à la double ionisation de l'état singulet ou triplet dans nos simulations ${}^4\text{He}$ -TDDFT pour une gouttelette de 1000 ou 5000 atomes, par rapport à l'expérience et aux valeurs en phase gazeuse. Dans le cas de $\text{Na}_2 \text{}^3\Sigma_u^+$, les valeurs de N^* correspondent aux simulations à densité gelée, et la colonne supplémentaire (corr*) à la valeur incluant une correction pour tenir compte de l'énergie supplémentaire transférée à l'hélium (voir texte). Les valeurs en phase gazeuse sont obtenues à partir de la valeur de l'interaction Ak^+-Ak^+ à $t=0$; Les valeurs expérimentales proviennent de Kristensen <i>et al.</i> , [99, 102] pour des gouttelettes moyennes d'environ 15 000 ${}^4\text{He}$ atomes.	226
F.13. FWHM des distributions d'énergie cinétique des ions suite à la double ionisation de Ak_2 sur ${}^4\text{He}_N$ dans l'état électronique singulet ou triplet, résultant de la distribution de longueur de liaison de $\text{Ak}_2(v=0)$ (voir texte). Les valeurs expérimentales sont de Kristensen <i>et al.</i> [99, 102].	228



Ernesto García Alfonso

PhD student

-  November 14th, 1996
-  Toulouse, France
-  +33 762995175
-  ernestogarciaalfonso96@gmail.com
-  <https://github.com/ErnestoGarciaALfonso>
-  <https://www.researchgate.net/profile/Ernesto-Garcia-Alfonso-2>

Skills

Spanish (mother tongue)


English (B2)

French (B1)

About me

During my free time, I like reading mystery and fiction books and practising some sports such as football, volleyball and biking. I like to spend time with my family and friends. I enjoy team work.

Education

 PhD: October 1st 2021-current


Title: Dynamics of pure and doped superfluid Helium droplets using ⁴He-TDDFT simulations.

Lab: Laboratoire Collisions Agrégats Réactivité (LCAR)

Thesis advisor: Nadine Halberstadt

- Superfluid ⁴He_N nanodroplets
- Helium Time Dependent Density Functional Theory (⁴He TD-DFT)
- Clusterization of foreign atoms within ⁴He nanodroplets.
- Quantum Vortices
- Coalescence of ⁴He_N nanodroplets
- Coulomb explosion of Ak₂ on ⁴He_N nanodroplets

During my PhD, I have developed and/or improved some skills such as teamwork, Fortran 90, C++ and Python programming as language, handling GIT-HUB repositories, and Unix system. I have delivered a certain amount of speeches both international and national. I have written papers which they have been very useful when writing in Latex code (scientific writing program)

 2015–2020

Master in physics. Havana University, Physics Faculty. Title: "Study of the Vibrational Predissociation of the NeBr₂ Complex by Computational Simulation Using the Trajectory Surface Hopping Method".

Thesis advisor: Maykel Marquez Mijares and Jesús Rubayo Soneira

- Van der Waals complexes
- Quasiclassic Method
- Trajectory Surface Hopping (TSH)
- C++ language (I built my own package for calculating TSH)
- Wolfram Mathematics

Conferences

Participation in national/international Conferences
[Poster (4/6) and Oral Presentation (5/10)]

[https://github.com/ErnestoGarciaALfonso/](https://github.com/ErnestoGarciaALfonso/Experience/blob/main/Professional_experience.pdf)

Experience/blob/main/Professional_experience.pdf



Publications

In international journals with peer review (9) <https://github.com/ErnestoGarciaALfonso/List-of-Papers/blob/main/Papers.pdf>

Stay Abroad

*[07/2019–10/2019] Participation. Project "Theoretical study of helium nanodroplets dynamics: alkali dopants and quantum Vortex; rare gas dopants and cluster formation" in Toulouse, France. Participants: Nadine Halberstad, Manuel Barranco and Martí Pi from University of Barcelona.

*[04/03-27/2024] "Photodissociation of Ak₂ induced by the helium environment. A DIM (Diatomics in Molecules) model to describe the interactions between the diatomic and the ⁴He_N nanodroplet and the couplings between the electronics states of the diatomic molecule induced by helium". Consejo Superior de Investigaciones Científicas (CSIC), Madrid Spain.

Membership

2023 Confined Molecular Systems: From a new Generation of Materials to the Starts (COSY) Work Group 4

 Publications

- 2024 Ernesto García-Alfonso, Manuel Barranco, Nadine Halberstadt and Martí Pi. "Time-resolved solvation of alkali ions in superfluid helium nanodroplets". *J. Chem. Phys.* 160, 164308 (2024)
- Loidel Puentes-Milián, Ernesto Garcia-Alfonso, Maykel MARQUEZ-MIJARES, and Jesús Rubayo-Soneira. "Vibrational predissociation study of NeIBr(A) using Quasiclassical Trajectories and Trajectory Surface Hopping methods". *Chemical Physics Letters.* 849, 141427 (2024)
- 2023 Loidel Puentes-Milián, Ernesto Garcia-Alfonso, Maykel MARQUEZ-MIJARES, and Jesús Rubayo-Soneira. "NeI2 Photofragmentation Dynamics Through Quasiclassical and Semiclassical Studies". *ChemPhysChem* e202300406, 2023
- Ernesto García-Alfonso, Francesco Ancilotto, Manuel Barranco, Martí Pi, Nadine Halberstadt. "Quantized vortex nucleation in collisions of superfluid nanoscopic helium droplets at zero temperature". *J. Chem. Phys.* 159, 074305 (2023)
- 2022 Ernesto García-Alfonso, Maykel Márquez-Mijares, Jesús Rubayo-Soneira, Nadine Halberstadt, Kenneth C. Janda and Craig C. Martens. "Photofragmentation dynamics study of ArBr₂ ($\nu = 16 \dots 25$) using two theoretical methods: trajectory surface hopping and quasiclassical trajectories". *Eur. Phys. J. D.* 76, 79. 2022.
- Ernesto García-Alfonso, Manuel Barranco, David A. Bonhommeau, Nadine Halberstadt, Martí Pi and Florent Calvo. "Clustering, collision, and relaxation dynamics in pure and doped helium nanoclusters: Density - vs particle -based approaches". *The Journal of Chemical Physics.* 157, 014106. 2022.
- 2020 Ernesto García-Alfonso, Francois Coppens, Manuel Barranco, Martí Pi, Frank Stienkemeier and Nadine Halberstadt. "Alkali atoms attached to vortex-hosting helium nanodroplets". *The Journal of Chemical Physics.* 152, 194109. 2020.
- Ernesto García-Alfonso, Maykel Márquez-Mijares, Jesús Rubayo-Soneira, Nadine Halberstadt, Kenneth C. Janda and Craig C. Martens. "Study of the Vibrational Predissociation of the NeBr₂ Complex by Computational Simulation using the Trajectory Surface Hopping Method". *Sigma Mathematics.* 8, 2029. 2020.
- 2019 C. Calvo-Mola, S. López Pérez, E. García Alfonso, and J. Cerutti-Torres. "Determination of the Planck Constants through the use of LEDs". *Revista Cubana de Física,* 36, 125. 2019.

Conferences

- 07/1-5/2024 **Oral Presentation** 24th European Conference on the Dynamics of Molecular Systems, Aarhus, Denmark.
- 06/23-26/2024 **Poster** The 15th International Conference on Quantum Fluid Clusters, Aarhus, Denmark.
- 06/18-21/2024 **I have run a section in the training school** COST COSY training school "Confined molecular systems in Helium nanodroplets" at Eli beamline, Prague, Czech Republic.
- 01/03-09/2024 **Poster** Molecular and Ionic Clusters. Gordon Research Conference (GRC). Ventura (California). United States. (Due to U.S policy aim to Cuban people I was unable to get a visa, so Nadine Halberstadt presented my poster on site)
- 07/03-07/2023 **Oral Presentation+Poster** Congrès Général des 150 ans de la Société Française de Physique. Paris, France
- 06/20-21/2023 **Poster** AtmChemClimate workshop in Montpellier. France
- 06/01-02/2023 **Oral Presentation** XVèmes Journées de l'ED. Toulouse
- 03/01-03/2023 **Oral Presentation** First COSY General Meeting, Cadiz, Spain.
- 01/24/2023 **Oral Presentation** First meeting of the CONFINED MOLECULAR SYSTEMS: FROM A NEW GENERATION OF MATERIALS TO THE STARS (COSY), COSY Working Group 4 (Helium nanodroplets in science and engineering) (online)
- 11/11/2022 **Poster** (online) PHOTODYNAMICS 2022, XI International Meeting of Photodynamics, La Havana, Cuba
- 11/7-8/2022 **Oral Presentation** Les Toulousaines du Calcul Atomique et Moléculaire (TouCAM), Toulouse, France
- 10/19/2022 **Oral Presentation** at Instituto de Física Fundamental (IFF-CSIC) Departamento de Procesos Atómicos, Moleculares y en Superficies Consejo Superior de Investigaciones Científicas, Madrid Spain. "*Coulomb Explosion of Alkali Dimers on Helium Droplets. Is Really Triplet State Dominant?*"
- 09/05-09/2022 **Participation in training school** "Machine Learning and Quantum Computing for Quantum Molecular Dynamics" (CECAM-FR-MOSER). Gustave Eiffel Université, (Paris), France.
- 08/7-12/2022 **Poster** Molecular and Ionic Clusters. Gordon Research Conference (GRC) , Lucca (Barga), Italy.
- 08/6-7/2022 **Oral Presentation** Molecular and Ionic Clusters. Gordon Research Seminar (GRS) , Lucca (Barga), Italy.
- 04/18-23/2022 **Oral Presentation + Poster** The 14th International Conference on Quantum Fluid Clusters, Erice, Sicily, Italy.
- 03/10-11/2022 **Poster** NanoX-FerMI days. Toulouse, France.
- 11/2021 **Oral Presentation** Réunion annuelle du GDR THEMES. Toulouse, France.
- 06/2021 **Oral Presentation** (online). XV Taller de Física de la Materia Condensada y Molecular. Cuernavaca, Morelos, Mexico.
- 10/2020–08/2021 I taught Atomic and Molecular Physics online (on-site classes were forbidden because of COVID-19) to two groups of 3rd year (20 students each)
- 03/2020 **Poster**. XV Simposio y XIII Congreso de la Sociedad Cubana de Física. La Habana, Cuba.
- 03/11-15/2019 **Oral Presentation** VIII Taller Iberoamericano de Enseñanza de la Física Universitaria. ("Determination of the Planck Constants through the use of LEDs") La Havana, Cuba
- 2018 **Presentation** Scientific day ICIMAF ("Study of the Vibrational Predissociation of the NeBr₂ Complex by Computational Simulation using the Trajectory Surface Hopping Method") Cuba

-
- 2018–2021 **Participation**. Research Project (National Basic Sciences Program). “*Study of confinement, relaxation and energy transfer processes of atomic and molecular systems*”. Department of Atomic and Molecular Physics. Higher Institute of Technologies and Applied Sciences (InSTEC), University of Havana. Cuba
- 2016–2017 **Participation**. InSTEC Research Project (Financier: InSTEC). Physico-chemical study of atomic and molecular systems with interest for the environment. Department of Atomic and Molecular Physics. Higher Institute of Technologies and Applied Sciences (InSTEC). Cuba

Titre : Etude théorique de la dynamique de nanogouttes d'hélium superfluide : formation d'agrégats, solvation d'ions, explosion coulombienne, et nucléation et détection de vortex quantiques.

Mots clés : Hélium superfluide, 4He-(TD)DFT, solvation d'ions, explosion coulombienne, vortex quantiques, collisions entre nanogouttes

Résumé : On étudie des processus dynamiques de nanogouttes d'hélium-4 (HND), en relation avec des expériences. Les HND sont des agrégats de centaines à des centaines de milliards d'atomes d'⁴He aux propriétés remarquables : très basse température (~0.4K), superfluidité, capacité à capturer n'importe quel dopant, interaction faible avec tout atome ou molécule. Les processus étudiés se rangent selon deux axes: caractérisation de propriétés superfluides dans un système de taille finie (nucléation et détection de vortex quantiques), et utilisation de HND comme environnement idéal pour étudier la spectroscopie et la dynamique de dopants (formation d'agrégats, solvation d'ions et explosion coulombienne).

L'outil principal des simulations est l'approche de la fonctionnelle de la densité d'hélium indépendante(4He-DFT) ou dépendante du temps (4He-TDDFT). Elle permet de simuler la structure et la dynamique de gouttelettes de plusieurs milliers d'atomes et donne un aperçu détaillé de la dynamique du système qui n'est pas accessible expérimentalement : visualisation des couches de solvation, nature des excitations de l'hélium

On étudie la formation d'agrégats de gaz rares (Rg) en nanogouttes en modélisant la collision d'un atome de Rg avec un agrégat solvato de n atomes pour former l'agrégat (n+1). La 4He-TDDFT, qui décrit mieux les effets quantiques et de superfluidité, est comparée à des méthodes atomistiques approchées. Plusieurs résultats sont communs: on n'obtient généralement pas la configuration la plus stable en phase gazeuse, mais un isomère avec moins de liaisons, et/ou des structures diluées par la couche rigide de solvation d'hélium autour des atomes Rg.

La solvation de cations d'alcalins (Ak) dans les HND est simulée parallèlement à des expériences du groupe de Stapelfeldt (Aarhus) d'ionisation soudaine de l'atome Ak initialement en surface, en complément d'études antérieures sur Na⁺. L'objectif est d'éclairer les étapes élémentaires de la solvation. La formation de la première couche de solvation des ions s'avère progressive, et compatible avec un mécanisme de Poisson où chaque hélium se lie à l'ion de façon indépendante. Pour les alcalins plus légers, cette couche est incomplète à la fin de la dynamique, ce qui indique un contrôle cinétique plutôt que thermodynamique de sa formation.

Des simulations d'explosion coulombienne par ionisation instantanée de molécules Ak₂ initialement en surface de nanogouttes sont effectuées afin de comprendre l'effet des HND sur la dynamique de fragmentation d'Ak₂⁺⁺. L'expérience correspondante menée dans le groupe de Stapelfeldt visait à mesurer la proportion d'état triplet/singulet dans la formation d'Ak₂, et à imager la fonction d'onde vibrationnelle. On examine dans les simulations l'influence de la taille des nanogouttes, du mouvement de point zéro de la vibration d'Ak₂ et de la distribution d'orientations d'Ak₂ en surface. Les résultats valident l'approche expérimentale et montrent une importance inattendue de la courbure des trajectoires des ions qui pourrait être utilisée pour mesurer la taille des gouttelettes, ce qui n'a été possible jusqu'à présent que pour de très grandes tailles (par diffraction des rayons X)

La nucléation de vortex quantiques, caractéristique de la superfluidité, a été démontrée dans de très grosses gouttelettes (VLD) et attribuée au moment angulaire créé par friction du liquide dans la buse avant expansion et refroidissement. On étudie ici les collisions entre gouttelettes comme mécanisme alternatif. Les résultats montrent la nucléation de tourbillons quantiques au niveau d'indentations de la gouttelette fusionnée, un mécanisme général pour toutes les tailles. Cependant, aucune signature n'a été trouvée jusqu'à présent pour détecter des vortex dans les plus petites gouttelettes. Ce travail propose la spectroscopie de fluorescence d'atomes Ak en montrant qu'un vortex déplace et élargit leur spectre de façon mesurable au-dessus des premiers états excités.

Title: Theoretical study of superfluid helium nanodroplet dynamics: cluster formation, ion solvation, Coulomb explosion, and nucleation and quantum vortex detection.

Key words: Helium Superfluid, 4He-(TD)DFT, Ion solvation, Coulomb explosion, Quantum vortices, collisions between nanodroplets

Abstract: Several dynamical processes involving Helium-4 nanodroplets (HNDs) are studied theoretically, in relation with experiments. HNDs are clusters of several hundred to several hundred billions of ⁴He atoms which exhibit remarkable properties: very low temperature, T~0.4K, superfluid properties, ability to pickup any dopant, weak interaction with any atom or molecule. The studied processes reflect the two main interests in HNDs: characterizing superfluid properties in a finite-size system (quantum vortex nucleation and detection), and using HNDs as an ideal environment to study dopant spectroscopy and dynamics (clustering, ion solvation, and Coulomb explosion).

Extensive simulations are conducted using 4He-Density Functional Theory (4He-DFT) and its time-dependent version (4He-TDDFT). This approach can successfully simulate the equilibrium and dynamics of droplets of several thousand of atoms and provide detailed insight into the structural dynamics of the entire system which is not accessible experimentally: visualization of solvation shells, nature of helium droplet excitations.

Rare gas (Rg) cluster formation is studied inside HeN under realistic conditions where one Rg atom collides with a solvated n-atom cluster to form the (n+1)-atom cluster. The 4He-DFT simulation results are compared to those of approximate atomistic approaches. Although quantum and superfluidity effects are better described with 4He-TDDFT, several common features are demonstrated. The most stable gas phase configuration is usually not produced, but an isomer with fewer bonds instead, and/or more dilute structures because of the rigidity of the helium solvation shell around the Rg atoms.

The sinking of alkali (Ak) cations in HNDs is simulated in parallel with experimental investigations in the group of Stapelfeldt (Aarhus), in complement to earlier studies on Na⁺ sinking. It aims at shedding some light on the primary steps of solvation, by suddenly ionizing the alkali atom sitting in a dimple at the droplet surface. The build up of the first solvation shell around the ions is shown to be progressive, pointing to a Poissonian mechanism in which each He atom binds independently to the ion. For the lighter alkalis, the solvation shell is incomplete at the end of the dynamics, suggesting a kinetic rather than thermodynamical control of its formation.

Coulomb explosion simulations of Ak₂ molecules initially sitting at the droplet surface and suddenly ionized are conducted in order to understand the effect of the HNDs on Ak₂⁺⁺ fragmentation dynamics. The corresponding experiment in Stapelfeldt's group in Aarhus aimed at measuring the proportion of triplet to singlet state in the formation of Ak₂, and at imaging the vibrational wave function. Several parameters are examined in the simulations: droplet size, zero point motion of Ak₂ vibration, and orientational distribution of Ak₂ on the droplet surface. The results validate the experimental approach, and evidence an unexpected curvature of the ion trajectories which could be used to measure droplet sizes individually, something that has only been possible up to now for very large sizes (by X-ray diffraction).

The nucleation of quantum vortices, a characteristic of helium superfluidity, has been revealed in very large droplets (VLD) and attributed to angular momentum created by friction of the liquid in the nozzle prior to expansion and cooling. Here droplet-droplet collisions are explored as an alternative mechanism. The results show the nucleation of quantum vortices at indentations of the merged droplet, a mechanism general for all droplet sizes.

However, no signature has been found to detect vortices in smaller droplets so far. In this work, fluorescence absorption or excitation spectroscopy of alkali atoms is proposed: a vortex is shown to shift and broaden the alkali spectrum. The effect could be measurable above the first excited states.